DISSERTATION

MEASUREMENT OF THE MUON ANTI-NEUTRINO CHARGED CURRENT DOUBLE DIFFERENTIAL CROSS SECTION WITH NO PIONS IN THE FINAL STATE ON WATER USING THE PI-ZERO DETECTOR AT T2K

Submitted by

Thomas Campbell

Department of Physics

In partial fulfillment of the requirements

For the Degree of Doctor of Philosophy

Colorado State University

Fort Collins, Colorado

Spring 2018

Doctoral Committee:

Advisor: Walter Toki

Sandra Biedron
Norm Buchanan
Robert J. Wilson

ABSTRACT

MEASUREMENT OF THE MUON ANTI-NEUTRINO CHARGED CURRENT DOUBLE DIFFERENTIAL CROSS SECTION WITH NO PIONS IN THE FINAL STATE ON WATER USING THE PI-ZERO DETECTOR AT T2K

The T2K (Tokai to Kamioka) experiment is a long baseline neutrino oscillation experiment where a narrow band (by energy) neutrino beam of primarily muon neutrinos or muon anti-neutrinos is produced in Tokai and directed towards Kamioka in Japan. Neutrinos in the beam are first detected at the T2K near detector complex 280 m from the beam source (ND280) and then travel 295 km before being detected again at the Super-Kamiokande (Super-K) water-Cherenkov detector. In addition to measuring the flux of neutrinos in the T2K beamline en route to Super-K, other physics analyses are performed at ND280. This thesis describes one such measurement where the π^0-detector (PØD) and a time projection chamber at ND280 were used to measure the charged-current cross section for muon anti neutrinos with water as the interaction target and no pions in the final state. Such a cross section is a T2K and world first. This cross section was measured differentially by the outgoing lepton true kinematics using a binned likelihood fitting framework recently developed at T2K. The thesis will provide: an introduction to neutrinos in the context of a cross section measurement, a description of the T2K experiment including common software tools used in analysis, a general discussion of concerns in differential cross section measurements, a mathematical formulation of the likelihood fitting procedure, details of the neutrino event selection process, the chosen parameterization and validation of the fit, and finally, the cross section results in data with a discussion of the significance and conclusions of the measurement.

The total cross section integrated over all differential bins considered in the analysis is measured to be:

$$\sigma = (7.844 \pm 1.316) \times 10^{-39} \frac{\text{cm}^2}{\text{water molecule}}$$

TABLE OF CONTENTS

LIST OF TABLES

LIST OF FIGURES

Chapter 1

INTRODUCTION

This thesis describes a measurement of the muon anti-neutrino ($\overline{\nu}_\mu$) induced charged current cross section with no pions in the final state (CC-0π) where water is the interaction target using the π^0-detector (P$\emptyset$D) at the Tokai to Kamioka (T2K) neutrino oscillation experiment in Japan. Introductory material needed to understand what the previous statement means will be first presented, followed by a detailed description of the analysis which includes the neutrino event selection, analysis strategy, validation of the framework used, and data results. This measurement is both a T2K and a world first measurement of its kind. The main utility of the analysis is a recently developed likelihood fitting framework that was developed to address some very important issues in cross section measurements that many past neutrino cross section analyses have had difficulty handling properly. The structure of the document will be as follows.

The first chapter will introduce the reader to all the necessary concepts and background information needed to understand a cross section measurement at T2K. This will also motivate why such a measurement is interesting to the larger neutrino community. A general introduction to neutrino physics is first presented followed by the experimental details of T2K. The procedure for collecting data using the T2K detectors as well as the simulation of the response of the detectors to neutrino interactions will then be discussed. Finally, specific software tools at T2K used in this analysis for the selection of neutrino events in data and simulation as well as the propagation of systematic uncertainties will be introduced.

With all the basic knowledge of neutrino interactions at T2K and some ideas about cross section measurements, the second chapter will present additional, more in-depth conceptual details of problems faced by many cross section measurements made today. This should also serve to motivate why this specific measurement and the methods used to produce it are of

interest and importance to the neutrino cross section community by the introduction of a problem common to many cross section analyses.

The third chapter mathematically formulates a solution to the problem introduced in the second chapter. The formulation is kept general so that future readers of this document might more easily see how a similar solution could be adopted to a problem they face in their work.

Chapter four will focus on the selection of neutrino events in the T2K data for this analysis and will present both the details of the selection procedure and simulated studies of how well it performs.

All of the necessary introductory material being in place to discuss the thorough details of the analysis, the fifth chapter presents the detailed description of the analysis including the parameterization of the problem in the likelihood fit, propagation of uncertainties to the final results, and rigorous validation tests of the likelihood framework.

The document then concludes with a description of procedures followed when unblinding the analysis to real data, a presentation of the data results and a discussion of their significance.

Before embarking on this journey through a neutrino cross section measurement, a brief aside highlighting some of my additional contributions at T2K outside of those presented in the remainder of the document:

I played a major role in an analysis that resulted in a Physical Review D publication in July of 2017. This analysis was to measure the charged current inclusive cross sections for both muon neutrinos and muon anti-neutrinos and form the ratio of the two. This was an example of a single bin measurement. The next chapter of this thesis will explain the differences between this sort of measurement and the much more complicated and subtle measurement like the one detailed in the remainder of the document. I co-authored a T2K internal technical document on the analysis as well as the actual PRD publication and of course served on the various T2K committees that take an analysis from technical note to journal publication.

For the ratio analysis, a PØD reconstruction-only selection was used as the primary selection. I developed a parallel selection in the Highland 2 framework that served as a valuable utility for making cross checks and validating the PØD standalone selection. Using this selection I was also able to perform in-depth studies of the uncertainty arising from the simulated beam flux which served also as validation for the methods used in the PØD standalone work. I also performed studies on how the selection could be improved and developed tools in the PØD standalone selection that were implemented in the final used framework. Finally on this point, I helped address the impact on the ratio analysis of some very subtle and only recently surfaced concerns regarding efficiency corrections in a one bin measurement. Many of the problems we faced with these topics served as driving motivation for many of the methods used in the thesis analysis. A description of some of these problems is presented in the second chapter.

Outside of physics analysis, I have also contributed in the operation and maintenance of the ND280 detectors. I was involved in work where two of the PØD water bags and several water level monitoring sensors were replaced. I also performed a calibration of all of the water sensors during that work. I also helped in two different attempts to measure the mass of water in a collection of individual water bags and made measurements to classify and roughly quantify a 'bulging' effect of the PØD. This work is mentioned again later in the document. I have also several times served as the 'PØD Water Expert' when ND280 was taking data where I was responsible for monitoring and diagnosing problems with the water system.

In addition to work relevant only to the PØD, I have played a major role in operation of the other Trip-t detectors (TTD) including a great deal of work transitioning the PØD into a unified framework for one particular aspect of how the TTD detectors are operated. Similar to the PØD expert shifts, I served also several times as the TTD Expert where I was responsible for monitoring and operating certain aspects of all the Trip-t detectors. I also served for one data collection period as the TTD Coordinator where I was responsible for generally overseeing operations of the TTD system throughout the run period. I made sure

that expert shifts were filled for that running period, provided training for new experts and served as a point of contact for when issues arise that the expert could not solve themselves.

I also wrote an MS thesis detailing a mathematical formulation of how the vanilla Standard Model can be altered to accommodate neutrino mass generation through several different generalized Higgs mechanisms. This thesis also included a calculation using public T2K oscillation results to demonstrate how well one of these theories agrees with observation.

The work described in the remainder of this document was also written up in an internal T2K document and is in the final stages of the T2K internal review process. The work is expected to make it into an additional publication in the coming months.

On the subject of this analysis, as will be argued in this chapter, such a measurement can help theorists developing neutrino cross section models to tune the parameters in their models. This can be said of any well done cross section measurement. It is the opinion of the author that the contributions of this work go much farther than just to help tune future models. The second chapter will include a general discussion of a problem in experimental cross section measurements that many past analyses to have come out of T2K and other experiments have arguably failed to properly address. The methods used in this analysis were developed with this problem in mind, and this analysis is the first example of an application of those methods for the measurement of a double differential cross section and additionally for the measurement of a cross section whose interaction target is isolated. The application of the ideas presented here along with their validation might help future cross section analyzers perform better measurements which in turn benefit the whole of the neutrino physics community.

1.1 Introduction to Neutrinos

First postulated by Wolfgang Pauli in 1930 to preserve energy and momentum conservation in nuclear beta decay observations, neutrinos are neutrally charged, massive, weakly interacting fundamental particles. They are present throughout the universe and can be created in a laboratory. They have enjoyed quite the interesting journey though physics during the last almost 100 years including the award of many Nobel prizes for measurements of their properties. They have been given the distinctive colloquial name of 'ghost particle.' This name is both interesting and descriptive: because neutrinos interact only via the weak nuclear force and gravity, they rarely interact (besides gravitationally) with ordinary matter. As many as 100 billion [1] neutrinos produced in nuclear reactions in the sun pass through your thumb nail each second. Many of these neutrinos (during the daytime) will then pass from thumb straight all the way through the earth to continue on their cosmic journey without interacting with anything at all. When propagating through a medium of solid lead, an interaction mean free path of neutrinos of a particular energy is around a light year. Surely even ghosts would tire after passing through so much lead; however, neutrinos do not.

1.1.1 The Standard Model

Because neutrinos are fundamental particles, they have a spot reserved for them in the Standard Model of Particle Physics next to other more familiar fundamental particles such as the electron fermion. The set of fundamental particles in the Standard Model is comprised of matter particles (particles that make up matter) and force exchange particles (vector bosons) that mediate the fundamental forces between particles of the Standard Model. Additionally, the recently discovered Higgs particle can generate mass for the massive fundamental particles. The matter particles are divided into two sub-classes: quarks and leptons. All of the ordinary matter that surrounds us every day is comprised of only 2 types of quarks (up and down) and one type of lepton (electron). Figure 1.1 provides a chart summarizing the fundamental particles in the Standard Model.

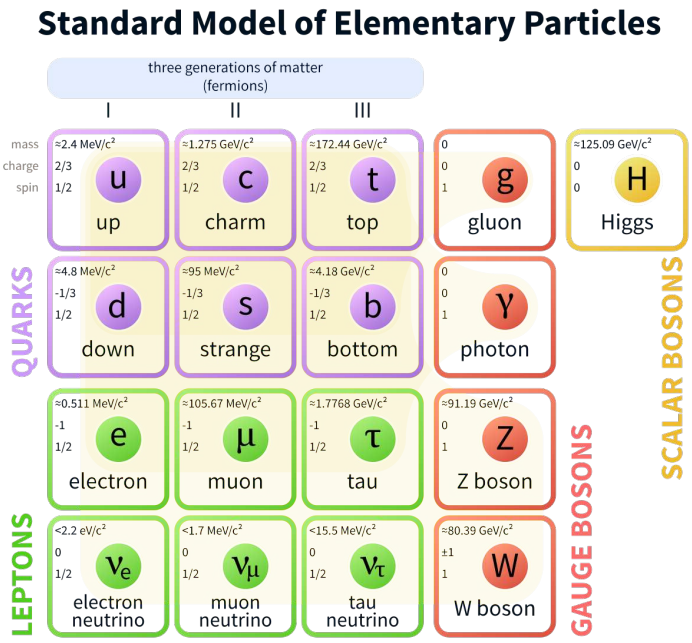

Figure 1.1: Pictorial summary of fundamental particles in the Standard Model taken from [2].

For neutrino interaction physics, we are concerned only with the bottom portion of this table which contains the leptons and the weak nuclear force mediation exchange bosons (the W and the Z). We see that in addition to the familiar electron, e, there are two heavier charged leptons, the μ and the τ. Below each of the charged leptons is a neutrino labeled by the charged lepton above it. There are three types of neutrinos we know of, one corresponding to each charged lepton, e, μ, and τ. They are labeled as such: ν_e, ν_μ, and ν_τ. Along with each particle in the Standard Model, there is also a corresponding anti-particle with the same mass, but opposite electric charge for charged particles, and for neutrinos, opposite helicity which is a measure of the alignment (or anti-alignment) of the particles spin angular momentum with its linear momentum.

The neutrino/charged lepton pairs form what is called a weak isospin doublet in the Standard Model. These doublets are locally gauge invariant under a SU(2)xU(1) symmetry which leads to the required existence of the photon and W and Z bosons. The vanilla Standard Model assumes massless neutrinos, which we now know not to be the case. The

author's Master's thesis [3] has a nice mathematical formulation of the gauge symmetries of the Standard Model and additionally a demonstration of alterations that can be made to the Standard Model to generate mass for the neutrinos by altering the Higgs mechanism.

1.1.2 Cross Sections

Particle interactions are classified primarily through their cross sections. This subsection will introduce the concept of a cross section in particle scattering starting with a very basic classical example and then build to how cross sections are calculated in the Standard Model formalism, hopefully also painting a picture for the reader along the way of how a cross section might be measured in experiment.

A working definition of a scattering cross section is as follows. For a flux, Φ of incident particles on some target, the differential cross section, $\frac{d\sigma}{d\Omega}$, is defined by,

$$\frac{d\sigma}{d\Omega} = \frac{1}{\Phi}\frac{dn}{dt}$$

where $\frac{dn}{dt}$ is the rate of scattered particles traveling through differential solid angle, $d\Omega$, far from the scattering target.

The classical, non-differential equivalent definition: the total cross section is defined to be the number of particles that scatter per unit time per incident flux. With this definition, the basic illustrative example proceeds.

Figure 1.2 provides a schematic of a very simple classical scattering problem. During some unit of time a flux, Φ, of point particles is incident on a target of cross sectional area, a. Some of the particles physically collide with the target and scatter. Suppose in some area, A with $A > a$, some N incident particles per unit time reach the target plane, and n of those particles scatter. Consider the classical total cross section definition previously introduced:

$$\sigma = \frac{n}{\Phi} = \frac{n}{\frac{N}{A}} = \frac{n}{N}A$$

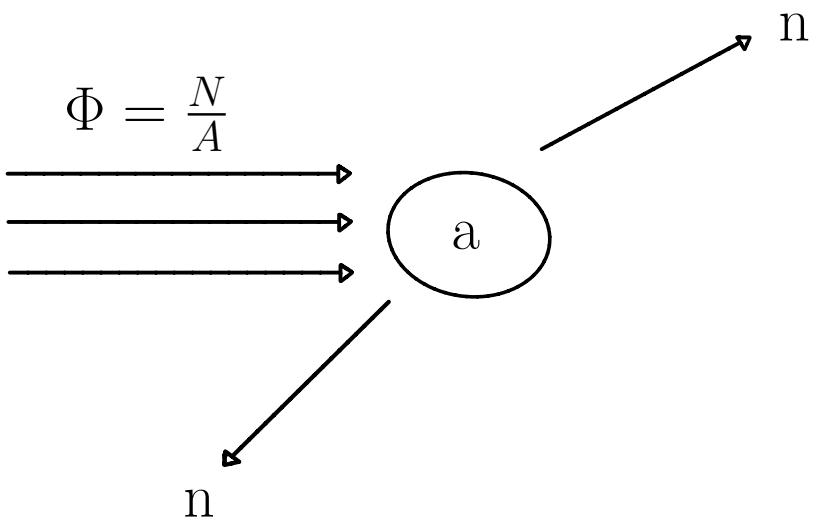

Figure 1.2: Diagram of a flux of point particles scattering off of target with cross sectional area a. The number of particles that scatter is n. N particles are incident through some area, A ($A > a$) so that the flux is: $\Phi = \frac{N}{A}$.

The quantity $\frac{n}{N}$ is just the fraction of the particles that scatter, which in this simple geometrical example is also given by, $\frac{a}{A}$, so that:

$$\frac{n}{\Phi} = \frac{a}{A}A = a$$

In this example, the total cross section, $\sigma = \frac{n}{\Phi}$, is seen to be equal to the cross sectional area of the target. In general, classical scattering cross sections will always be related to some physical cross sectional area that the two objects scattering off of one another 'see.' Of course, neutrinos being quantum scale fundamental particles will not behave classically; however, very simple single bin measurements of a total cross section in particle physics might look quite similar to the $\frac{n}{\Phi}$ quantity from this example, and furthermore, the general interaction rate per flux idea is common across any cross section measurement.

Experiments do not directly measure the cross section, but rather produce a beam of known flux and then measure rates of the scattered particles. Following this, the cross

section from an experimental point of view can be taken to be defined by,

$$R = \sigma\Phi$$

where R is the rate that experiments actually measure, σ is the cross section, and Φ is the known flux.

The working definition for the differential cross section given above applies both to classical and quantum mechanical scattering. An example of the quantum mechanical case will now be provided.

Figure 1.3 gives a schematic diagram of quantum mechanical scattering for the example here. A standard spherical coordinate system is used where $\theta = 0$ corresponds to the incoming wave function direction. Asymptotic forms are assumed for the wave function before and after scattering. Using the probability current densities for the incoming and scattered wave functions, a cross section result will be obtained.

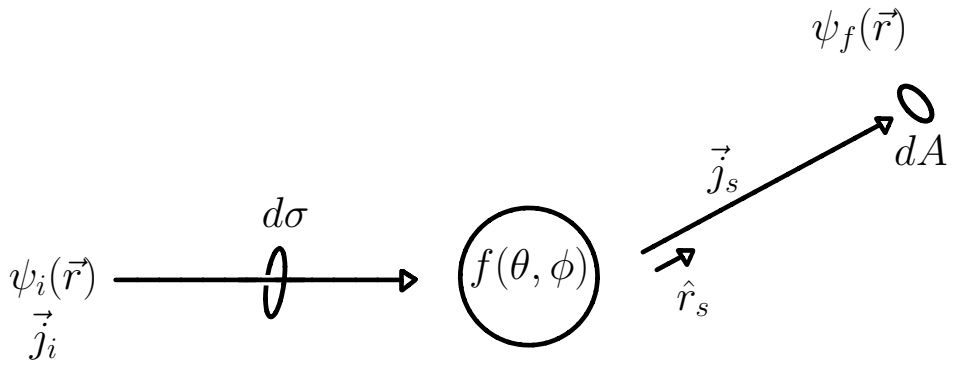

Figure 1.3: Diagram of quantum mechanical scattering. Incoming plane wave, $\psi_i(\vec{r})$, with probability current, $\vec{j}_i$, through differential area, $d\sigma$, scatters with some scattering amplitude of $f(\theta, \phi)$. Far from the interaction after scattering probability current, $\vec{j}_s$, flows through differential area, dA, the wave function has the form of $\psi_f(\vec{r})$.

Before scattering, the wave functions is assumed to have the form of a plane wave:

$$\psi_i(\vec{r}) = e^{i\vec{k}\cdot\vec{r}}$$

After scattering, it is assumed to have the asymptotic form,

$$\psi_f(\vec{r}) = f(\theta,\phi)\frac{e^{i\vec{k}\cdot\vec{r}}}{r}$$

where $f(\theta,\phi)$ is known as the scattering amplitude which classifies the effects of the scattering process and is a function of the angular coordinates.

The total scattered wave function ignoring normalization is then the sum:

$$\psi = \psi_i + \psi_f = e^{i\vec{k}\cdot\vec{r}} + f(\theta,\phi)\frac{e^{i\vec{k}\cdot\vec{r}}}{r}$$

Consider a flux of particles through differential area, $d\sigma$, which then scatter and propagate to differential area, dA, as shown in figure 1.3. Let $\hat{r}_s$ be a unit vector pointing from the scattering center to dA. The rate, R, of particles through each is the same by definition and can be written in terms of the incoming and scattered probability currents labeled in the figure:

$$R = (\vec{j}_i \cdot \hat{k})d\sigma = (\vec{j}_s \cdot \hat{r}_s)dA \tag{1.1}$$

The current operator gives the probability current for a wave function:

$$\vec{j} = \frac{\hbar}{m}\mathrm{Im}\big(\psi^*\vec{\nabla}\psi\big)$$

Substituting the initial and scattered wave functions gives the currents:

$$\vec{j}_i = \frac{\hbar k}{m}$$

$$\vec{j}_s = \frac{\hbar}{m}\mathrm{Im}\left((e^{i\vec{k}\cdot\vec{r}} + f(\theta,\phi)\frac{e^{i\vec{k}\cdot\vec{r}}}{r})^*\vec{\nabla}(e^{i\vec{k}\cdot\vec{r}} + f(\theta,\phi)\frac{e^{i\vec{k}\cdot\vec{r}}}{r})\right)$$

For equation 1.1, only the radial component of the gradient is needed because of the dot product into $\hat{r}_s$. Pulling off only the leading order, radial term that is purely imaginary and neglecting terms with an complex exponential that will rapidly oscillate (and average to 0 anyway), $\vec{j}_s$ becomes:

$$\vec{j}_s = \frac{\hbar}{m}\left(k\frac{f^*(\theta,\phi)f(\theta,\phi)}{r^2} + O(\frac{1}{r^3})\right) \approx \frac{\hbar k}{m}\frac{|f(\theta,\phi)|^2}{r^2} \tag{1.2}$$

Substituting the probability currents into equation 1.1 gives,

$$\frac{\hbar k}{m}\frac{|f(\theta,\phi)|^2}{r^2}dA = \frac{\hbar k}{m}\frac{|f(\theta,\phi)|^2}{r^2}r^2 d\Omega = \frac{\hbar k}{m}d\sigma$$

where $d\Omega$ is the differential solid angle in terms of the angular coordinates. The differential cross section is then given by:

$$\frac{d\sigma}{d\Omega} = |f(\theta,\phi)|^2 \tag{1.3}$$

The differential cross section has the loose interpretation of being the probability for a single particle incident on a target being observed scattered at solid angle $d\Omega$.

Moving from non-relativistic to relativistic quantum mechanics, the wave functions become spinors and the operators take on new forms. A thorough mathematical formulation of some of this can be found in the author's Master's thesis [3]. Even with the different mathematical framework of relativistic quantum mechanics, equation 1.3 takes a very similar form[4].

$$d\sigma = |\mathscr{R}|^2\frac{dQ}{F} \tag{1.4}$$

The role of the scattering amplitude is now played by the *invariant amplitude*, $\mathscr{R}$; it is where all of the real physics in a scattering calculation resides. The remaining factors are commonly referred to as 'book keeping' terms as they are secondary to the invariant amplitude with respect to physically classifying interactions. The quantity, dQ, is the differential Lorentz invariant phase space factor; it is related to differential volume elements in the momentum

phase spaces of the outgoing particles. The incident particle flux in the target rest frame is F.

In the center of mass frame for a general $AB \to CD$ scattering process, the differential cross section takes the simple form[4],

$$\frac{d\sigma}{d\Omega} = \frac{1}{64\pi^2 s}\frac{p_f}{p_i}|\mathscr{R}|^2 \tag{1.5}$$

where $s = (E_A + E_B)^2$, $p_i = p_A = p_B$ and $p_f = p_C = p_D$.

In the Standard Model, for a given Feynman diagram, a set of rules can be followed to explicitly write down the invariant amplitude, $\mathscr{R}$. To calculate cross sections for real fundamental interactions, one simply follows these rules, square the amplitude, average over initial and final states if desired, determine the specific form of the 'book keeping' factors, and then it is only a matter of algebra to get the final cross section.

Only cross sections for very simple Feynman diagrams are relatively easy to calculate. Furthermore, as will be discussed more in the next sub-section, these simple cross section calculations are for only the ideal case which of course is never fully representative of reality. In neutrino cross section physics specifically, calculating a simple cross section from a Feynman diagram and then designing an experiment to directly measure that cross section is something that simply does not happen.

1.1.3 Neutrino Interactions

Neutrinos interact only via the weak nuclear force, aside from gravity in which all massive particles participate. This force is mediated by the exchange of either a W^+, W^-, or a Z gauge boson. Interactions that involve the exchange of a $W^\pm$ boson are called charged-current interactions whereas those where a Z boson is exchanged are called neutral current interactions. The analysis detailed in this document focuses on a particular subset of the charged-current interactions for neutrinos. A Feynman diagram for a typical charged-current interaction observed at T2K is given in figure 1.4. This interaction has an incoming muon

anti-neutrino exchange a W^- with a proton producing an anti-muon and a neutron. This particular interaction is called Charged Current Quasi Elastic or CCQE. For this interaction mode, mass is approximately conserved between the initial and final states. Accordingly, it is named in reference to two body classical elastic scattering. It is the dominant interaction type for muon anti-neutrinos at the neutrino energies relevant for T2K. A more detailed mathematical formulation of neutrino interactions (and mass generation) can be found in the author's Master's thesis [3].

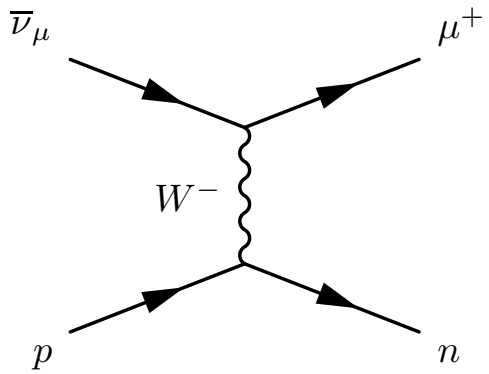

Figure 1.4: Feynman diagram for a $\overline{\nu}_\mu$ CCQE interaction. The incoming anti-neutrino exchanges a negative W boson with a quark inside the proton producing an anti-muon and a neutron. Throughout this document, the time axis for Feynman Diagrams moves from left to right.

To date, neutrinos are only directly observable through their weak interactions. It is asserted in the Standard Model that each charged lepton has a corresponding neutrino. Together, they form a doublet in the mathematical formulation of the Standard Model.

The muon neutrino for example will always produce a muon in the interaction described above. Likewise, an electron neutrino will always produce an electron in that interaction. Similarly, a neutrino produced by pion decay in the decay channel, $\pi^+ \rightarrow \mu^+ + \nu_\mu$, is said to have been created as a muon type neutrino. The lepton labels for neutrinos are referred to as flavor states. Neutrinos are said to come in three flavors: electron, μ, and τ.

Figure 1.4 depicts the interaction of a muon anti-neutrino scattering off a *free* proton. Real detectors are not comprised of free nucleons, but rather of nucleons bound inside the nucleus of atoms. When a neutrino interacts with a bound nucleon, nuclear effects can alter the products of the interaction. The relevant kinematics of the particles produced in the interaction can be affected, and additionally, the existence of those particles at all from an observational perspective can change compared to free nucleon scattering. This leads to the distinction between point interactions (free nucleon scattering) and so called post 'final state interactions' (FSI). Post FS interactions consider only particles that are observable in experiment.

For example, a neutrino may scatter off a bound neutron and produce a pion through resonance (explained below). The pion may then be reabsorbed before it leaves the nucleus so that to an observer outside of the nucleus, the interaction with pion production will look identical to a true CCQE interaction. In addition to particles not making it to the observable final state, when the neutrino transfers significant momentum to the nucleus, additional protons may be produced in the final state by so called 2-proton-2-hole (2p2h) processes. These protons may also not escape the nuclear medium so again we may experimentally confuse a 2p2h or other non-CCQE intra-nuclear events with a true CCQE one.

It is for these reasons that in experimental neutrino cross section physics, it is almost always more physically meaningful to define signals based on the observable final state topology rather than "true" theoretical interaction modes at the vertex. Instead of trying to measure a true CCQE cross section, one could measure a CC-0π (charged-current interaction with no pions in the final state) cross section. For interactions induced by neutrinos, a true CC-0π signal would have one muon, zero pions and any number of protons in the observable final state.

The analysis described in this thesis has a $\overline{\nu}_\mu$ CC-0π definition, so muon anti-neutrino interactions where one μ^+, zero pions and any number of protons exist in the observable final state is considered to be signal. Precision measurements of CC-0π cross sections, particularly single target type measurements can help resolve theoretical discrepancies between different

models involving 2p2h processes. This is a driving motivation for analyses like the one presented here.

The largest dominant background for the event selection described later is CC-1π^- whose topology definition is those interactions where there is precisely 1 μ^+ and 1 π^- in the observable final state. The dominant interaction mode for such events at the energies relevant for T2K is the resonant pion production channel (CC-RES). Figures 1.5 and 1.6 present the Feynman diagrams for an example of resonant pion production for muon neutrinos and muon anti-neutrinos respectively. The quark level interactions in figures 1.5 and 1.6 are represented by $\nu_\mu + d \rightarrow u + \mu^-$ and $\overline{\nu}_\mu + u \rightarrow d + \mu^+$ respectively. Single pion production can also occur by the neutrino coherently interacting with the nucleus rather than a point interaction like those in figures 1.5 and 1.6. This process is referred to as charged-current coherent pion production (CC-COH).

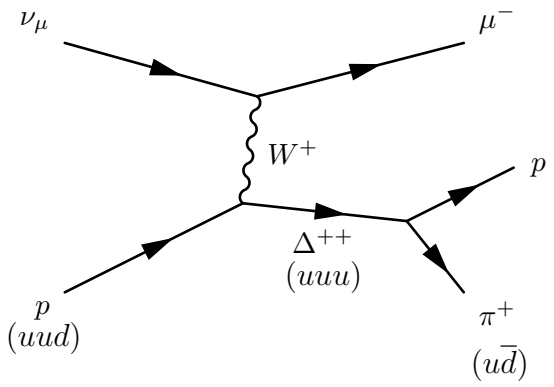

Figure 1.5: Feynman Diagram for a ν_μ CC-RES interaction. Relevant quark content shown in parentheses. The incoming neutrino exchanges a positive W boson with a quark inside the proton producing a Δ^{++} resonance which quickly decays producing a proton and a π^+.

For this thesis, all other charged-current interactions are grouped into a CC-Other topology categorization that includes interactions like charged-current neutral pion production (CC-π^0) and deep inelastic scattering (DIS). The collection of all charged current interactions is referred to as charged-current inclusive (CC-Inclusive, CC-Inc). From a point

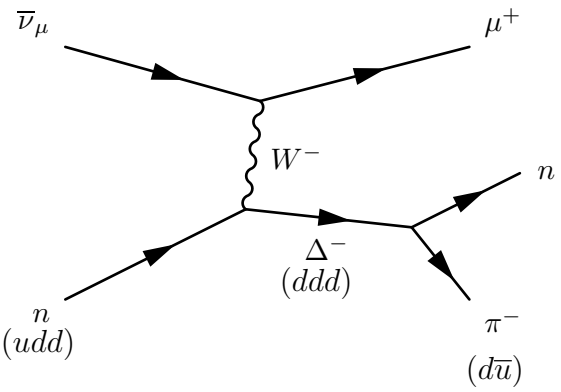

Figure 1.6: Feynman Diagram for a $\overline{\nu}_\mu$ CC-RES interaction. Relevant quark content shown in parentheses. The incoming anti-neutrino exchanges a negative W boson with a quark inside the neutron producing a Δ^- resonance which quickly decays producing a neutron and a π^-.

interaction view, this corresponds to any neutrino interaction where a charged W was exchanged at the primary interaction vertex where from a topology point of view this would include all neutrino interactions where there is a muon (for ν_μ CC-Inc) in the final observable state.

1.1.4 Neutrino Oscillations

Perhaps the most interesting behavior that neutrinos exhibit is that as they travel through space and time, they can change flavor. That is to say, if a muon type neutrino is created and then travels for some distance, there is a chance that upon detecting it, it will be an electron or tau type neutrino. This phenomenon is referred to as neutrino oscillations. It is a main driving force for neutrino physics research today. The analysis described here does not focus on neutrino oscillations, so a detailed description of the physics involved is somewhat outside of the scope of this document. However, cross section measurements help paint a more complete picture of neutrinos and can possibly improve precision measurements of neutrino oscillation parameters. A detailed description of neutrino oscillations can be found in [5], and a nice overview can be found in [6].

Neutrino oscillation directly follows from basic relativistic quantum mechanics and the assertion that neutrinos have separate and distinct flavor (type) states and mass states. The flavor states have already been introduced: ν_e, ν_μ, and ν_τ. Suppose also that there exist three distinct mass states: ν_1 with mass m_1, ν_2 with mass m_2, and ν_3 with mass m_3. A unitary transformation can be set up between the different bases:

$$|\nu_\alpha\rangle = U_{\alpha i}^{PMNS} |\nu_i\rangle \tag{1.6}$$

Where U^{PMNS} is a specific parameterization of this unitary transformation, the Pontecorvo-Maki-Nakagawa-Sakata (PMNS) matrix. Any unitary transformation in the above can be parameterized by three angles and a complex phase. ν_α are the flavor states: $\alpha = e, \mu, \tau$ and ν_i are the mass states: $i = 1, 2, 3$. The PMNS matrix is parametrized by three mixing angles: θ_{12}, θ_{13}, and θ_{23} and one complex phase, δ.

Equation 1.6 has the following form with the U^{PMNS} matrix explicitly defined:

$$\begin{bmatrix} \nu_\alpha \\ \nu_\beta \\ \nu_\gamma \end{bmatrix} = \begin{bmatrix} c_{12}c_{13} & s_{12}c_{13} & s_{13}e^{-i\delta} \\ -s_{12}c_{23} - c_{12}s_{23}s_{13}e^{i\delta} & c_{12}c_{23} - s_{12}s_{23}s_{13}e^{i\delta} & s_{23}c_{13} \\ s_{12}s_{23} - c_{12}c_{23}s_{13}e^{i\delta} & -c_{12}s_{23} - s_{12}c_{23}s_{13}e^{i\delta} & c_{23}c_{13} \end{bmatrix} \begin{bmatrix} \nu_1 \\ \nu_2 \\ \nu_3 \end{bmatrix} \tag{1.7}$$

In the above, $c_{12} = \cos\theta_{12}$ and $s_{23} = \sin\theta_{23}$ and so on. All this equation says is that if a neutrino is produced in some definite flavor state, it is a superposition of the three mass states. It follows directly from this equation and the application of the standard quantum mechanical propagator operator that neutrino oscillations occur. Furthermore, should there exist three definite mass states for neutrinos, oscillations directly follow. An observation of neutrino oscillations then provides pretty strong evidence that neutrinos are in fact massive. This observation was indeed made, with Takaaki Kajita and Arthur B. McDonald sharing the 2015 Nobel Prize in physics for their work in pioneering experiments that make these observations possible. Takaaki Kajita's work was at Super-Kamiokande, which is now the far detector of the T2K experiment.

Combining equation 1.7 with the quantum mechanical propagator can yield formulas for the probability of observing a neutrino in some state different than the state it was produced in at some distance from where it was created at some energy in terms of the mixing angles from the PMNS matrix and the mass squared splittings (difference of the mass squared between different mass states). By fixing the neutrino energy and distance between production and observation, experiments can measure these probabilities to constrain the parameters of the PMNS matrix and additionally the mass squared splittings, denoted Δm^2_{ij}. Because only the mass squared splittings appear in the oscillation probabilities in vacuum, a neutrino oscillation measurement in vacuum is completely insensitive to the absolute neutrino mass and also which of the mass states is the most massive and which is the lightest. The ordering by mass of the mass states is referred to as 'mass hierarchy,' and even though the vacuum probabilities are insensitive to determining the hierarchy, second order corrections from neutrinos propagating through matter rather than vacuum introduce some modest sensitivity. If the mass of neutrino mass state 2 is less than that of state 3, the hierarchy is said to be normal (NH) and conversely the hierarchy is said to be inverted (IH).

Neutrino oscillation experiments constrain these various parameters mainly by measuring what are referred to as 'appearance' and 'disappearance' probabilities. 'Appearance' refers to the appearance of a type of neutrino different than the type originally produced in an experiment, and 'disappearance' refers to an observed deficit of the type of neutrinos originally produced relative to a no-oscillation hypothesis.

Measurement of the mixing angles and mass squared splittings have been the main focus of neutrino oscillation experiments since the discovery of the oscillations. The fourth parameter in the PMNS matrix, δ is perhaps even more interesting as it relates to Charge-Parity violation for neutrinos and can perhaps provide insight as to why in the early universe, there was slightly more matter created than anti-matter which in turn allowed for the observable universe around us composed predominantly of matter to exist today. For these reasons, determining δ, and first determining if it is nonzero modulo π, is the main goal of next generation neutrino oscillation experiments.

1.2 The T2K Experiment

The Tokai to Kamioka (T2K) long-baseline neutrino oscillation experiment in Japan provides a means for physicists to study the neutrino oscillations presented in the previous section. A relatively pure beam of either muon neutrinos or muon anti-neutrinos is produced in Tokai and then travels 295 km through the landmass of Japan to the Kamioka mine. Neutrinos are detected both near the beam source ($\approx$ 280 m) and at Kamioka so that the comparisons can be made on how often neutrino oscillation occurs after traveling 295 km.

The physics goals of the experiment are (were) to discover $\nu_\mu \rightarrow \nu_e$ neutrino oscillations, precision measurements of ν_μ disappearance probability parameters, and to search for sterile neutrino contributions in ν_μ disappearance by looking at neutral current interactions. T2K has achieved the first two goals, with the accomplishment of the first goal resulting in the collaboration being awarded the Breakthrough Prize in Fundamental Physics in 2016, which some consider to be the 'Oscar of Science.'

Figure 1.7 provides a pictorial view of the T2K experiment. First, a beam of neutrinos is produced at the Japan Proton Accelerator Research Complex (J-PARC). The neutrinos in the beam are then first studied by the near detectors. ND280 (Near Detector, 280m from beam source) is a collection of sub-detectors that detect neutrino interactions. The neutrinos are additionally studied by the INGRID detector which lies near ND280.

The neutrinos then travel underground 295 km where they are studied a second time by the Super-Kamiokande (SK) detector, which is a massive water Cherenkov detector roughly a kilometer underground. ND280 and SK lie roughly 2.5° off axis with respect to the neutrino beam center produced at J-PARC. INGRID lies on axis. The off axis effect will be discussed in greater detail later in this section, but generally it provides ND280 and SK with a much more narrow band neutrino energy beam which optimizes T2K's sensitivity for accomplishing its physics goals.

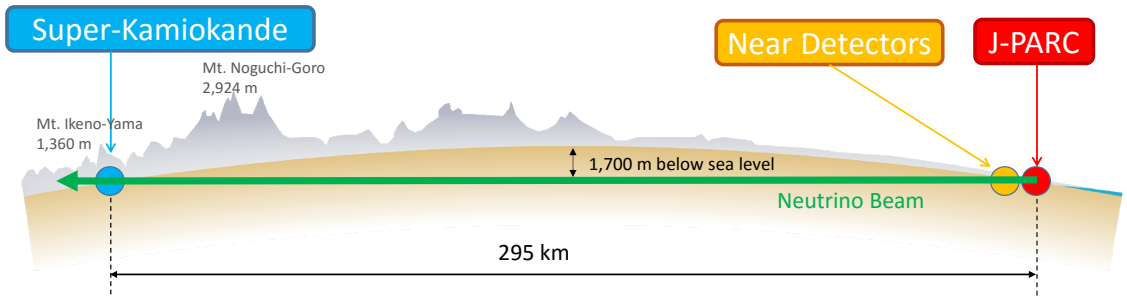

Figure 1.7: Cross sectional overview of the T2K experiment. A beam of neutrinos is produced at J-PARC and passes through the near detector complex on its way to the far detector, Super-K which is 295 km from J-PARC.

1.2.1 Beam

The relatively pure beam of either muon neutrinos or anti-neutrinos is produced at the J-PARC accelerator complex in Tokai, Japan by colliding a beam of high energy protons with a graphite target. The proton beam is produced in three main stages.

First a LINAC is used to accelerate H^- ions to around 400 MeV. The ions are then stripped of their electrons using charge stripping foils. The now proton beam is then further accelerated in a Rapid Cycling Synchrotron (RCS) to around 3 GeV and is fed into the Main Ring Synchrotron where the protons are accelerated to their final energy of 30 GeV. Figure 1.8 gives and areal view of the accelerator complex with the LINAC, RCS, and Main Ring labeled.

The beam is then delivered in 8 spill bunches to the graphite target where secondary mesons are produced in the carbon-proton interactions. These mesons are then focused by a series of magnetic horns which pulse to produce a field of 1.7 T. By choosing the sign of current in the horns, either positively or negatively charged mesons can be selected. The focused mesons then pass into a 96m long He filled decay volume where they predominantly decay in flight producing neutrinos before the beam reaches the terminal beam dump. T2K

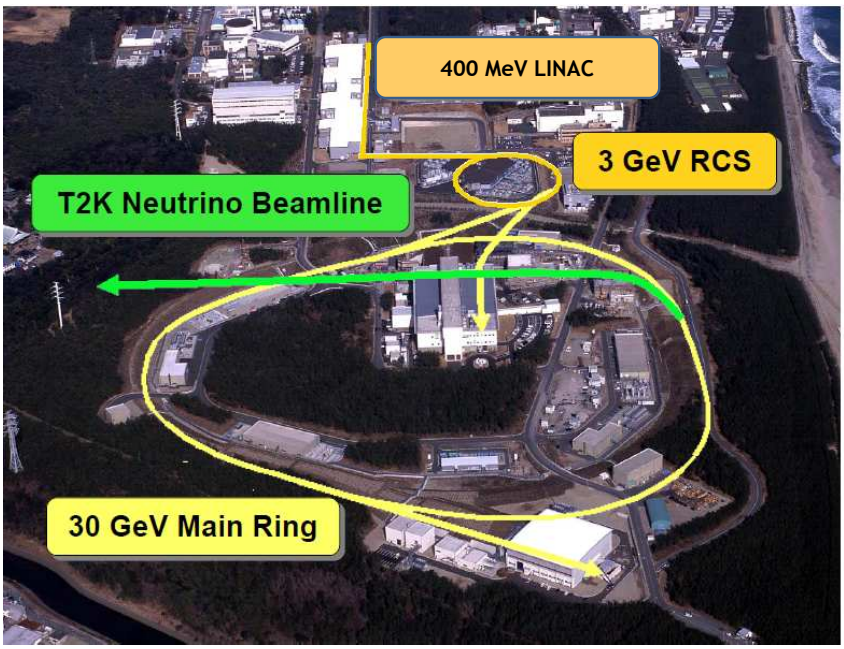

Figure 1.8: Areal overview of J-PARC. Labeled are the LINAC where protons are produced and initially accelerated, the Rapid Cycling Synchrotron where they are further accelerated, the Main Ring Synchrotron where they reach their final energy of 30 GeV, and the neutrino secondary beamline.

first took neutrino data in 2010, and since then, the beam energy has increased from around 40 kW to over 450 kW. Figure 1.9 provides a schematic diagram of the secondary beam line, consisting of the target area, decay volume and beam dump.

Increasing the beam energy delivers more protons to the graphite target which in turn produces more mesons which decay, producing more neutrinos. The number of protons on target, abbreviated 'PoT' throughout the document, is a good measure of the number of neutrinos delivered to ND280. For this reason, when comparing data sets, PoT normalization is often used. Independent of the beam energy, the observed neutrino interaction rates normalized by PoT are relatively constant. When comparing simulation of neutrino beam interactions to real data, it is also common to measure the size of the simulated sets in terms of 'generated equivalent PoT.'

The beam is monitored throughout its progression by 50 beam loss monitors, 21 electrostatic monitors, 19 secondary emission monitors, and 5 current transformers yielding a

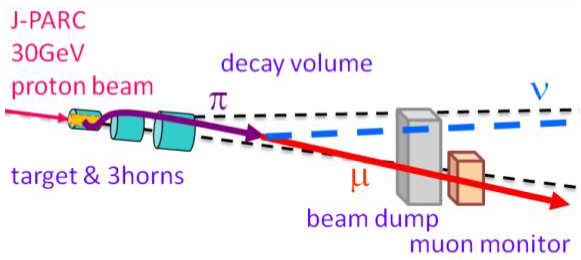

Figure 1.9: Diagram of the secondary beamline where protons collide with a graphite target and the resulting secondary mesons are focused by three magnetic horns, decaying primarily in the decay volume. The result is a relatively pure beam of either muon neutrinos of muon anti-neutrinos depending on the chosen horn current. The muon monitor provides an initial measurement of the muon flux for beam characterization.

measurement of the number of protons delivered to the target within 2% uncertainty. Additionally, monitors beyond the terminal beam dump including a nuclear emulsion detector and a muon monitor help to precisely measure the muon flux and momentum for muons produced in the meson decays from the decay volume. Monitoring combined with external data from the NA61 [7] experiment provide a reliable prediction with appropriate uncertainty for the neutrino flux delivered to ND280.

ND280 lies 280 meters from the target area and 2.5° off axis with respect to the neutrino beam center. Super-K is also off-axis by the same amount and is roughly 295 km from ND280. Being slightly off axis proves to be quite beneficial by providing a more narrowly peaked beam neutrino energy spectrum (at around 600 MeV) by suppressing the high energy tail present in the beam directly on axis. Figure 1.10 shows and overlay of the neutrino energy spectrum expected at the ND280 detectors for different choices of the off-axis angle. Also given are the electron appearance and muon disappearance probabilities as a function of neutrino energy. With a sharp peak at around 600 MeV, Super-K sits near a minimum for muon neutrino survival probability and a maximum for electron neutrino appearance probability, enhancing T2K's sensitivity in measuring oscillation parameters.

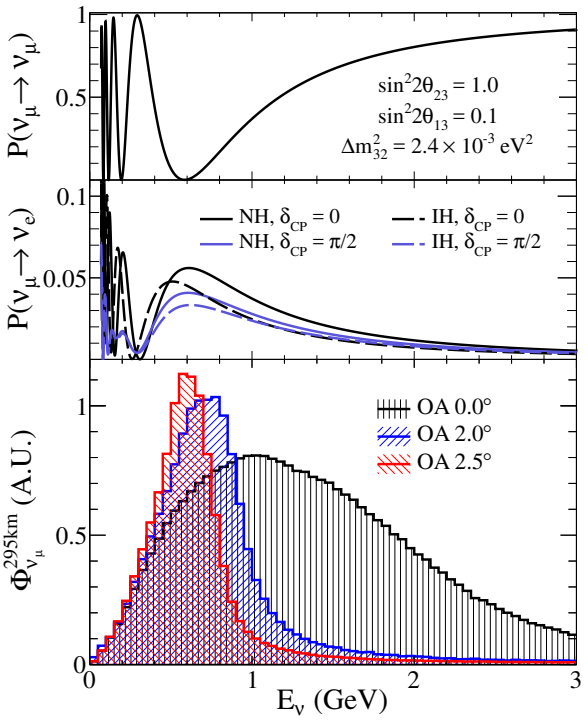

Figure 1.10: Comparison of the predicted un-oscillated flux of muon neutrinos at Super-K (bottom) overlaid with the electron appearance probability at SK (middle) and the muon disappearance probability (top) all given as a function of neutrino energy on the same scale.

The off-axis spectrum effect is easily demonstrated using some basic particle physics. For a pion decaying in flight to a muon and a neutrino:

$$\pi^- \rightarrow \mu^- + \overline{\nu}_\mu$$

The 4-momentum must be conserved between the initial and final states. Conserving the three momentum gives:

$$\vec{p_\pi} = \vec{p_\mu} + \vec{p_\nu} \Longrightarrow \vec{p_\pi} - \vec{p_\nu} = \vec{p_\mu}$$

Squaring both sides and rewriting p_μ^2 in terms of Energy and mass gives,

$$p_\pi^2 + p_\nu^2 - 2p_\pi p_\nu \cos\theta_{\pi\nu} = E_\mu^2 - m_\mu^2$$

where $\theta_{\pi\nu}$ is the angle between the incoming pion and outgoing neutrino directions in the laboratory frame. Conserving energy in the decay gives:

$$p_\pi^2 + p_\nu^2 - 2p_\pi p_\nu \cos\theta_{\pi\nu} = (E_\pi - E_\nu)^2 - m_\mu^2$$

Assuming that the neutrino mass is negligible so that $E_\nu = p_\nu$ and multiplying out the quadratic term on the right gives:

$$p_\pi^2 + E_\nu^2 - 2p_\pi p_\nu \cos\theta_{\pi\nu} = E_\pi^2 + E_\nu^2 - 2E_\pi E_\nu - m_\mu^2$$

So that:

$$p_\pi^2 - 2p_\pi p_\nu \cos\theta_{\pi\nu} = E_\pi^2 - 2E_\pi E_\nu - m_\mu^2$$

Solving for E_ν and rewriting p_π gives E_ν as a function of E_π and $\theta_{\pi\nu}$, the angle of the neutrino with respect to the pion momentum direction in the laboratory frame, which is the same as the off-axis angle for T2K:

$$E_\nu = \frac{m_\pi^2 - m_\mu^2}{2(E_\pi - \sqrt{E_\pi^2 - m_\pi^2}\cos\theta_{\pi\nu})} \tag{1.8}$$

Figure 1.11 plots this function for several different choices of the pion-neutrino angle. As this angle increases from 0° to 3°, the maximum neutrino energy produced in the pion decay decreases so that the suppression of the high energy tail in the neutrino energy distribution in an off-axis detector is seen directly from this plot.

1.2.2 ND280

ND280 is a suite of sub-detectors, each designed with particular physics goals. Figure 1.12 shows the collection of the ND280 sub-detectors. Being that the analysis of this thesis uses only 2 sub-detectors at ND280, reasonably thorough details will be provided for these

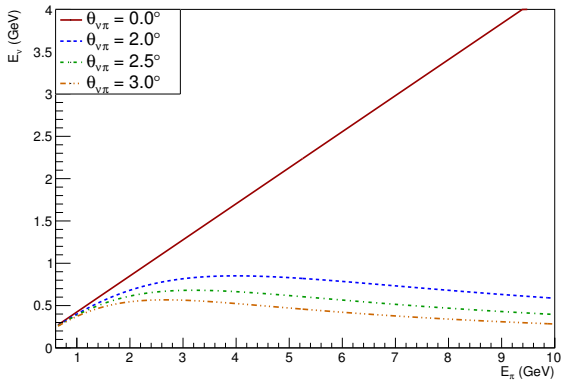

Figure 1.11: Neutrino energy in pion decay as a function of the pion energy for different choices of the neutrino direction relative to the incoming pion direction in the lab frame.

sub-detectors in the throughout the remainder of this chapter with only general details for the sub-detectors not used by this analysis included.

With the beam coming from left to right on the page in figure 1.12, it first encounters the π^0-detector (PØD) consisting of a central water target sandwiched between two electromagnetic calorimeters (ECal). Directly downstream of the PØD is one of three time projection chambers (TPC) followed by an alternation of 2 fine grain detectors (FGD) and the other two TPCs. Finally, most downstream is another ECal. This sequence of sub-detectors is surrounded by more ECals which are in turn surrounded by the re-purposed UA1/NOMAD magnet providing a 0.2T field in the X direction as labeled in the figure. Each sub-detector has some degree of tracking and/or calorimetric capabilities. The magnetic field allows for both identification of and momentum reconstruction for charged particles produced in neutrino interactions.

In addition the ND280 detector suite, an on-axis detector, INGRID, provides valuable beam characterization measurements and additionally has the capability for other physics measurements. It is made up of 14 sub-modules where alternating layers of scintillator planes and iron sheets provide both tracking and calorimetric abilities.

The ND280 detectors rely on the detection of charged particles either directly produced in neutrino interactions or produced in the subsequent decays of neutral particles produced

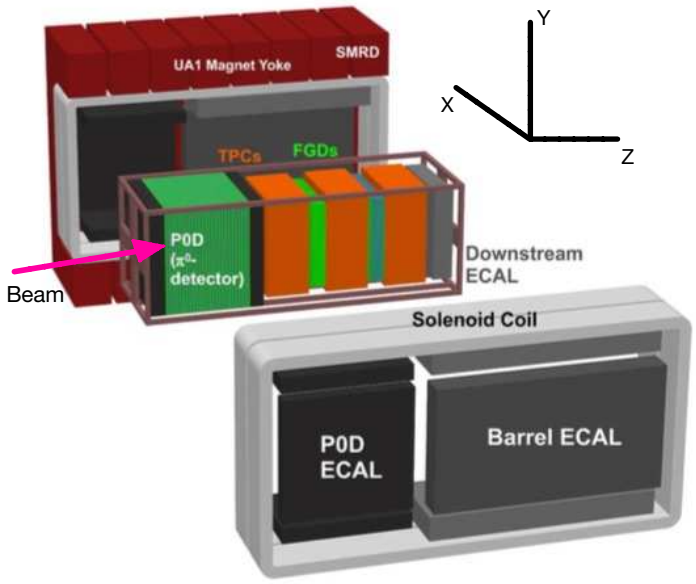

Figure 1.12: Overview of the suite of ND280 detectors. The beam direction and ND280 coordinate system are shown. The PØD, TPCs, FGDs, and Downstream ECal are surrounded by more ECals which are in turn surrounded by the UA1 magnet and SMRD.

in the original neutrino interactions. The detection of these charged particles in turn depends on two phenomenon, scintillation and ionization.

Ionization is probably more familiar to a general audience. When a charged particle travels through matter, it can interact with an electron bound in an atom transferring energy to the electron causing it to be ejected. The result of which is an ion and a now free electron. The TPCs rely on detecting the ejected electrons from ionization of Argon gas to infer that a charged particle passed through.

Scintillation is a similar process, but instead of ejecting electrons bound in atoms and molecules making up components of the detectors, the atomic or molecular states are exited to a higher energy state which then relax, omitting light in the process. This light is referred to as scintillation light. The PØD, ECals, SMRD, and FGDs rely on collecting scintillation light for detecting the charged particles produced in neutrino interactions.

1.2.3 PØD

The PØD consists of 40 sub-modules referred to as PØDules. There are two types of PØDules corresponding to those that make up the ECals and those that make up the water target region. A single PØDule consists of a scintillating plane and a layer of dead material, stainless steel surrounded lead for ECal PØDules and brass/water-bag combination for water target PØDules. The water bags have the option to both be filled with water and not, allowing for data to be taken in both configurations. A system of electronics read out scintillation light collected in the scintillator planes. Figure 1.13 provides a drawing of the PØD; the active dimensions of it are 2103 mm (width) x 2239 mm (height) x 2400 mm (length).

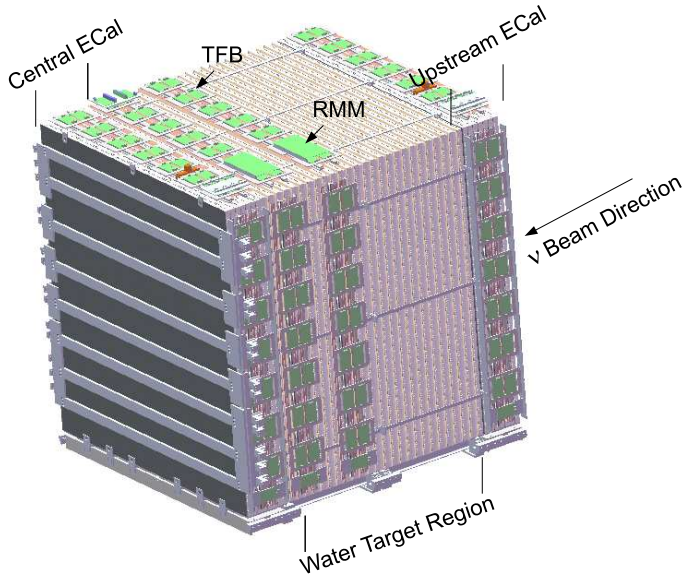

Figure 1.13: Drawing of the π^0-Detector. The water target region is sandwiched between to ECals. RMMs and TFBs are electronics for data readout and are explained in depth later.

Figure 1.14 gives a more detailed representation of the PØD components. In each PØDule, the scintillating plane is constructed of many individual triangular bars arranged as shown in figure 1.14 to form scintillating layers. Bars are arranged both in a vertical and horizontal

orientation forming a X (vertical) and Y (horizontal) layer that together form one scintillating plane. This configuration allows for three dimensional tracking for charged particles traversing the detector, as each time a particle crosses a scintillating plane, the vertical bars can produce an x-coordinate and the horizontal ones a y-coordinate. Each plane having a fixed z-coordinate allows for the reconstruction of 3-D particle tracks. In each plane, there are a total of 134 horizontal bars which are 2133 mm long and 126 vertical bars that are 2272 mm long.

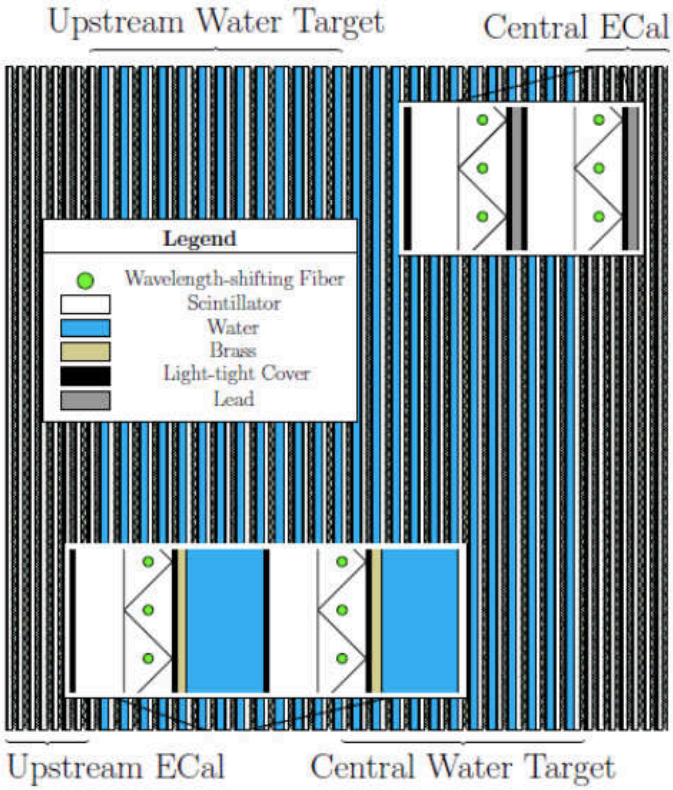

Figure 1.14: Schematic diagram of the PØD structure consisting of alternating layers of scintillating planes and lead (ECal regions) and water+brass (water target region). The scintillating planes are constructed of an X and a Y layer consisting of vertical (X) or horizontal (Y) scintillator bars, each of which has a wavelength shifting fiber running through its central axis.

Each bar contains a single co-axial 2.6 mm hole housing a wavelength shifting fiber which is mirrored on one end and optically coupled to a single Hamamatsu Multi-Pixel Photon Counter (MPPC), which collects scintillation light from each bar. The triangular cross sectional dimensions of the bars are 17 mm high by 33 mm wide. The MPPCs are read

out by the Trip-t electronics system which will be described in more detail later. There are a total of 10,400 channels for the PØD.

The bars are constructed primarily out of polystyrene doped with scintillator originally developed for the inner detector of the MINERνA experiment [8][9]. Each bar is coated with a Titanium dioxide reflective layer which prevents scintillation light produced in one bar from being collected by the wavelength shifting fiber in a neighboring bar and additionally provides more efficient collection of light in each bar. A UV LED light injection system interfaces with each bar on the end opposite to the MPPC; the purpose of which is to monitor MPPC operation.

In addition to the scintillator planes, as was said before, the ECal PØDules contain a layer of lead encased in stainless steel. Each layer is 4.5 mm thick. The water target PØDules have a 1.28 mm thick brass sheet and a 28 mm thick water bag region containing a high-density polyethylene water bag that can be filled with water. The total mass of the PØD is approximately 15,800 kg when the bags are full of water and 12,900 kg when empty.

The electronics readout is handled by the Trip-t electronics system used commonly also for the other ECals, the SMRD, and INGRID. The MPPC output signal is read out via mini-coaxial cables by the Trip-t Front-end Boards (TFB). Each of the TFBs has 4 32-channel Trip-t Application Specific Integrated Circuit (ASIC) [10] chips. Each chip reads in up to 16 MPPCs simultaneously through a high gain and a low gain channel. The high gain readout can handle up to a 50 photo-electron (pe signal, and the low gain readout can handle up to 500 pe. Charge collected is integrated over 23 consecutive integration cycles that are synchronized with the expected beam spill time window periodicity so that both beam and cosmic ray triggers can be utilized.

Each TFB is operated by a Field Programmable Gate Array (FPGA) which simultaneously distributes operation commands and moves data from the TFBs to the back-end electronics. 174 TFBs are used to read out the PØDdata.

The TFBs for the PØD are read out by 6 Read-out Merger Modules (RMM) which are synchronized with a Cosmic Trigger Module (CTM), a Slave Clock Module (SCM), and a

Master Clock Module (MCM) which provides timing for all the Trip-t sub-detectors. The CTM, SCM, and MCM provide beam and cosmic triggering information to be passed from the RMMs to the FPGAs. In addition to providing triggering sequences to the TFBs, the RMMs merge and collect data from the TFBs to be passed to the Data Acquisition System (DAQ) which directly interfaces with the RMMs via a set of Front-end Processing Nodes (FPN), each controlling and reading 2 RMMs. These FPNs run a MIDAS [11] framework consisting of various control, monitoring and data collection clients, the primary one being the event processor which merges data from all Trip-t sub-detectors and the FGDs and applies very basic checks to write complete events to a buffer while an archiver process organizes full files to be simultaneously moved to long term storage and parsed to create an abbreviated preview file for real time DAQ monitoring and calibrations.

In parallel to the DAQ is another MIDAS package and a collection of monitoring equipment for measuring temperatures, voltages, etc. that form the Global Slow Control (GSC) system. This system provides real-time feedback about the overall health and stability of the detectors. Readout is archived into history for retro-active and long term monitoring and additionally, alarms are set so that when something goes wrong, quick action can be taken to remedy any issues.

1.2.4 PØD+TPC1

This analysis uses the PØD water target region as a target for neutrino interactions, as will be described in greater detail later, to select $\overline{\nu}_\mu$ CC-0π events. First the selection procedure attempts to identify μ^+ tracks originating in the PØD that propagate out of the PØD and through the first downstream TPC. The TPCs are argon gas based (Ar:CFi_4:C_4H_10) time projection chambers that have excellent positional resolution for tracks. The TPCs do not use pure Argon gas, but rather a mixture of Argon, isobutane, and carbon dioxide. The space point resolution accomplished by the TPCs is roughly 0.7 mm. Combining the precision tracking with the magnetic field the TPCs reside in allows for the measurement of the momentum of charged particles. Additionally, energy loss information along the

tracks passing through the TPC can allow for particle identification. Figure 1.15 provides a schematic diagram of one TPC.

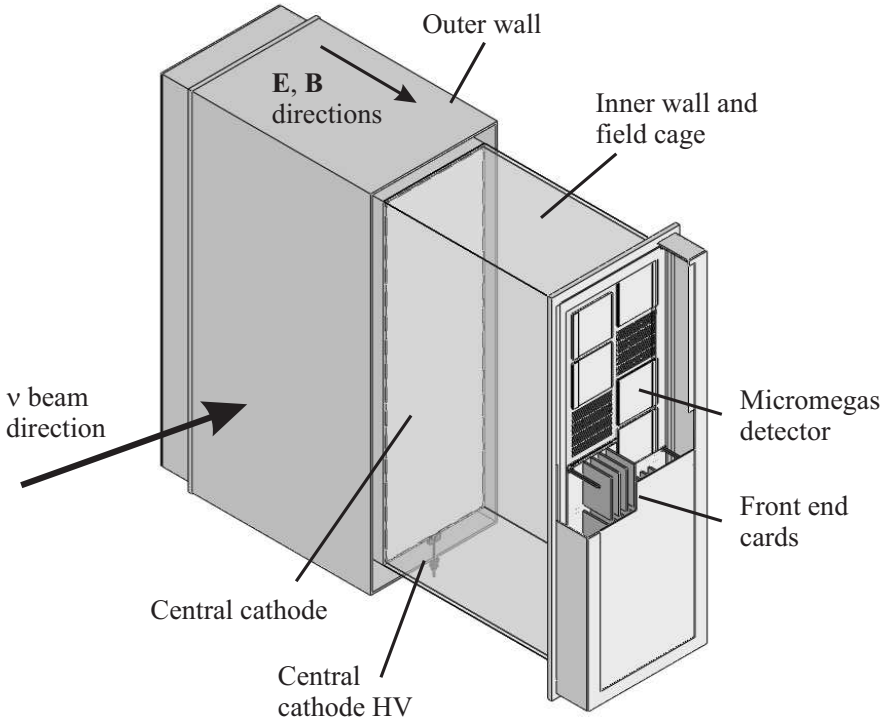

Figure 1.15: Schematic drawing of a TPC taken from [12]. Electric and magnetic field axes are shown as well as the neutrino beam direction. The central cathode plane and two (one on either side) anode charge collection plane form two regions of constant electric field (pointing in opposite directions). Ejected electrons from ionized argon gas are collected by the Micromegas detector plates.

One TPC consists of an inner gas-tight box filled with 1 atm of the argon gas mixture surrounded by another gas tight structure filled with CO_2 for insulation. Together, the central cathode and anode charge collection planes attain a maximum 5 kV/cm electric field whose direction is indicated in figure 1.15. When charged particles pass through the main gas chamber, the Argon gas is ionized producing electrons that drift through the electric field to be collected at the anode plane by the Micromegas detectors giving fine grain, planar spatial resolution. With the electric field being essentially constant throughout the chamber's

volume, the drift velocity of the ionization electrons is well known so that timing information for the collected charge can give the third spatial dimension.

1.3 Data and Monte Carlo Simulation

A complete simulation of how the ND280 detectors respond to the J-PARC neutrino beam is generated and serves many important roles in physics analyses at T2K. The full simulation procedure for ND280 analyses can be broken into three main pieces. First the neutrino production in the secondary beam line at J-PARC is simulated to get a prediction of the neutrino flux at ND280. Assuming this simulated neutrino flux, neutrino interactions inside of ND280 are generated. The detector response to the particles produced in those interactions is then modeled giving simulated digitized electronic response collected in a data file with the same structure as when taking real data.

As was described before, the 30 GeV proton beam produced at J-PARC is delivered to the secondary beamline where it collides with a graphite target. The simulation of the neutrino flux begins here where the proton-carbon hadronic interactions are generated. Further interactions and the decays of the secondary hadrons produced in these interactions are simulated giving a generated set of neutrinos produced in the secondary beam line.

The FLUKA [13] package models the proton-target interactions. It takes an input describing the proton beam from J-PARC and the target geometry to generate secondary particles. The remainder of the secondary beamline processes are simulated using a GEANT 3 [14] based simulation package called JNUBEAM. This simulation contains geometries for all of the sub-components in the secondary beamline. The particles that are produced using FLUKA are allowed to propagate through the simulated secondary beamline where hadronic re-interactions and decays are simulated using the GCALOR package.

Neutrinos produced in this process are then collected into an output containing the relevant kinematics for each generated neutrino. These neutrinos are then propagated to the ND280 complex and now constitute the input ND280 neutrino flux which can be used to generate neutrino interactions in the detectors.

Input parameters to the various stages of this simulation can be tuned according to the J-PARC beamline monitoring previously discussed and external experimental data. More

importantly, the inputs to the simulation can be varied according to assumed prior uncertainties to calculate the errors on the generated neutrino flux at ND280.

For a cross section measurement, this information is compactly summarized into a histogram of neutrino flux binned by neutrino flavor and energy and a covariance matrix containing the uncertainties on the binned flux and correlations between each of the bins.

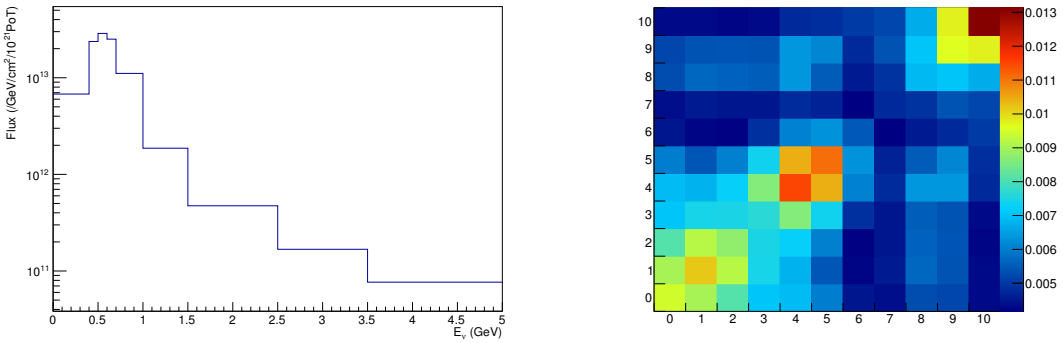

Figure 1.16: Left: Binned flux anti-neutrino flux prediction during anti-neutrino mode beam at ND280. Note that the highest energy bin actually extends to 30 GeV. Right: Covariance matrix in terms of the 11 $\overline{\nu}_\mu$ flux bins.

With a simulated flux of neutrinos incident on ND280, neutrino interactions in and around the detectors are then generated using primarily the NEUT [15] neutrino interaction generator. This package was originally developed for the generation of atmospheric neutrino events for the original Kamiokande experiment. It takes a target material and the simulated neutrino flux as inputs and outputs particles created in the interactions after FSI. The dominant interaction mode for neutrino energies relevant for T2K is the CCQE mode. NEUT uses the Llwellyn-Smith [16] model for QE interactions where the CCQE cross section is given by,

$$\frac{d\sigma}{dQ^2} = \frac{G^2 M^2}{8\pi E_\nu^2}\left(A - \frac{s-u}{M^2}B + \frac{(s-u)^2}{M^4}C\right) \tag{1.9}$$

where Q^2 is the 4-momentum transfer in the interaction, M is the target mass, G is the weak coupling constant, and s and u are Mandelstam variables of the center of mass energy

of the particle system. The A, B, and C are collections of various form factors related to nuclear effects: F_1 (Fermi), F_2 (Dirac), G_p (pseudo-scalar), and G_a (axial) [5]. The axial form factor can only be probed through weak interactions and is not currently well constrained, motivating CCQE-like neutrino measurements like the one presented in this thesis. The dipole form of G_a is given by:

$$G_a(Q^2) = \frac{g_A}{(1 + \frac{Q^2}{m_A^2})} \tag{1.10}$$

Neutron lifetime measurements [5] constrain g_a well, leaving m_A to be a particularly interesting parameter for CCQE-like neutrino processes. It is known as M_a^{QE}, the axial mass for CCQE interactions. There are current disagreements of CCQE neutrino scattering measurements from competing experiments as to the value of M_a^{QE}, making further investigation into CCQE-like cross sections interesting and well motivated.

Other modes of neutrino interactions are also simulated in NEUT but are less relevant to this work, since the analysis will not be sensitive to any of their underlying parameters. In addition to the nuclear effects already taken into account above and for other interaction modes, default NEUT uses an older model compared to other neutrino interaction generators, the so called Relativistic Fermi Gas (RFG) approximation [17]. It is worth noting, however, that tunings can be applied to the default NEUT to get closer to what the predictions would be using more recent models for nuclear effects such as the Spectral Function (SF) model and Relativistic Phase Approximation (RPA).

The GENIE [18] interaction generator can be used either instead of or as a cross check to NEUT. In this analysis, NEUT is used as the primary MC, but GENIE is used for some checks described near the end of the document. For the purposes of this document, a knowledge of only the general differences between the two are necessary. NEUT and GENIE have essentially identical QE interaction models, but they have significant differences in modeling for RES and DIS processes which are the dominant backgrounds in this analysis. Additionally, GENIE uses more modern nuclear models relative to default NEUT.

1.3.1 ND280 Event Reconstruction

The third step in the simulation described before is to simulate the ND280 detectors' responses to particles produced in neutrino interactions propagating through them. This will be described by introducing the whole of the ND280 software suite. Figure 1.17 shows the collection of packages along with the data flow and dependencies. Thorough knowledge of all of the packages represented in figure 1.17 is not needed for the purposes of this thesis, but the relevant ones will be described so that the reader might gain a general understanding of how both data and simulation turn into an analyzable structure. Two of the elements of figure 1.17 have already been introduced. In top left, is the MIDAS data collected using the procedure described in section 1.2.3. In the bottom left, is the neutrino interaction generation described in the previous sub-section.

With the ability to generate neutrino interactions in the ND280 geometry assuming the simulated flux, the resulting particles after FSI, are then allowed to propagate through the ND280 geometry by the nd280mc/elecSim package. This is a GEANT 4 [20] based simulation package developed and maintained at CERN that simulates the propagation of particles through matter. Output particles from the interaction generators after FSI are first organized into the beam spill structure described in section 1.2.1 and then allowed to propagate through the detector volumes. The charge deposit, energy loss, position, momentum, etc. along the particle trajectories is modeled and stored. Generator level information like the true neutrino interaction type and relevant corresponding particles produced in the interaction along with their generated kinematics is also preserved and stored in parallel to the GEANT simulated information.

There now exists a set of true particle trajectories that have information of physically how the propagation of secondary particles produced in neutrino interactions proceeds in the ND280 geometry. The elecSim package then takes information like the true amount of charge deposited by a trajectory and simulates electronic readout for the instrumented components of the ND280 detectors. This takes into account all of the specific details of the

ND280 instrumentation from the size and composition of the scintillator bars to the specific electronics chip used to read out light yield from the MPPCs. The simulation now includes what the detector electronics read out would look like for particles traversing the detectors for a simulation of the raw electronics readout.

The simulation aspect of ND280 is now complete. Starting from a simulation of the neutrino flux produced in the secondary beamline at J-PARC, neutrino interactions in ND280 are generated and the particles produced in those interactions are propagated through the detectors and the raw electronics readout is simulated.

Following the arrows in figure 1.17 from the nd280mc/elecSim just described, the MC and real data are now digitized and merged into a common format. The oaEvent class is a ROOT dependent data structure that stores events in data and simulation as a collection of raw digitized electronics readout. The class has also containers for information relevant only to data or MC like the true generator level information for MC and the beam monitoring summary data for data events. At this point in the data flow, data and simulated events have the same structure, so the remainder of the data flow proceeds identically for the two.

With the oaEvents now having only raw electronic readout information, a conversion to physically meaningful quantities is needed. For example, a single readout from an MPPC channel will be related to a raw count of the number of photons collected by the MPPC. This needs to be converted to something more physical like the energy deposited in the bar corresponding to that MPPC.

This is done in parallel separately for the three types of readout electronics at ND280: Trip-t used for the PØD, SMRD, and ECals, 'AFTER chips' used for the FGDs, and the MicroMEGAS for the TPCs using the oaCalib package and relevant packages for the individual read out electronics chips. To represent reality, calibrations for all the relevant instrumentation is applied at this step. In general, this is done by measuring the electronic response of the detectors to cosmic ray muons, as these deposit a known and relatively constant amount of energy when traversing the detectors and are relatively easy to identify. While taking beam data, cosmic triggers are also in place so that data for these calibrations is constantly

being collected so that calibrations can account for changes in the detector operation over the course of a beam data collection period.

The oaEvent data is now representable as a collection of 'hits' which are individual collections of charge deposit that have position, time, and energy deposit information. This collection of hits is now ready to be reconstructed into more complex objects motivated by physical processes. First, each sub-detector performs a local reconstruction that is unique to that detector. Final objects from these reconstructions are then passed to a global reconstruction algorithm that reconstructs objects that can traverse multiple sub detectors. Physics analyses can be performed either using standalone local reconstructed objects only, or using the global reconstruction. Both of these options have their advantages and disadvantages. This analysis primarily uses a global track based analysis, but a single selection cut does rely on PØD local reconstructed objects. In both the PØD reconstruction (PØDRecon) and the global one, important objects described in a general way for this analysis are given below.

- Cluster
  - this is a position and time localized group of hits
- Shower
  - this is a cluster cast in terms of an electromagnetic shower (EM shower). Information such as the shower position, total energy deposited, and cone size are now stored.
- Track
  - this is a cluster cast in terms of a single ionizing particle traversing the detectors. Post-hit information such as the start and end positions and energy loss along the track, $\frac{dE}{dx}$, is now stored. Additionally a collection of 'nodes' belonging to the track is now stored. In the PØD, these nodes correspond to a pair of hits, one in

an X layer and one in a Y layer. Node level information includes position and direction of the track at the node as well as the $\frac{dE}{dx}$ at the node.

- Vertex
  - this is a collection of other reconstructed objects determined to have a common origin. New information will be the vertex position which can be used as the original neutrino interaction point.

P∅DRecon is the main reconstruction used for this analysis. Figure 1.18 provides the procedure flow for the reconstruction. Rigorous details of how each piece works are not important to understand the impact of this work, but a description and conceptual details of the important pieces for this measurement will still be provided.

The first step is to clean the raw hits in each oaEvent by first separating the hits in the 23 integration cycles previously described. Then, requirements on each hit are enforced for it to be passed to the next stage of the reconstruction. Either the hit must have a 15 pe or greater signal, a 7 pe or greater signal and additionally a neighboring hit in the same scintillating plane within 30 ns and 10 cm, or a neighboring hit within 30 ns and 3.5 cm. Additionally, there must be at least 5 hits in an integration cycle for the reconstruction to continue.

After the hits are cleaned, the remaining collection of hits are passed through a Hough transform [22] which uses the tangential distance of the hits from lines of varying slope to get a 'track seed' which can be thought of as a small track where locally, the hits predominantly lie on a small straight line. This seed is then expanded layer by layer (a layer is a single scintillating plane, either X or Y) looking for new hits within 6 cm of the end of the current track and 1.5 radians of the track end direction. This procedure is done separately for hits corresponding to an X scintillating plane and a Y one. The end result of this procedure is a collection of 2-D tracks (2-D because they contain only X-Z or Y-Z spatial information). The 2-D tracks are then matched between the X-Z and Y-Z views to attempt to form complete 3-D tracks.

If a 3-D track contains hits from at least 6 layers, a fitting procedure based on a Kalman filter [23] is applied along the track; the end result of which is the collection of nodes described before. Hits from a minimum of six scintillating planes must be included in the track for the reconstruction to attempt this fit. The resulting object is now referred to a 3-D Kalman track. This analysis uses only this type of tracks for any track based object referred to in the remainder of the document.

Collections of hits failing the requirements to be a Kalman track are passed to the shower reconstruction. This analysis does use shower objects, but only as a veto as will be described later. Further reconstruction is performed on the Kalman tracks, but is not relevant to this work. The 3-D Kalman tracks are passed to the global reconstruction where they are potentially identified to be a sub-track of a larger track traversing multiple sub-detectors. The main track in the selection to be described later are tracks originating in the PØD that also have a component in the first downstream TPC of the PØD. The TPC reconstruction includes a charge identification and measurement of the tracks momentum made by looking at the curvature of the track in the magnetic field. The global reconstruction then projects back through the PØD, reconstructing the momentum by range along the track to its beginning. For most tracks, the uncertainty inherently coming from the TPC measurement is on the order of 10% or less and additional uncertainties from the momentum by range calculation are on the few percent level. A detailed description of how this is done can be found in [24].

Finally, after reconstructed objects are assembled, the oaAnalysis package applies what is called oaEvent reduction where the very large and complex data files are simplified to a format more easily accessible to users. This is done by reorganizing the information into a more concise format and additionally removing unnecessary library dependencies for the classes contained and saving the file in the pure ROOT format which has built in compression and a data analysis friendly structure.

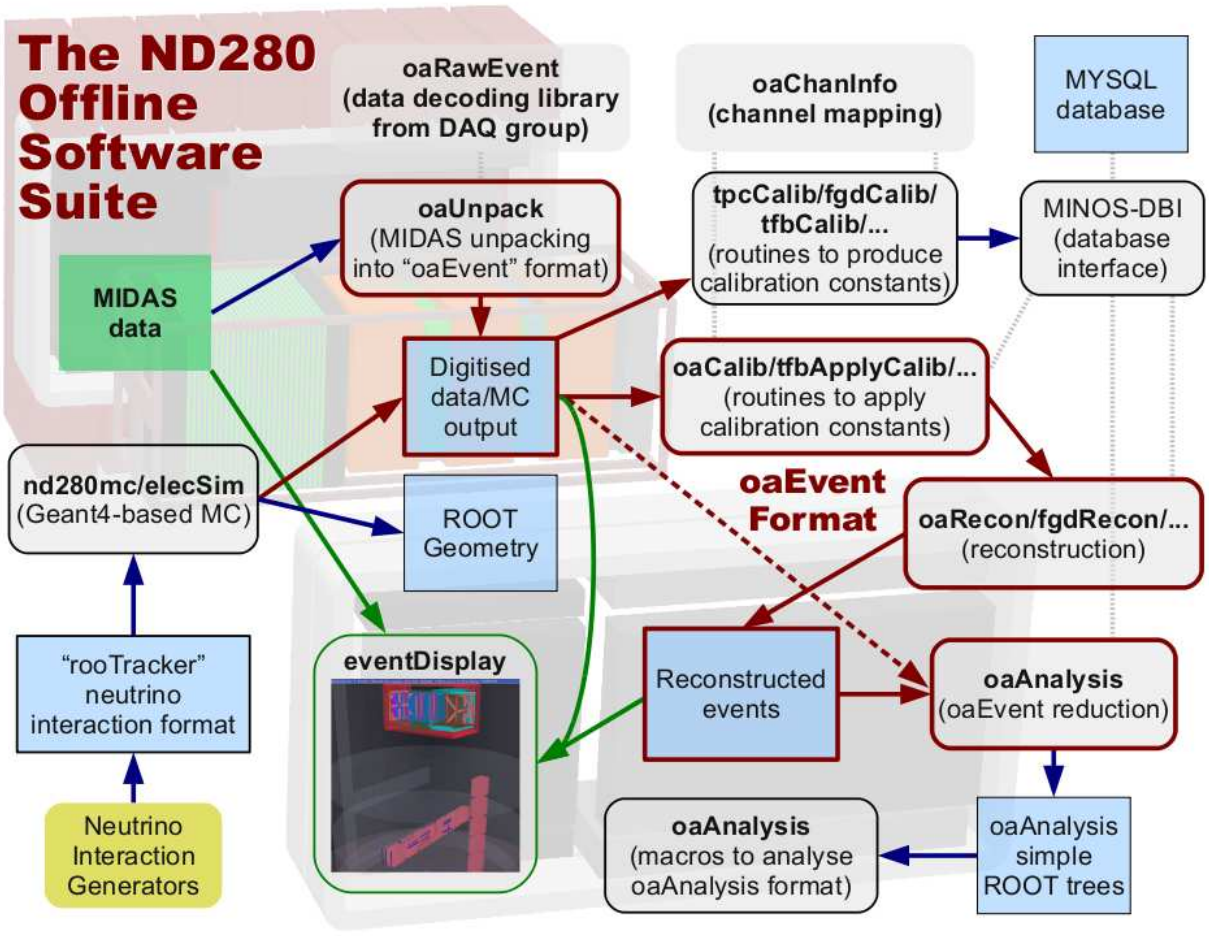

Figure 1.17: Software dependency and data flow chart for the ND280 software suite taken from [19]. Both data and MC are digitized, calibrated, reconstructed and then reduced before physics analysis begins.

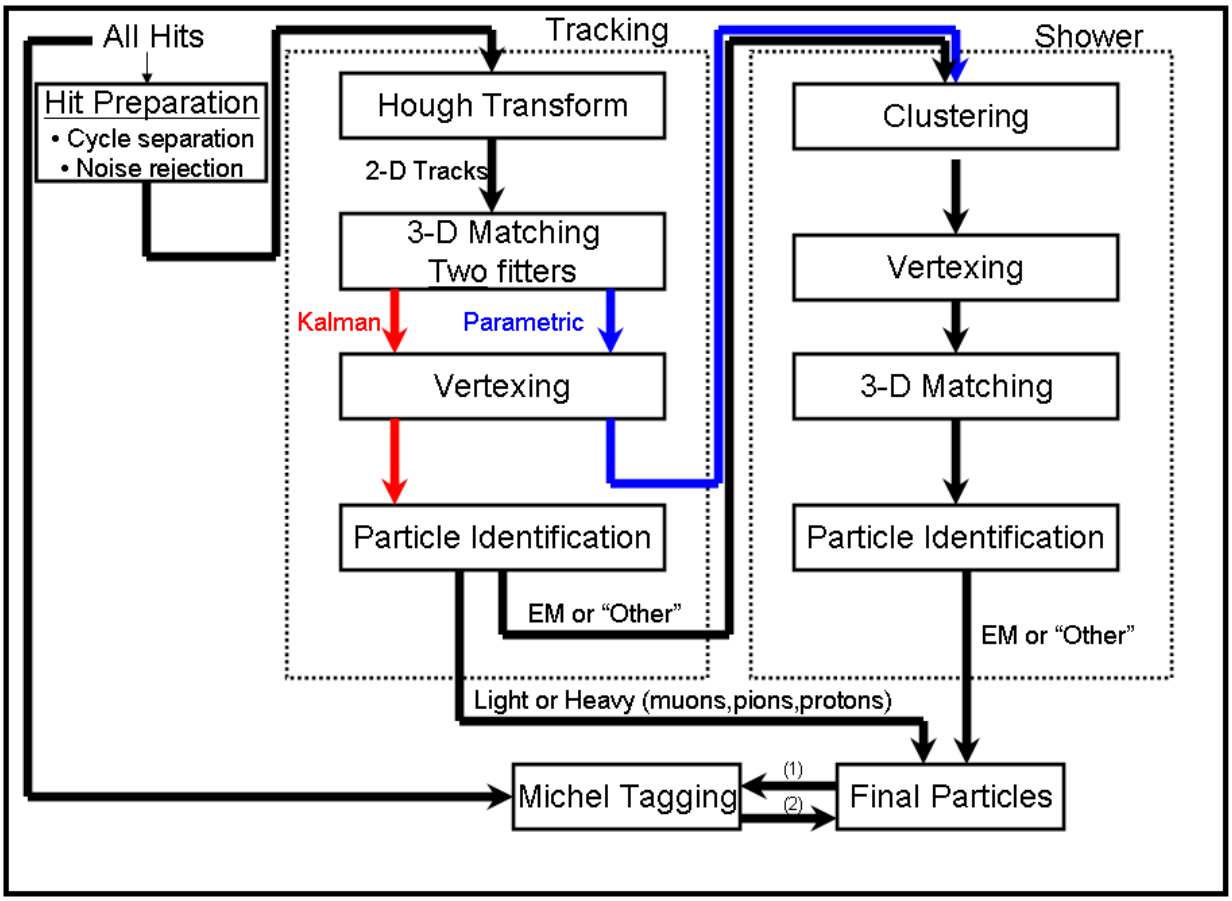

Figure 1.18: PØDreconstruction flow diagram taken from [21]. Hits are first cleaned and identified as 2D tracks which are then potentially matched to form 3D tracks. Long and high enough quality tracks are fit using a Kalman filter, other objects are then passed to form cluster objects which have the potential to be reconstructed as shower objects.

1.4 Selections, Systematics, and Highland2

With reconstructed objects from the data and simulation in hand, the real work in a cross section measurement can begin. The first step will be to attempt to use the reconstructed data to develop a selection of events in the data representative of a signal type.

The High-level Analysis at the Near Detector (Highland) package is a framework for developing event selections and propagating detector related systematic uncertainties to any extracted results. It is a new package, originating in 2014. It is now a standard utility at ND280, with the majority of cross section analyses and the whole of the ND280 component of the oscillation analyses beginning with the development of selections in Highland. This analysis uses the second iteration of the Highland framework, which is called Highland2.

Some terminology that will be used throughout the remainder of the document:

- Selection
  - A procedure to be applied to reconstructed objects in data and simulation that is meant to preferentially select events corresponding to some signal definition.
- Sample
  - A collection of events in data or MC. This could refer to a collection of events after a selection procedure has been applied, or simply a set of data files for some running period.
- Cut
  - A requirement on reconstructed objects or a function of their derived properties that will select some events and reject others.
- Systematic
  - Short for systematic uncertainty. Usually used when describing a single source of uncertainty; for example, 'momentum resolution systematic' refers to uncertainty

on some result arising from imperfections in how well the momentum of something can be resolved. Systematic might also be used in a more general sense to refer to the procedure by which some uncertainty is evaluated. In the previous example, 'momentum resolution systematic' in a different context might refer to the procedure used to evaluate the aforementioned uncertainty.

- Systematic Variation
  - A variation of some underlying parameters which describe a systematic's effect on the selection. This will become more clear in the rest of this section.
- Weight
  - A number assigned to each event in the selection procedure whose nominal value is 1. This will become more clear throughout this chapter, but weights (or reweighting procedures) are a mechanism through which the effect of a systematic variation can be applied to the selection.
- Toy Experiment
  - In the context of Highland, a 'toy' experiment refers to a selection procedure where a set of systematic variations have been applied. The systematic variations affect the selection procedure, a toy experiment is a selection procedure where one specific set of systematic variations have been applied.
- Throw
  - A single 'throw of the dice.' Meaning that when considering many systematic variations, a 'throw' could refer to a particular set of systematic variations. An example: 'many toy experiment throws,' refers to many systematic variations resulting in the generation of many toy experiments.

With this basic terminology introduced, figure 1.19 gives a pictorial overview of how Highland2 works.

A Highland selection macro takes oaAnalysis files as input and returns an output file tree containing 'micro-trees,' which are a compact summary of information extracted from events. The information included in the micro-tree is defined by the user and usually contains information like the number of certain suspected types of particles and their momentum, etc. For running over simulation, there is a micro tree both for only reconstructed events and one for all true generated events independent of whether or not they caused a signal resulting in the creation of any reconstructed objects. The existence of both of these trees in parallel with similar structure makes studying inefficiencies in the selection procedure fairly convenient for the user.

All of the things created and used by analyzers sits inside the event loop. The output oaAnalysis files from section 1.3.1 have each entry in the file corresponding to an entire beam spill. The event loop first breaks the spill into the bunch structure described in section 1.2.1. For the remainder of this discussion an 'event' in the event loop refers to a single bunch, not an entire spill.

The user can then define corrections to be applied to events such as if an entire sub-detector should not be used because there was some problem during the spill being analyzed.

The analyzer will have defined in Highland a set of actions and a set of selection cuts. An example of some actions could be a set of functions that look into the reconstruction and return objects of interest like tracks and showers in a particular sub-detector. Selection cuts are Boolean functions which take as an input objects returned by the actions for a particular event and return either *true* or *false*. If a selection cut returns *false*, the event loop breaks and it continues to the next bunch. Most analyses have several defined cuts, these are included in a particular order. Should the first cut return *true*, the second cut is called and so on. The user defines how many of these cuts must be passed for Highland to store information in the output micro-tree for selected events.

If the selection is being run in a mode where toy experiments are being generated, for each event, systematic variations are applied which effect the properties of and sometimes the existence of some reconstructed objects. The cut procedure is then applied again and if

the event passes enough cuts, the output is again written. The output micro-tree for when Highland is configured to run this way will have an entry for every toy for relevant output that changes with the systematic variations. For example, if the momentum of a type of particle in each event is being varied, the entry for the momentum of that type of particle in the micro-tree will not have a single value, but rather a set of values, one from each toy.

1.4.1 Covariance Matrices and Toy Experiments

A standard application of statistics throughout this analysis is that of random variables formulated in a matrix problem. A brief description of this application in the context of how it is used in this and many other similar analyses will now be presented to introduce the reader to terminology used later and also to demonstrate how these methods work.

Let $\vec{z}$ be a vector whose elements are Gaussianly distributed random variables. Suppose each of the variables is simultaneously sampled N times so that z_i^j is the jth measurement of variable z_i.

The sample covariance between each variable can then be calculated using the measured values:

$$\sigma_{ij}^2 = \frac{1}{N}\sum_{k=1}^{N}(z_i^k - \overline{z}_i)(z_j^k - \overline{z}_j) \tag{1.11}$$

In the above, $\overline{z}_i$ is the mean of the measurements of variable z_i. The σ_{ij} put into a matrix is an example of a *covariance matrix*. More compactly written,

$$\sigma = \hat{\mathbf{E}}(\vec{z}(\vec{z})^T)$$

where $\hat{\mathbf{E}}$ is the expectation operator.

A common use of covariance matrices, particularly in analyses like the one described in this document is essentially running the material just presented in reverse: given a covariance matrix for a set of random variables, generate properly correlated variations of those

parameters N times. This is done by calculating the Cholesky decomposition of the covariance matrix and multiplying it by a vector of randomly distributed Gaussian numbers many times, each time with a new vector of random numbers, and each time taking the output vector as one sampling of the distributions being built.

A common piece of terminology used when discussing applications of the concepts of this subsection in a cross section analysis might be, 'throw against the covariance matrix over many toys.' This is just a informal way of describing the above procedure. Each 'throw' is a multiplication of the decomposed matrix by a new vector of random numbers to get a properly (including correlations) varied set of the x_i variables. Each varied set of the x_i variables would constitute a 'toy variation.' The Cholesky decomposition exists for any semi-positive definite matrix and is readily computable numerically.

Why this procedure works can be easily seen. Let $\mathbf{V}$ be a covariance matrix for some set of random variables, $\vec{y}$. Let $\vec{x}$ be a vector of completely uncorrelated random variables with a mean of 0 and a variance of 1. It follows directly that,

$$\hat{\mathbf{E}}(\vec{x}(\vec{x})^T) = I$$

where I is the identity matrix. Let $\mathbf{C}$ be the Cholesky decomposition of $\mathbf{V}$:

$$\mathbf{V} = \mathbf{C}\mathbf{C}^T$$

Consider the vector, $\vec{t} = \mathbf{C}\vec{x}$. The covariance matrix for $\vec{t}$ is given by:

$$\hat{\mathbf{E}}(\vec{t}(\vec{t})^T) = \hat{\mathbf{E}}((\mathbf{C}\vec{x})(\mathbf{C}\vec{x})^T) = \hat{\mathbf{E}}(\mathbf{C}\vec{x}\vec{x}^T\mathbf{C}^T) = \mathbf{C}\hat{\mathbf{E}}(\vec{x}\vec{x}^T)\mathbf{C}^T = \mathbf{C}\mathbf{C}^T = \mathbf{V}$$

The third equality holds because expectation is linear and $\mathbf{C}$ is a constant matrix. It follows that the t_i variables have the same covariances as the y_i.

1.4.2 Detector Systematic Uncertainty

One of the main advantages to using Highland is that it is possible for analyzers to share systematics that are common between different selections. For example, the selection developed for the analysis of this thesis is first a trivial alteration and then further (non-trivial) refinement of a previously developed CC-Inclusive selection. Because of this, many of the dominant systematics are common to both analyses, and the systematics developed previously could be used for the thesis work rather than having to 're-invent the wheel' and re-develop a method for evaluating each source of systematic uncertainty.

In Highland, all detector systematics are evaluated in a similar way. There are two types of detector systematics: weight and variation. Variation systematics effect physical observables of particles in the selected events, for example, the momentum of the outgoing muon in CC interactions. Weight systematics are all other systematics that do not effect observables used in the analysis. Generally speaking, each systematic will attempt to parameterize some underlying process or feature of the detector and then vary the created parameters so that their effect on the selection process can be studied. Usually, the creator of a systematic would look in the MC simulation for quantities that can be accessed at the truth level for the reconstructed objects to form parameters describing some effect and then look to some real data results to determine a reasonable amount of variation to allow for the created parameters.

The use of 'variation' in 'variation systematic' is slightly different than 'variation' in the variation of parameters which both weight and variation systematics use. The 'variation' in 'variation systematic' refers to the variation of physical observables which is the mechanism variation systematics use to propagate the effect of the systematic variations to the selection.

The re-weighting and variation schemes used by Highland2 can also be thought of as shortcuts around an alternative of regenerating the entire simulation; re-weighting schemes used here and in the evaluation of other error sources in the analysis are examples of a formal concept from statistics known as *importance sampling*. To account for uncertainty in the

simulation based on the chosen value for some parameter that went into it, the parameter could be varied by some assumed uncertainty, and the simulation could be regenerated. The spread in the predictions of the simulation caused by the variations of the underlying parameter would then be representative of uncertainties coming from the uncertainty on the varied parameter.

To illustrate how a weight systematic works in the Highland2 framework and to clarify the terminology introduced at the beginning of the previous sub-section, take the example of the uncertainty arising from imperfect knowledge of the mass of various components of the detector. Suppose the detector is constructed of only two types of material: material A and material B. Physical measurements made when assembling the detector give the masses of each component as:

$$m_a = \overline{m}_a \pm \sigma_a$$

$$m_b = \overline{m}_b \pm \sigma_b$$

The total mass central value of material X is $\overline{m}_X$ and the uncertainty on the measurement is σ_X. If the mass of material A were to increase by 10%, it would be expected that the number of events that occurred in material A would increase by that same amount. A re-weighting procedure will use this idea to account for uncertainty on the selection by doing the following: over many toy experiments, a weight will be assigned to each event whose value is a function of the uncertainties from the physical measurements as defined below and two Gaussianly distributed random numbers, x and y, with zero mean and unit variance which are generated differently for each toy.

$$w = \begin{cases} (1 + x\sigma_a) & \text{if event truly occurred on target A} \\ (1 + y\sigma_b) & \text{if event truly occurred on target B} \\ 1 & \text{else} \end{cases}$$

To summarize, over many toys (say N_t), random numbers, x and y, are generated. All events are then looped over and for each event, the weight defined above is assigned. The result of this process will be N_t copies of the selected events where in each of the copies the events have different weights.

Now, consider the total number of events, N_e. To calculate the uncertainty on N_e coming from the uncertainty on the masses of the detector components, we can sum over the weights for each event in each toy and look at the variation in their sum. The nominal number of events is trivially given by,

$$N_e = \sum_{i=1}^{N_e} 1$$

and the re-weighted sum for toy k is given by,

$$N_e^k = \sum_{i=1}^{N_e} w_i^k$$

where w_i^k is the weight from before for event i in toy k. If in toy k the generated random number, x was say 0.1, All events in the simulation that were generated in material A will be given a weight of $(1 + 0.1\sigma_a)$, corresponding to a 10% fractional uncertainty increase in the weight of material A. The total number of events counted (sum of weights) to have been generated on material A will increase by the same amount as expected.

By forming a distribution of the N_e^k over all the toys, the spread in this distribution should be representative of the uncertainty on N_e caused by the uncertainty on the component masses. This process can be thought of creating a 'dial' that affects the mass of each component and then tweaking that dial and looking at how the selection results change. By tweaking the dial over some range corresponding to the uncertainly of what the dial should have been set to, the resulting change in the selection is representative of the uncertainty in the selection coming from uncertainty on the dial's value.

Colloquially put, this might seem a bit like 'opening a beer with a jackhammer.' And in some sense it is. The example above very simplistic as to not bog the reader down in complications of a more subtle systematic. It would have been much cleaner to evaluate

this systematic by simply analytically propagating the uncertainty on the total number of selected events using the known uncertainties and asking the simulation the number of events generated on targets A and B. However, evaluating all detector systematics in this manner allows for correlations between different sources of systematics to be easily included and kept track of.

Suppose the individual mass components of the detector from the previous example had relatively large uncertainties from measurements when it was assembled, but then some collaborator comes up with a clever way of measuring the total mass of the detector to very fine precision without taking it apart into its individual components. Now, each component mass has uncertainty, but the total mass essentially does not. It might then be of interest put some ad hoc correlations on the variations allowed between the two masses so that if one mass increases in a variation, the other decreases, keeping the variations on the total mass small. This can easily be done by correlating the random variables, x and y.

Tunings to the simulation can also be applied in this scheme. In the two component detector example from before, if it was determined that the measured total mass of material A not only suffered from large uncertainty but was also biased such that the central value should have been 5% higher than was reported, the weight definition could be altered:

$$w = \begin{cases} (1.05 + x\sigma_a) & \text{if event truly occurred on target A} \\ (1 + y\sigma_b) & \text{if event truly occurred on target B} \\ 1 & \text{else} \end{cases}$$

Now, every event that occurred in material A will have a nominal (zero variation) weight of 1.05, and the corresponding event rates will increase by the same amount in each toy such that the mean of the N_e distribution over the toys will be shifted by the appropriate amount corresponding to the 5% increase in material A.

Variation systematics proceed in an essentially identical way, but instead of assigning each event a weight based on the variation of some underlying systematic parameters, the

value of some observable quantity in the event is assigned a new value in each toy. For example, the momentum of the outgoing muon in CC interactions could be varied in each toy. The result of the systematic toy throws would then be toy copies of the selection with each toy having a different value for the muon momentum in each event. The selected event rate binned by the muon momentum might be of interest. This distribution could then be built in each toy and the collection of the distributions would constitute a set of samplings of a set of random variables like the $\vec{z}$ of section 1.4.1. Variances of and covariances between the momentum binned event rates can then be calculated using equation 1.11.

1.4.3 T2KReWeight and Model Uncertainties

Now that the Pandora's box of discussing systematic variations, throws against covariance matrices, toy experiments, re-weighting schemes, and so on has been opened, the framework at T2K for evaluating uncertainties coming from imperfections or lack of knowledge in the physics modeling used in simulation will be presented.

The T2KReWeight package is a utility for generating weights in a similar manner to those discussed in the Highland2 framework. The underlying parameters are now a set of so called 'model parameters,' many of which are actual model parameters such as the m_a^{QE} previously introduced and the others being parameters introduced by the T2KReWeight developers, but that do not necessarily correspond to an actual parameter from some specific model. Instead of acting on reconstructed objects like the Highland2 weight systematics, T2KReWeight takes as an input the rooTracker information at the bottom left of figure 1.17. The rooTracker information is generator level and would include things like the true neutrino interaction type, the number of particles produced and their kinematics both pre and post FSI, and other things of this nature.

To use it, an analyzer would have an event (maybe one selected by a Highland2 selection procedure) and then ask the event for its rooTracker information and pass this to T2KReWeight along with a parameter name and a value for that parameter. T2KReWeight then returns a weight for that event. For example: the m_a^{QE} parameter from before directly

effects the CCQE neutrino cross section. Suppose for our purposes here that an increase of m_a^{QE} to 1.5 from its nominal value of 1.2 corresponds to a uniform increase in the CCQE cross section by 30%.

Now, suppose an event selection has been developed containing events both of true CCQE origin and not. In looping over the selected events, the rooTracker information for each event is passed to T2KReWeight along with the parameter name for m_a^{QE} and a value of 1.5. T2KReWeight would then return a weight of 1.3 for events that are truly of CCQE origin and a value of 1.0 for events that are not of true CCQE origin, corresponding to the aforementioned 30% increase in the CCQE cross section. This was of course a simple example; T2KReWeight has a collection of parameters (also referred to as 'dials' or 'knobs') that affect both the overall event rates of entire interaction channels and individual event rates binned by underlying particle kinematics to allow for shape variations in the selection's resulting distributions.

1.4.4 Neutrino Flux Uncertainties

Being that the neutrino flux uncertainty is compactly summarized for analyzers in a covariance matrix as described in section 1.2.1, the methods described in section 1.4.1 can be directly applied. The flux covariance matrix is Cholesky decomposed and then thrown against over many toys. At each toy, there is now one sampling of the binned neutrino flux distribution (one sampling from a distribution of flux distributions). This sampling can be integrated over relevant bins to form distributions of integrated fluxes which can be used to calculate a total uncertainty on the incoming flux of a particular type of neutrino that might appear in a cross section formula like presented in section 1.1.2.

In addition, an analyzer could loop over the events in a selection and ask each event for the true energy of the neutrino that created it. Then, in each toy from above, the sampling of the corresponding neutrino flux bin for that toy can be taken to be a weight in a re-weighting scheme. The uncertainty on the simulated neutrino beam flux can now be propagated to any derived quantities from the selection.

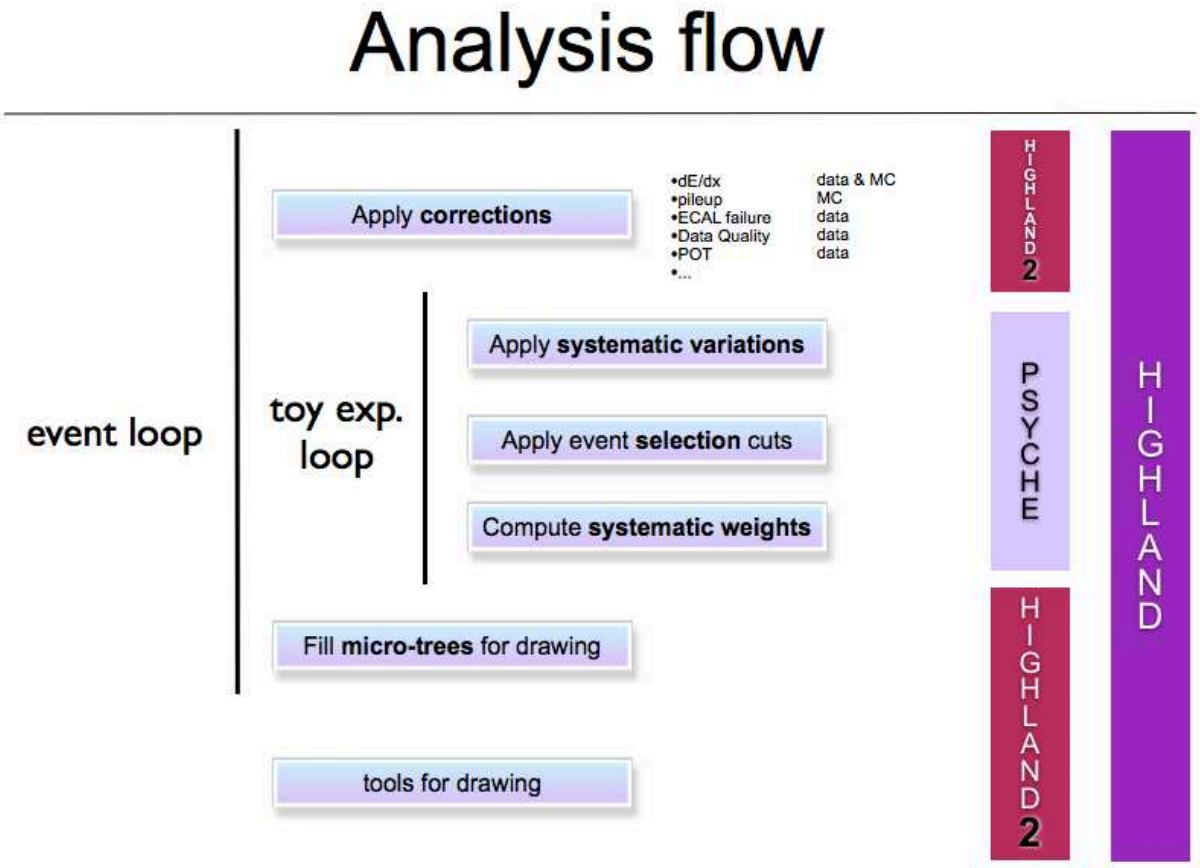

Figure 1.19: ND280 Highland2 event loop taken from [25]. For each event, the cut procedure is repeated over many systematic toys when evaluating systematic uncertainties, and event weights are applied to propagate the effect of the systematic variations to the output selection. Input is oaAnalysis files and output is a file containing several 'micro-trees' with a convenient data structure for physics analyses. In moving from Highland to Highland2, the toy experiment loop was optimized and formed into the light weight package, psyche. Throughout the remainder of the discussion, 'Highland2' refers to the total Highland2+psyche.

Chapter 2

DIFFERENTIAL CROSS SECTION CONCEPTS AND GENERAL FITTER IDEAS

2.1 Cross Section Formulation

A simple cross section measurement can be thought of as a counting experiment. First, a signal is defined that is meant to represent some interaction mode. For example: all CC-Inclusive interactions induced by an incident muon neutrino in the fiducial volume of a detector. A selection procedure to act on the reconstructed objects in data to attempt to preferentially select signal events is then developed. This procedure is of course not 100% efficient. Some events will be selected that are not truly signal and some events that were truly signal will be missed by the selection procedure.

To account for this, the MC simulation of the detectors response to generated neutrino interactions in the detector can be used to study how often either of the two mentioned issues occurred. Selected events that are not signal are referred to as background events and the ratio of the number of selected signal events to the total number of generated signal events is referred to as the selection efficiency. In a simple minded cross section extraction, both of these quantities could just calculated directly from the MC simulation.

A basic expression for extracting a flux integrated cross section from some data sample is given by:

$$\sigma = \frac{N_{sel,data} - B}{\epsilon \phi N_T}$$

In the above: ϵ is the selection efficiency given by:

$$\epsilon = \frac{N_{sel,MC} - B}{N_{Gen}}$$

The integrated flux of muon neutrinos is given by ϕ, and N_T is the number of targets. $N_{sel,X}$ is the number of selected events in data (X=data) or MC (X=MC). The quantity B is the number of selected events in MC that are not signal so that if B is scaled by the relative size of the MC sample compared to data, $N_{sel,data} - B$ is the expected number of signal events selected in the data.

2.1.1 Isolating Water as the Interaction Target

In addition to measuring different cross sections with different signals, it is also interesting to measure cross sections on a particular interaction target rather than averaging over all materials in a detector. Because the far detector of T2K has only water as the neutrino interaction target, cross sections where water is isolated as the target are quite interesting for T2K. Historically, measurements of this type in the PØD have been done using a so called "water subtraction."

The principal idea behind the method is that the number of interactions in the detector when it is filled with water is a sum of the number of interactions that occurred in the water and the number that occurred elsewhere in the detector. The water can then be removed from the detector and more data taken so that one can measure the non-water event rate and this can be subtracted from the water+non-water event rate. This difference should then be a good approximation of the interaction rate on water alone.

One could also imagine treating the non-water events as a background in the signal event selection (events that occurred on water). When using the simple technique described above for extracting the cross section, this clearly does not seem as strong as the traditional water subtraction. One would just be asking the MC whether an event occurred on water or not and then correcting the data accordingly. As will be shown later, using a binned likelihood technique it is possible to isolate interactions on water without relying on the water subtraction method used historically.

2.1.2 From Single Bin to Differential

It is often of interest to measure the cross section differentially by some observable physical quantities measured in the detector. Following the definitions for extracting a cross section given in the previous subsection, the cross section can be measured simultaneously for many sub sets of events defined by values of some observable characteristic of the particular interaction.

An example: for the CC-Inclusive signal definition from before, the muon kinematics could be measured and then the variation of the cross section in terms of those kinematics could be studied. To do this, the selected events could be binned by the observable of interest (muon momentum for example) and the cross section would be calculated using the events in each of these bins. If one chose to divide the selection into 10 bins, there would be 10 cross sections calculated, one for each bin.

In practice, how one chooses the binning (which observables, what bins) is decided by two main factors:

1. Interest from the community of the dependence of a particular cross section on a particular observable

2. Detector acceptance and reconstruction efficiency in the selection

The reason for point (1) should be clear, an example could be that there is significant disagreement among particular interaction models as to how the cross section of interest changes with an observable measurable in the detector. Point (2) can be a little more subtle. Obviously, one cannot measure a cross section in a bin where there are no events reconstructed; however, even in regions of the observable variable phase space where the detector acceptance is non-zero, concerns may arise about how the selection is behaving locally. For example, if in one single bin, there is a very rapid change in the selection efficiency, it might be better to choose smaller bins so that the efficiency is more slowly varying across each bin.

2.1.3 Control Samples

In the method outline for a simple cross section extraction given above, the MC simulation of both the neutrino interactions and the propagation of final state particles through the detector and reconstruction is heavily relied upon. Of course, this is less than desirable as there is the potential to introduce bias on the resulting cross section depending on what was put into the MC simulation used. There is a great deal of effort in the neutrino cross section community currently to find ways to limit this bias and to make measurements as independent from the choice of modeling in the MC as possible.

One way to remove potential bias coming from the background interaction model is to constrain the MC background prediction using control samples. By making additional selection procedures meant to preferentially select background events of a particular type rather than signal events, attempts can be made to estimate the background rate in some selection from real data rather than just blindly asking the MC. Exactly how these control samples are used depends on what background parameters they are constraining and how the background is dealt with in the cross section extraction framework.

2.2 True and Reconstructed Phase Space

If a differential cross section by some observable quantities in the detector is to be measured, it is important to understand how well the detector can measure these quantities. Furthermore, if this differential cross section is to be measured in one detector and then measured in a different detector perhaps at a different experiment in the same way, the results should be consistent. It then becomes important to ask the question: if some set of particles were created in the detector with some true values of an observable, what values of the observable are measured in our detector for that set of particles? Are the measured values the same as the true values? If not, are the measured values in our detector the same as the measured values in some other detector? The answer to all three of these question in practice is no. It is then important to carefully understand how to interpret and present the

results gotten from one detector so that the result is general enough to be reproduced in a different detector.

Suppose for some selection, it is of interest to measure a cross section differentially by some set of observables related to the kinematics of the out going particles. A "kinematic phase space" refers to the variable space formed by all kinematic observables of interest. For example, if it was of interest to measure a cross section differentially by the momentum and angle with respect to the incident neutrino momentum of an outgoing particle in the final state, the kinematic phase space would be p-θ space. A point in this space, (p,θ) would represent an out going particle with momentum, p, and angle, θ. As was mentioned before, when a particle is created in the detector with a set of true kinematics, the detector will likely measure a set of slightly different kinematics. We refer to the true kinematic phase space to mean the kinematic space corresponding to the true kinematics of some set of events and the reconstructed phase space to mean the kinematics space corresponding to the measured kinematics in the detector.

We now have two spaces relevant for a differential cross section measurement. One could guess that it is of interest to attempt to set up mappings between the two. Before we attempt this, it is important to pause and think which quantities from our simple cross section extraction formula are defined in which spaces as we move from a single bin measurement to a differential one. The selected data events for example will have only reconstructed kinematics defined for them since we can not know what the true kinematics were from the data alone. The selected events in MC however, have both reconstructed kinematics and true kinematics. This is because for each event selected in the MC, a true particle was generated with a set of true kinematics and then this particle was propagated through the detector and given reconstructed kinematics based on the simulated signal produced in the detector. In general, the number of generated signal events will have only true kinematics. This is because not every generated event will be reconstructed so not every generated event will be assigned reconstructed kinematics. This information is visually summarized in Figure 2.1.

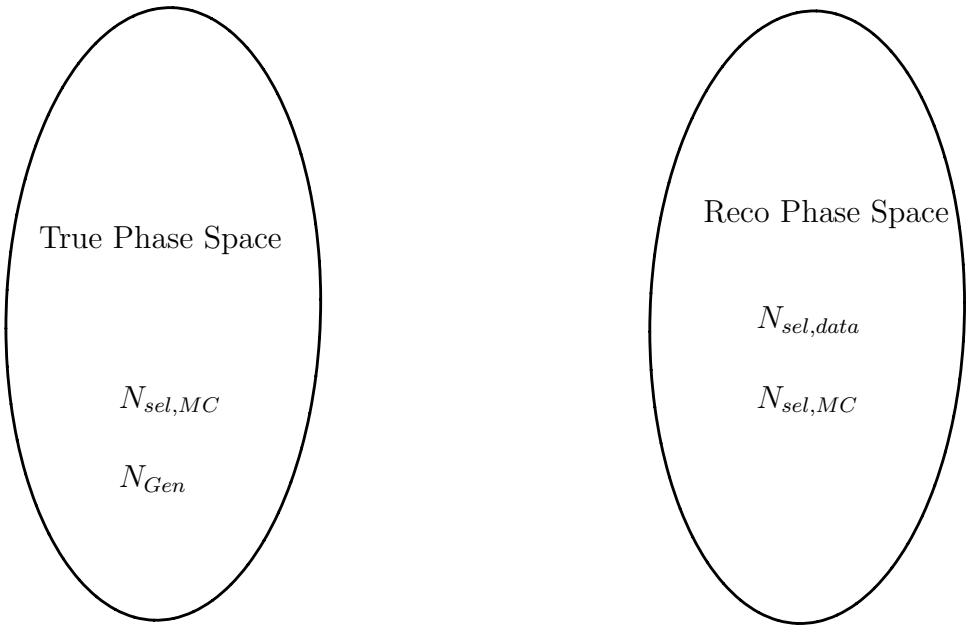

Figure 2.1: Visual representation of the true phase space (left) and the reconstructed phase space (right). We will see diagrams similar to this throughout the note. This one simply shows which of the "ingredients" for a cross section extraction are well defined in each space. Notice that the selected MC ($N_{sel,MC}$) is well defined both places whereas the selected events in data ($N_{sel,data}$) and complete set of generated events (N_{Gen}) are each well defined in only one of the two spaces.

Now the problem should be clear: we wish to measure a differential cross section by some kinematics, but the various ingredients to make the measurement are not wholly defined in either of the two kinematic phase spaces. We now would like to set up mappings between the two spaces so that we can map all of the quantities into either the true kinematic space or the reconstructed one and then perform the differential cross section extraction there. The process of attempting to map from the reconstructed space to the true one is referred to as *unfolding*. The process of mapping from the true space to the reconstructed one is referred to in this thesis as *forward folding*.

For the selected MC events, both the true kinematics and the reconstructed ones are well defined. The mapping from the true space to the reconstructed one can be easily defined and studied. Suppose we separate both spaces into discrete bins; each bin will correspond to

a range of values for each kinematic quantity. Suppose we label these bins with an integer 1,...,N_{bins} Now, we can formulate the mapping as a matrix problem:

Let the vector $\vec{t}$ be the vector whose elements t_i are the number of MC selected events with true kinematics corresponding to bin i. Similarly, let $\vec{r}$ be the vector whose elements r_j are the number of MC selected events with reconstructed kinematics corresponding to bin j. We define the smearing matrix $\hat{S}$. The elements S_{ij} are given by,

$$S_{ij} = \frac{N^{true\_in\_i}_{reco\_in\_j}}{N^{true\_in\_i}}$$

where $N^{true\_in\_i}_{reco\_in\_j}$ is the number of selected MC events that had true kinematics corresponding to bin i and reconstructed kinematics corresponding to bin j. $N^{true\_in\_i}$ is then the number of selected MC events that had true kinematics corresponding to bin i. One can easily see that the elements of the smearing matrix are just the probability that an event that had true kinematics corresponding to bin i and was reconstructed in bin j.

We have that:

$$\vec{r} = \hat{S}\vec{t}$$

The smearing matrix transforms true event spectra (binned event distributions) into reconstructed ones. For reasons that might be obvious, it may be of interest to attempt the inverse mapping so that the cross section extraction can be done in the true space. In practice one way this can be attempted is to try to invert the smearing matrix and then unfold the data to the true space before extracting the cross section. There are many subtleties in this problem, but in summary the main issues arise from the fact that the smearing matrix is easy to define, but upon attempted inversion of the smearing matrix, small variations in the reconstructed space can lead to large variations in the true space. There are always uncertainties on the data signal, when these uncertainties lead to large variations in the true space or even degeneracies, the problem becomes less well defined (or even undefined). In Figure 2.2 we see a visual representation of the general issue.

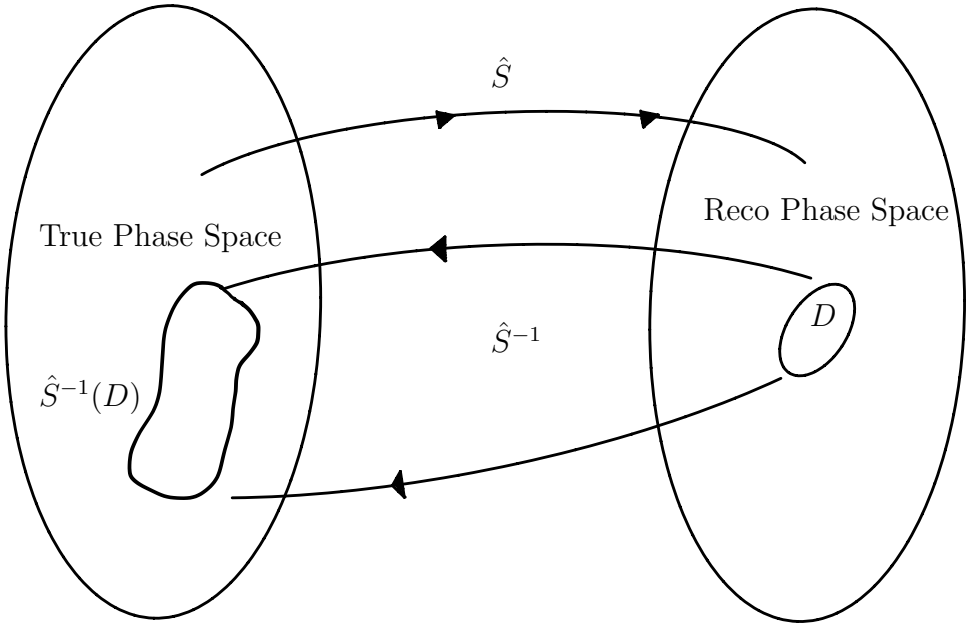

Figure 2.2: The inverse problem: the mapping $\hat{S}$ carries elements of the true space to the reco space. For some subset of the reco space D the inverse mapping (more formally the pre-image) of the set D, $\hat{S}^{-1}(D)$, may cover a larger relative portion of the true space than D covered in the reco space.

2.2.1 Unfolding Discussion

With the inverse problem introduced, it is worth briefly discussing the options for analyzers when attempting to measure a differential cross section. Consider first why measurements of differential cross sections are interesting to the neutrino physics community:

1. Provide data to help tune model parameters that go into neutrino interaction simulations

2. Cross validation across different experiments

3. Provide a particular experiment internal data to tune their internal simulation

4. General interest, expand empirical knowledge of neutrino interactions

Before discussing options for measuring a cross section, it is important to think about whether a cross section measurement is really even the best option given the end goals of

some analysis. Suppose that the primary goal for an analyzer was (3) in the above list. In a T2K like experiment, suppose that theoretical uncertainties for the cross section of the dominant background at the far detector was the leading source of uncertainty for neutrino oscillation analyses. The near detector sits in the same beam as the far detector and likely will have a higher rate of these background interactions. The analyzer hopes to precisely measure the cross section for this background in the near detector so that the uncertainties in the far detector can be constrained.

In this case, a cross section is of course a good candidate measurement to accomplish the analyzer's goal, but it is not the only one. Since the far detector and the near detector are in the same beam, a simple rate measurement might be good enough particularly if the near and far detector had very similar acceptances and detector uncertainties. Measuring only the rate might not require as strong of an efficiency correction and this analysis may be able to skirt around the problem of unfolding all together to accomplish its goals.

Another example taken from a current effort at T2K: rather than measure a cross section for theorists/other experiments to compare to, an analyzer measures only the reconstructed event rate in a detector for a particular signal. The analyzer the plans to publish this result and along side it, a software package that lets outside users statistically compare their predictions to the measured rate. Now potentially points (1) and (2) are solved without strictly measuring a cross section and again the problem of unfolding is avoided.

In the case an analyzer still want to measure a cross section, consider the simple one bin cross section formula,

$$\sigma = \frac{N_{sel,data} - B}{\epsilon \phi N_T}$$

with:

$$\epsilon = \frac{N_{sel,MC} - B}{N_{Gen}}$$

For any selection procedure that is not 100% efficient, the efficiency correction, ϵ, is needed and therefore, the number of generated signal events, N_{Gen} is also needed. Looking at figure 2.2, this quantity is in general only defined wholly in the true phase space. Again,

this comes from the fact that not all generated events are necessarily reconstructed and then assigned reconstructed kinematics. On the surface, this might seem to imply that it is not possible to measure a cross section in the reconstructed phase space and that some form of unfolding is always necessary in any differential cross section measurement.

In coming to the apparent conclusion of the last paragraph, the main assumption was that in the efficiency correction, there are generated events that are not reconstructed at all. One 'trick' cross section analyzers can play is to cleverly redefine their signal definition so that it is still somewhat physically meaningful and useful, but it now gives an efficiency correction where all generated events are reconstructed and thus the number of generated events is completely defined in both the true and reco spaces. Now it is possible to consider measuring a cross section in the reco space alone (though now the cross section has a very different interpretation as it is only valid in the reconstructed space for a single detector). With the trade off of altering the interpretation of the cross section, the problem of unfolding has been essentially avoided completely.

The unfolding problem potentially still remains in attempting to compare results to theory or between different experiments. For the comparison to theory case, models will generate interactions in terms of the true kinematics. An experimentalist could provide the reco space cross section and additionally the smearing matrix and then the theorist could forward fold their predictions to the reconstructed space of the measurement and do their comparisons there. For comparing different experimental results, one of the results will need to be unfolded and then could be forward folded to compare to the other, so the ability to *directly* compare different experimental results seems to still require some form of unfolding. One could certainly imagine doing some sort of simultaneous fit to two different experimental results, each with their own smearing matrix, to draw some potentially meaningful conclusions about how well the two results compare.

There are also other interesting alternatives to unfolding being developed currently at T2K, and hopefully more new ideas will follow. However, the analysis of this thesis does implement an unfolding method so too much discussion on these is probably out of scope,

but the discussion already presented does beg the question: if it is seemingly possible to get around the problem of unfolding, why unfold?

The obvious benefit of unfolding is that it requires less work to compare the result to different experiments and theory; the obvious disadvantage is that in unfolding, the inverse problem needs to be dealt with. Essentially, the choice of whether or not to unfold can be made by getting an idea of how badly the analysis and unfolding method will suffer from the adverse effects of the inverse problem. First, if in the analysis binning, the smearing matrix is essentially diagonal, then the potential for the large fluctuations in the true space previously mentioned is likely smaller than the alternative. Second, methods exist (referred to as *regularization*) for dealing with the large fluctuations in the true space; if in a particular analysis, it can be shown that the large fluctuations can be suppressed without introducing any other problems into the analysis procedure, then unfolding may still be viable. Generally speaking, for measurements where the primary physics involved is already relatively well modeled and the relevant kinematic resolution is pretty good, unfolding can certainly still be considered. Measurements with more exotic, complicated, or difficult to resolve signals will likely suffer more from the inverse problem maladies, and avoiding unfolding all together could certainly be the easier and perhaps statistically better choice. It of course also depends what the purpose of making the measurement is: is it important for the result to be comparable to other experiment or to outside theorists or can theory comparisons/phenomenology be done internally at the experiment?

As it turns out, the analysis here has a relatively well understood signal and additionally a relatively diagonal smearing matrix. It was decided to attempt to unfold and upon doing so, the procedure was seen to exhibit some of the large fluctuation behavior previously mentioned so a form of regularization was implemented. This chosen form of regularization was rigorously tested to demonstrate that it was not affecting the statistical significance of results or introducing any significant bias across many mock data fits.

It is the opinion of the author that unfolding still has a very important place in neutrino cross section measurements where it can be done without biasing or otherwise damaging

the end results. This analysis was lucky in the sense that the unfolding and regularization methods previously developed worked very well according the tests performed. Not all measurements will be as lucky and alternatives to unfolding are equally important to consider when designing an analysis. Following this discussion, the remainder of this chapter will focus on the general concepts of how some sort of fitting scheme might be used to handle unfolding in a cross section measurement.

2.3 Fitting as an Unfolding Method

Before discussing how a likelihood fitter might be used to address the problem of unfolding, the general concepts of how a fitter might be used in the context of a cross section measurement will be presented. In general the idea is that various parameters from the MC are allowed to vary subject to some well defined constraints. The varied MC is then compared to the data signal until a best-fit set of parameters in the MC is found such that the MC agrees maximally with the data. These best-fit parameters are then used to extract a cross section.

For example, suppose the cross section for charged current interactions induced by muon neutrinos where there is exactly 0 pions in the final state (ν_μ CC-0π) is to be measured differentially by the outgoing muon momentum.

The parameters to be fit could then be the number of ν_μ CC-0π events in each momentum bin along with various model parameters that effect the backgrounds (CC-1π, CC-Other, etc.). The fitter could then vary the background model parameters simultaneously with the fluctuated number of signal events in each bin. With each variation, a new distribution of the number of signal+background events in each momentum bin could be compared to the data. The set of parameters that have maximal agreement with the data would then include the number of signal events events in each momentum bin.

This is equivalent to the $(N_{sel,data} - B)$ term from section 1.2. Once we have this, we efficiency correct and divide by the flux and number of targets to get the cross section in each bin. This scheme has of course ignored the issue of unfolding. To address that, one

option could be to define the parameters to be fit as the number of signal events in each true momentum bin along with the model parameters. The MC could then be varied in the true kinematic space and then "forward folded" or "smeared" to the reconstructed space. Then the smeared, varied MC could be compared to the data signal and the set of parameters that has maximal agreement with the data could be used similarly to before.

The data has now been effectively unfolded and background subtracted so that an estimate of the number of signal events in true momentum bins in the data has been obtained. This was done with minimal assumption of the signal model and without having to attempt to invert or find a pseudo-inverse of the smearing matrix. Only the smearing matrix itself was used which is well defined here. There are of course more subtleties to be discussed, but this is generally how a likelihood fitter might be used to simultaneously unfold and subtract the backgrounds for a particular measurement. The fitter can also study how each of the parameters of interest vary with respect to one another, and can calculate a covariance matrix in the fitted parameters space. This covariance matrix would contain errors relevant to the statistical uncertainty from the data and uncertainties from the background model in this example. Figure 2.3 gives a visual representation of how this process generally works.

2.4 Likelihood Fitter for Cross Section Extraction

It is now worth discussing some more general ideas about how a likelihood fitter could be used in a cross section extraction. It has been argued previously how a data signal could in theory be simultaneously unfolded and background subtracted using a likelihood fitting scheme, but the details were glossed over. This section will still present only general ideas, but will attempt to provide a more complete picture of what could be done. A more formal mathematical formulation of the framework will be given later.

As was seen previously, the general idea of how the fitter will work in the context of a differential cross section measurement could be to vary a set of parameters in the MC until a maximal agreement with the data is found. The best-fit values of the parameters in the MC could then be used to calculate the results. The fitter could take inputs relevant to

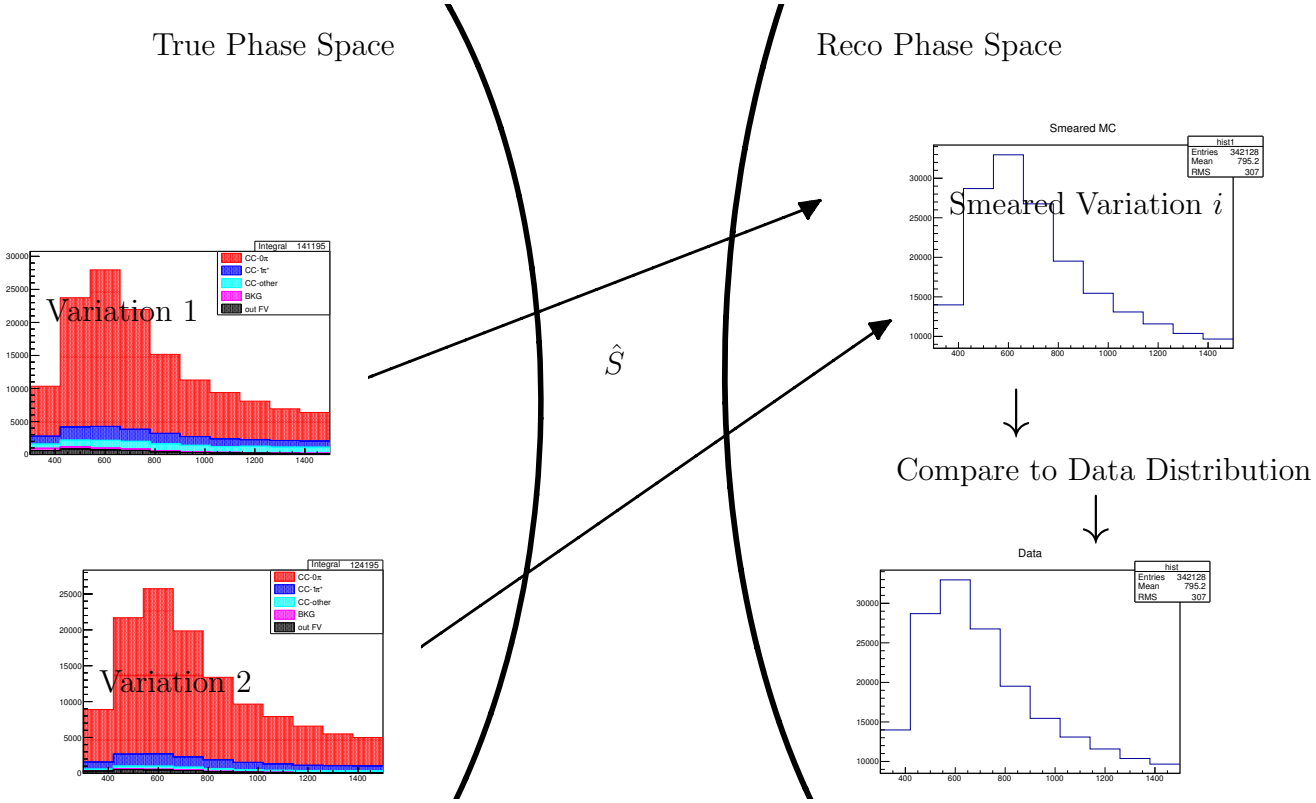

Figure 2.3: Illustration of the general concept of fitting to unfold: on the left is the true momentum space. The histograms are varied MC toy distributions with the signal and background components given in each true momentum bin. Each variation is then smeared to the reconstructed momentum space and then compared to the data to determine how well it agrees. This can be done many times until maximal agreement with the data is achieved.

both the MC and the data and output the best-fit parameters along with uncertainties and information about the quality of the end fit.

2.4.1 Inputs to the Fitter

First and foremost, the fitter will need to be provided with a set of parameters to be fit. In the example previously presented, the set of parameters was the number of signal events in each true momentum bin and the background model parameters. A detail that

was omitted before was how the fitter knows how to vary the model parameters "subject to some constraints."

For each set of parameters given to the fitter that effect some sort of systematic uncertainty, the fitter will need to be told how it is allowed to vary those parameters. This knowledge can enter in the form of a covariance matrix in terms of those parameters containing information of all the prior assumed uncertainties and correlations between the parameters. There are more sources of uncertainty than just the background model as well. There will also be uncertainties arising from the beam flux and from detector related effects.

In this scheme, the fitter of course also needs to be provided with at least one data and MC sample. The real power of the fit comes in passing it more than just a signal selection data and MC sample. Control samples with background pure selections can be simultaneously fit with the signal sample to possibly constrain parameters that the signal selection might have little sensitivity to. The dominant background for many previous CC-0π selections at T2K is CC-1π. If a CC-1π selection is developed in addition to the CC-0π one, an additional data and MC sample corresponding to the CC-1π selection could be simultaneously used in the fitting procedure. In doing this, we are giving the fit more data to use to constrain the input MC parameters; specifically since the CC-1π control sample will be very pure in CC-1π events, that sample should in theory have good power in constraining the model parameters relevant to CC-1π interactions. By constraining background sources with control samples, the power to constrain the background model parameters is possibly increased which in turn could lower the final uncertainty on the results due to uncertainty in those parameters.

This covers all of the basic inputs to the fitter that the proposed analysis plans to use. To summarize, the fitter will be passed:

1. The set of MC parameters to be fit

2. For each parameter sub-set relevant to a source of systematic uncertainty, a covariance matrix in those parameters will be provided.

3. The signal selection data and MC samples

4. Any number of control samples meant to constrain sources of backgrounds in the signal selection (data and MC samples to be passed)

2.4.2 Outputs of the Fitter

As was described before, the fitter will take the input MC samples and vary the parameters it was told to fit. It will then compare the varied MC distributions to the data until it finds the maximal agreement to data. As it varies each parameter, a covariance matrix containing information of the uncertainties on the best-fit parameters and how each of the parameters are correlated to each other can be constructed.

For each parameter that is fit, the size of the output covariance matrix is increased. If there are 10 signal bins, 5 background model parameters, 3 detector systematic parameters, and 14 neutrino flux parameters, the covariance matrix that is returned by the fitter would be a $10 + 5 + 3 + 14 = 32 \times 32$ matrix. In addition to the covariance matrix, the best fit values for each of the 32 parameters would also be returned.

2.4.3 Propagation of Uncertainties

With the set of best fit parameters output from the fitter, we now have an estimate for the number of signal events in each true kinematic bin defined by the input to the fitter. As was said before these are then used to calculate the cross section. The output covariance matrix has all the necessary information about the uncertainty on the number of signal events in each true bin due to each source of uncertainty considered in developing parameters to be fit and how the event rate in each true kinematic bin is correlated to the others.

The covariance matrix can then be Cholesky decomposed to generate properly correlated variations on the number of signal events in each true kinematic bin. Over many variations (colloquially "toy experiments") derived quantities from the unfolded event rate can be calculated in distribution. The mean and spread in the resulting distribution of the derived quantity (cross section, etc.) can be taken to be the central value and error for that quantity.

2.4.4 Fitting for the $\overline{\nu}_\mu$ CC-0π Double Differential Cross Section on Water

This note describes the application of a likelihood fitting technique to extract the $\overline{\nu}_\mu$ CC-0π cross section with water alone as the interaction target. As will be presented in more detail later, a signal (CC-0π) and one control (CC-1π) selection have been developed using the PØD which can separately take data in a water-in and water-out configuration. MC samples for both signal and control in water-in and water-out mode are simultaneously fit (4 samples total) to the corresponding data samples.

Parameters describing the signal event rates binned by the outgoing μ^+ momentum and $\cos\theta$ serve as the main parameters of interest. Separate sets of these parameters for signal interactions where water was the true interaction target and where non-water targets were the interaction target are fit to get separately the unfolded event rate on water and non-water targets.

Additionally, parameters to allow for systematic variations due to the detector simulation, the neutrino interaction model, and the incident neutrino flux on the PØD are included.

After the fit, the parameters for the CC-0π event rate with water as the interaction target can then be used to calculate the cross section by performing an efficiency correction and dividing by the integrated flux, the number of water targets in the detector, and the bin width in terms of the μ^+ momentum and $\cos\theta$.

Over many toy experiments, the unfolded signal event rate on water can simultaneous be varied along with the efficiency, flux, and number of targets to get a distribution of varied cross sections in each bin. Appropriate variances and covariances of the cross section in each bin can be computed across these variations to yield the final results.

Chapter 3

LIKELIHOOD FORMULATION

With the general ideas of how a binned likelihood fit might be used in a cross section extraction, the mathematical formulation of the fitting framework will now be presented. The formulation will begin with that for the case of using one selection to extract the event rate in a set of true kinematic bins with signal interactions occurring on any target in the detector. The analysis described in this document will use multiple samples to extract the event rate in a set of true bins with water alone as the interaction target. The formulation presented initially will then be generalized to accommodate these differences at the end of the section. This section is intentionally general. Specific details of how the problem is parameterized for the analysis of this thesis is given in detail in chapter 5.

The way the fitter will extract the best estimate of the signal event rate in each true analysis bin will be to re-weight the input MC event rates in each true analysis bin.

$$N_j^{signal} = c_j N_j^{signal,\ MC}$$

In the above, N_j^{signal} is the estimate of the number of signal events in data in true analysis bin j. The main free parameters of the fit are the c_j factors, and $N_j^{signal,\ MC}$ is the number of signal events in the MC in true analysis bin j. The data will have both signal and background components so that the number of events (signal+background) in true bin j is given by:

$$N_j = c_j N_j^{signal,\ MC} + \sum_{k}^{bkgd\ types} N_j^{bkgd\ k,\ MC}$$

As was explained previously, to get from the true kinematic space to the reconstructed kinematic space, the transfer or smearing matrix previously defined as S_{ij} is used. For the number of events (signal + background) in reconstructed bin i:

$$N_i = \sum_{j}^{bins} \left(c_j N_j^{signal,\ MC} + \sum_{k}^{bkgd\ types} N_j^{bkgd\ k,\ MC} \right) S_{ij} \tag{3.1}$$

The c_i parameters are then fit using the data by minimizing the likelihood [26]:

$$\chi^2_{stat} = \sum_{i}^{bins} 2(N_i - N_i^{obs} + N_i^{obs} \ln \frac{N_i^{obs}}{N_i}) \tag{3.2}$$

Where N_i^{obs} is the observed number of events in data in reconstructed bin i.

3.1 Systematic Uncertainties

In the MC simulation, there are many things that can effect the event rate calculated in equation 3.1. The dominant effects can be classified into three categories:

- Background model effects
- Incident neutrino flux effects
- Detector response simulation effects

The above are all simulated in the MC, but of course the simulation cannot be perfect. Because equation 3.1 will depend on the MC simulation, uncertainties on how these effects are simulated need to be propagated. The following subsections will present how each of these sources of uncertainty are handled in the fit. In general, this is done by parameterizing the source of uncertainty and then propagating how variations of the parameters affect the relevant event rates. The uncertainties and correlations of all parameters is specified so that now, at each iteration in the minimizer, the χ^2 is calculated with varied c_i and varied systematic parameters. So now in addition to the main fit parameters c_i, the systematic parameters are also fit.

3.1.1 Background Model

As was mentioned in general before, since the MC simulation is used to predict the background event rates in data, it is important to propagate uncertainties on the background simulation to the results. This is done by taking a parametrization of the background physics models and using this to vary the background distributions to study variations on the extracted results due to the background model variations. Re-weighting functions are introduced into equation 3.1 that vary the number of events in each bin when the background parameters are varied. In addition a penalty term is added to equation 3.2 so that when the background parameters are varied the total χ^2 increases.

The number of events in reconstructed bin i now becomes:

$$N_i = \sum_{j}^{bins} \left(c_j N_j^{signal,\ MC} + \sum_{k}^{bkgd\ types} N_j^{bkgd\ k,\ MC} \prod_{a}^{model} w(a)_j^k \right) S_{ij} \tag{3.3}$$

The $w(a)_j^k$ are the response functions that apply variations on event rate k in true bin j for a value of background model parameter a.

A penalty term is added to equation 3.2:

$$\chi^2_{bkgd\ model} = (\vec{a} - \vec{a}_{prior})(V_{cov}^{model})^{-1}(\vec{a} - \vec{a}_{prior})$$

V_{cov}^{model} is a covariance matrix containing information about the uncertainties and correlations of the background parameters.

3.1.2 Flux Model

In addition to the background model simulation, the incident neutrino flux model can also affect the results. To account for uncertainties in the flux model, equation 3.3 is modified to include parameters that allow for flux variation:

$$N_i = \sum_j^{bins} \left(c_j N_j^{signal,\ MC} + \sum_k^{bkgd\ types} N_j^{bkgd\ k,\ MC} \prod_a^{model} w(a)_j^k \right) S_{ij} \sum_n^{E_\nu} f_n^i \tag{3.4}$$

The above term $\sum_n^{E_\nu} f_n^i$ is a normalized sum over fractional variations of the incident neutrino flux binned by energy. Nominally (nominal values for the parameters), the sum evaluates to one. As the minimizer varies these parameters, however, the sum need not evaluate to one so that both the shape (in the 14 bins) and normalization of the flux are allowed to vary and are fit.

An additional penalty term is added to equation 3.2:

$$\chi^2_{flux\ model} = (\vec{f} - \vec{f}_{prior})(V_{cov}^{flux})^{-1}(\vec{f} - \vec{f}_{prior})$$

V_{cov}^{flux} is the covariance matrix containing information of the uncertainties and correlations of the flux parameters.

3.1.3 Detector Model

Finally, to account for the MC modeling of the detector response, additional parameters are included to allow for variations in the event rates from detector systematic effects:

$$N_i = \sum_j^{bins} \left(c_j N_j^{signal,\ MC} + \sum_k^{bkgd\ types} N_j^{bkgd\ k,\ MC} \prod_a^{model} w(a)_j^k \right) S_{ij} r_i \sum_n^{E_\nu} f_n^i \tag{3.5}$$

The r_i are parameters that fractionally vary the event rate in each reconstructed bin due to variation of all detector systematic sources.

Another penalty term is added to equation 3.2:

$$\chi^2_{det\ model} = (\vec{r} - \vec{r}_{prior})(V^{det}_{cov})^{-1}(\vec{r} - \vec{r}_{prior})$$

V^{det}_{cov} is the covariance matrix calculated in the following way:

All sources of detector related uncertainty are allowed to vary the event rate in each reconstructed bin over many toys. The fractional variances and covariances for these event rates are calculated and form the V^{det}_{cov}.

3.1.4 Signal Model

Because it is of great interest to extract a measurement for a given signal definition with as little assumption of that signal as possible, the variations of the signal model parameters are not included in the same was as the background model. Instead, the c_i parameters are completely free parameters in the fit so that the event rate in data can be extracted with no explicit assumption on the signal physics model.

3.2 Isolating Water as the Interaction Target

To utilize the PØD's ability to take data in both the water-in and water-out configurations, signal interactions that occur on a target other than water are treated in the fit similar to a background, but with one important difference: the number of non-water signal events are allowed to freely vary in the fit. Equation 3.5 now becomes:

$$N_i = \sum_j^{bins} \Bigg(c_j N_j^{signal,\ water,\ MC} + d_j N_j^{signal,\ not\ water,\ MC} + \sum_k^{bkgd\ types} N_j^{bkgd\ k,\ MC} \prod_a^{model} w(a)_j^k \Bigg) S_{ij} r_i \sum_n^{E_\nu} f_n^i \quad (3.6)$$

The d_i are now additional free parameters for the fit so that the number of signal events on water and on non-water targets are allowed to independently and simultaneously vary in the fit.

3.3 Control Samples

If in addition to the signal selection, other selections meant to select different types of backgrounds can be developed, the fitting procedure can be applied in each sample simultaneously. The sum of the χ^2 for each sample is minimized. In principal, the best case would be to have a selection for each N_j term in equation 3.6 for a measurement on water. So, in the case of a CC-0π measurement on water, there would be a sample sensitive to CC-0π on both water and separately non-water (signal selection in water-in mode and water-out mode of the P$\emptyset$D) and control samples for any significant background (CC-1π, etc.).

In addition to minimizing the sum of χ^2s, the many different samples will have correlations between them with respect to the detector systematics. This is taken into account by enlarging the detector systematic parameter covariance matrix to include one dimension per parameter per sample so that covariances between each parameter in each sample are calculated.

3.4 Realistic Implementation

The material presented in the preceding section is a very nice and compact summary of the what the fitter is doing. However, in the real world computational problems, for example those for analysis in this thesis, things proceed in a slightly different, more challenging manner. For example, the true to reconstructed kinematic mapping is actually handled on an event-by-event basis rather than a simple matrix multiplication as appears in the preceding equations. The equalities presented do still hold, but there is never any explicit matrix multiplication for the detector response in the software developed.

In addition to the detector response mapping, the flux re-weighting arising from particular values of the fitted flux parameters is done on an event-by-event basis. But again, all the equalities presented still hold.

3.4.1 xsLlhFitter Package

The application of all the material presented in this chapter in the analysis described in this thesis was done using a recently developed package known as the xsLlhFitter (cross section likelihood fitter). It was developed internally at T2K primarily by S. Bolognesi, S. Dolan, and others, and it consists of a set of C++ classes and macros specifically designed for minimizing a χ^2 of the form like in equation 3.2 for a differential cross section measurement. The MINUIT [27] package is used for the minimization of the χ^2 and optionally for the propagation of uncertainties. The package is written in quite a general way, making it fairly versatile. Aside from its application in this thesis work, it has been used already in one published T2K result [28], one official result that is in the process of producing a publication [29], and additionally several other analyses at T2K at various stages of the T2K internal analysis procedure. The analysis presented in this thesis is planned to produce the third publication from T2K using this package.

From a user standpoint, the package is quite simple. The first step is to define a signal (CC-0π, etc.) and variables with corresponding binning definitions for the differential measurement (muon momentum and bin edge definitions, etc.).

Additionally, the user provides processed data and MC files. For MC files, a list of the selected events with both reconstructed and true information is provided. Each entry in this list contains the reconstructed and true values for the relevant binning variables, as well as information like the true interaction type (for this work, by topology: CC-0π, CC-1π, and so on) and the true neutrino energy of the parent neutrino for flux uncertainty considerations. The data will contain only the list of selected events with their reconstructed values for the relevant binning variables.

For applications of the package like this one where systematic parameters are fit, a definition of these parameters is provided and additionally, as was described in this chapter, necessary covariance matrices and in the case of the model parameters, response functions are also provided.

Chapter 4

PØD CC SAMPLES

As was described in general in chapters 1 and 2, when measuring the cross section for a particular signal definition, a signal selection must first be developed. In this analysis, this was done by developing a set of selection "cuts," where a cut is a requirement made on reconstructed objects in the data that preferentially selects a particular type of neutrino interaction. An illustrative example: for developing a selection of ν_μ CC-Inclusive events, a cut can be developed to attempt to tag events where there is a reconstructed object that looks like a muon. This is well motivated, as all ν_μ CC-Inclusive events will have an outgoing muon produced in the interaction. In the ND280 detectors, muons are quite penetrating; they typically form long track objects. An example cut could be: reject events where there are no tracks longer than 30 cm present. When looping through all events in a data sample, events where there are no tracks longer than 30 cm will be rejected while ones where there is a track longer than 30 cm will be accepted and are said to have "passed" the cut.

The subset of all the initial events in the data sample where this cut was passed should then be more pure in CC-Inclusive (CC-Inc) events since CC-Inc events are more likely to pass this cut.

What is to be presented in this section is the first case of a selection procedure in the PØD for true CC-0π that does not have any cut on track multiplicity so that CC-0π events where a proton is reconstructed will still be accepted. This was done mainly by the development of a simple muon-like - proton discriminator tool. This tool determines the charge deposited by reconstructed tracks in the event and uses this to distinguish μ-like tracks from non-μ-like tracks.

4.1 Selection Cut Flow

This analysis uses a refinement of an existing charged current inclusive selection made using the Highland2 framework used in [24].

This package was developed for selecting ν_μ CC-Inclusive events where the out going muon originates in the fiducial volume of the PØD and has its momentum measured in the first TPC downstream of the PØD. This package tagged the μ^- by selecting the highest momentum negatively charged track beginning in the fiducial volume of the PØD with a good reconstructed momentum from the TPC (*fiducial volume* being a sub volume of the total active volume of the detector).

In this analysis, the package was used to select the highest momentum positively charged track with the same properties as before in hopes of tagging the outgoing μ^+ of $\overline{\nu}_\mu$ CC events. This forms a $\overline{\nu}_\mu$ CC-Inclusive pre-selection that is defined by cuts (1)-(3) below. Additional cuts are then applied to clean the pre-selection into a $\overline{\nu}_\mu$ CC-Inclusive selection. After an event is selected as CC-Inc, first CC-π^0 events are rejected and then the remaining events are separated by the number of muon-like tracks in the event to form the signal (CC-0π), sideband (CC-1π) and remainder (CC-Other) selections.

The charged current analysis cut flow for anti-neutrino mode beam running is as follows:

1. Overall ND280 data quality flags are good
2. There is at least one track reconstructed in TPC1
3. There is a reconstructed track in the PØD matching a track in the TPC with the start of the track reconstructed in the fiducial volume of the PØD water target.
4. The highest momentum positively charged track is the highest momentum track in the event, and has a muon-like pull in the TPC
5. There are no reconstructed showers in the event
6. Number of muon-like tracks (explained in 4.1.1)

Cuts 1-3 define the CC-Inc selection previously developed. The highest momentum positively charged track in the event is assumed to be the μ^+ candidate. Cut 4 attempts to remove ν CC-1π events where the π^+ is reconstructed to have greater momentum than the μ^- and additionally ν DIS events where the proton is the highest momentum positive track in the event. Cut 5 removes CC-π^0 events. Cut 6 separates the remaining events into the CC-0π, CC-1π and CC-Other selections. For CC-0π, the event must have exactly one muon-like track. For CC-1π, two of the reconstructed tracks must be muon-like. CC-Other is everything else.

4.1.1 PØD μ-Proton Discriminator

With cuts (1)-(5) above, the selection is a good $\overline{\nu}_\mu$ CC-Inclusive selection with CC-π^0 removed where the outgoing μ^+ has been tagged. To refine this selection to include only events where there are exactly 0 charged pions in the observable final state, a tool was developed to attempt to distinguish tracks caused by muons/pions and protons. The tool relies on the idea that when a charged pion is reconstructed in the detector, the track will deposit charge in a manner more similar to the μ^+ candidate than a proton which will deposit much more charge.

The tool works in the following way: For each reconstructed track in the event, the average charge deposited per node (set of X, Y hits) in the "middle" the track is compared to that for the μ^+ candidate. The ratio of these two quantities is cut on so that events where this ratio is close to 1 (the charge deposit per node of the track is very close to that for the μ^+ are tagged as muon-like).

Figure 4.1 gives an overlay in data and MC for the water-in mode of the number of reconstructed tracks for events that pass cuts (1)-(5), all cuts prior to the μ-proton discriminator. Good agreement is seen between the data and simulation in the 1 track sample and the simulation is seen to be lower than the data for multi-track events.

Figure 4.2 gives a distribution of the formed ratio in the water-in MC selection broken down by interaction type. In generating this plot, events with more than 1 reconstructed

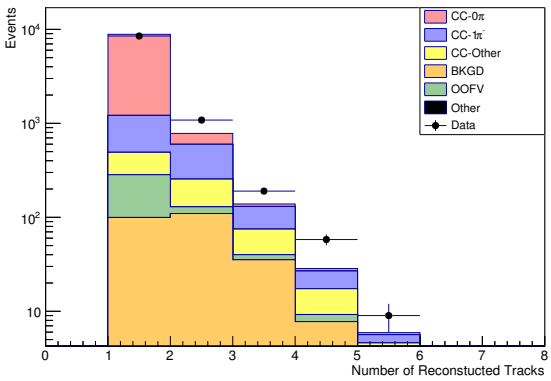

Figure 4.1: Overlay of the number of reconstructed tracks for events passing cuts (1)-(5) in the water-in MC and data.

track had this ratio formed for each track in the event. The lowest value of this ratio for all tracks in the event is plotted. From this plot, it is evident that the CC-1π and CC-Other events tend to have a ratio closer to one compared to that for CC-0π where the second track is likely a proton. The multi-track CC-0π events have this ratio mostly uniformly distributed (out past the tail of this plot as well). Tracks where this ratio is 1.5 or less are considered to be muon-like. The number of muon-like tracks in the event is then stored so that the selection can be split into the categories as previously mentioned.

In the above description, "middle" of the track refers to: if there are N nodes in the track, nodes $\frac{N}{4}$ (rounded down to the nearest integer) to $\frac{3N}{4}$ are used to determine the average charged deposited per node. The tool cuts only on the ratio of the charge deposit per node so that detector gains and calibration uncertainties should not play a significant role in the data. As is also mentioned in the caption for figure 4.2, this cut retains 91.6% of multi-track CC-0π events passing cuts (1)-(5) corresponding to only a 0.17% overall loss of CC-0π events remaining after cuts (1)-(5).

4.1.2 PØD μ-Proton Discriminator Systematic Error

The dominant source of uncertainty resulting from this cut will come from the precision to which the average charge deposited per node can be determined for each track in the event. Figure 4.3 gives the distribution of the charge deposited per hit for the tagged μ^+

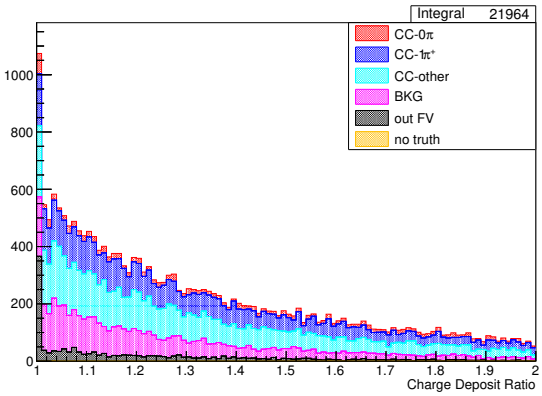

Figure 4.2: Charge deposit ratio for events with more than one reconstructed track in the water in selection. The ratio is given for the "most MIP like" track in events where there were more than 2 reconstructed tracks (the lowest value of the ratio). We can see that the CC-0π events are uniformly distributed while the CC-1π and CC-Other events are more closely distributed near 1. With the cuts as defined, in the water-in MC simulation, 91.6% of CC-0π events with more than 1 reconstructed track are retained by the cut. This corresponds to only a 0.17% loss of all CC-0π events passing cuts (1)-(5).

in the water-in CC-Inclusive sample. We see that there is little systematic shift in the data compared to the simulation. There will be an inherent statistical uncertainty in the average charge deposit per node whose fluctuations will dominate any uncertainty coming from some systematic bias.

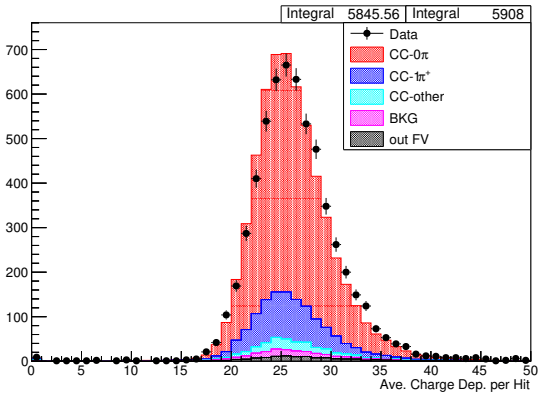

Figure 4.3: Charge deposited per hit in the middle of the track as previously defined for the tagged μ^+ in the water-in CC-Inclusive selection. Run 7 data is overlaid on the simulation.

In forming the charge deposit ratio for each additional track to the tagged muon, an uncertainty on the ratio is formed to account for these statistical fluctuations: $\sigma_t = \sqrt{\sigma_\mu^2 + \sigma_t^2}$

where σ_μ is the error on the mean ($\frac{RMS}{\sqrt{N}}$) in the calculation for the average charge deposit per node for the tagged muon, and σ_t is the same but for the track being compared to the tagged muon.

Detector systematic toy throws can then be performed varying the ratio for each track in each event, in turn varying the number of muon-like tracks in the event, to propagate this uncertainty to any results.

4.2 $\overline{\nu}$ Selections

As was stated before, the selection package was ran over T2K NEUT MC files for the Monte Carlo studies. MC files for both anti-neutrino beam running with water in the P0D and water drained from the P0D were used. All available anti-neutrino, water-in MC was used, but only a sub-sample of the available anti-neutrino water-out MC was used so that the two MC samples both have an equivalent PoT exposure of 208.0×10^{19} PoT.

4.2.1 Selection Results

Table 4.1 contains the percent breakdown by topology of the CC samples for both water-in and water-out modes in the PØD.

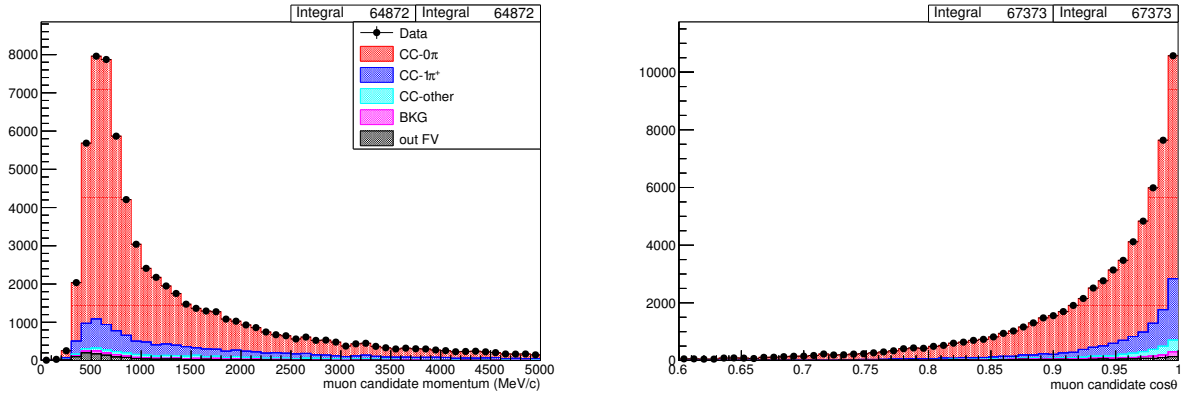

Figure 4.4: Muon candidate reconstructed kinematics in the $\overline{\nu}$ Water-in CC-0π selection. Data points are input MC shown only to illustrate MC statistical errors.

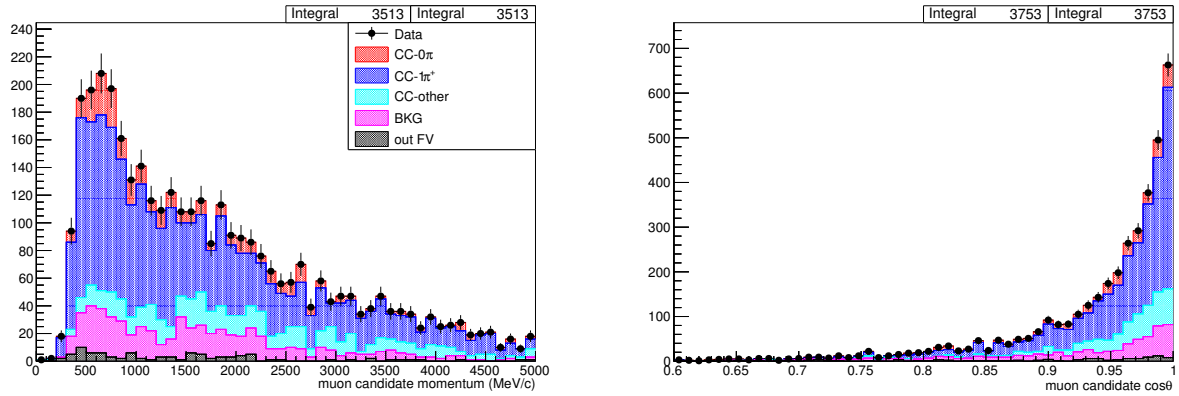

Figure 4.5: Muon candidate reconstructed kinematics in the $\overline{\nu}$ Water-in CC-1π selection. Data points are input MC shown only to illustrate MC statistical errors.

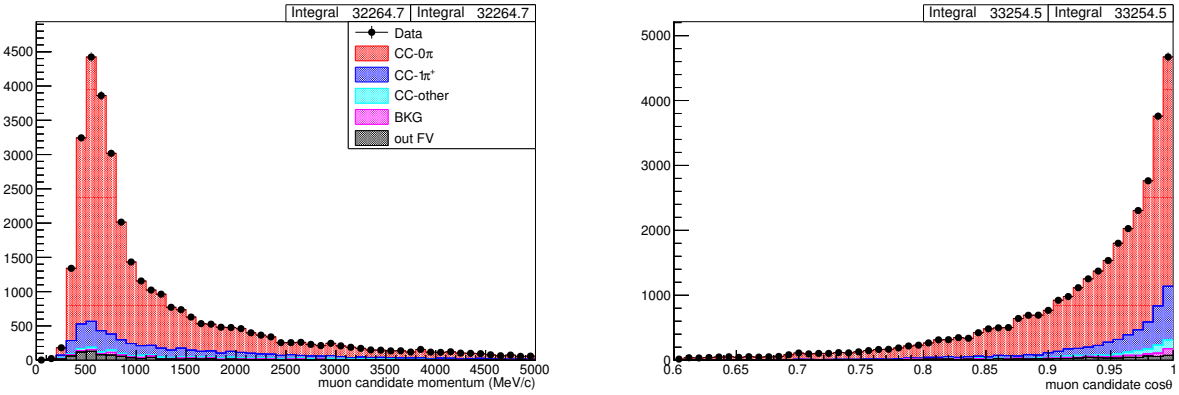

Figure 4.6: Muon candidate reconstructed kinematics in the $\overline{\nu}$ Water-out CC-0π selection. Data points are input MC shown only to illustrate MC statistical errors.

The true lepton kinematics separated into color bands by true topology for the selected events in the CC samples are given in Figures 4.4 - 4.7.

The 2D selection selection efficiencies by true lepton kinematics are given with the chosen analysis bins overlaid in figure 4.8. The bin definitions by true lepton kinematics are given in table 5.1.

As a check of the ability for the sideband selection to represent the background in the signal selection, Figure 4.9 gives an overlay of the muon kinematic distributions for both the background contamination in the signal selection and the sideband.

We see that the selection procedure described produces reasonably pure and efficient CC-0π and CC-1π selections in both water-in and water-out configurations of the PØD. With

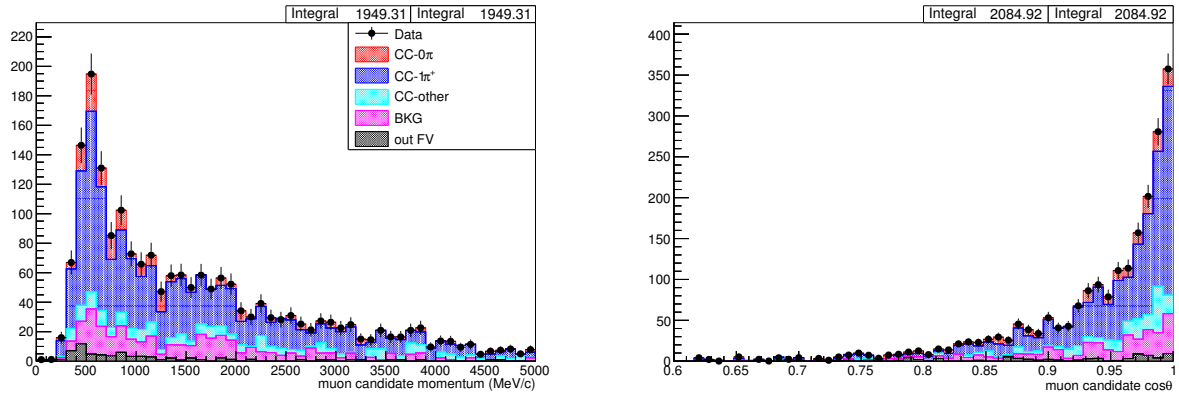

Figure 4.7: Muon candidate reconstructed kinematics in the $\overline{\nu}$ Water-out CC-1π selection. Data points are input MC shown only to illustrate MC statistical errors.

these selections in hand, we can move forward towards the double differential cross section on water by filling in the details of how the forward-folded likelihood fitting scheme is applied.

Table 4.1: Percent purities by true topology in the PØD samples. The columns are the different CC samples and the rows are the true topology components in those samples. For example, the $\overline{\nu}$ CC-Inc water-in sample contains 60% CC-0π events and 12% CC-Other. $\epsilon_{relative}$ is the selection efficiency relative to the CC-Inc sample that the topology based samples came from. For example the $\overline{\nu}$ water-in CC-0π selection retains 96% of the true CC-0π events that were present in the parent CC-Inc selection

Water-in mode:	% in Sample		
Topology	CC-Inc	CC-0π	CC-1π
CC-0π	60	80	10
CC-1π^+	17	13	57
CC-Other	13	3	15
BKGD	7	1	15
OOFV	4	2	3
$\epsilon_{relative}$	100	96	14
Water-out mode:	% in Sample		
Topology	CC-Inc	CC-0π	CC-1π
CC-0π	58	82	11
CC-1π^+	16	12	57
CC-Other	12	2	14
BKGD	8	1	14
OOFV	5	2	4
$\epsilon_{relative}$	100	95	15

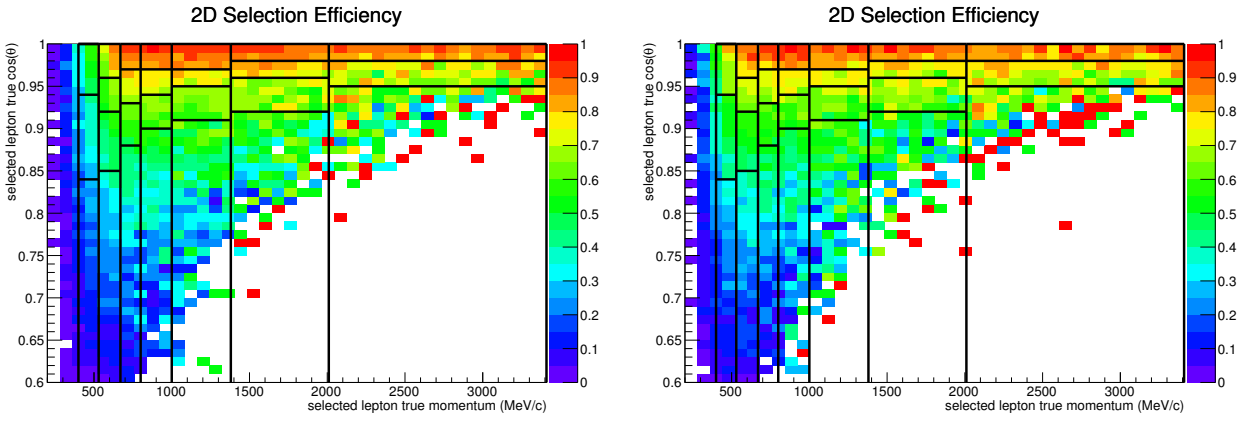

Figure 4.8: 2D CC-0π selection efficiencies by true lepton kinematics with differential bins as defined in table 5.1 overlaid in black. Left: water-in mode, Right: water-out mode.

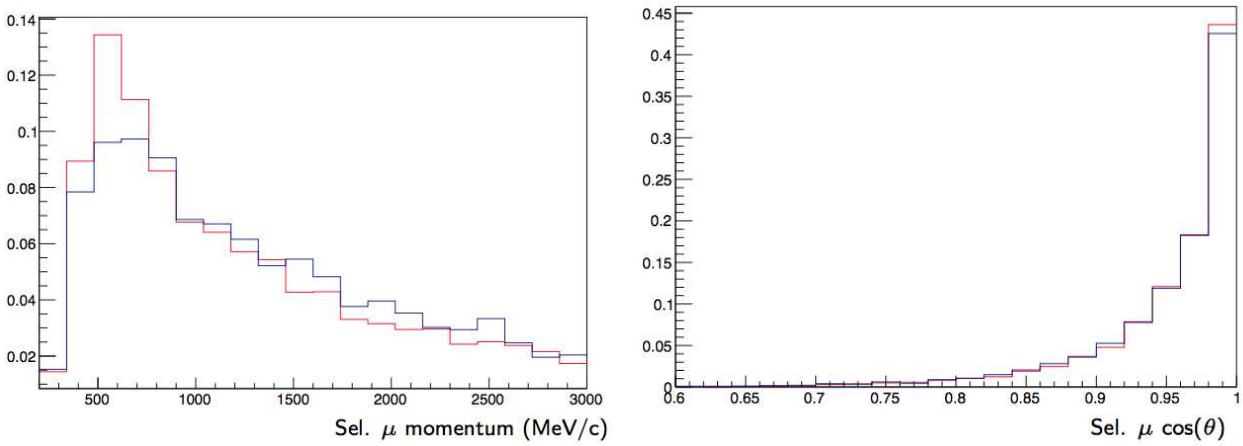

Figure 4.9: Overlay of the lepton kinematic distributions for the CC-1π background (red line) in the CC-0π water-in selection and the water-in CC-1π sideband (blue line) both normalized to unity. We see that the distributions are quite similar in shape.

Chapter 5

$\overline{\nu}$ DOUBLE DIFFERENTIAL CROSS SECTION ON WATER

The measurement of this analysis is a double differential by muon momentum and $\cos\theta$ CC-0π cross section with water alone as the target. The forward-folded binned likelihood procedure previously described is used to extract the CC-0π event rate in each true kinematic analysis bin. This rate is then efficiency corrected to estimate the total event rate in each bin to calculate the final cross section.

The fitter is passed 4 samples: the CC-0π and CC-1π selections in both water-in and water-out modes of the P$\emptyset$D.

5.1 Choice of Binning

Many factors can motivate a choice of analysis bins for a measurement. In this analysis the bins were chosen by balancing the following criteria:

1. There should be on the order of 100 or greater expected signal events in data in each analysis bin

2. The selection efficiency in each analysis bin should be relatively high and not vary too much across each individual bin

3. The bins should be appropriately sized with respect to the detector resolution

    - The bins should be fine enough so that local detector resolution effects are reasonably represented
    - The bins should be coarse enough so that the detector resolution does not cause too large of an uncertainty on the results

Of course, the above criteria are rather imprecise. In general: (1) is a minimum requirement on the signal events to ensure a reasonable statistical uncertainty on the results. (2) attempts to ensure that the efficiency correction in the measurement is well behaved. (3) balances too coarse of bins where bias to the simulation of the detector response will be greater and too fine of bins where bin-to-bin migrations from the detector resolution uncertainty will dominate the total uncertainty.

In the fit, the full muon kinematic phase space is divided into bins as to properly allow for migration of events throughout the whole of the possible phase space. Some of these bins will have very low selection efficiency so that the efficiency correction for a cross section measurement will be relatively large and thus the measurement itself in those bins will rely heavily on the modeling of the signal physics. For this reason, bins with very low efficiency will not be included in the final cross section measurement. Bins that are to be included in the measurement are referred to as in-phase-space (IPS) bins. Bins that are outside of the phase space where the cross section is to be measured are referred to as out-of-phase-space (OOPS). The full phase space binning used in the fit are indexed using an index referred to from here on as "bin index." The IPS bins where the cross section is to be measured are indexed by "analysis bin index." In the validation results for the fitter, fit results primarily for the IPS bins will be presented, these will be labeled by "analysis bin index." Tables 5.1 and 5.2 give the definition of the bins to be passed to the fitter by the true muon kinematics and which bins used in the fit correspond to an analysis bin where the cross section is to be measured (map from bin index to analysis bin index).

Figure 5.1 gives the expected true CC-0π on water event rate in a realistic sized (compared to the data) MC sample. Figure 5.2 gives the smearing matrix in terms of the 28 bins given before.

5.2 Fit Formulation Revisited

Section 3 described generally the mathematical details of how the fitting framework extracts the signal event rate in bins of the true kinematics. The final formula for the event

Table 5.1: Bin edge definition in terms of the true lepton kinematics for each bin. The full true muon kinematic phase space is divided into 28 bins.

Bin Index	True Momentum MeV/c	True $\cos(\theta)$ Bin Edge
1	0-400	-1, 1
2-4	400-530	-1, 0.84, 0.94, 1
5-8	530-670	-1, 0.85, 0.92, 0.96, 1
9-12	670-800	-1, 0.88, 0.93, 0.97, 1
13-16	800-1000	-1, 0,90, 0.94, 0.97, 1
17-20	1000-1380	-1, 0.91, 0.95, 0.97, 1
21-24	1380-2010	-1, 0.92, 0.96, ,0.98, 1
25-27	2010-3410	-1, 0.95, 0.98, 1
28	3410-50000	-1, 1

Table 5.2: Mapping from analysis bin index to bin index as defined in table 5.1. From table 5.1, only bins where the selection efficiency is reasonably high are used in calculating the cross section.

Analysis Bin Index:	1	2	3	4	5	6	7
Bin Index:	3	4	6	7	8	10	11

Analysis Bin Index:	8	9	10	11	12	13	14
Bin Index:	12	14	15	16	18	19	20

Analysis Bin Index:	15	16	17	18	19
Bin Index:	22	23	24	26	27

rate in reconstructed kinematic bin i that is to be compared to the data rate at each iteration of the fit was given by equation 3.6:

$$N_i = \sum_{j}^{bins} \Bigg(c_j N_j^{signal,\ water,\ MC} + d_j N_j^{signal,\ not\ water,\ MC} + \sum_{k}^{bkgd\ types} N_j^{bkgd\ k,\ MC} \prod_{a}^{model} w(a)_j^k \Bigg) S_{ij} r_i \sum_{n}^{E_\nu} f_n^i$$

It is now important to describe each piece of this formula in terms of what was done in the actual analysis. The signal definition of this analysis as was previously stated is $\overline{\nu}_\mu$

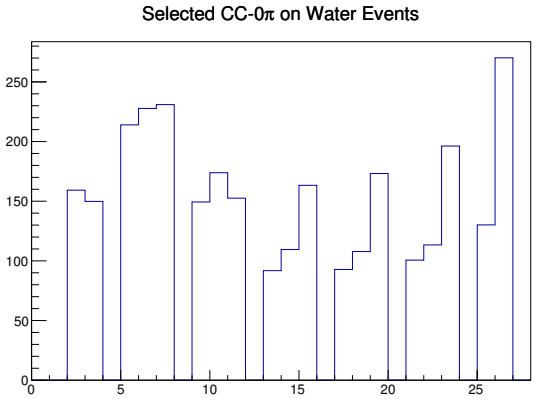

Figure 5.1: Expected true CC-0π on water event rate in each of the 19 IPS analysis bins for a MC sample with approximately 30×10^{19} equivalent PoT.

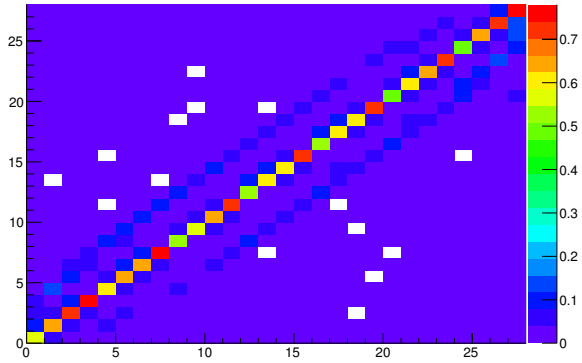

Figure 5.2: Detector response or "smearing" matrix for the water-in CC-0π selection.

CC-0π interactions. The backgrounds are labeled by (index k in the equation) $\overline{\nu}_\mu$ CC-1π, $\overline{\nu}_\mu$ CC-Other, out of fiducial volume (OOFV), and Other (everything else).

We note that the parameters of interest are the c_j. These are the MC scaling factors that are the main free parameters of the fit so that $c_j N_j^{CC-0\pi\ MC}$ is the estimate of the unfolded CC-0π event rate on water in the data. The d_j are the equivalent to the c_j but for non-water CC-0π events. The fitter is passed 4 samples: CC-0π and CC-1π samples for both water-in and water-out modes of the P$\emptyset$D. So there are 4 equations like the above to compare to 4 data samples.

The $w(a)_j^X$ are response functions used to re-weight the various background event rates when the background systematic parameters, $\vec{a}$, are changed from their nominal value. To be explicit, the nominal value of each background parameter is 1. When the minimizer adjusts

a background parameter to say 1.5 this physically means that that parameter was increased by 0.5σ where σ is the predefined 1-σ uncertainty in that parameter. The $w(a)_j^X$ response function will then have a value that re-weights event rate X (X=CC-1π, CC-Other, etc.) in true bin j. These response functions were formed by studying variations in the relevant event rates in the different bins as variations were applied to the model parameters. The quantity, $w(a)_j^X$, is a weight; specifically, it is the response of event rate X in true bin j for a parameter value changing from nominal to a so that a actually has a dual meaning in the notation. There is a specific parameter with a specific value being represented by a. The $\vec{a}$ parameters are allowed to vary subject to a prior covariance matrix.

S_{ij} is the smearing or detector response matrix that maps binned event rates in the true kinematic space to the reconstructed kinematic space. The sum of the f_n^i at the end of the equation is a sum over fractional contributions to the total $\overline{\nu}_\mu$ incident flux such that the sum nominally evaluates to 1. More details about this are given later.

The r_i are detector systematic parameters. These also have a nominal value of 1 and are allowed to vary according to the detector systematic covariance matrix that contains fractional variances and covariances between the event rates (signal+background) in each reconstructed kinematic bin in each sample so that correlations between the different data samples are taken into account. The detector systematic covariance matrix is formed by calculating the variances of and covariances between the total event rates (signal + background) in each reconstructed bin in each sample over many Highland2 toys where all sources of detector systematic uncertainty are simultaneously allowed to vary.

The next section will present the details of how each source of systematic uncertainty is parameterized.

5.3 Systematic Uncertainty Parameterization

As was presented generally in section 3, to propagate systematic uncertainties in the fit, sources of uncertainty are parametrized. Their effect on relevant event rates are included in

the fit directly as parameters or using response functions of the chosen parameters. This section will give the specific parameterization for the relevant sources of systematic uncertainty and the details of how their effect is included in the fit.

5.3.1 Background Model

The main tool used to evaluate the systematic uncertainty arising from the MC physics modeling of the background event rates is T2KReWeight. The canonical choice for parameterization for these sources of uncertainty is then the same as is used in the T2KReWeight package. The T2KReWeight parameters included in the analysis along with their nominal values and errors are summarized in table 5.3.

Table 5.3: Summary of the background model T2KReWeight parameters included in the fit along with their nominal values and errors given to T2KReWeight in the reweighing procedure.

T2KReWeight Knob Name	Parameter	Nominal Value	Error
kNXSec_CA5RES	a_0	1.01	0.12
kNXSec_MaNFFRES	a_1	0.95	0.15
kNXSec_BgSclRES	a_2	1.3	0.2
kNIWG2012a_ccnueE0	a_3	1	0.03
kNIWG2012a_dismpishp	a_4	0	0.4
kNIWG2012a_cccohE0_C	a_5	1	1
kNIWG2012a_cccohE0_O	a_6	1	1
kNIWG2012a_nccohE0	a_7	1	0.3
kNIWG2012a_ncotherE0	a_8	1	0.3

For our purposes, only a general idea of what the parameters are doing is needed rather than a detailed understanding of why this parameterization was chosen and how each individual name concisely summarizes what each parameter does. The first three parameters in table 5.3 (a_0-a_3) affect both the shape (in terms of the relevant kinematic observables) and normalization of CC-1π events produced through resonant pion production in the simulation. Parameter a_3 affects the ν_e event rate, a_4 the DIS event rate, a_5 and a_6 affect the CC-Coherent pion production event rates on carbon and oxygen targets respectively, a_7

affects the NC-Coherent pion production event rate, and finally, parameter a_8 affects the event rate for all non-coherent neutral current events.

To form the necessary response functions, the 4 samples passed to the fitter were re-weighted by varying each of the included dials by $\pm 3\sigma$ from their nominal values as given in table 5.3. The fractional variation from the nominal event rate in each true analysis bin in each sample for each true topology reaction type was then calculated and the response functions then take on those values. A sample response function is given in figure 5.3. The covariance matrix for the model parameters is given in figure 5.4.

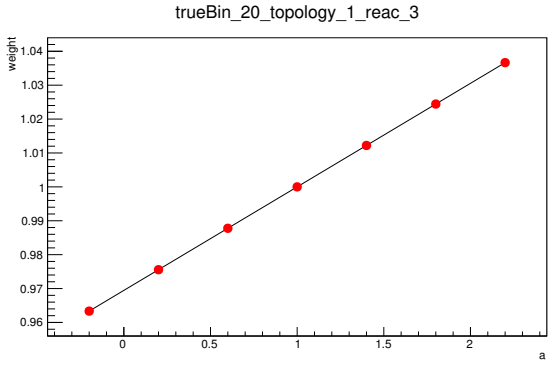

Figure 5.3: Sample response function. This response function includes the information for the effect of the dismpishp T2KReWeight knob (parameter given in Fig. 5.4) on the CC-Other (reac_3) event rate in true analysis bin 20 in the water-in CC-0π (topology_1) selection.

This procedure is repeated for the π-FSI parameters summarized in table 5.4. The covariance matrix for the FSI parameters is given in figure 5.5. Again, only a general idea of what these paramters are doing is needed; all of the π-FSI parameters effect the relevant kinematics of pions (and other particles produced in iteractions where a pion is produced) in the final interaction state after all particles have escaped the interaction medium. Addtionally, these parameters effect whether or not a pion that is produced in an interaction exisists at all in the final state.

	CA5RES	MaNFFRES	BgSclRES	ccnueE0	dismpishp	cccohE0_C	cccohE0_O	nccohE0	ncotherE0
CA5RES	0.01412	0	0	0	0	0	0	0	0
MaNFFRES		0.03905	0	0	0	0	0	0	0
BgSclRES			0.02367	0	0	0	0	0	0
ccnueE0				0.0004	0	0	0	0	0
dismpishp					0.16	0	0	0	0
cccohE0_C						1.0	0	0	0
cccohE0_O							1.0	0	0
nccohE0								0.09	0
ncotherE0									0.09

Figure 5.4: Covariance matrix for the background model parameters.

	InelLow_pi	InelHigh_pi	PiProd_pi	Abs_pi	CExLow_pi	CExHigh_pi
InelLow_pi	0.17	-0.00278	0	0.0227	0.005	0
InelHigh_pi		0.114	-0.167	0.00126	-0.00208	-0.0926
PiProd_pi			0.25	0	0	0.139
Abs_pi				0.169	-0.00227	0
CExLow_pi					0.321	0
CExHigh_pi						0.0772

Figure 5.5: Covariance matrix for the FSI parameters.

Table 5.4: Summary of the π-FSI parameters included in the fit and the nominal values and errors passed to T2KReWeight during the reweighing procedure.

T2KReWeight Knob Name	Parameter	Nominal Value	Error
NCasc_FrInelLow_pi	a_9	1	0.41
NCasc_FrInelHigh_pi	a_{10}	1	0.34
NCasc_FrPiProd_pi	a_{11}	1	0.5
NCasc_FrAbs_pi	a_{12}	1	0.41
NCasc_FrCExLow_pi	a_{13}	1	0.57
NCasc_FrCExHigh_pi	a_{14}	1	0.28

5.3.2 Flux Model

The uncertainty arising from the neutrino flux modeling in the MC enters the fit as a set of 14 fit parameters defined by neutrino energy bins. The definition of these parameters is given in table 5.5, and the covariance matrix used for their variation is given in figure 5.6.

Table 5.5: Neutrino energy bin definitions for the 11 $\overline{\nu}_\mu$ flux parameters included in the fit.

Parameter	E_ν Bin Low (GeV)	E_ν Bin High(GeV)
f_0	0	0.4
f_1	0.4	0.5
f_2	0.5	0.6
f_3	0.6	0.7
f_4	0.7	1.0
f_5	1.0	1.5
f_6	1.5	2.5
f_7	2.5	3.5
f_8	3.5	5.0
f_9	5.0	7.0
f_{10}	7.0	30.0

5.3.3 Detector Model

The detector modeling uncertainty enters the fit as a set of fit parameter where there is one parameter for each reconstructed analysis bin.

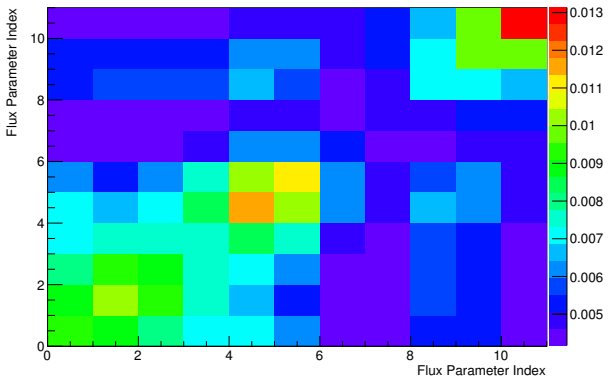

Figure 5.6: Pre-fit covariance matrix used to correlate the flux parameters. This matrix is calculated by T2K collaborators who specialize in the operation of the accelerators and beamlines previously described.

All dominant sources of uncertainty for the used selections can be categorized into two types:

- Variation systematics
- Weight systematics

Variation systematics are systematics that effect an observable quantity in the detector that effects which analysis bin an event is reconstructed in. These systematics are generally evaluated by providing a varied set of observables for each event with each variation of an underlying parameter.

Weight based systematics are all systematic sources that do not effect the relevant observable quantities. These are evaluated by assigning each event a weight with each variation of an underlying parameter.

With a few minor exceptions, all detector related systematics included are evaluated using the Highland2 framework. These systematics were developed and used in [24]. These include the dominant momentum reconstruction related systematics. A summary of the included systematics along with their approximate effect on one example analysis bin is given in table 5.6. The approximate effect on the example analysis should be a good guide as to which sources of uncertainty are the dominant ones.

Table 5.6: Summary of detector systematic sources included in the fit. For variation systematics, only the total effect is presented as the various sources correlate in a non-trivial way making their individual effects not as physically meaningful as the net effect.

Systematic	Fractional Error
Variation:	
Tracker Momentum Resolution	
Tracker Momentum Scale	
P0D Momentum Resolution	
P0D Momentum Scale	
B-Field Distortion	
Total Variation	6.1%
Systematic	Fractional Error
Weight:	
Tracker Charge ID	0.075%
TPC Tracking Eff.	0.46%
TPC Clustering Eff.	0.51%
P0D-TPC Matching Eff.	2.3%
Total Weight:	2.53%

The total effect of all sources of detector systematic uncertainty on the reconstructed event rate in each analysis bin in each sample is then studied to form the relevant covariance matrix for the detector systematic parameters. This is done by generating many (1000) toy throws of the MC, simultaneously varying all sources of detector systematics and calculating the variances and covariances of the event rates in each reconstructed analysis bin in each sample over the toys to form the covariance matrix.

5.3.4 Detector Mass Uncertainty

The systematic uncertainty arising from imperfect knowledge of the mass of the various parts of the detector was evaluated outside of the Highland 2 framework using a stand-alone tool developed for this analysis. Uncertainty on the results comes from two sources:

- uncertainty on the mass of the (non-water) detector components
- uncertainty on the mass of water present in the water target fiducial volume

For the non-water components, a similar approach for propagating the uncertainty was taken as used in [24]. For the water mass, recent investigations of the water mass in each PØDule when the PØD was filled with water has caused question about previous estimates of this uncertainty. It was found that there may be previously unaccounted for bag-to-bag fluctuations in the amount of water filled in each bag. The total bag-to-bag variation is believed to be around 10% by volume. This does not scale linearly with the amount of water in the fiducial volume portion of each bag as adding more water in theory only fills the bag to a higher level above the fiducial volume boundary. However, it was also observed there there can be significant "bulging" of the PØDules caused by the pressure of the water bags being full. The bulging of individual PØDules could lead to extra bag-to-bag variation in the fiducial mass. For this effect, a conservative approach was taken where individual bag fiducial masses were allowed to vary according to a Gaussian distribution by 10% in an MC re-weighting scheme. This was also done in [24].

It was also found that the most up-stream PØDules might have as much as $\approx$ 10% additional extra water in them from extra bulging caused by there being no brace on the upstream part of the P0D. These PØDules were allowed to Gaussian vary by 20% around a mean of 110% of nominal in a conservative re-weighting scheme.

It was also discovered that a single water bag might have had significantly less water filled in it than the other bags for the anti-neutrino data period used. The measurement suggested the bag had roughly 70% of the nominal bag mass. Events in this bag were re-weighted with a mean of 75% nominal with a 25% Gaussian uncertainty.

The re-weighting scheme proceeded in exactly the same was as a traditional Highland 2 weight systematic is evaluated and then the weights were used in calculating the detector covariance matrix. This extra uncertainty will also effect the efficiency and the total water mass used in the cross section calculation. Details of how this is included in the final cross section results are provided in a later section.

5.4 Regularization

In choosing the analysis bins and the set of parameters to be passed to the fit, there are multiple effects that need to be simultaneously considered. When the analysis bins are too coarse and the freedom of the fit too restricted (too few parameters), there is an inherent dependence on the input MC simulation of the detector response (from true to reconstructed space). On the other hand, when the analysis bins are very fine and the freedom of the fit is very great, the possibility of multiple degenerate solution sets for the minimization problem can arise. This issue essentially comes from the fit having the capability to adjust the true event rate in neighboring bins in an anti-correlated way to get the same agreement in the reconstructed space. The fit can reduce the event rate in true bin i and increase the event rate in bin $i+1$ and get a similar reconstructed event rate. This is a common issue historically in fits that proceed in the way used here. A more detailed description of the underlying issue can be found in [29].

This problem is solved by implementing a form of Tikhonov regularization where the fit is penalized when it tries to adjust the true event rates in the anti-correlated way described before. This is done by imposing a restriction that neighboring bin differences not be greatly different from those in the input MC. This of course may introduce a shape bias to the input MC, but it is very important to note that if the bins are chosen in such a way that such anti-correlations do not arise, it is thought to be very likely that there is an inherent MC bias from not giving the fit enough freedom. The idea is that is safer to have finer bins where these anti-correlations arise and then to tune the regularization strength to optimally balance bias to the input MC and the avoidance of the non-physical fit behavior. One could imagine optimizing the binning and parameterization to achieve the same goal, but in practice that can prove to be a very tricky and time consuming procedure.

An illustration of the observed anti-correlations in a test fit to realistic PoT fake data is given in figure 5.7. An illustration of the effect of regularization on a test fit is given in figures 5.8 and 5.9.

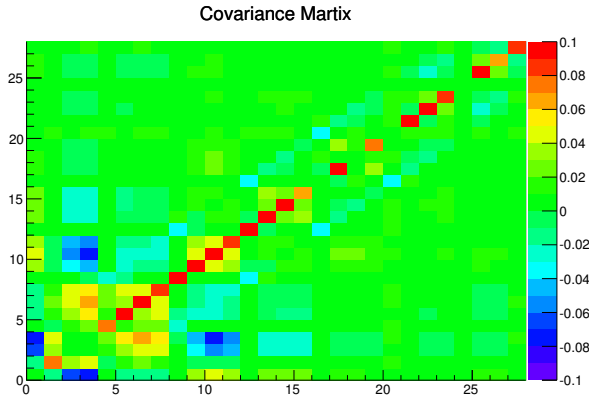

Figure 5.7: Illustration of observed anti-correlations in the fit output covariance matrix. The example here was a statistically varied fake data set with realistic expected data PoT. The blue off diagonal terms are the anti-correlations. The index is the same as defined in table 5.1. We see that neighboring momentum bins demonstrate anti-correlations while neighboring $\cos\theta$ bins do not.

With the implementation of this form of regularization, there is a well defined procedure to tuning the strength so that the non-physical solutions can be avoided while minimizing the bias to the input MC. In this analysis, it was observed that this issue occurs only between neighboring momentum bins, likely because the momentum resolution is worse than the $\cos\theta$ resolution. For this reason, the regularization is only applied between neighboring momentum bins, not $\cos\theta$ bins.

The regularization enters the fit in the form of a penalty term to the χ^2:

$$\chi^2_{reg} = p \sum_{i}^{true\ bins} (N_i - N_{\hat{i}})^2 = (\vec{c} - \vec{c}_{prior})(V^{reg}_{cov})^{-1}(\vec{c} - \vec{c}_{prior}) \tag{5.1}$$

In the above, p is the regularization strength, N_i is the event rate in true analysis bin i, $\vec{c}$ is a vector of the c_i fit parameters, $\vec{c}_{prior}$ is the vector of prior values for the c_i (all 1), and V^{reg}_{cov} is the regularization covariance matrix that is defined such that the above equality holds. The index $\hat{i}$ is the bin index of the neighboring momentum bin to bin i for an equivalent $\cos\theta$ bin.

To take a minimalistic approach here, only the in-phase-space (IPS) bins are affected by the regularization. The regularization should have as little a role as possible to just negate the anti-correlations behavior that is known to be unphysical. Anti-correlations in the IPS

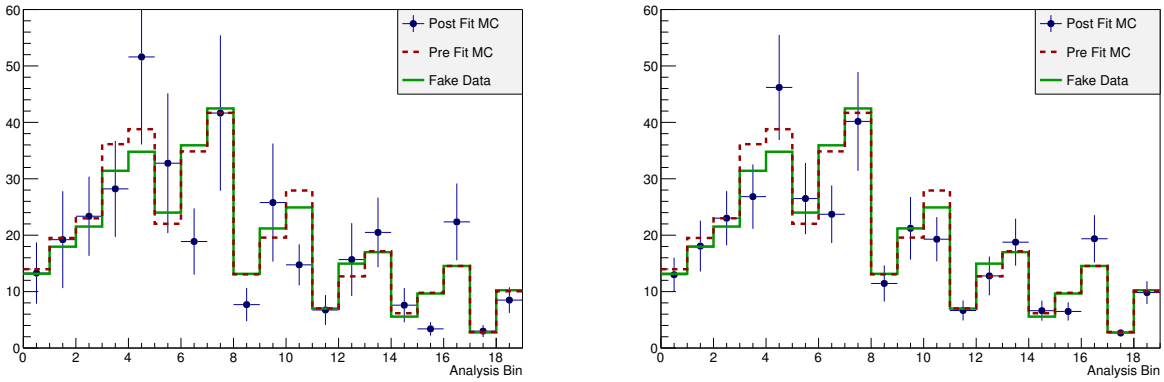

Figure 5.8: Example of the effect of regularization on the best fit event rates and errors. On the left is an overlay of the pre-fit MC, post-fit MC, and fake data true event rates normalized by analysis bin width with no regularization. The same results for a fit with regularization in given on the right.

bins is obviously less desirable to that in the OOPS bins, so that targeting the IPS bins may be a good first approach as some unfortunate behavior in the OOPS bins might be tolerable in the end while it would certainly be optimal to have the fit behaving in these bins as well.

The regularization strength is chosen by the so called "L-curve" method. The method involves generating an "L-curve" that is a graph of a normalized penalty term, $\frac{\chi^2_{reg}}{p}$, from the regularization in the fit versus the total χ^2 of the fit for several different choices of the regularization strength, p. The regularization strength that is considered optimal is the one that maximizes the curvature of the L-curve. An example L-curve is given in figure 5.10. In this example, a regularization strength of about 1-2 seems reasonable. In practice, when analyzing a new data set, an L-curve is generated to choose the appropriate regularization strength and then the fit performed again with the chosen strength to get the results.

5.4.1 Intended Role of Regularization

At the beginning of this section it was stated that freedom in the fit parameters can lead to multiple degenerate solutions in the minimization problem. This is a broad statement

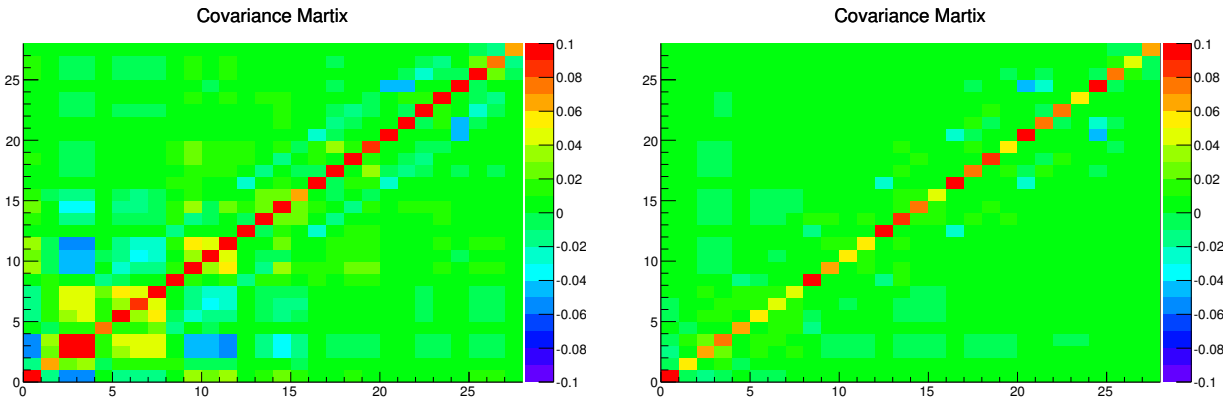

Figure 5.9: Output covariance matrices as presented in figure 5.7 with no regularization (Left) and with regularization (Right). We see that the observed anti-correlations shown in figure 5.7 are suppressed with the implementation of regularization.

that doesn't capture what is believed to be occurring. Instead, the "problem" that can arise can be thought of as a flattening of the χ^2 space around the minimum so that the central values of the best fit results may have higher sensitivity to statistical fluctuations in the data and the error bars may be enlarged beyond what would be physically expected.

In a fitting framework, however, the real result of interest is not the central values of the individual fit points, but rather the calculated χ^2 goodness of fit of the data to different input MC samples coming from different theoretical predictions. This is how the data actually has power to gain further insight into our knowledge of neutrino interactions. The χ^2 goodness of fit should not be significantly changed from an input of regularization. Regularization in this analysis is meant only to be "aesthetic" in the sense that in its implementation we might expect the central values of individual fit points to change slightly, the error bars to reduce, but the overall statistical significance should remain predominantly unchanged. Furthermore, the results with and without regularization should be fairly consistent with each other, and the contribution to the final total χ^2 from the regularization should be relatively small. Section 5.7 and others will present rigorous tests of the fitting framework

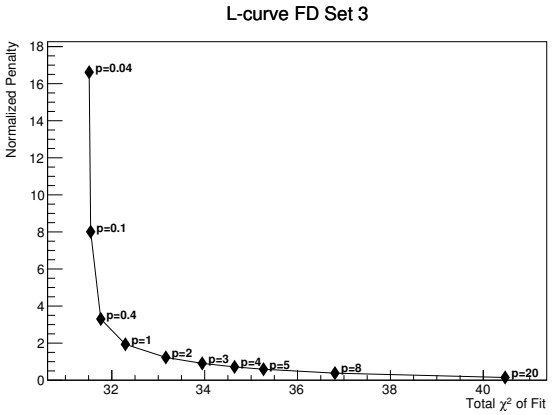

Figure 5.10: Example L-curve that would be used to determine the regularization strength. A strength of 1 seems to be the optimal choice in this example.

by testing the results of the fit with different fake data samples. In these tests, it will be argued that the choice of regularization presented here satisfies the above criteria.

5.5 Final Fit Parameters

In summary, the fit will be provided with the following parameter sets:

- 28 MC scaling factors for CC-0π events on water targets
- 28 MC scaling factors for CC-0π events on non-water targets

These parameters are allowed to vary subject to the constraint of the regularization covariance matrix (when regularization is used).

In addition to the parameters relevant to the signal, the systematic parameters are included:

- 9 background model parameters
- 6 pion FSI parameters
- 14 $\overline{\nu}_\mu$ flux parameters
- 76 detector systematic parameters

Each of the above sets of systematic parameters vary subject to their corresponding covariance matrices previously defined.

Table 5.7 summarizes each fit parameter, assigns an index for looking at covariance matrices, and provides the prior constraint used.

Table 5.7: All parameters to be included in the fit with a global index, parameter type, parameter label, and assumed prior constraint.

index	type	parameter	prior constraint
0-27	Signal Water	c_0-c_{27}	Regularization Covariance Matrix
28-55	Signal Non-water	d_0-d_{27}	Regularization Covariance Matrix
56-66	Neutrino Flux	f_0-f_{10}	Neutrino Flux Covariance Matrix
67-142	Detector Systematic	r_0-r_{75}	Detector Covariance Matrix
144-158	Physics Model	a_0-a_{14}	Model Covariance Matrix

5.6 Uncertainties in the Fit

In addition to the best fit values for all of the fitted parameters, a covariance matrix in terms of the parameters can be calculated in the minimization problem. This is done using the HESSE[27] tool in the MINUIT package. This tool uses the second derivatives of the χ^2 with respect to the parameters to map out the χ^2 space around the minimum. By studying the variation of the fit parameters around the minimum, the range of values and correlations between the parameters are calculated.

With the output covariance matrix from the fit, the standard method of throwing toy experiments against this covariance matrix is then implemented by Cholesky decomposing the covariance matrix and generating a vector of random variations to multiply the decomposed matrix by. In doing so, the fit parameters are allowed to vary in a correlated way. The event rates and any other quantities of interest are calculated for each toy. The error on the calculated quantity is take to be the RMS of the resulting distributions.

In the process of throwing many toys with the output covariance matrix, a new covariance matrix in terms of only some quantities of interest can be calculated in the standard way. A

final covariance matrix in terms of the cross section in each analysis bin will be calculated to be released along with the final cross section result.

In addition to a covariance matrix in terms of the cross section, a covariance matrix in terms of the signal fit parameters can be calculated. This matrix can be useful in calculating χ^2s between different true event rates which is a measure of whether the fit results agree better with one distribution compared to another.

We define the χ^2 goodness of fit of the best fit results to some distribution X to be:

$$\chi^2_{fit} = (\vec{c}_{fit} - \vec{c}_X) V^{-1}_{fit\ params} (\vec{c}_{fit} - \vec{c}_X) \tag{5.2}$$

where $V^{-1}_{fit\ params}$ is the inverted covariance matrix in terms of the fit parameters, $\vec{c}_{fit}$ is the vector of the best fit c_i parameters and $\vec{c}_X$ is a set of c_i parameters corresponding to the distribution X. In practice, X could be the input nominal MC ($c_i = 1$), or the fake data true spectrum in a fit to some fake data. One could also make comparisons of a real data fit to different choices in the MC in an attempt to determine if the data favors one physics model or another. The smaller this quantity is, the better the agreement is. Uncertainties and correlations are taken into account.

5.7 Validation

This section will present the results of many different tests of the fitting framework where the nominal MC is fit to various fabricated fake data samples.

5.7.1 Asimov Fit

An Asimov fit involves fitting a data set to itself for the primary purpose of checking the closure of the fitting framework. As an initial check, the nominal MC was fit to itself to demonstrate closure in this analysis. In these results, the fake data is the same as the input MC.

Additionally, other fits were performed where the input MC was re-weighted so that the signal interactions on water and non-water targets are increased separately as a trivial test of the extraction of the rate on water alone. The signal event rates were increased uniformly by 50% in each.

Figure 5.11 shows the fit result in each analysis bin for the Asimov fit (fake data is identical to the input MC). The equivalent plots for the fake data sets where the signal water and non water events are increased are given in 5.12.

The plots display the event rate normalized by bin width in each true analysis bin for the input MC, the fake data truth, and the best fit result overlaid. The error bars drawn on on the best fit points include all sources of uncertainty.

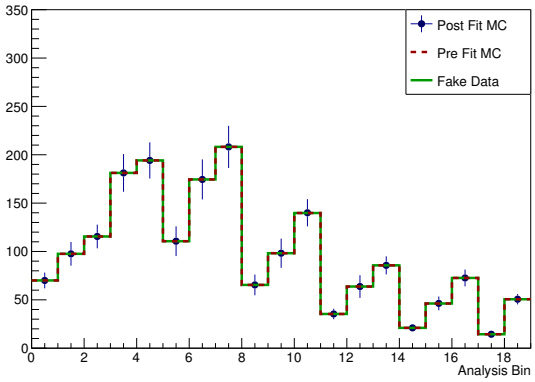

Figure 5.11: Overlaid event rates for a fit of the nominal input MC to itself. We see that the fit reproduces the nominal event rate as it should. The error bars on the best fit points include all sources of uncertainty.

5.7.2 Systematic Errors Contribution Fits

In an attempt to get an idea of how each of the classes of systematic uncertainties contribute to the total error, the Asimov fit from the previous section was run in different configurations with only some of the parameters enabled. The main free parameters must always be included for the fit to function properly. Three fits were run where only a single subset of the fit parameters were included (flux, detector, model) in addition to the signal

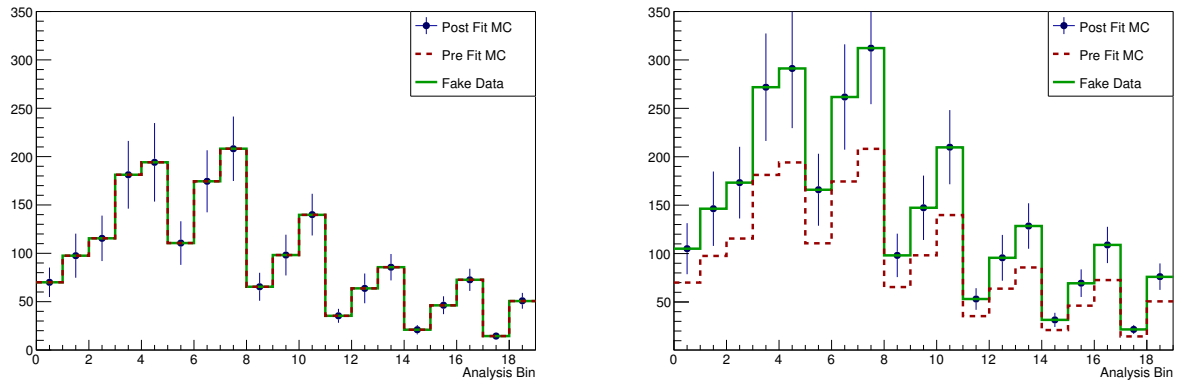

Figure 5.12: Overlaid event rates for the fit of the nominal input MC to the same MC but with the CC-0π event rate increased by 50% on non-water targets (left) and water targets (right). We see that the fit perfectly reproduces the true event rate in both cases.

scaling ones. Comparing the resulting errors in each of the three fits can give insight into the relative contributions to the total error from each of the three sources.

For each of the three fits where only the signal scaling parameters and parameters corresponding to a single source of systematic uncertainty were enabled, the resulting uncertainty on the unfolded event rate in each of the 19 analysis bins was calculated. The same uncertainty from a fit where only the signal scaling parameters were included was then subtracted in quadrature from each of the three fit uncertainties in each bin. The quantity that remains is perhaps close to what we would expect the relative error contribution from that source of systematic uncertainty to be. All of this ignores correlations between each parameter set in the fit, so care should be taken in rigorously interpreting the results and comparing them to other results presented elsewhere throughout the note. The results here are to give an idea of the size of the relative contributions from each source. Figures 5.13 through 5.15 give the quadrature subtracted error in each bin for each source of uncertainty.

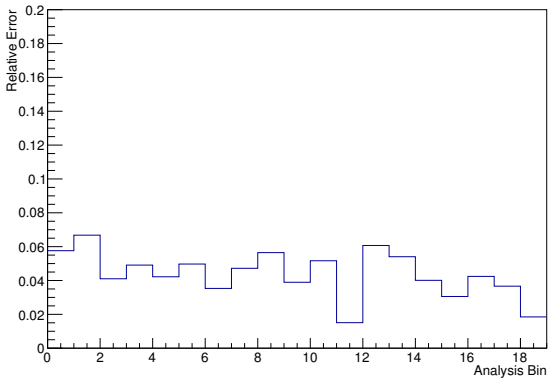

Figure 5.13: Estimate of the relative error contribution on the unfolded CC-0π event rate on water arising from the neutrino flux systematic parameters.

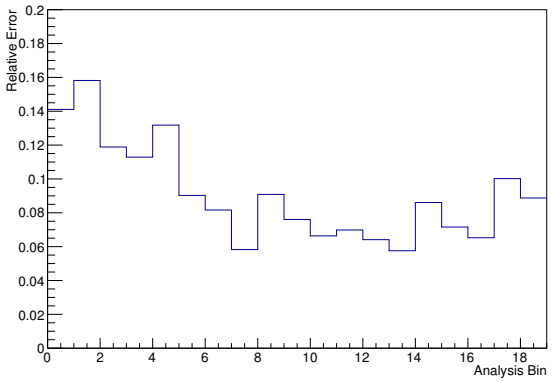

Figure 5.14: Rough estimate of the relative error contribution on the unfolded CC-0π event rate on water arising from the detector systematic parameters.

5.7.3 Realistic Expected PoT Nominal Fake Data

Demonstrating closure of the framework and an initial check to its ability to extract the event rate on water are important checks. The next logical check is to see how the framework behaves when fitting the MC to data sets that have realistic sizes relative to the expected real data. To do this, the input MC was divided into 5 equally sized samples. The input MC has roughly 208×10^{19} equivalent PoT exposure in both modes so that each of these 5 fake data sets will have roughly 42×10^{19}, which is about the amount expected in the real data. Because these fake data sets are not completely statistically independent from the input MC, statistical fluctuations were applied to each by varying the total signal+background event rate in each bin according to a Poisson statistic. This was done for each of three MC

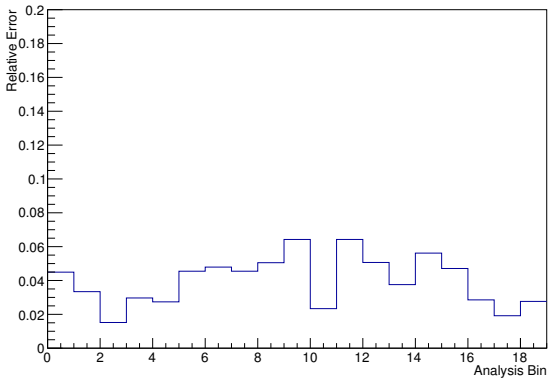

Figure 5.15: Rough estimate of the relative error contribution on the unfolded CC-0π event rate on water arising from the background model systematic parameters.

samples used in the previous section: Nominal MC, Signal-water increased MC, Signal-non-water increased MC.

These tests provide an initial idea of how the fitter might behave when fitting to real data and additionally a more realistic check of the ability to isolate water alone as the interaction target. The fit results in each of the 5 fake data (FD) sets for the fit to the nominal fake data sets with no regularization are given in figure 5.16. The results with regularization are given in figure 5.17. Additionally the post-fit values and uncertainties for each parameter for the fits with regularization are given in figures 5.18 through 5.21. The results for the signal-water increased FD sets without and with regularization are given in figures 5.28 and 5.29 respectively, and the results for the signal-non-water increased FD sets are given in 5.22 and 5.23. The results for each parameter in these fits are given in figures 5.30 through 5.33 and figures 5.24 through 5.27 respectively. The regularization strength was chosen to be 1 in all the sets using the L-curve method previously described. The error bars on the fit results include all sources of uncertainty.

We define the fractional bias in bin i to be:

$$b = \frac{(N_i^{fit} - N_i^{FD\ truth})}{\sigma_i} \tag{5.3}$$

where N_i^{fit} is the best fit event rate normalized by bin width in bin i, $N_i^{FD\ truth}$ is the same, but for the true distribution in the fake data set, and σ_i is the uncertainty on N_i^{fit} calculated from the fit output covariance matrix.

The fractional bias in each bin over all 5 fake data set fits for the nominal sets, non-water increased sets and water increased sets with and without regularization are given in figures 5.34, 5.35 and 5.36 respectively.

As a check on the effect the regularization has on the fit sensitivity, the χ^2 goodness-of-fit for the fit results relative to both the input MC and fake data truth are given for different regularization strengths in figure 5.37. Changes in the difference between the χ^2 goodness of fit relative to the fake data truth from that for the input MC, $\chi^2_{FD} - \chi^2_{MC}$, can show if the fit sensitivity is significantly changing with the regularization strength. Figure 5.38 gives this difference in each of the sets for different choices of the regularization strength.

Tables 5.8, 5.9 and 5.10 give the χ^2 contributions at the best fit point in each of the 3 configurations of fake data.

Table 5.8: χ^2 contributions from each source at the best fit point for the fits to the nominal fake data sets. We see that the regularization is not a major contributor in each of the fits.

	w/o Reg			w/ Reg		
FD Set	Stat χ^2	Syst χ^2	Reg χ^2	Stat χ^2	Syst χ^2	Reg χ^2
1	34.5	0.8	0	34.9	1.1	2.3
2	34.7	1.3	0	35.5	1.6	2.5
3	31.6	1.2	0	32.1	1.4	1.8
4	32.3	1.1	0	33.8	1.3	4.6
5	45.3	1.8	0	45.8	2.0	3.3

Table 5.9: χ^2 contributions from each source at the best fit point for the fits to the non-water increased fake data sets. We see that the regularization is not a major contributor in each of the fits.

	w/o Reg			w/ Reg		
FD Set	Stat χ^2	Syst χ^2	Reg χ^2	Stat χ^2	Syst χ^2	Reg χ^2
1	36.4	2.5	0	37.1	4.3	3.6
2	36.8	2.6	0	38.1	4.1	3.6
3	33.7	3.1	0	34.7	4.5	3.0
4	34.3	2.90	36.7	5.2	6.8	
5	48.3	4.2	0	49.0	5.8	4.2

Table 5.10: χ^2 contributions from each source at the best fit point for the fits to the water increased fake data sets. We see that the regularization is not a major contributor in each of the fits.

	w/o Reg			w/ Reg		
FD Set	Stat χ^2	Syst χ^2	Reg χ^2	Stat χ^2	Syst χ^2	Reg χ^2
1	34.6	1.1	0	35.1	1.8	4.8
2	35.7	1.5	0	36.7	2.3	5.1
3	31.8	1.2	0	32.5	1.7	3.9
4	33.3	1.0	0	35.2	1.6	8.0
5	45.7	2.0	0	46.5	2.6	5.9

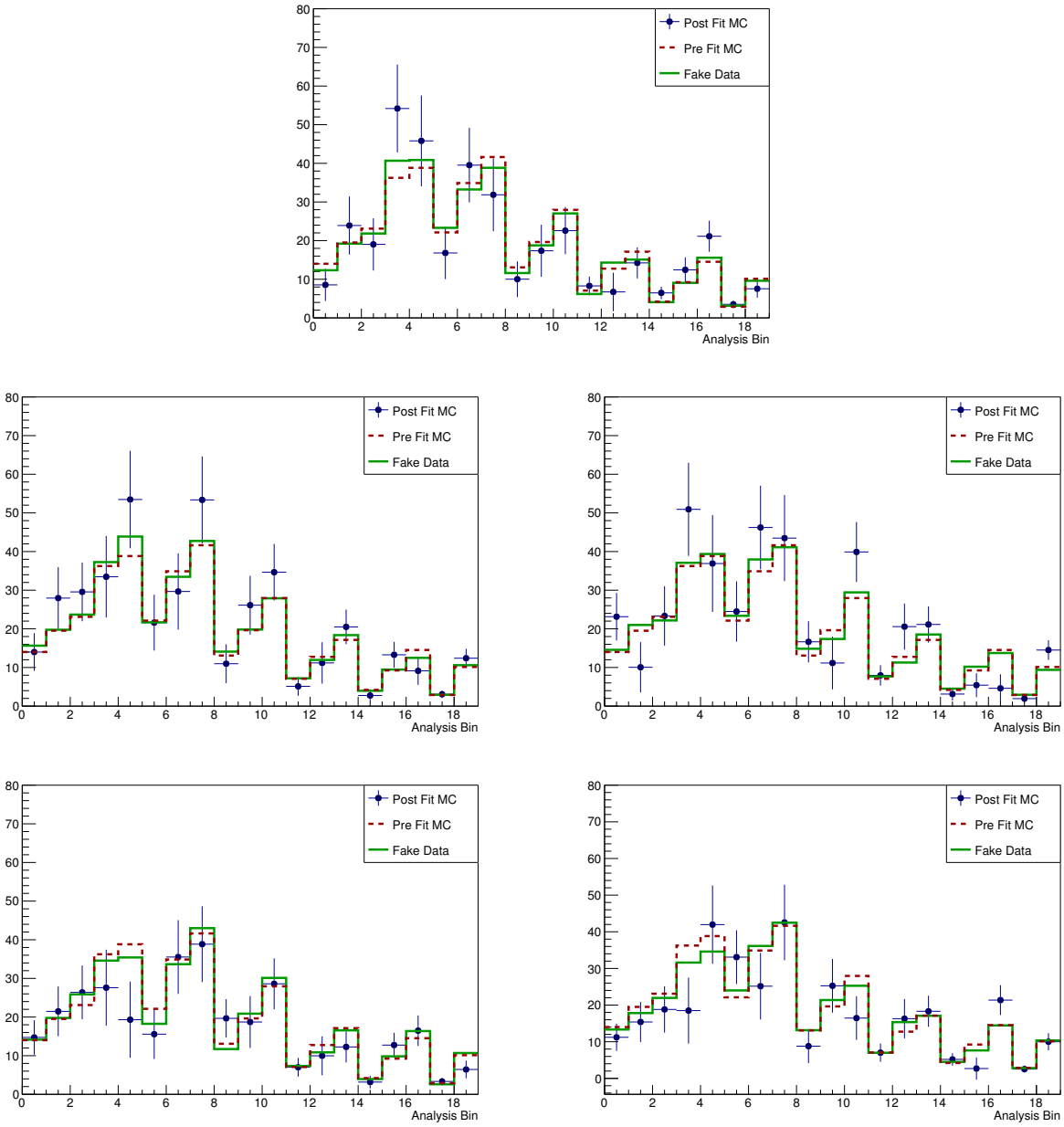

Figure 5.16: Overlaid event rates for the fit to realistic sized fake data sets generated with no additional variations fitted with no regularization. We see that in each of the 5 fits, the fake data truth is well captured by the best fit points.

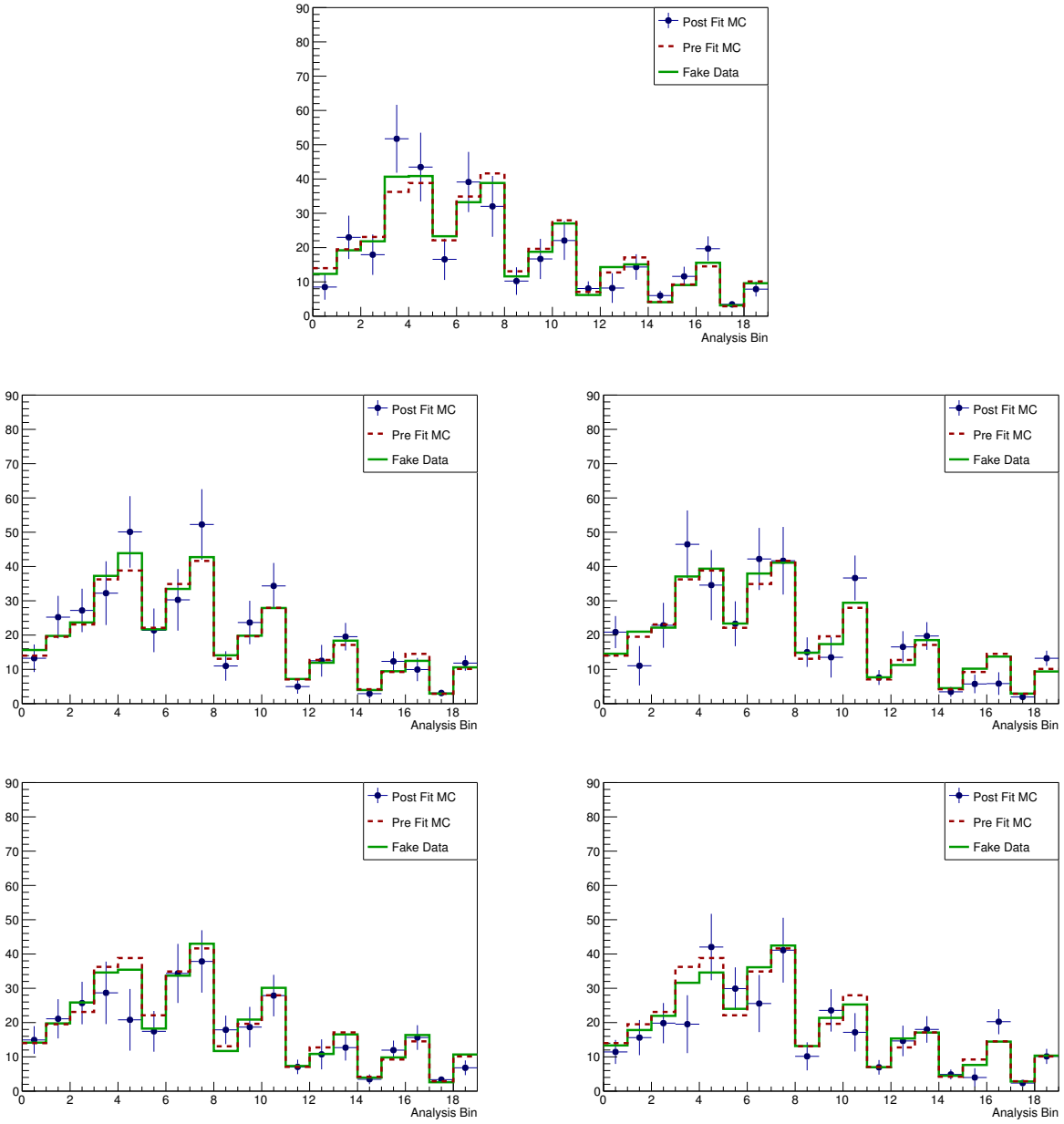

Figure 5.17: Overlaid event rates for the fit to realistic sized fake data sets generated with no additional variations fitted with regularization (p=1 in all). We see that in each of the 5 fits, the fake data truth is again well captured by the best fit points, and the results are not significantly different from those with no regularization.

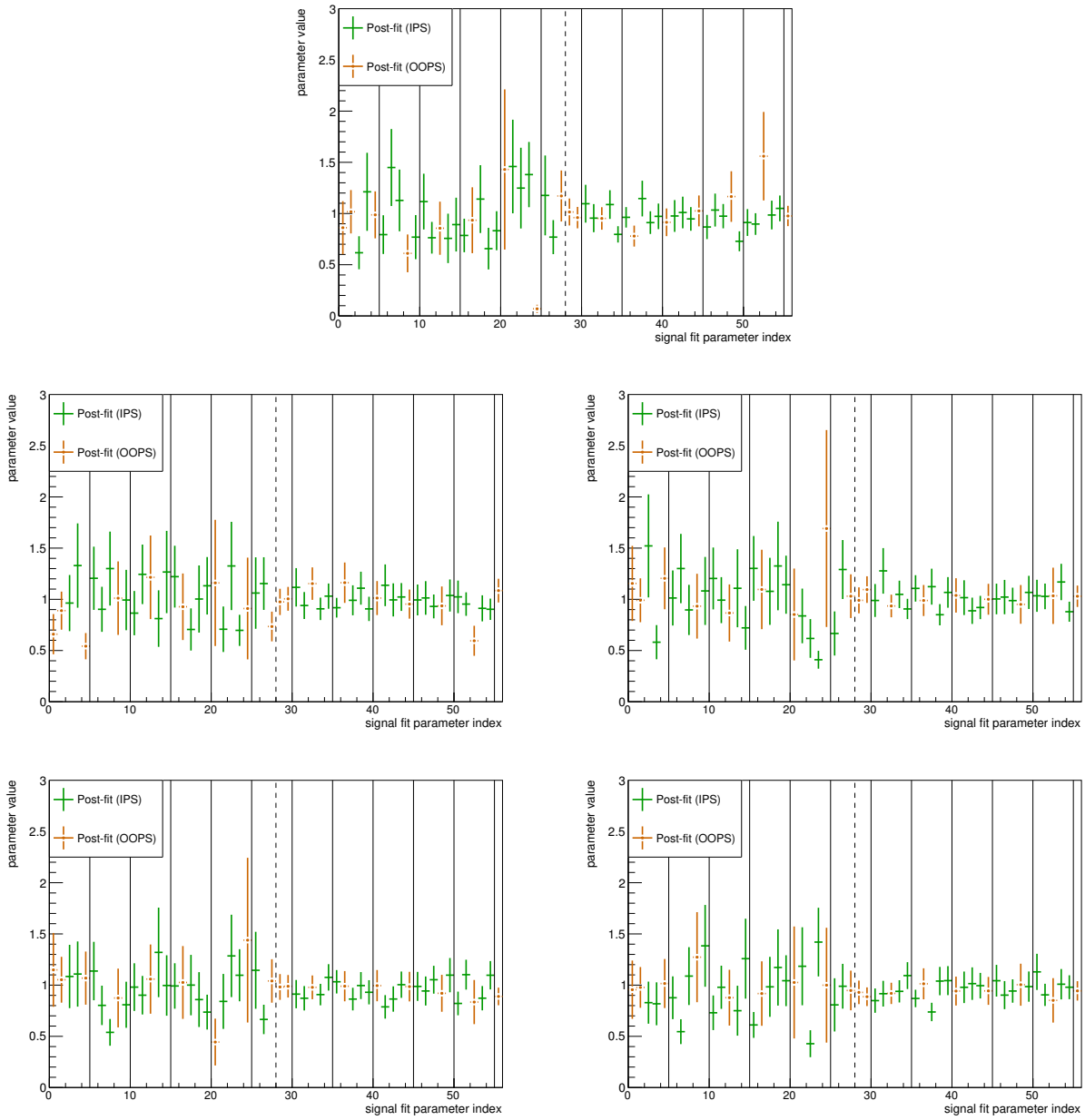

Figure 5.18: Post-fit results (best-fit value and full uncertainty) for the c_i and d_i parameters in the nominal fake data fits with regularization. As a reminder, IPS stands for in-phase-space and OOPS stands for out-of-phase-space.

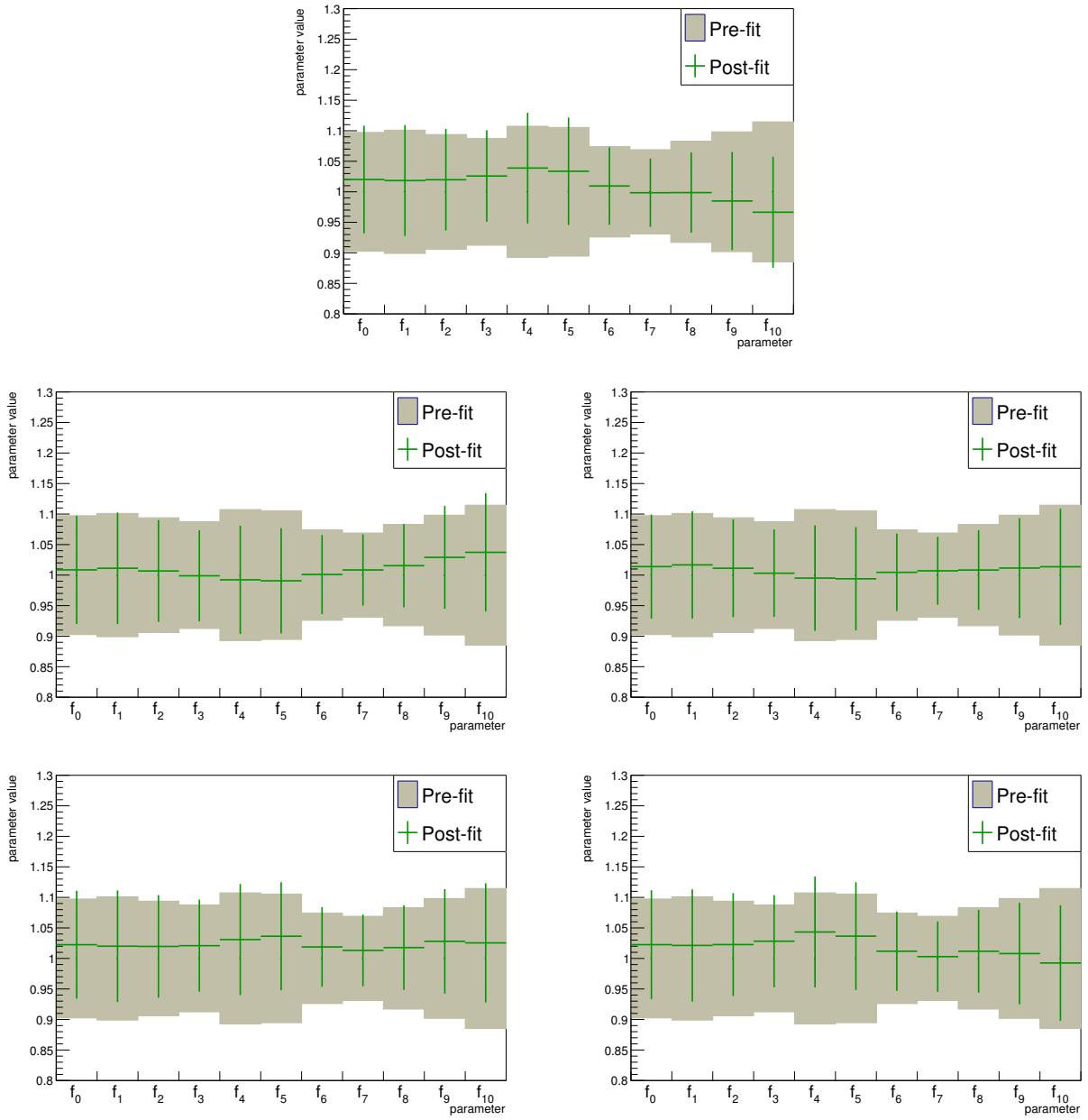

Figure 5.19: Post-fit results (best-fit value and full uncertainty) for the neutrino flux (f_i) parameters in the nominal fake data fits with regularization overlaid with the pre-fit uncertainties (shaded region).

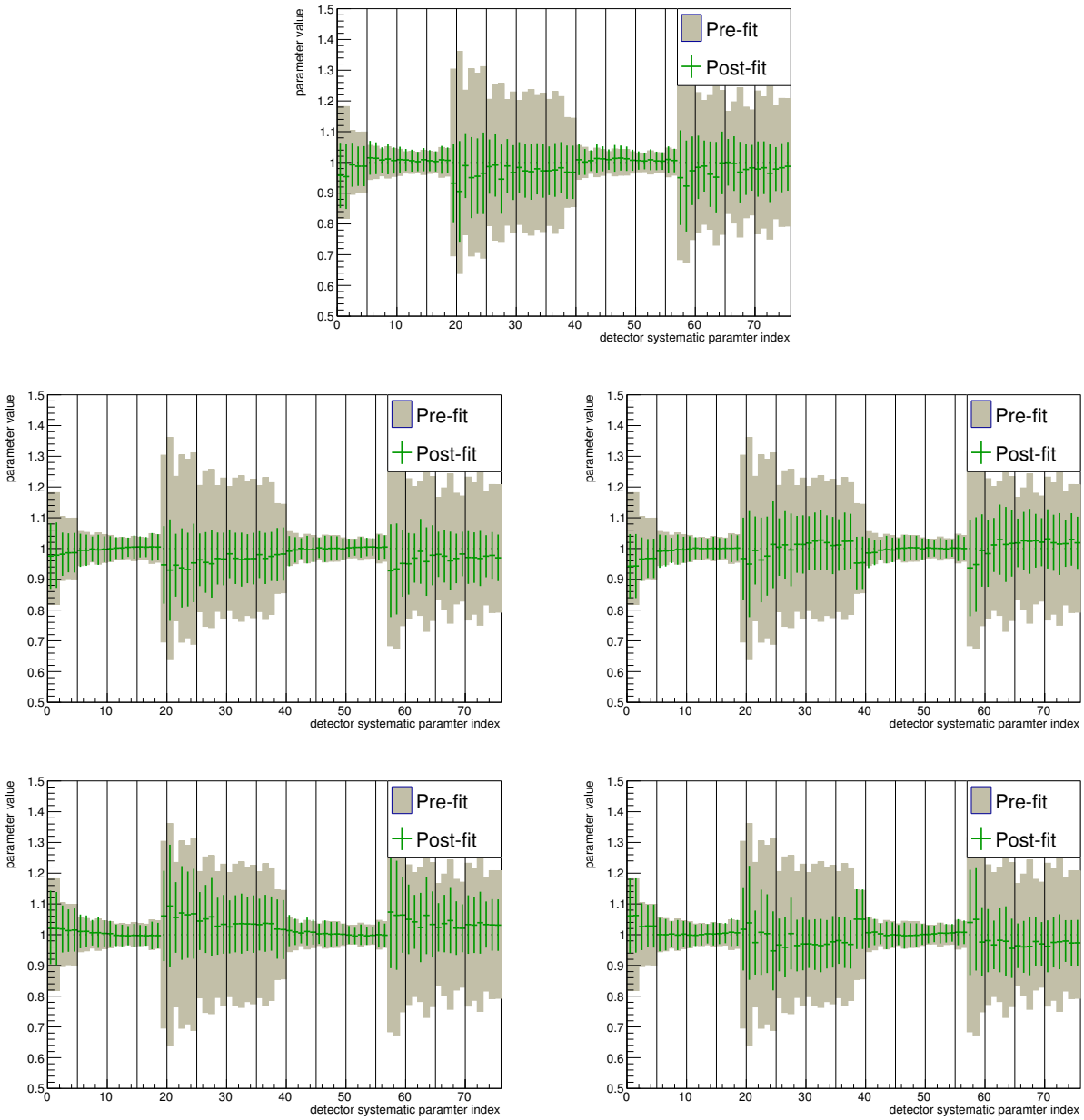

Figure 5.20: Post-fit results (best-fit value and full uncertainty) for the detector systematic (r_i) parameters in the nominal fake data fits with regularization overlaid with the pre-fit uncertainties (shaded region).

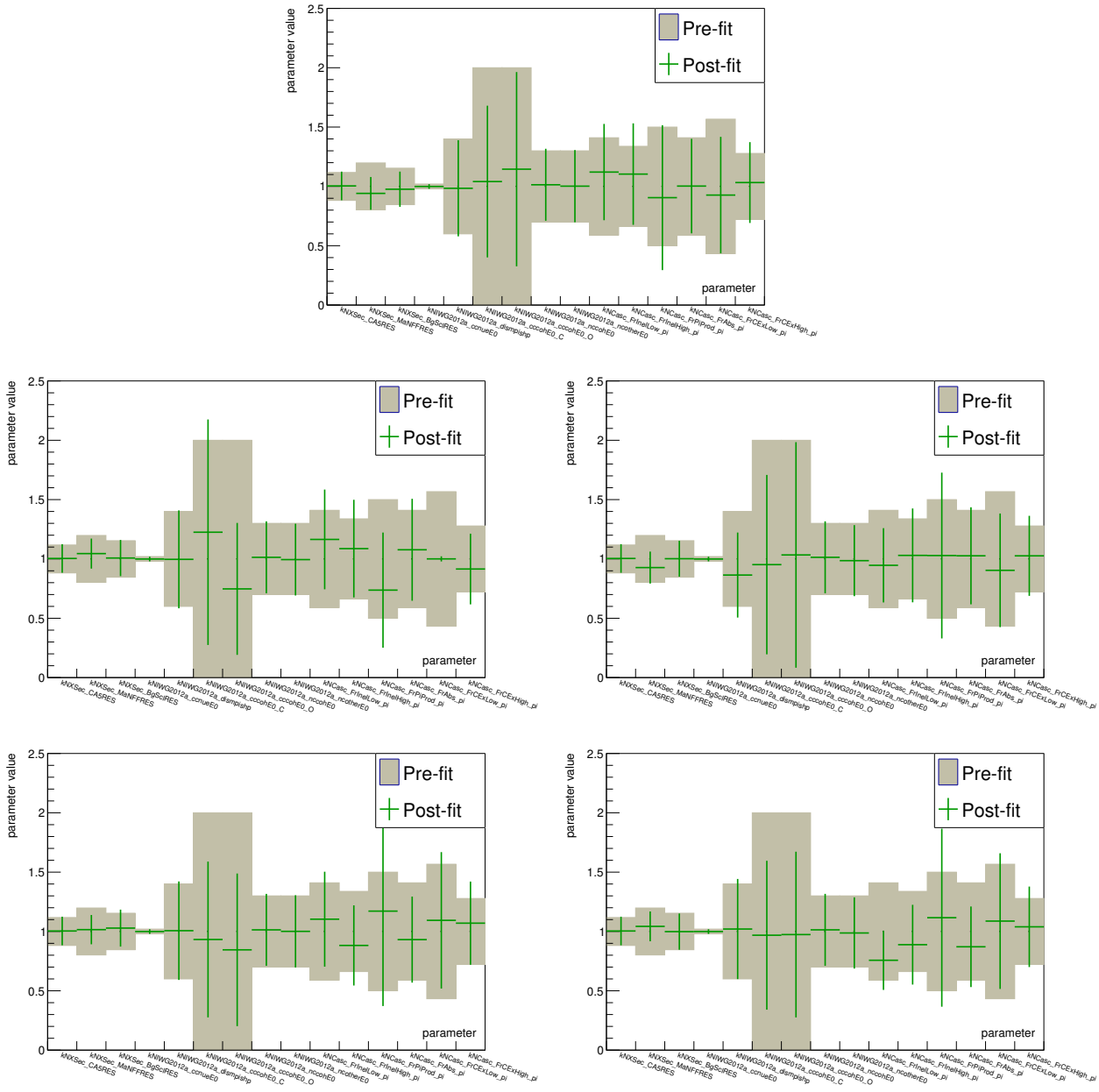

Figure 5.21: Post-fit results (best-fit value and full uncertainty) for the background model parameters in the nominal fake data fits with regularization overlaid with the pre-fit uncertainties (shaded region).

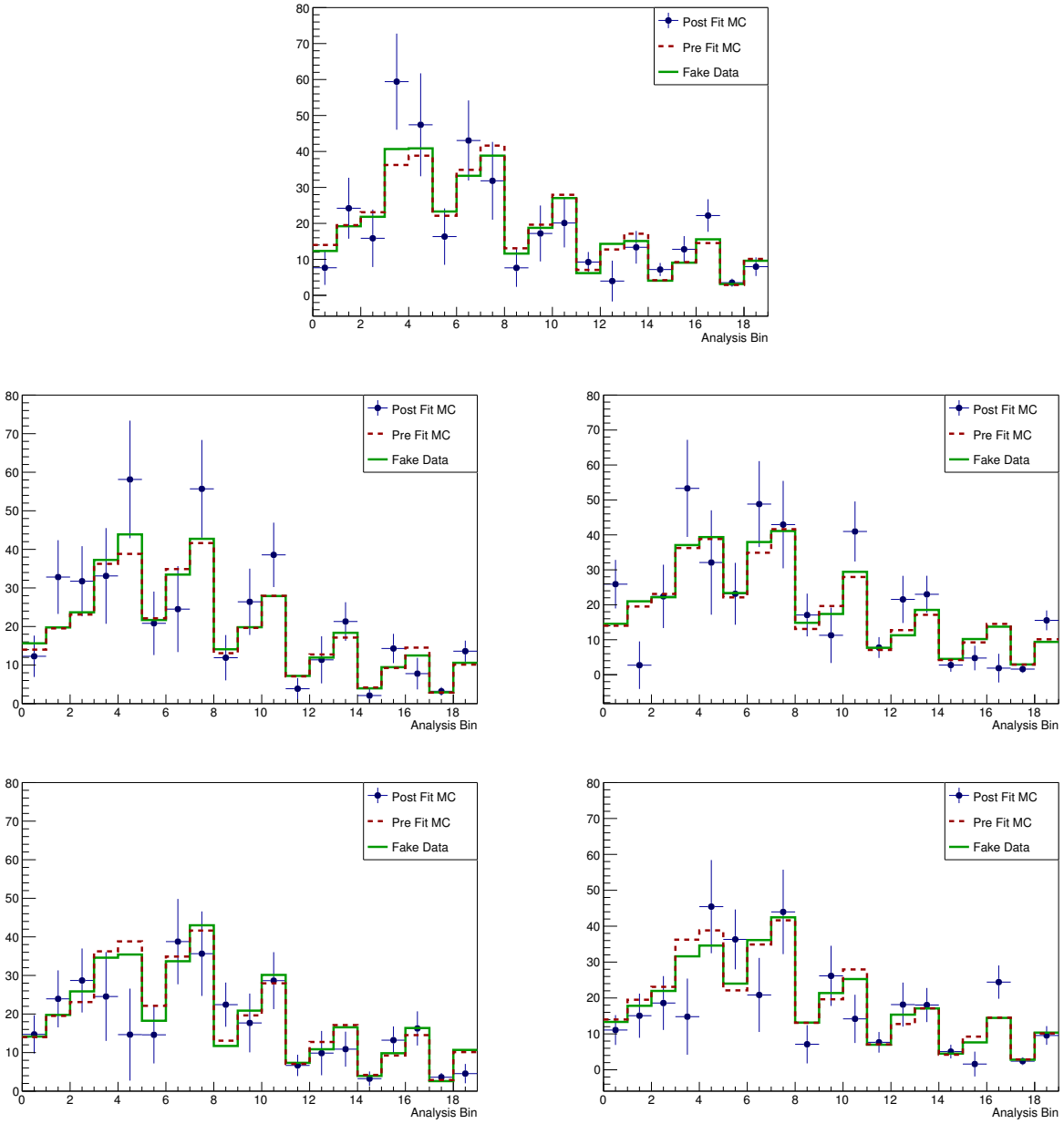

Figure 5.22: Overlaid event rates for the fit to realistic sized fake data sets generated with CC-0π events on non-water targets increased by 50% fitted with no regularization. We see that in each of the 5 fits, the fake data truth is well captured by the best fit points.

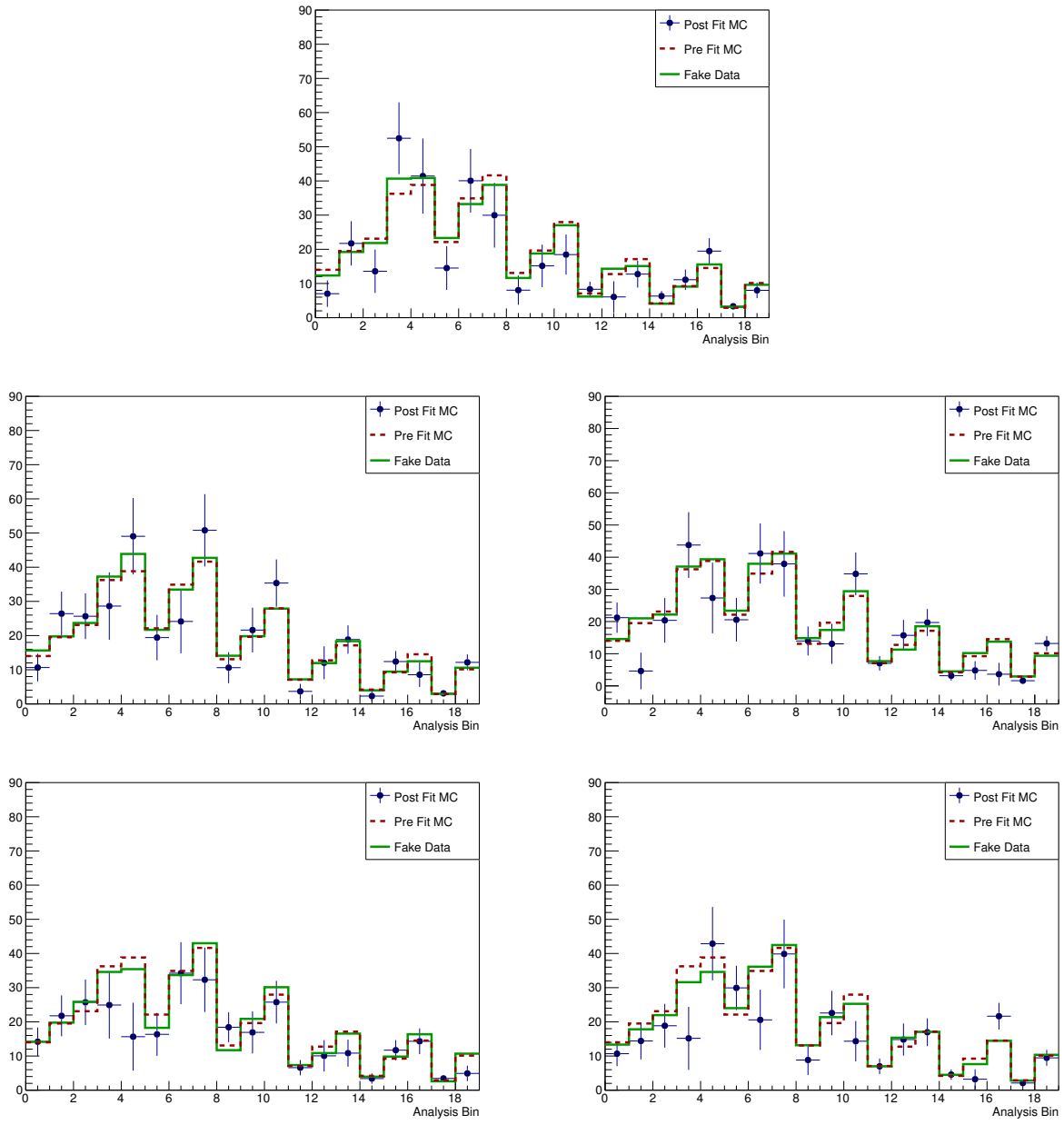

Figure 5.23: Overlaid event rates for the fit to realistic sized fake data sets generated with CC-0π events on non-water targets increased by 50% fitted with regularization (p=1 in all). We see that in each of the 5 fits, the fake data truth is again well captured by the best fit points, and the results are not significantly different from those with no regularization.

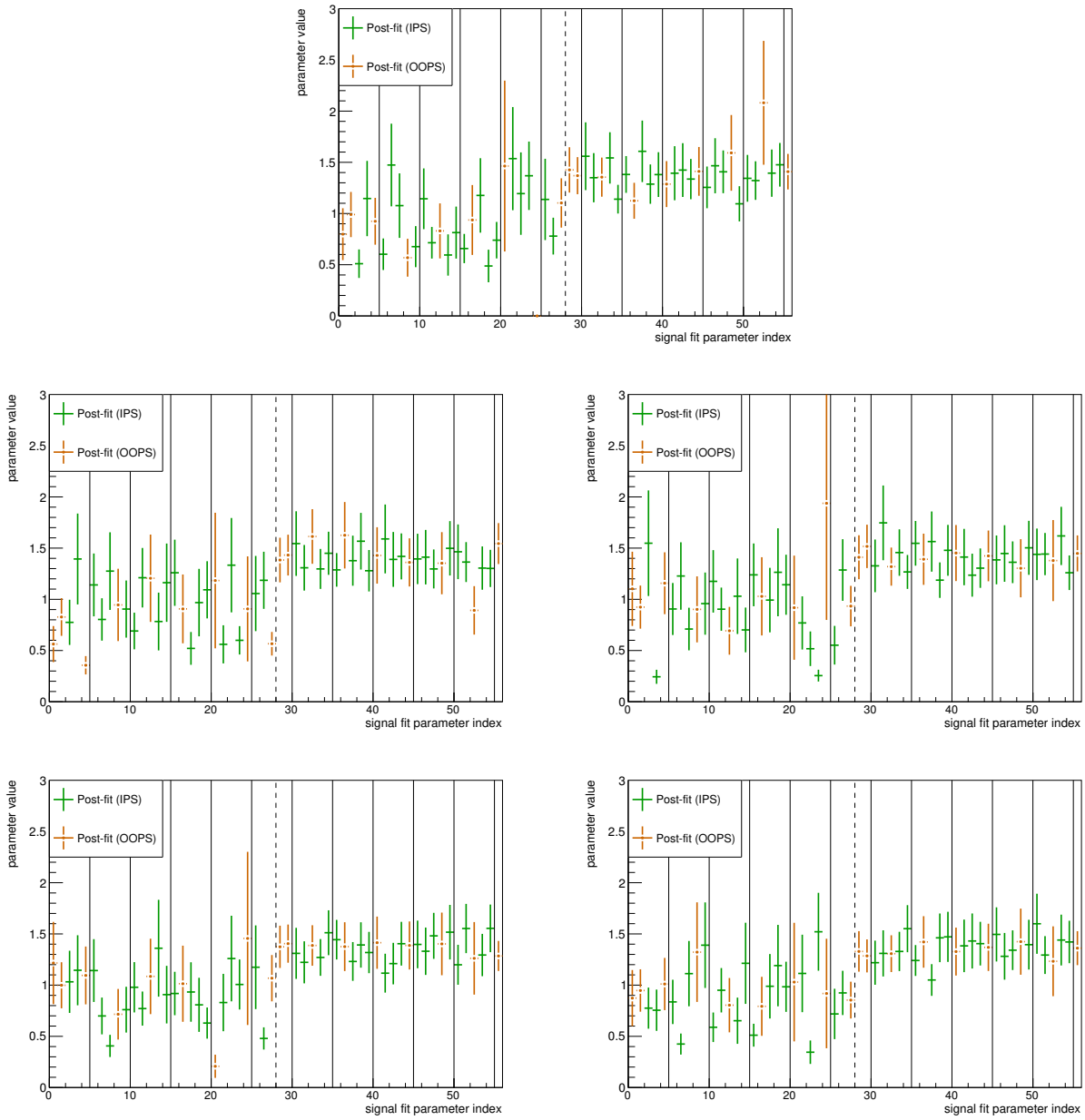

Figure 5.24: Post-fit results (best-fit value and full uncertainty) for the c_i and d_i parameters in the non-water increased fake data fits with regularization. As a reminder, IPS stands for in-phase-space and OOPS stands for out-of-phase-space.

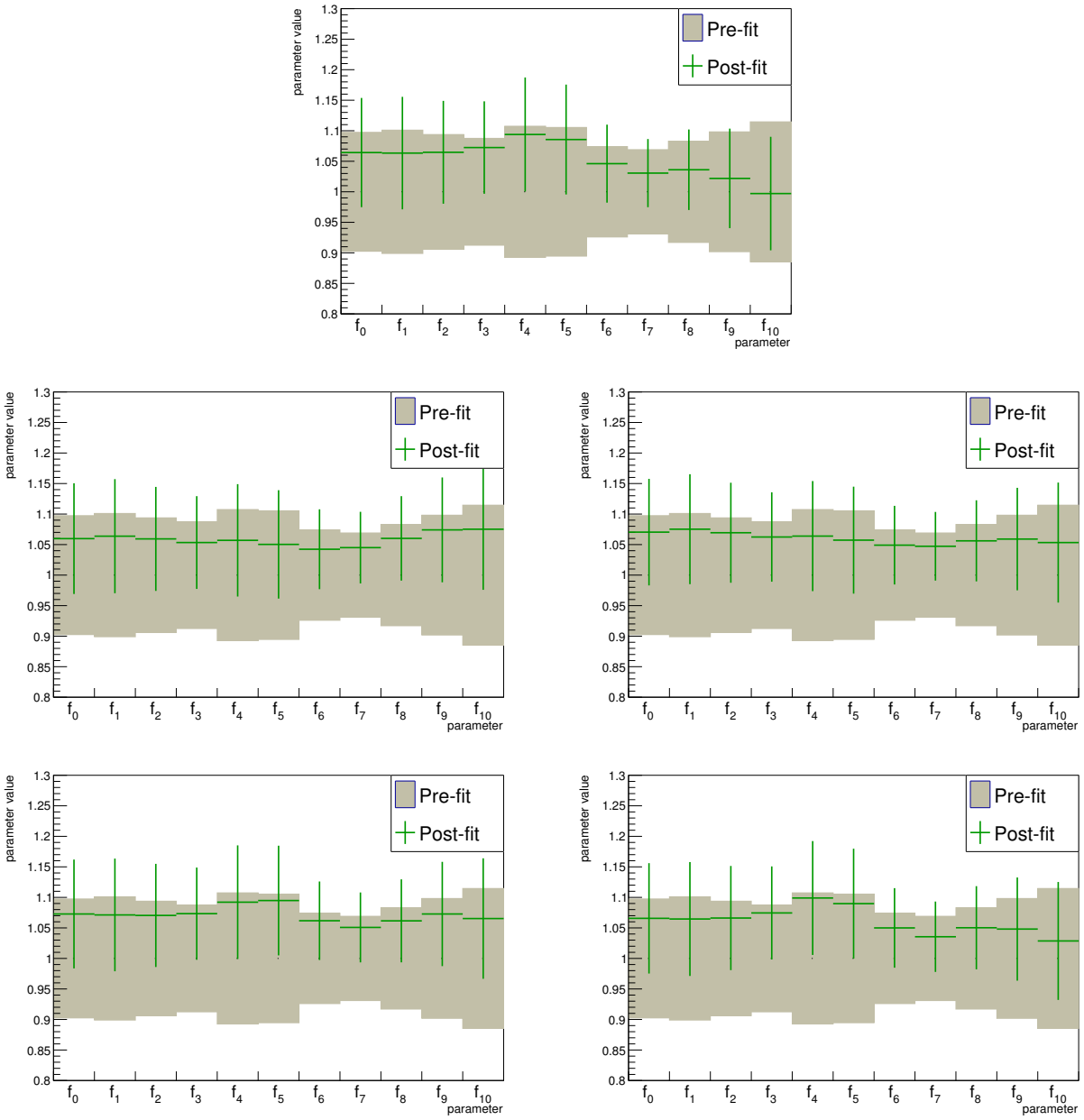

Figure 5.25: Post-fit results (best-fit value and full uncertainty) for the neutrino flux (f_i) parameters in the non-water increased fake data fits with regularization overlaid with the pre-fit uncertainties (shaded region).

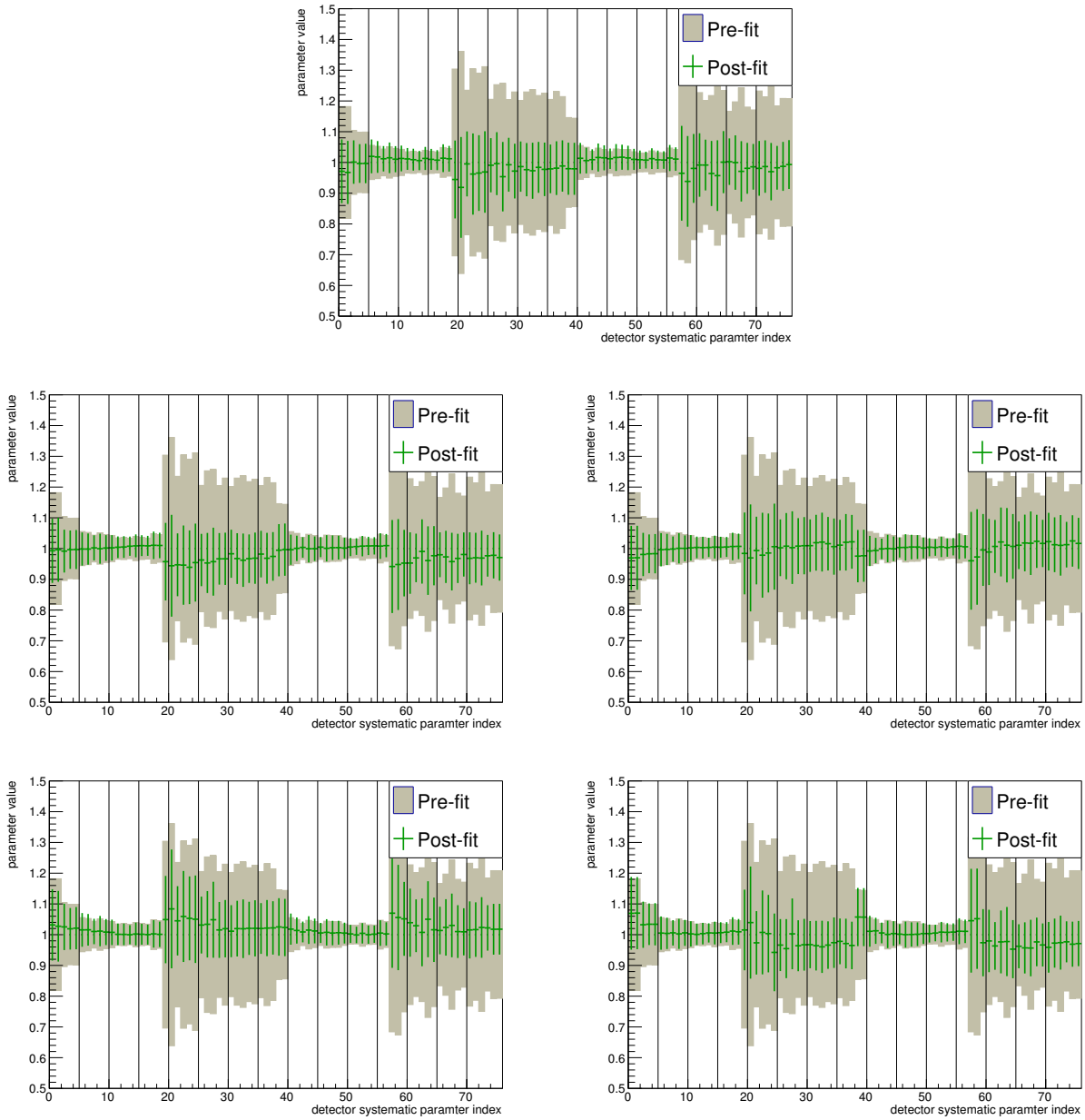

Figure 5.26: Post-fit results (best-fit value and full uncertainty) for the detector systematic (r_i) parameters in the non-water increased fake data fits with regularization overlaid with the pre-fit uncertainties (shaded region).

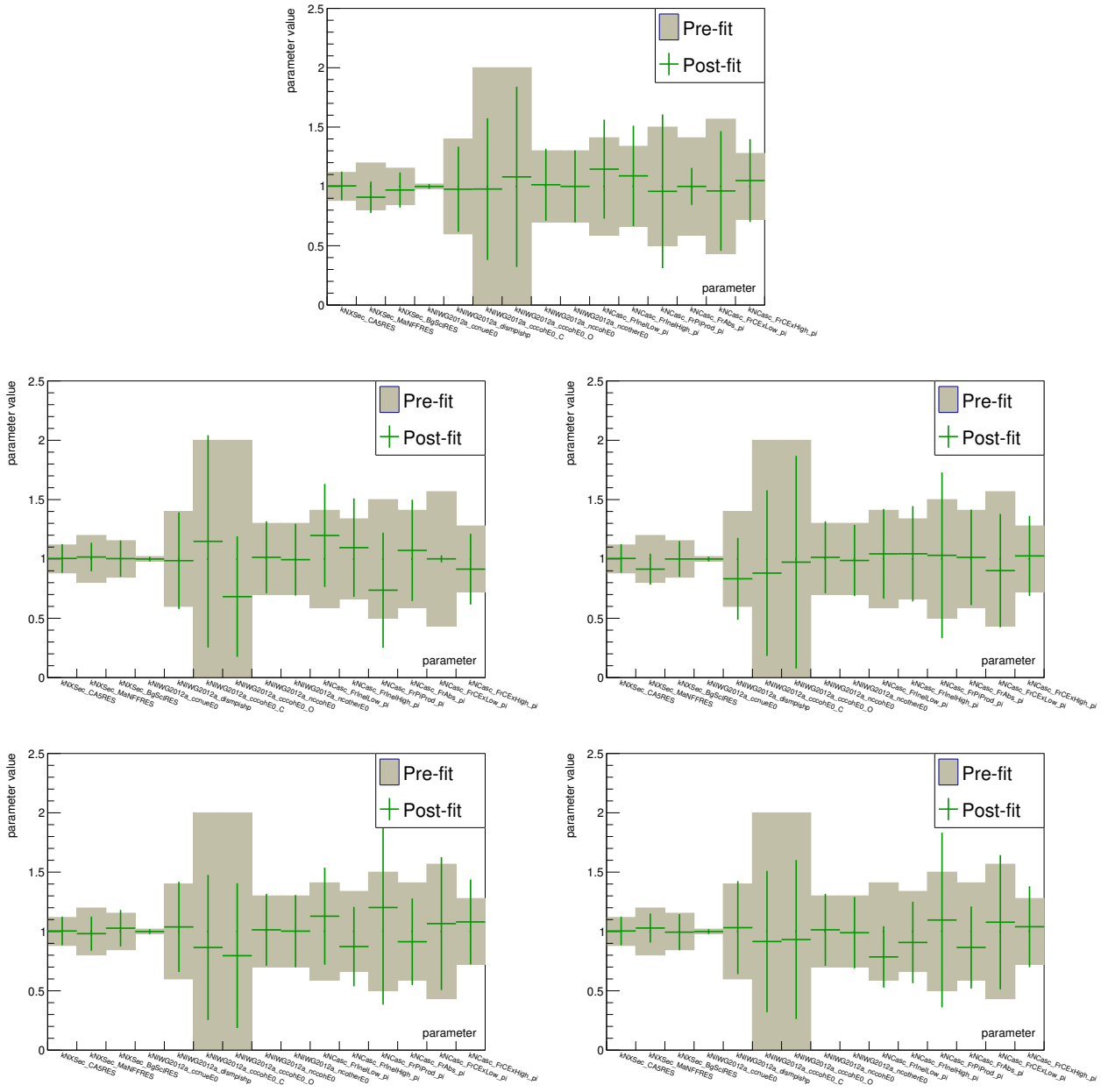

Figure 5.27: Post-fit results (best-fit value and full uncertainty) for the background model parameters in the non-water increased fake data fits with regularization overlaid with the pre-fit uncertainties (shaded region).

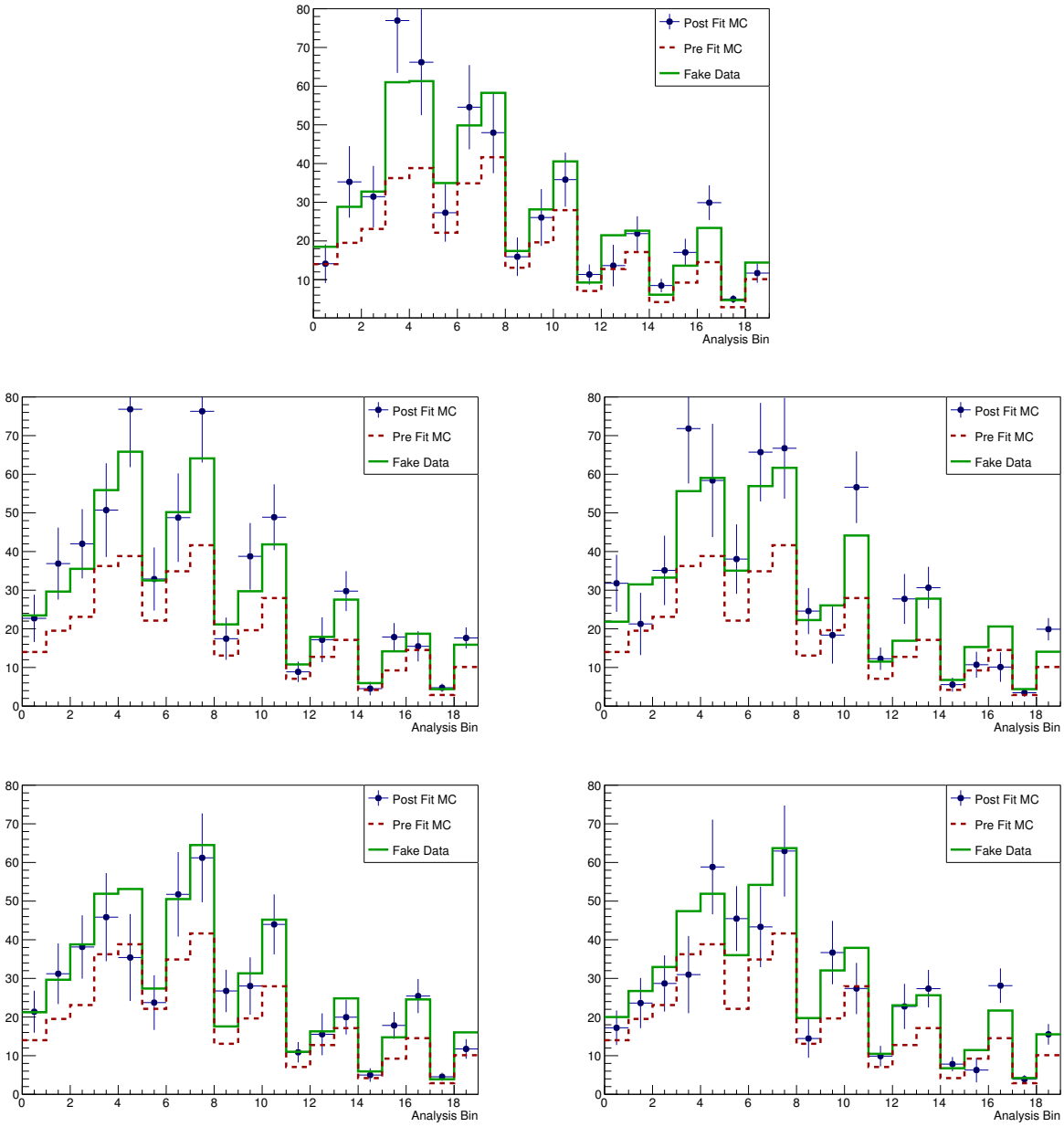

Figure 5.28: Overlaid event rates for the fit to realistic sized fake data sets generated with CC-0π events on water targets increased by 50% fitted with no regularization. We see that in each of the 5 fits, the fake data truth is well captured by the best fit points.

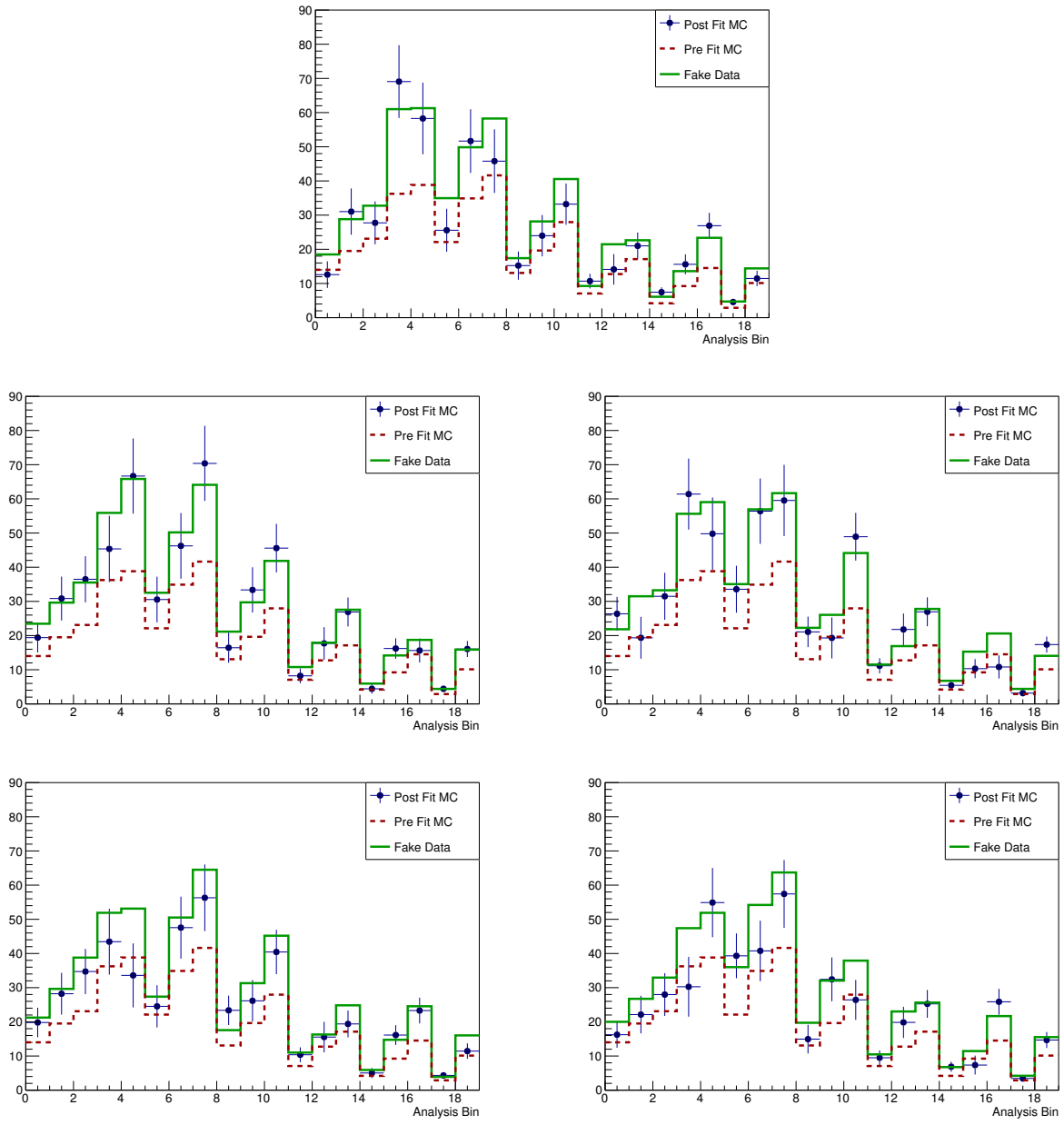

Figure 5.29: Overlaid event rates for the fit to realistic sized fake data sets generated with CC-0π events on water targets increased by 50% fitted with regularization (p=1 in all). We see that in each of the 5 fits, the fake data truth is again well captured by the best fit points, and the results are not significantly different from those with no regularization.

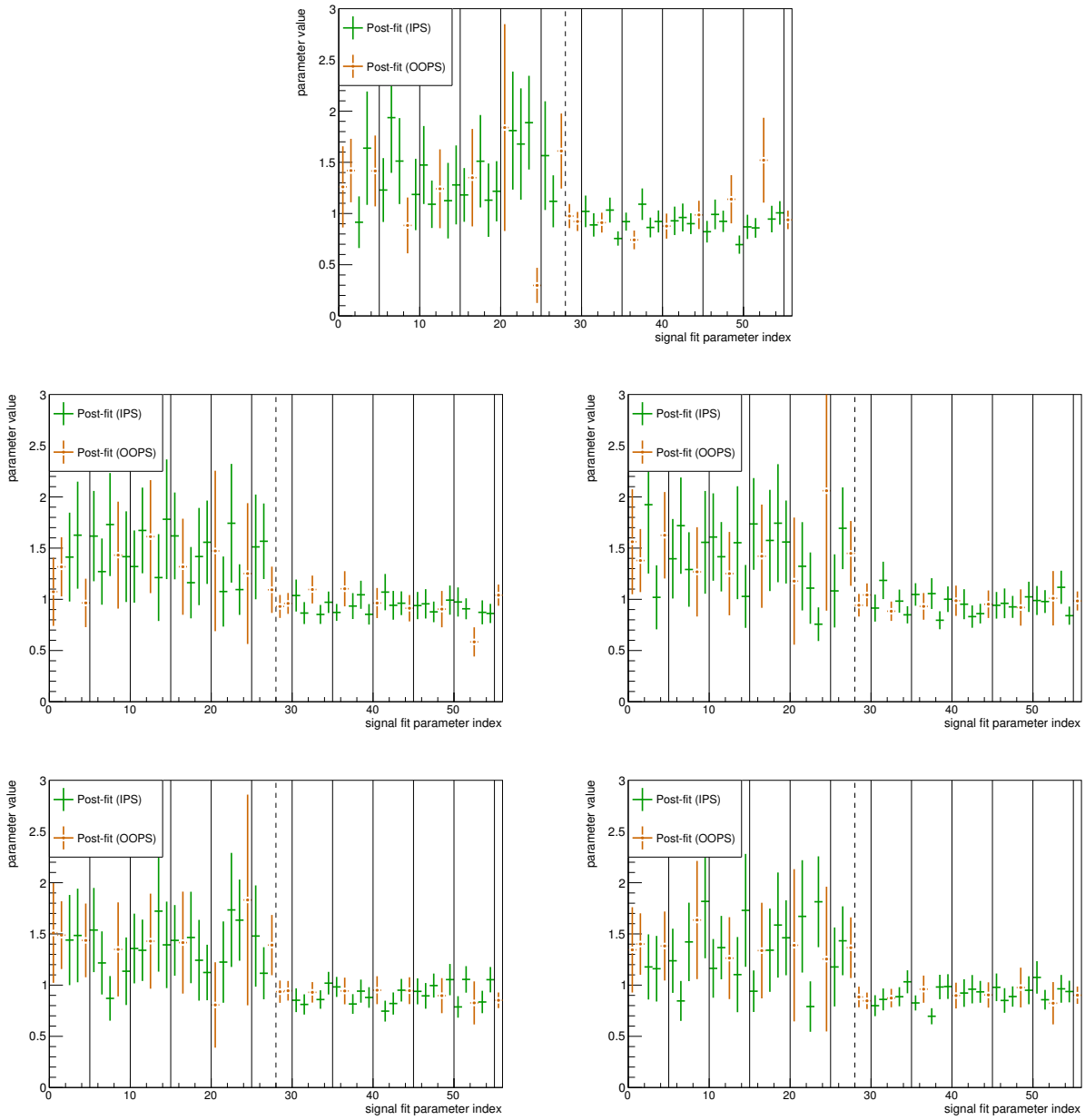

Figure 5.30: Post-fit results (best-fit value and full uncertainty) for the c_i and d_i parameters in the water increased fake data fits with regularization. As a reminder, IPS stands for in-phase-space and OOPS stands for out-of-phase-space.

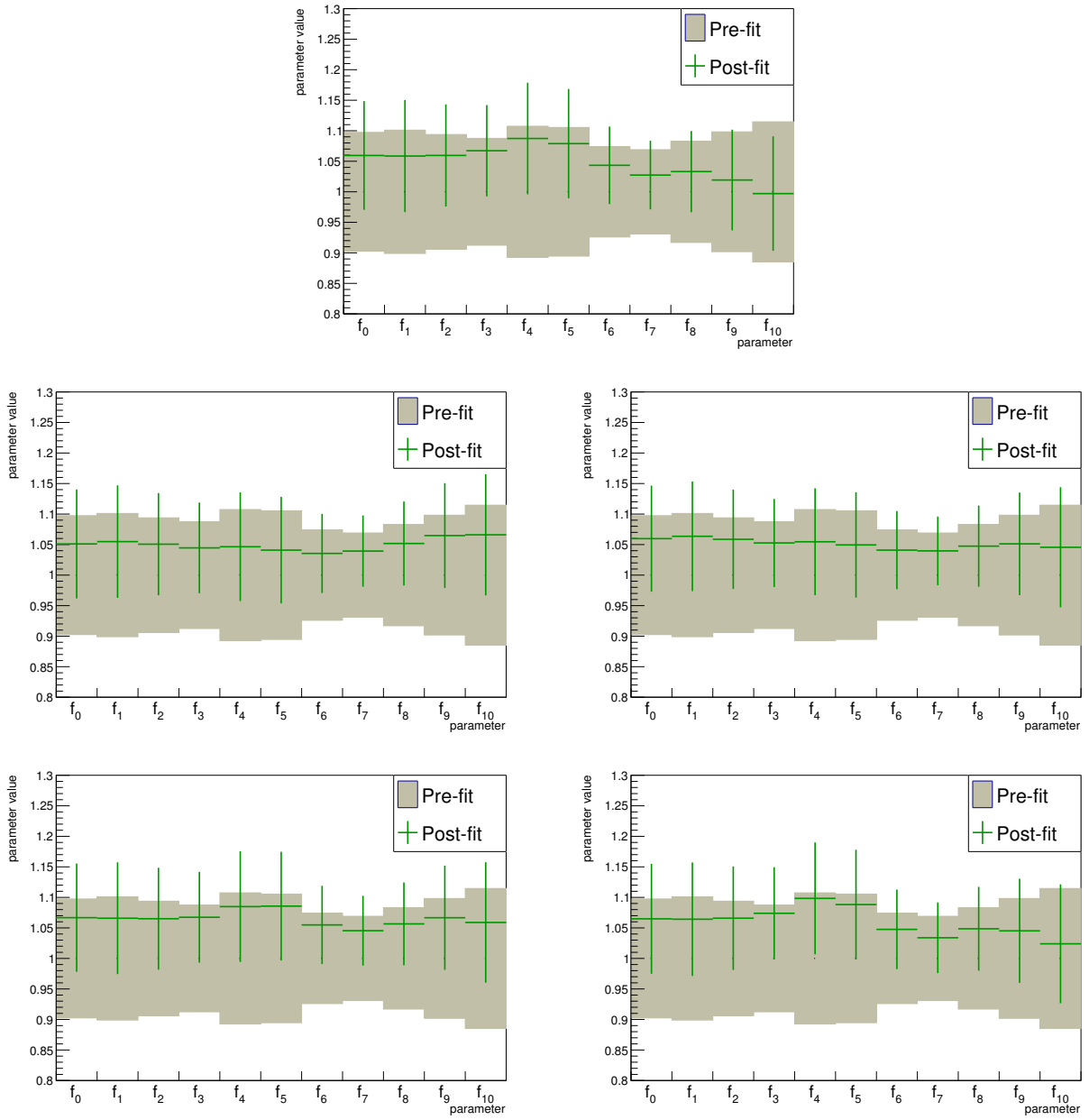

Figure 5.31: Post-fit results (best-fit value and full uncertainty) for the neutrino flux (f_i) parameters in the water increased fake data fits with regularization overlaid with the pre-fit uncertainties (shaded region).

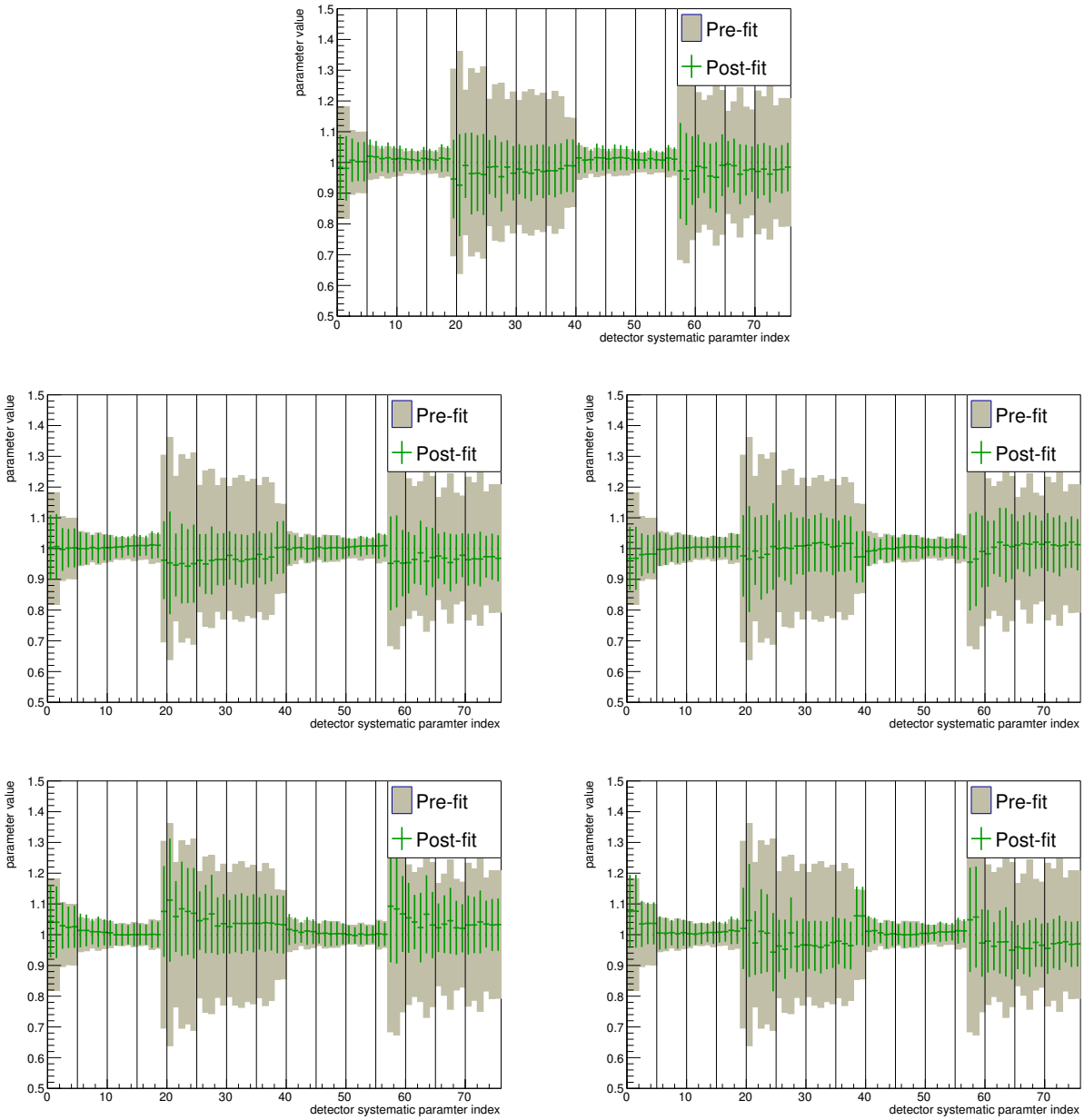

Figure 5.32: Post-fit results (best-fit value and full uncertainty) for the detector systematic (r_i) parameters in the water increased fake data fits with regularization overlaid with the pre-fit uncertainties (shaded region).

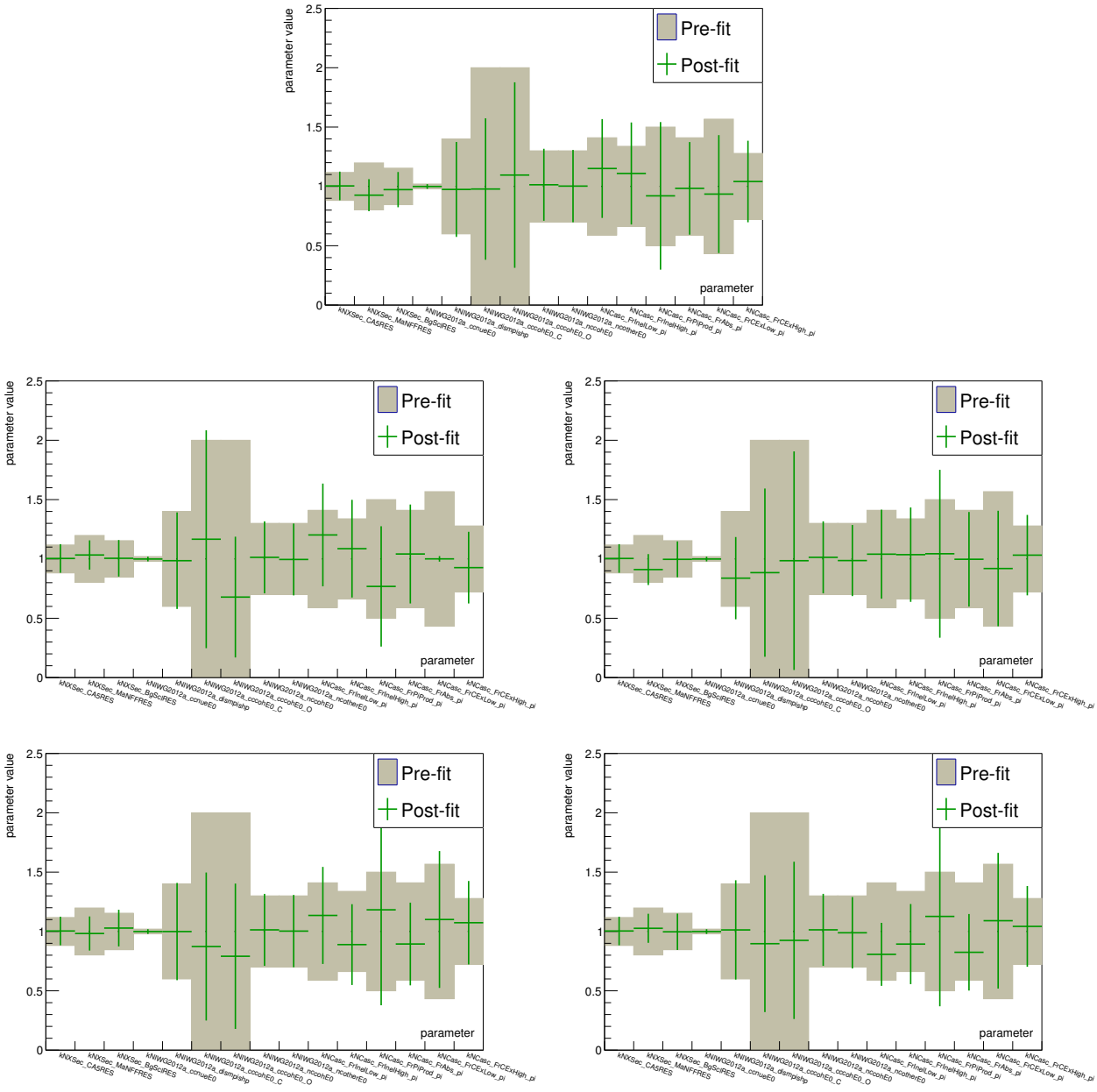

Figure 5.33: Post-fit results (best-fit value and full uncertainty) for the background model parameters in the water increased fake data fits with regularization overlaid with the pre-fit uncertainties (shaded region).

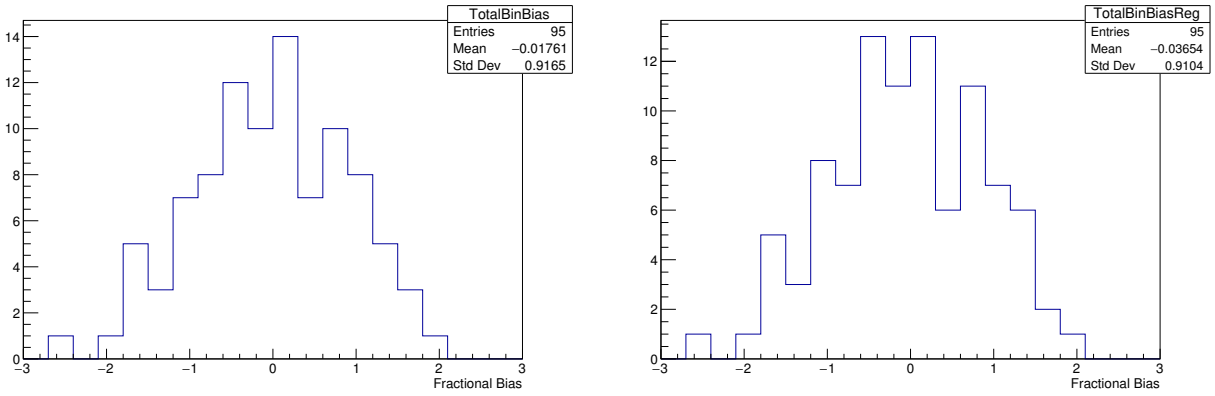

Figure 5.34: Bin bias as defined in equation 5.3 in each bin in each of the 5 nominal fake data sets with no regularization (left) and with regularization (right).

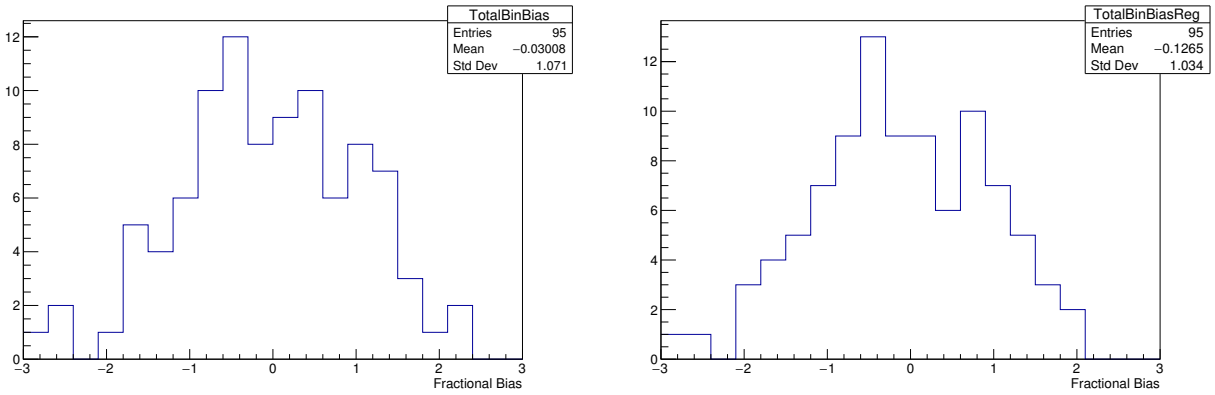

Figure 5.35: Bin bias as defined in equation 5.3 in each bin in each of the 5 non-water increased fake data sets with no regularization (left) and with regularization (right).

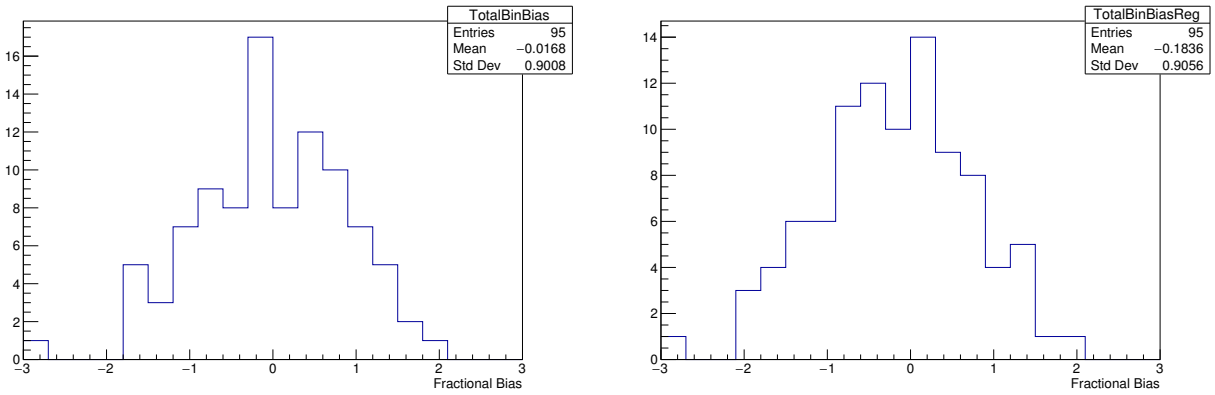

Figure 5.36: Bin bias as defined in equation 5.3 in each bin in each of the 5 water increased fake data sets with no regularization (left) and with regularization (right).

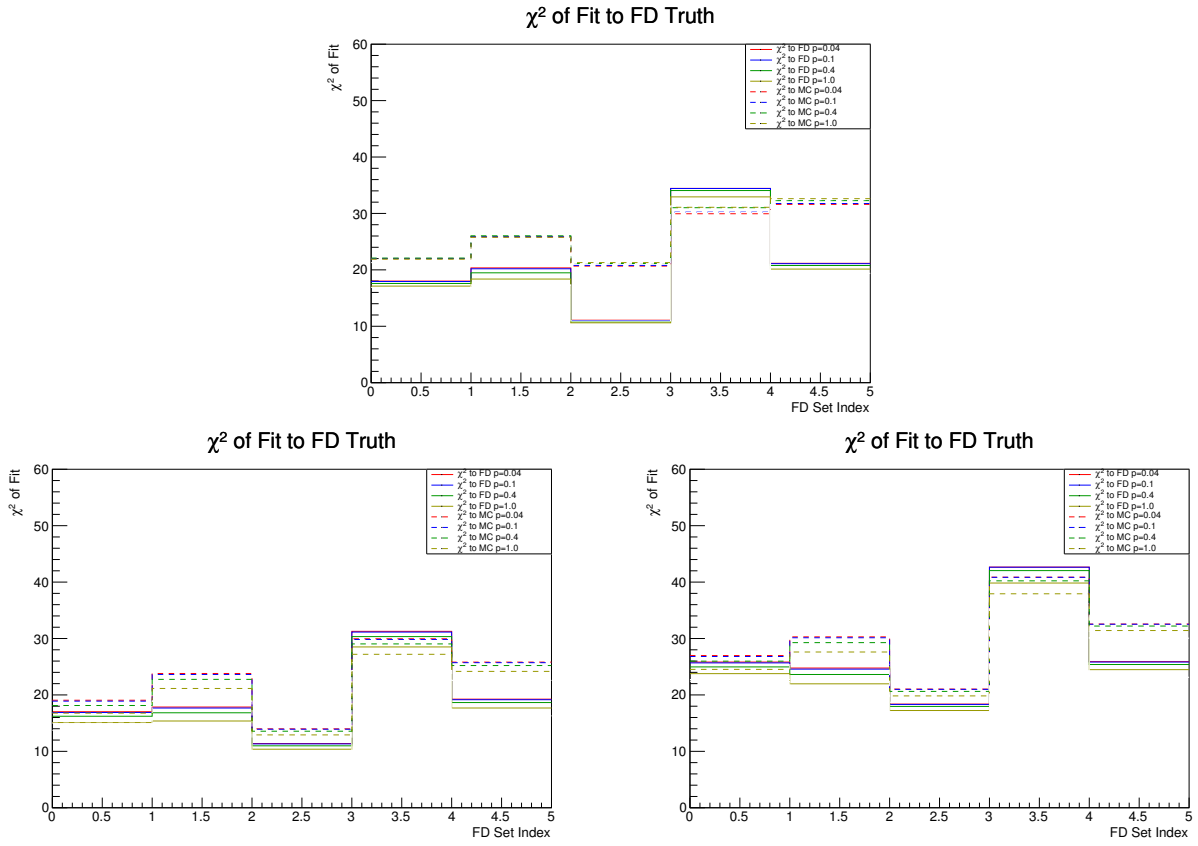

Figure 5.37: Overlay of the χ^2 of fit to the fake data truth and nominal MC as defined in equation 5.2 for different choices of the regularization strength for the nominal fake data sets (bottom-left), the non-water increased fake data sets (bottom-right) and the water increased fake data sets (top). We see that in each fake data set, the χ^2 is not significantly changing with the implementation of the regularization or the changing of its strength.

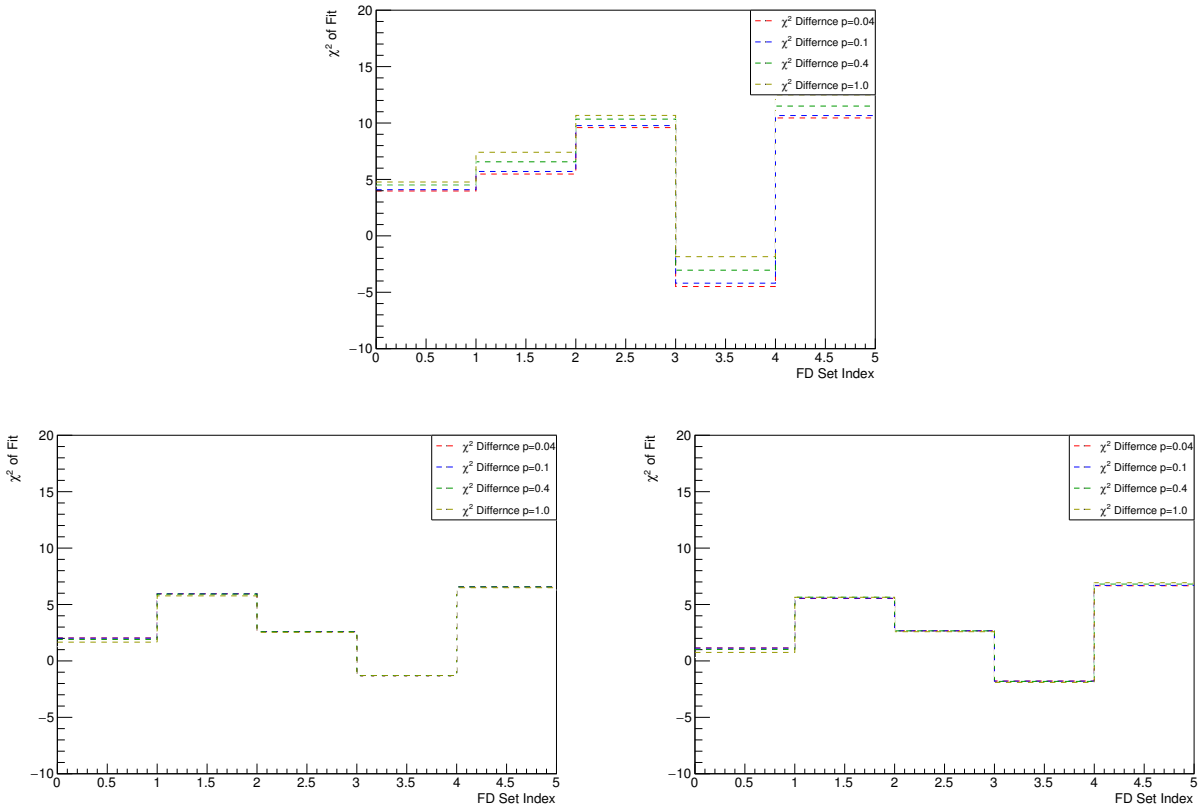

Figure 5.38: Overlay of the difference of the χ^2 of fit to the fake data truth minus that for the nominal MC as defined in equation 5.2 for different choices of the regularization strength for the nominal fake data sets (bottom-left), the non-water increased fake data sets (bottom-right) and the water increased fake data sets (top). We see that in each fake data set, the difference is not significantly changing with the implementation of the regularization or the changing of its strength.

5.7.4 Realistic Expected PoT Fluctuated Fake Data

As a rigorous test of the fitters ability to produce reasonable results for fake data that is significantly different to the input MC, the 5 nominal FD sets from the previous subsection were re-weighted so that the signal and dominant background distributions differ in both shape and normalization relative to the input MC. The CC-0π and CC-1π events were re-weighted according to the functions given in figure 5.52. The resulting fake data sets were used to fit the nominal input MC and all the results of the previous subsection were produced. Figures 5.39 and 5.40 give the event rate overlays for with and without regularization respectively. The post-fit values and uncertainties for each parameter in the regularized fits are given in figures 5.41 through 5.44. The total bin bias distributions are given in 5.45. The χ^2 overlay and χ^2 difference plots are given in figure 5.46.

Table 5.11 gives the χ^2 contributions from all sources at the best fit point for the fluctuated fake data sets.

Table 5.11: Contributions to the χ^2 at the best fit point for each source in the fits to the fluctuated fake data sets. We see again that the regularization is not a major contributor in each fit.

	w/o Reg			w/ Reg		
FD Set	Stat χ^2	Syst χ^2	Reg χ^2	Stat χ^2	Syst χ^2	Reg χ^2
1	39.2	2.4	0	39.7	3.8	3.7
2	39.1	2.7	0	40.4	4.0	5.1
3	32.7	2.3	0	33.4	3.4	3.3
4	31.1	1.8	0	33.4	3.5	8.0
5	50.7	3.3	0	51.2	4.7	4.2

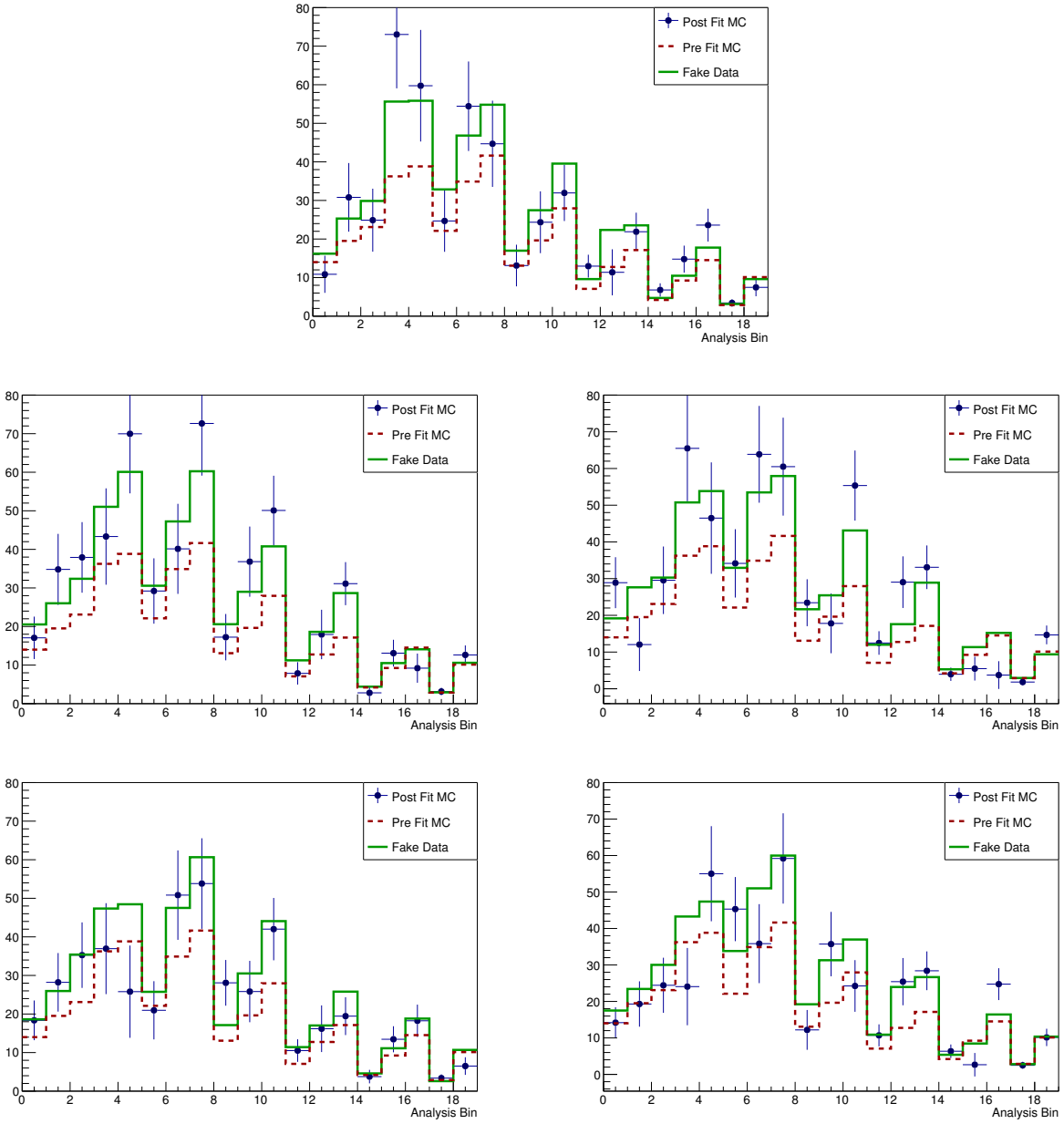

Figure 5.39: Overlaid event rates for the fit to realistic sized fake data sets generated with shape and normalization variations applied as described fitted with no regularization. We see that in each of the 5 fits, the fake data truth is well captured by the best fit points.

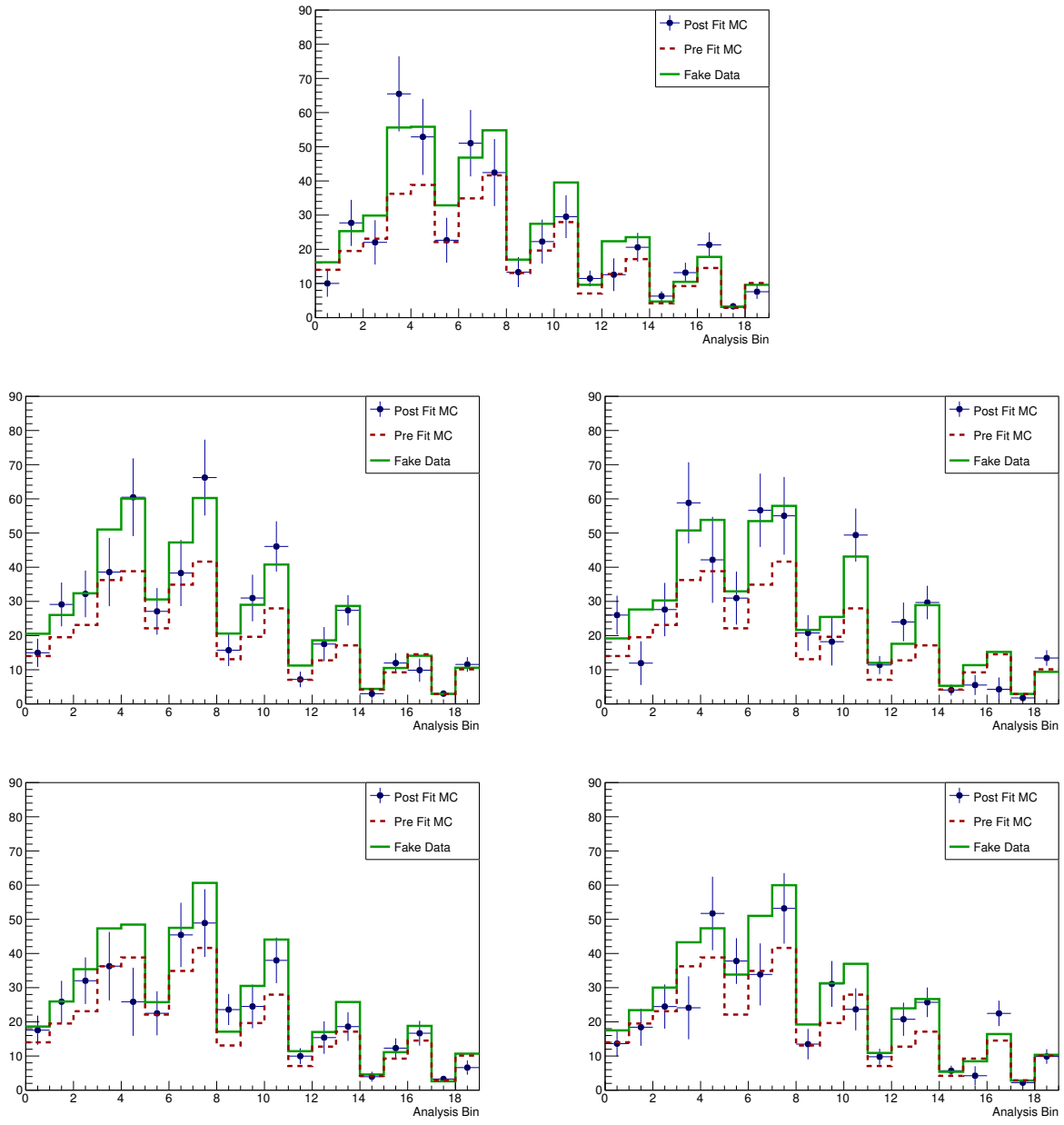

Figure 5.40: Overlaid event rates for the fit to realistic sized fake data sets generated with shape and normalization variations applied as described fitted with regularization (p=1 in all). We see that in each of the 5 fits, the fake data truth is again well captured by the best fit points, and the results are not significantly different from those with no regularization.

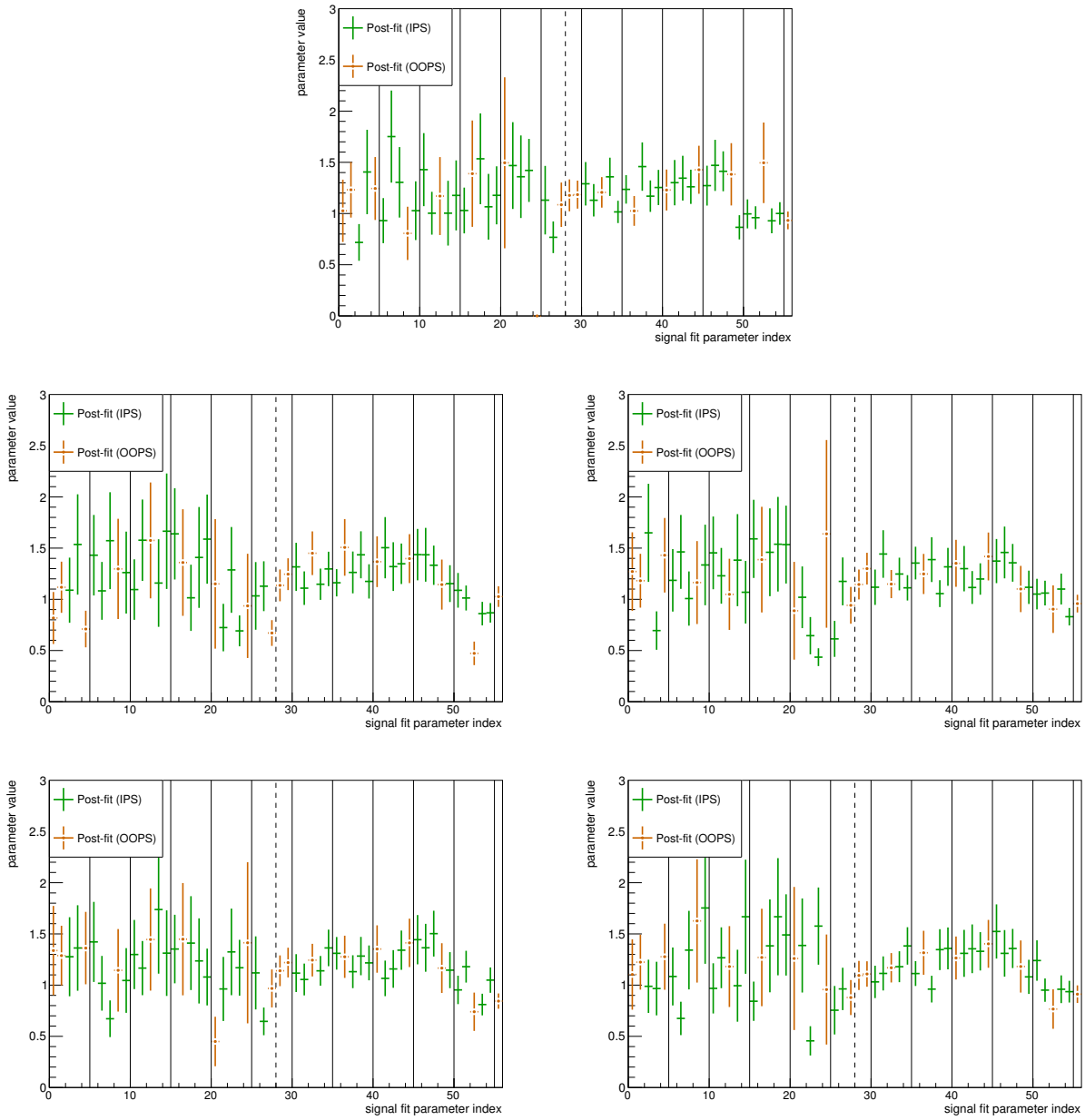

Figure 5.41: Post-fit results (best-fit value and full uncertainty) for the c_i and d_i parameters in the fluctuated fake data fits with regularization. As a reminder, IPS stands for in-phase-space and OOPS stands for out-of-phase-space.

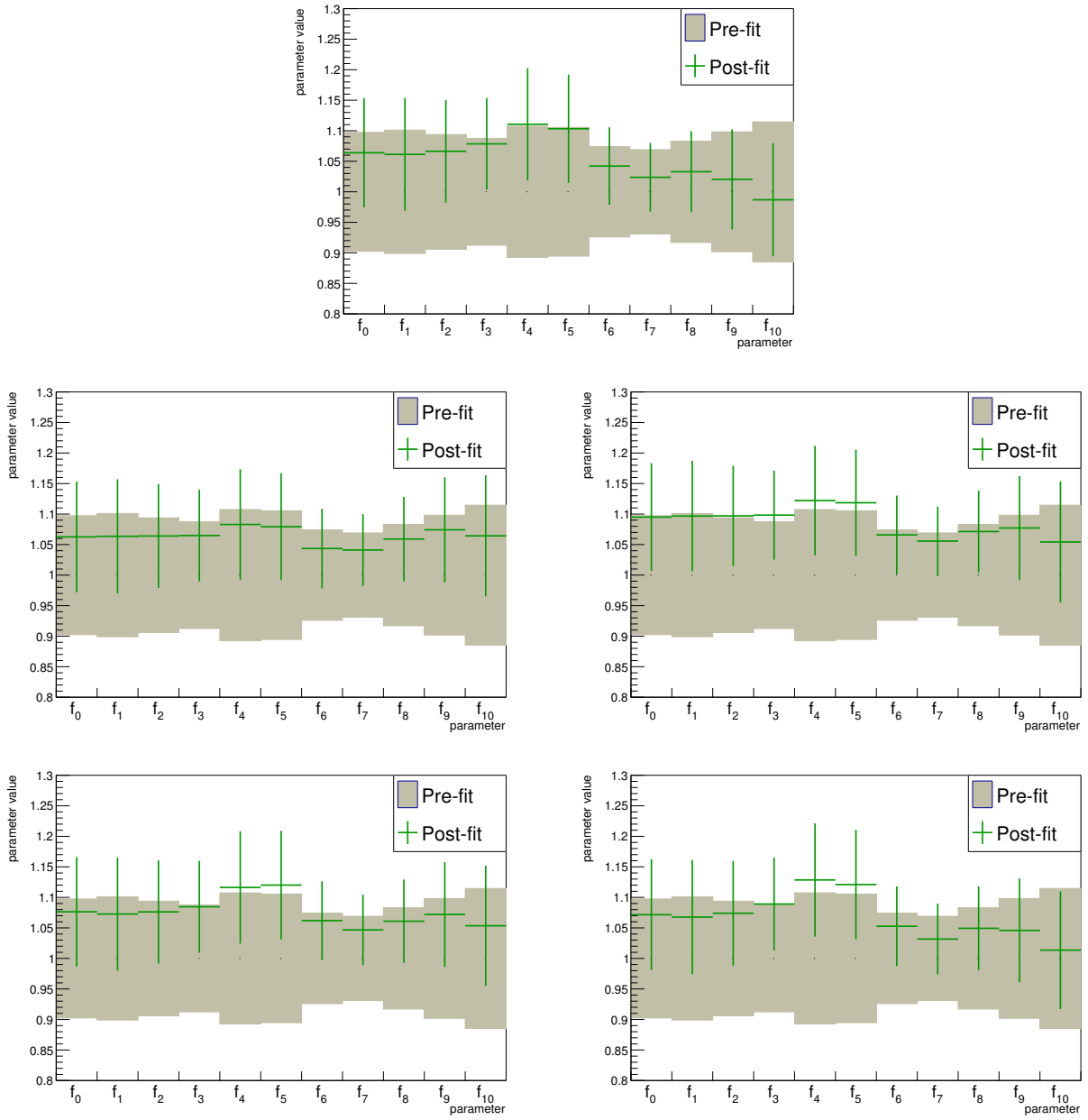

Figure 5.42: Post-fit results (best-fit value and full uncertainty) for the neutrino flux (f_i) parameters in the fluctuated fake data fits with regularization overlaid with the pre-fit uncertainties (shaded region).

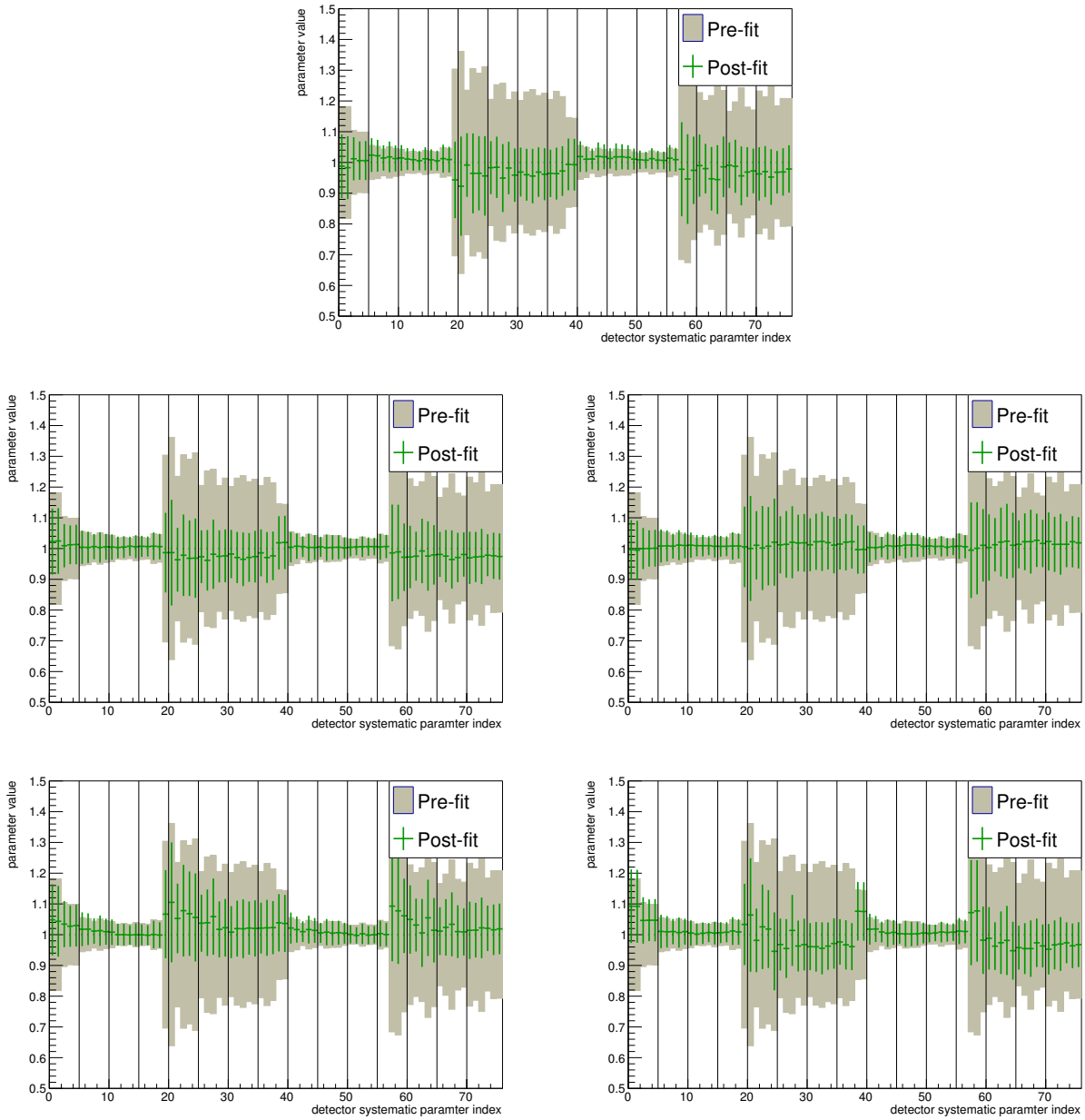

Figure 5.43: Post-fit results (best-fit value and full uncertainty) for the detector systematic (r_i) parameters in the fluctuated fake data fits with regularization overlaid with the pre-fit uncertainties (shaded region).

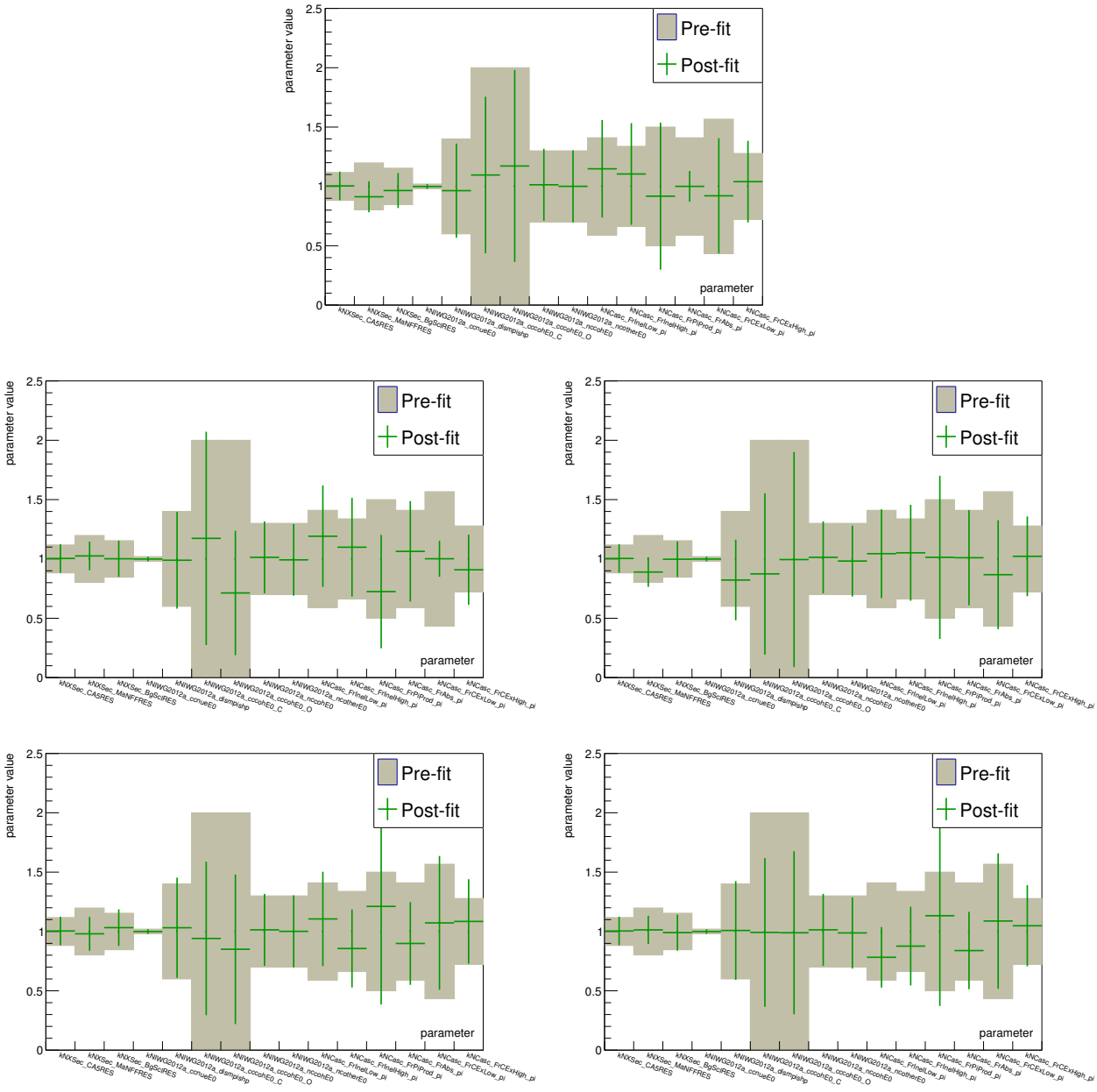

Figure 5.44: Post-fit results (best-fit value and full uncertainty) for the background model parameters in the fluctuated fake data fits with regularization overlaid with the pre-fit uncertainties (shaded region).

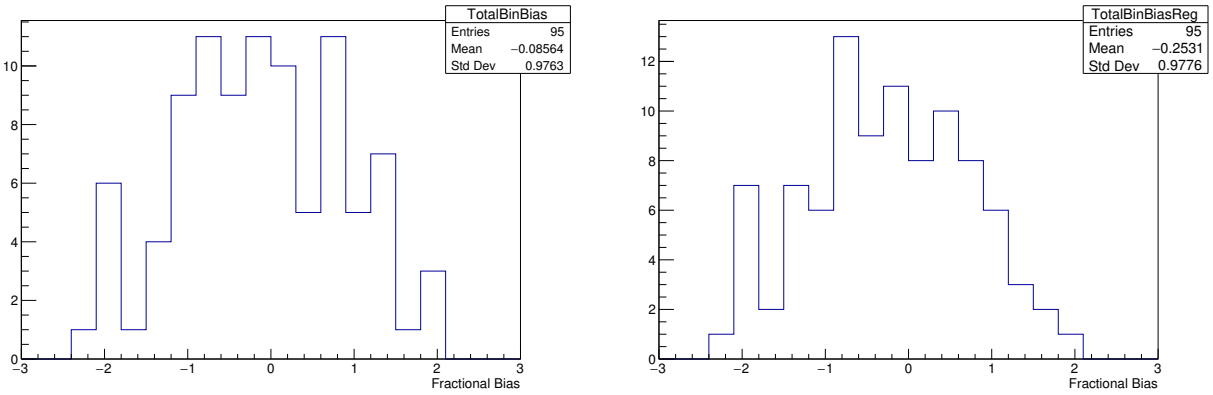

Figure 5.45: Bin bias as defined in equation 5.3 in each bin in each of the 5 fluctuated fake data sets with no regularization (left) and with regularization (right).

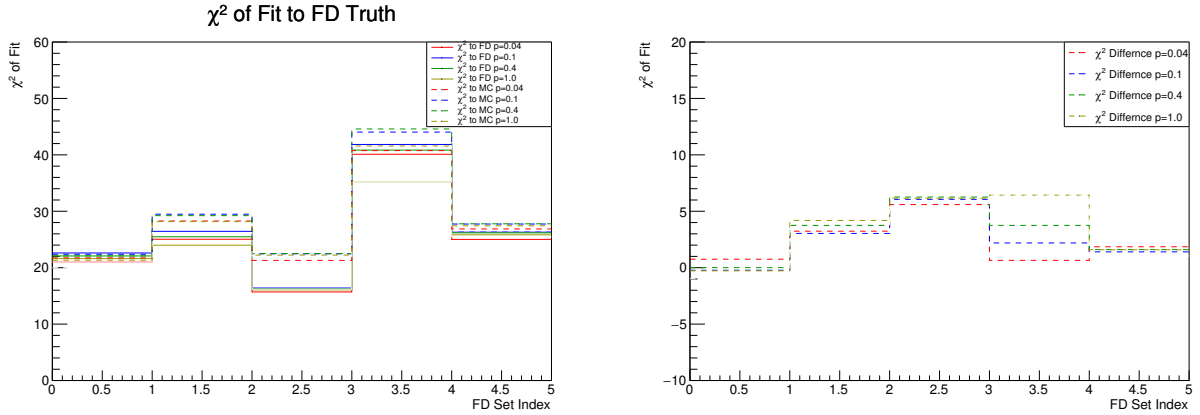

Figure 5.46: Overlay of the values (left) and difference (right) of the χ^2 of fit to the fake data truth and that for the nominal MC as defined in equation 5.2 for different choices of the regularization strength for the fluctuated fake data sets. We see that in each fake data set, the difference is not significantly changing with the implementation of the regularization or the changing of its strength.

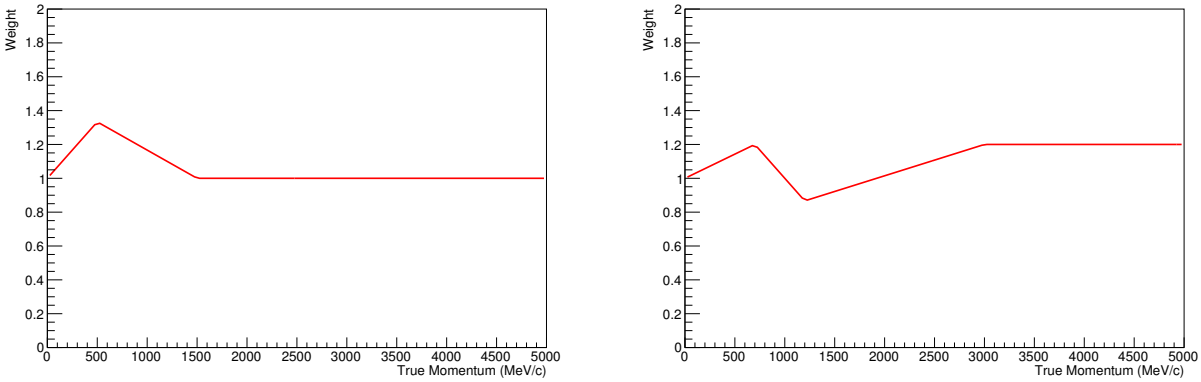

Figure 5.47: Re-weighting functions used to apply the fluctuations to the CC-0π (left) event rates and CC-1π (right) event rates in the fluctuated fake data sets.

5.7.5 Toy Statistical Fluctuation Fits

To check the propagation of the statistical uncertainties in the fitting (and unfolding) procedure for a given fit to a fake data set, Poisson fluctuations were applied to the signal+background event rates in the fake data set being fit many times to produce a set of 100 statistically fluctuated toy data sets. Each of these sets was then fit using only the main fit parameters (no systematics) and a fractional bias in each bin was calculated for each bin for each toy. The resulting distributions can then be compared to the statistical error from fitting to the underlying fake data set using only the main fit parameters. The uncertainty from this fit should be comparable to the spread (RMS) of the toy distributions. If the error bars are too small, the spread of the toy distributions would be larger than the error bars indicating that the fit is underestimating the statistical uncertainties. Getting the statistical error bars correct in unfolding has proven to be a great challenge historically in different unfolding procedures. Following figures will give the RMS of the distribution of fractional biases in each analysis bin over the 100 toys divided by the nominal fit error. If the error bars were perfectly representing the proper statistical variation, each point in these plots would have an error bar of 1.

To be formal, the fractional bias in some toy in bin i is given by:

$$B_i = \frac{(N_i^{fit} - N_i^{FD})}{\sigma i} \tag{5.4}$$

where N_i^{fit} is the best fit event rate in bin i and N_i^{FD} is the same but from the fake data truth. σi is the uncertainty arising from only variation of the main fit parameters in bin i; this is equivalent to the nominal statistical uncertainty in the fit.

Because fitting to so many fake data sets is very computationally intensive, this procedure was done for only a small sub-set of all the fake data sets presented in the previous subsections. The procedure was done for both with regularization (only the chosen optimal strength, $p = 1$ in all sets) and without regularization for each fake data set used here.

Figure 5.48 gives the mentioned distributions for the procedure applied to one of the nominal, realistic PoT exposure fake data sets from before. Figure 5.49 gives the same for one of the signal+background varied fake data sets from the previous subsection.

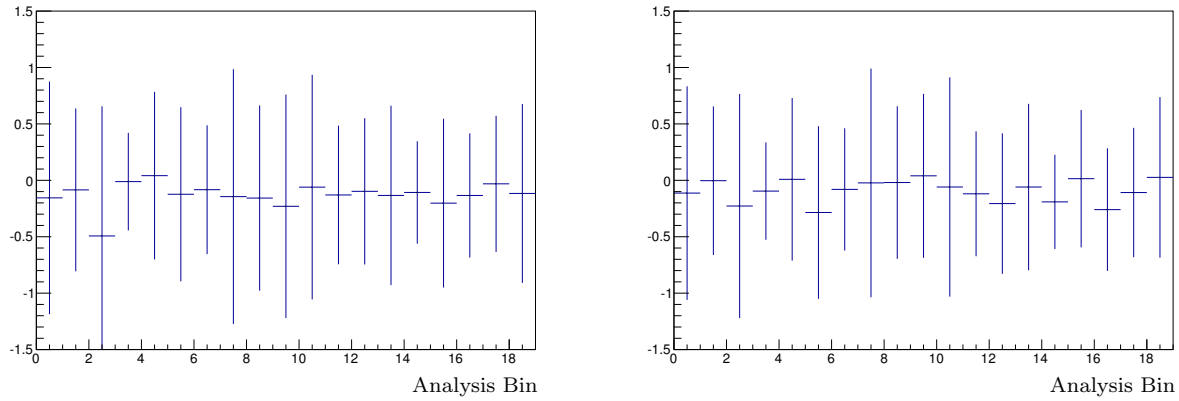

Figure 5.48: Mean (data points) and RMS (error bars) of the distributions of the bias in each analysis bin as defined in equation 5.4 in fits with no regularization (left) and with regularization (right) in statistical fluctuations on top of one of the nominal realistic sized fake data sets. First, we see that with no regularization, in each bin, the RMS of the distribution of the fractional bias is less than 1. This suggests that the statistical error bars are larger than actual statistical fluctuations coming from the defined Poisson fluctuations on fake data set. This would suggest that the error bars are appropriately covering the statistical fluctuations. Next we notice that the implementation of the regularization does not significantly alter these results so that the regularization is not leading to under-representation of the statistical errors.

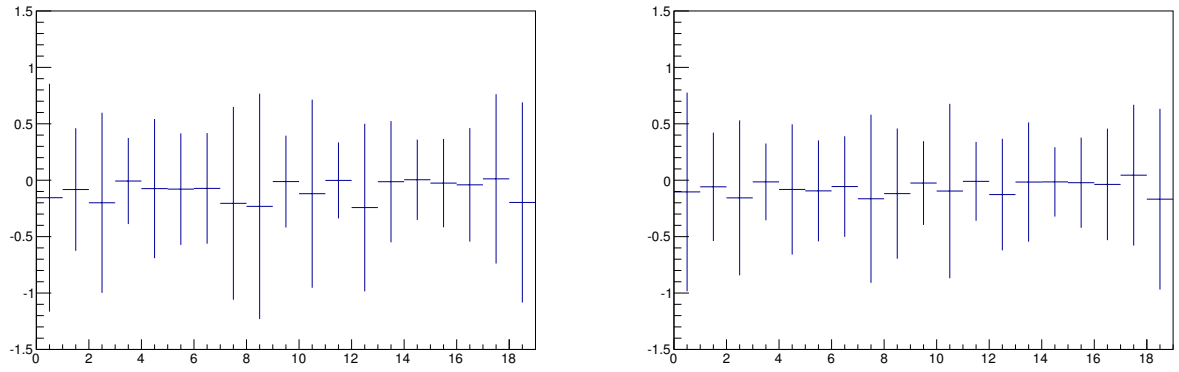

Figure 5.49: Mean (data points) and RMS (error bars) of the distributions of the bias in each analysis bin as defined in equation 5.4 in fits with no regularization (left) and with regularization (right) in statistical fluctuations on top of one of the fluctuated fake data sets of section 5.7.4. First, we see that with no regularization, in each bin, the RMS of the distribution of the fractional bias is less than 1. This suggests that the statistical error bars are larger than actual statistical fluctuations coming from the defined Poisson fluctuations on fake data set. This would suggest that the error bars are appropriately covering the statistical fluctuations. Next we notice that the implementation of the regularization does not significantly alter these results so that the regularization is not leading to under-representation of the statistical errors.

5.7.6 Realistic Expected PoT "Very Large Fluctuations" Fake Data

As a test of the limits of the framework to produce reasonable results for data that is very different than the input MC, the fluctuations applied to the fake data sets in section 5.7.4 were increased in magnitude until the results presented broke down in some sense. Figure 5.52 gives the re-weighting function used to fluctuate the data sets in this example. Figures 5.50 and 5.51 give the corresponding event rate plots. Here the fitter "failed" in two of the 5 fake data sets in the sense that a parameter's best fit value was determined to be at a physical limit (zero in this case). The resulting covariance matrix was not invertible so that the χ^2 goodness of fit as defined in equation 5.2 could not be computed. The Cholesky decomposition still exists however, so the error calculation in each bin should still be somewhat interpretable. However, this study was not redone with the final (correct) detector systematic errors, so comparing the results here to those in other sections should be done cautiously. The intent of the results in this section are to demonstrate a failure mode of the fitting scheme which could still happen with the correct (smaller) pre-fit detector systematic uncertainties, though it would likely require fairly more fluctuated data than what was used in this section.

The bins where the fit parameters were found to be zero were already low statistic bins relatively speaking. It is also worth noting that the implementation of regularization prevents the fit in this case from putting the best fit point at zero in all bins. Fortunately, the fits to real data did not exhibit any ill behavior like that observed in this section.

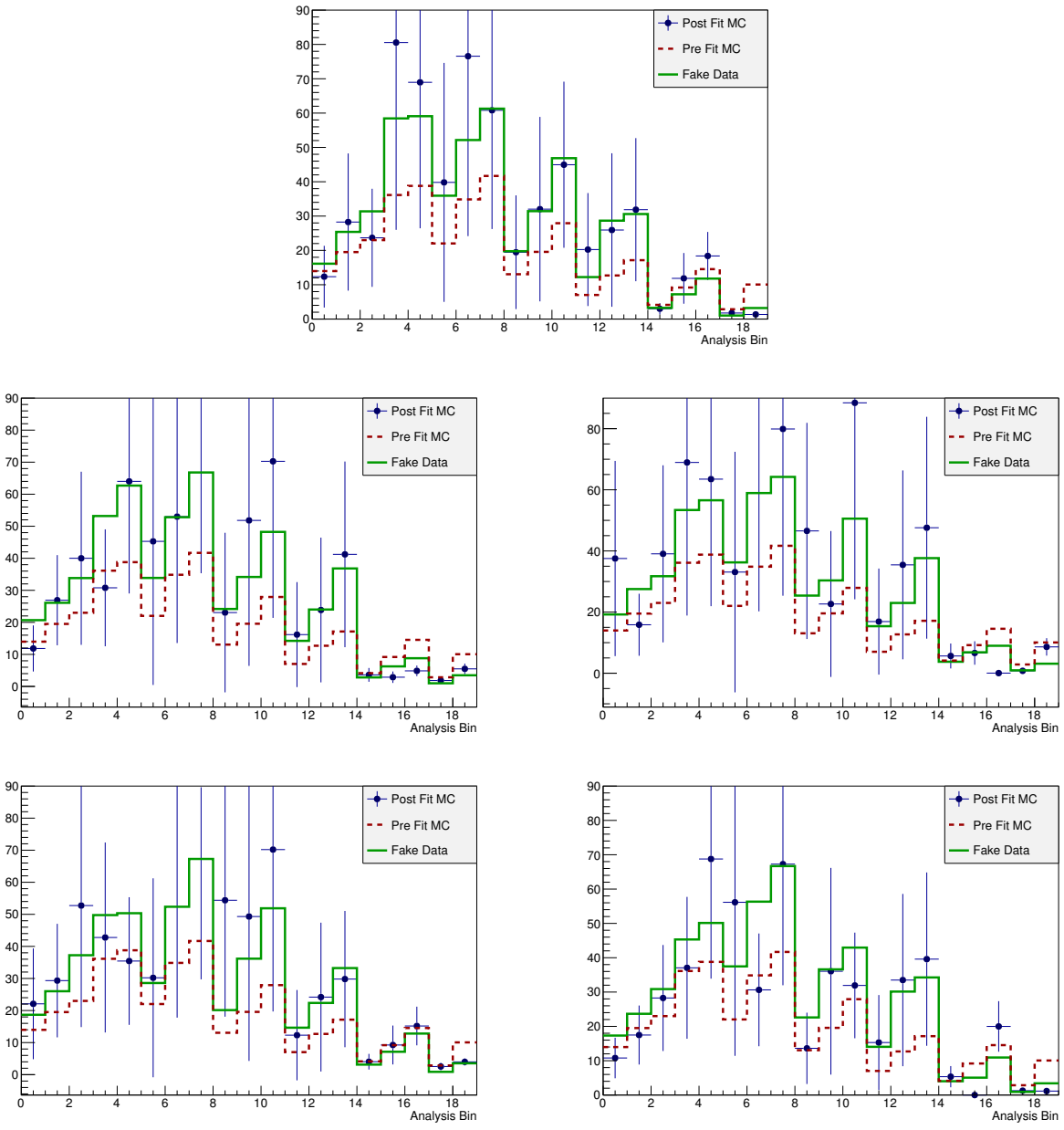

Figure 5.50: Overlaid event rates for the fit to realistic sized fake data sets generated with "very large" shape and normalization variations applied as described fitted with no regularization. We see that in each of the 5 fits, the fake data truth is well captured by the best fit points with the exception of the points where the best fit point was found to be zero.

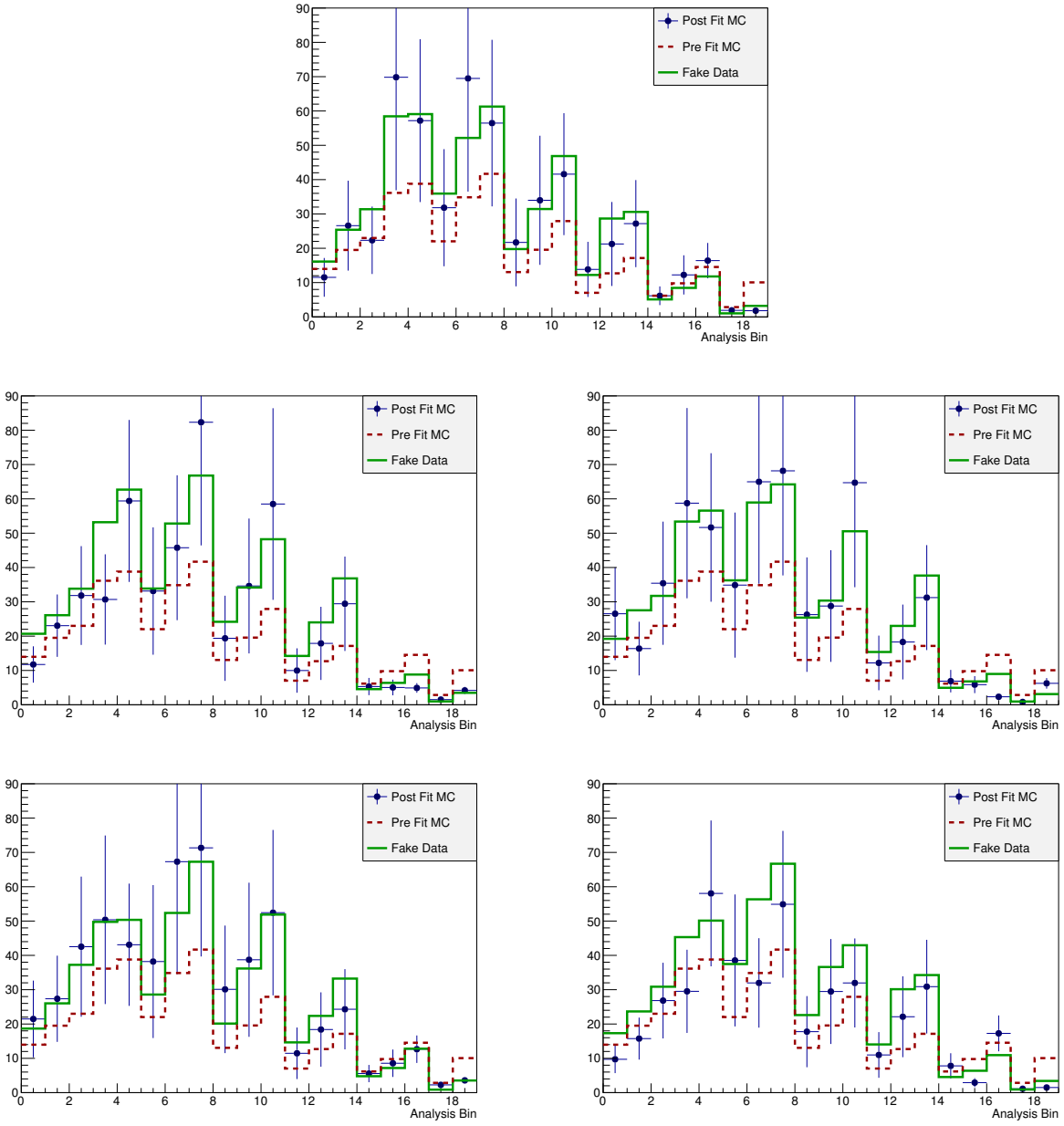

Figure 5.51: Overlaid event rates for the fit to realistic sized fake data sets generated with "very large" shape and normalization variations applied as described fitted with regularization (p=1 in all). We see that in each of the 5 fits, the fake data truth is again well captured by the best fit points, and the results are not significantly different from those with no regularization with the exception that the fit points that were determined to be zero in the fit without regularization are no longer zero.

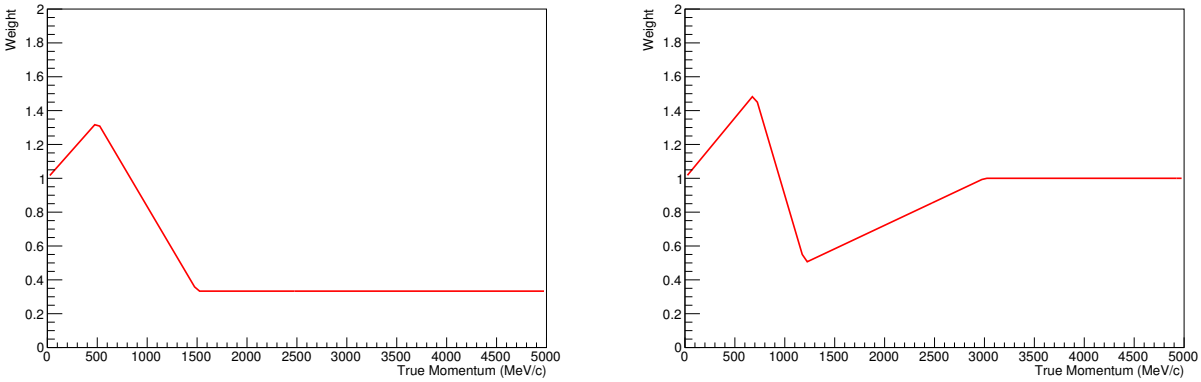

Figure 5.52: Re-weighting functions used to apply the fluctuations to the CC-0π (left) event rates and CC-1π (right) event rates in the "very fluctuated" fake data sets.

5.7.7 Discussion

Overall, the fitter is seen to be producing reasonable results both with and without regularization. Furthermore, the regularization seems to satisfy the criteria previously mentioned. We see that the overall contribution to the total χ^2 of the fit is small, the results with and without regularization are fairly consistent with each other, and the statistical error coverage is not greatly changed by the regularization. We see also that the sensitivity is not being unreasonably, artificially changed by the regularization. In figure 5.53 we can see that the fractional contribution to the χ^2 is relatively independent of the fake data's difference in shape to the input MC so that any resulting bias from the regularization on the MC shape is likely very small. In generating this plot, the FD to MC shape difference metric is given by:

$$D = \sum_{i}^{bins} \frac{(\hat{N}_i^{FD} - \hat{N}_i^{MC})^2}{(\hat{N}_i^{MC})^2} \tag{5.5}$$

where $\hat{N}_i^{FD(MC)}$ is the signal event rate in the fake data (MC) normalized to unity so that only shape differences will effect the metric.

In many fits, we see that the regularization might not really even be necessary; however, it is still an important tool so that the framework is ready for what ever the real data has in store for it. Upon the unblinding of the analysis to real data, the results are presented both with and without regularization.

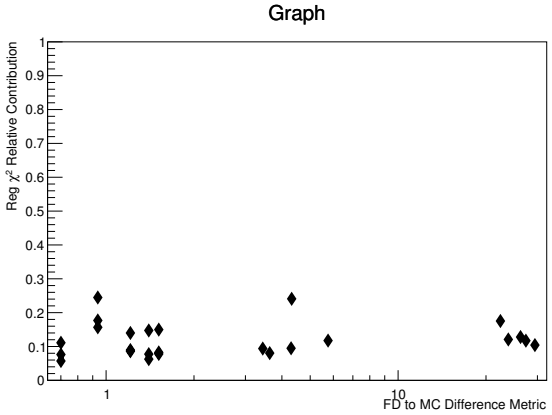

Figure 5.53: Fractional regularization contribution at the best fit point in each of the 25 fake data sets presented as a function of the FD to MC shape difference metric given in equation 5.5. We notice that even as the fake data has a greatly different shape than the input MC, the relative contribution from the regularization to the final χ^2 is not significantly changing.

5.8 From Fit Result to Cross Section

The fit output gives the CC-0π event rate on water in the true kinematic bins with all associated uncertainties. To get from these rates to the cross section, an efficiency correction needs to be applied and to get a corrected event rate. This rate then needs to be divided by the number of targets and integrated flux that appear in the basic cross section formula from section 2.1.

The efficiency correction in each bin is directly calculated from the nominal MC. The number of targets is calculated using the measured mass of the detector components and the integrated flux calculated using the data from the T2K beam group.

5.8.1 Additional Systematics

In addition to all the sources of uncertainty already taken into account in the fit, there is additional uncertainty on the three quantities mentioned above. The efficiency will have uncertainties arising from the flux simulation and from the signal model parameters. The integrated flux will also have uncertainty from the flux simulation, and the number of targets will have uncertainty from the uncertainty on the PØD water mass. Table 5.12 gives the included T2KReWeight dials included for the signal physics model variations.

Table 5.12: Signal model parameters included in variations of the selection efficiency.

T2KReWeight Knob Name	Nominal Value	Error
kNXSec_MaCCQE	1.15	0.41
kNIWG2014a_pF_C12	223	31
kNIWG2014a_pF_O16	225	31
kNIWGMEC_Norm_C12	1	1
kNIWGMEC_Norm_O16	1	1
kNIWG2014a_Eb_C12	25	9
kNIWG2014a_Eb_O16	25	9

There is already flux uncertainty on the unfolded event rates as the flux enters the fit as a set of parameters. To be conservative though, the uncertainty from flux on the efficiency and

integrated flux is calculated using the standard procedure with the BANFF pre-fit covariance matrix, rather than the post-fit uncertainty for the flux parameters.

The signal model parameters uncertainty on the efficiency is calculated using T2Krw.

Over many toys (400 for now) the unfolded event rate is simultaneously varied according to the fit output covariance matrix along with all sources of uncertainty on the quantities mentioned above. The cross section is then calculated for each toy and a new covariance matrix in terms of the cross section in each bin is calculated. The cross section central value is taken to be the mean of the distributions over the toy throws and the uncertainty is taken to be the RMS.

With the cross section covariance matrix, the χ^2 goodness of fit of the unfolded cross section to the true MC cross section can be calculated using a similar equation to equation 5.2.

5.8.2 Water Mass Uncertainty

For the uncertainty on the total water mass in the fiducial volume of the detector, the nominal value was taken from previous estimates [21] and divided by the number of bags to get a nominal mass per bag. The mass in each bag was then allowed to vary according to the means and uncertainties of section 5.3.4 for each toy. The total mass is then calculated by summing the individual bag masses in each toy.

5.8.3 Unfolded Cross Section in the Nominal Fake Data Sets

Figure 5.54 gives an overlay of the unfolded cross section in each analysis bin and the true cross section from the parent MC for each of the "nominal" FD sets from before. The result presented here are for the case without regularization. The χ^2 of the fit as previously described is given in each plot. Figure 5.55 gives an example of the cross section covariance matrix from one of the fits.

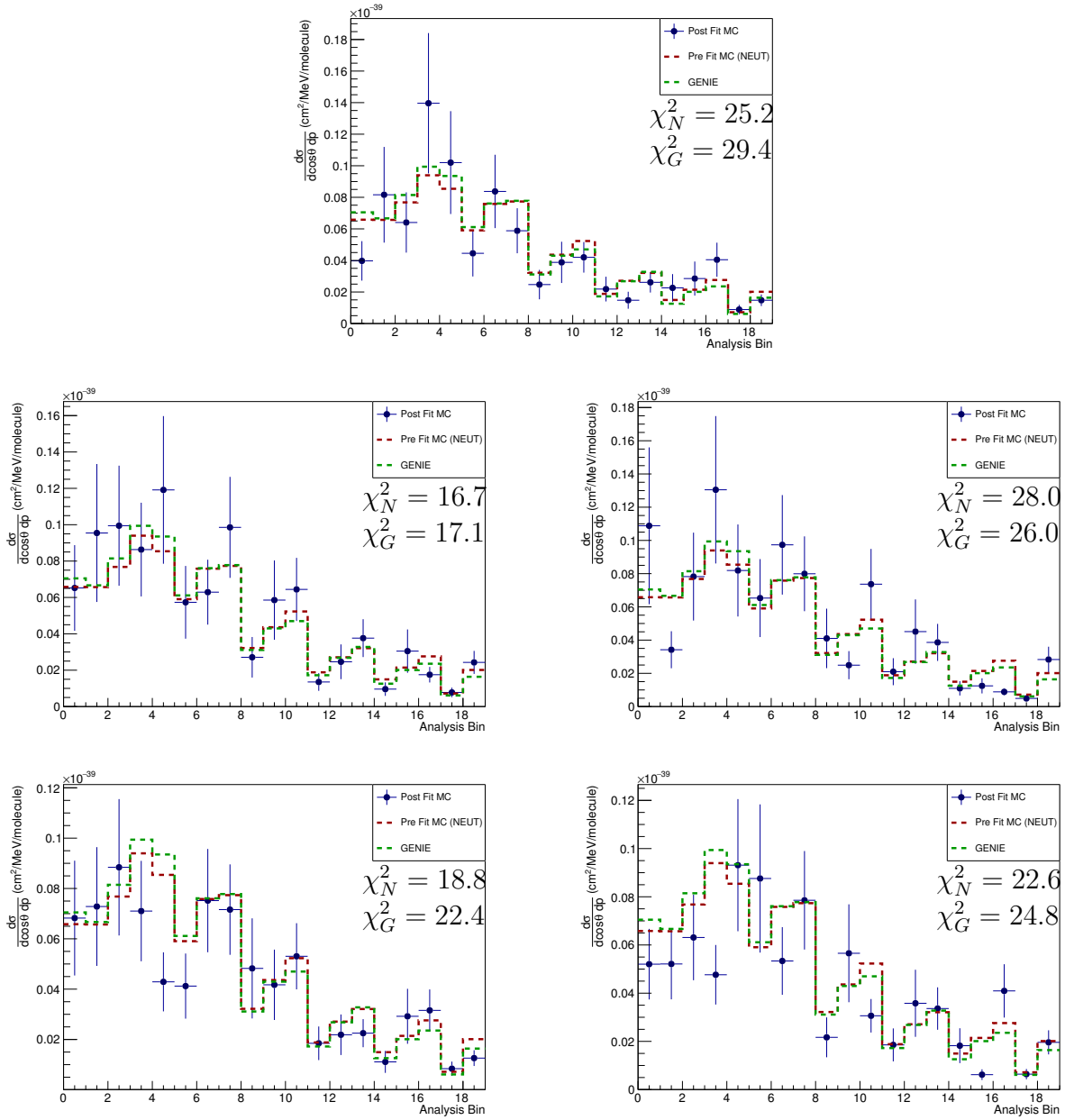

Figure 5.54: Unfolded cross section in each analysis bin in the "nominal FD" sets overlaid on the true cross section from the pre-fit MC (NEUT) and additionally the GENIE prediction.

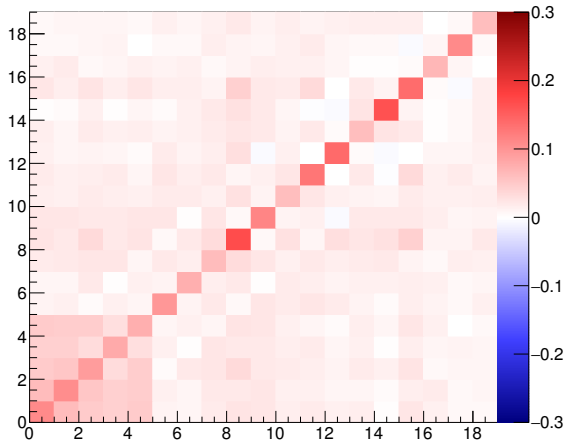

Figure 5.55: Example cross section covariance matrix

Chapter 6

UNBLINDING THE ANALYSIS TO REAL DATA

The plan for unblinding the analysis to the real data is given in the following steps:

1. Check the event rates in the reconstructed kinematic variables (momentum and $\cos\theta$)

    - Check the agreement between the observed distributions in data compared to the MC prediction. The motivation for this is to hopefully prevent behavior in the fitting procedure demonstrated in section 5.7.6 where fake data sets with significant deficits in the signal data distributions compared to the MC prediction were fit. This was the only observed case throughout the fake data studies where the fitting framework failed in some way. With this motivation, acceptable agreement for the purposes of proceeding in the unblinding procedure will correspond to data to MC discrepancies on the order of 10-20% or less.

2. Perform the fit to real data and check only the sideband results

    - Before producing results in the signal region, it should first be checked that the background model parameters are converging to sensible values in the fit while achieving reasonable agreement (χ^2/dof around 1 with improvement in post-fit compared to pre-fit) between the MC prediction and the data in the reconstructed kinematic space. This examination assures that the background model parametrization has enough freedom to properly fit the sidebands in real data.

3. Fully unblind the analysis, Fit to real data and produce the final results, the unfolded double differential cross section on water.

6.1 Data Samples

Table 6.1 gives the data samples included in the analysis along with their PØD water status, software production, and integrated protons on target (PoT).

Table 6.1: Data samples used in the fit with their corresponding PØD water status, ND280 software production, and integrated number of protons on target.

T2K Run Number	PØD Water Configuration	Software Production	Total PoT
5	Water In	6C	0.43×10^{20}
6	Water Out	6M	3.42×10^{20}
7	Water In	6N	2.44×10^{20}

6.2 MC Samples

Table 6.2 gives the Monte Carlo samples included in the analysis along with their PØD water status, software production, and integrated protons on target (PoT).

Corrections are applied to the nominal NEUT production described before. The standard flux tuning using T2K flux release 13a is applied by the Highland2 framework. On top of this, a tuning of the CC-Coherent interactions is applied following the procedure in [30].

Table 6.2: MC samples used in the fit with their corresponding PØD water status, ND280 software production, and integrated number of protons on target.

T2K Run Number	PØD Water Configuration	Software Production	Equivalent Total PoT
5	Water In	6B	20.8×10^{20}
6	Water Out	6B	20.9×10^{20}

6.3 Kinematic Comparisons

Figures 6.1 through 6.4 give the kinematic binned distributions in both the MC and data samples used to produce the final results. Reasonable agreement is seen across all 4 selections.

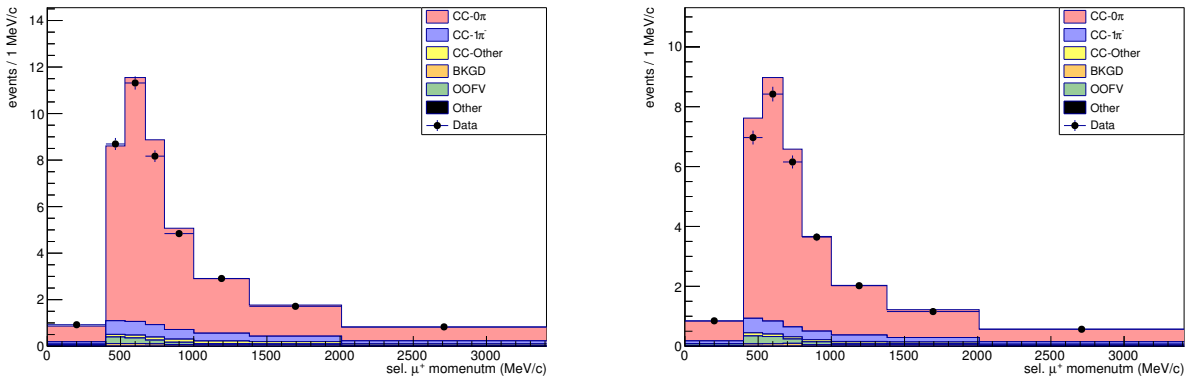

Figure 6.1: Reconstructed selected μ^+ momentum in the PØD water-in (left) and water-out (right) CC-0π selections. Acceptable agreement is seen for the purposes of continuing in the unblinding procedure.

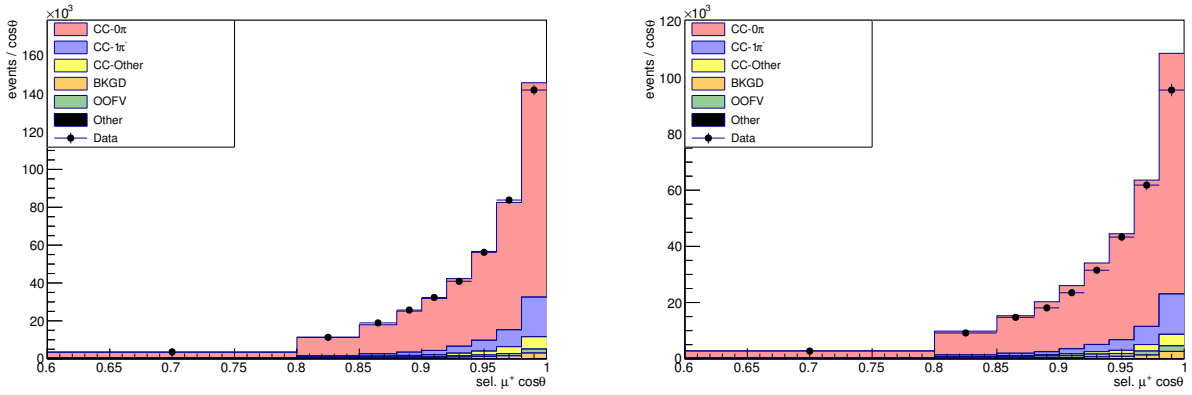

Figure 6.2: Reconstructed selected μ^+ $\cos\theta$ in the PØD water-in (left) and water-out (right) CC-0π selections. Acceptable agreement is seen for the purposes of continuing in the unblinding procedure.

6.4 Sideband Fit Results

Table 6.3 gives the pre-fit and post-fit values of the model parameters in the fit to real data. Figures 6.5 and 6.6 show the pre-fit and post-fit MC predictions for the reconstructed selected μ^+ momentum compared to the data in the CC-1π selections.

6.5 Discussion

From the kinematic binned distributions, agreement is good enough to continue in the unblinding procedure.

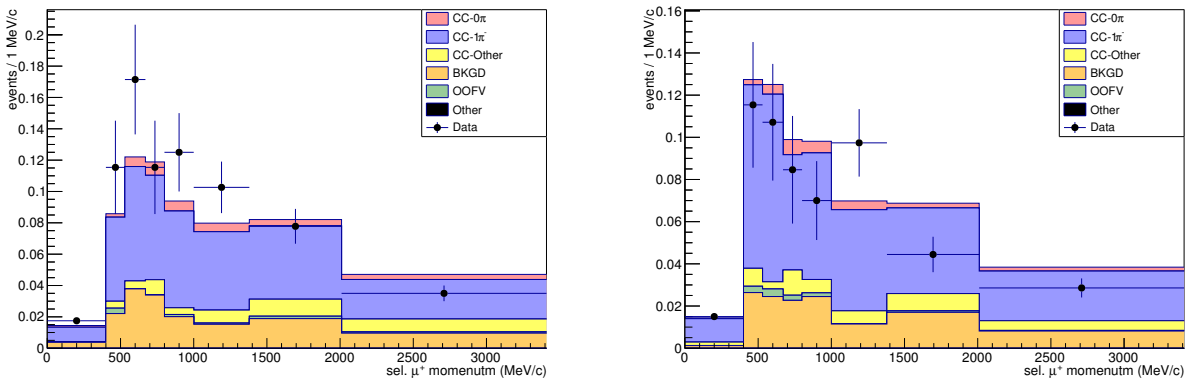

Figure 6.3: Reconstructed selected μ^+ momentum in the PØD water-in (left) and water-out (right) CC-1π selections. Acceptable agreement is seen for the purposes of continuing in the unblinding procedure.

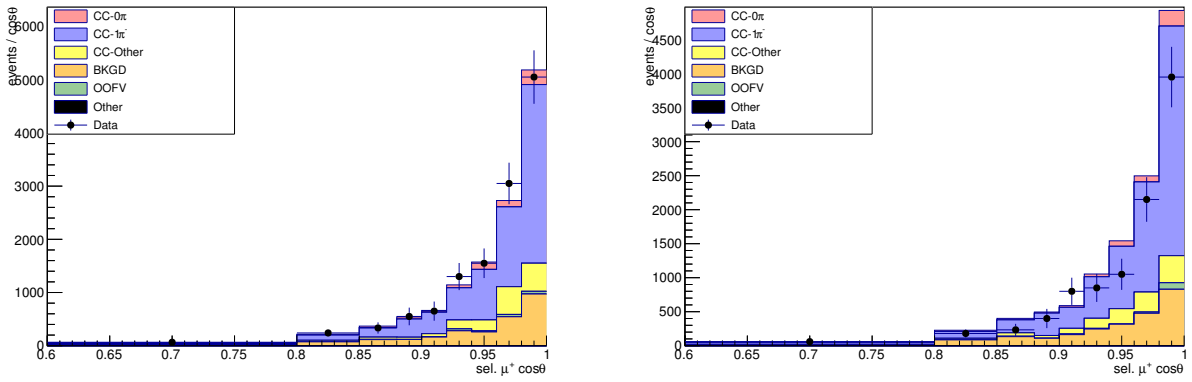

Figure 6.4: Reconstructed selected μ^+ $\cos\theta$ in the PØD water-in (left) and water-out (right) CC-1π selections. Acceptable agreement is seen for the purposes of continuing in the unblinding procedure.

From the sideband fit results, we see that the model parameters converge to sensible values while achieving decent agreement between the post-fit MC prediction and the data. This suggests that the background model parametrization is good enough to properly cover the observed data to MC discrepancies.

Table 6.3: Pre-fit and post-fit values for the background model parameters included in the fit for the fit to real data. Remember that these values are fractional so that a post-fit value for some parameter of 0.9 equates to a 0.1σ decrease from nominal for that parameter.

Parameter	Pre-fit value	Post-fit value
CA5RES	1	1.00
MaNFFRES	1	0.88
BgSclRES	1	1.03
ccnueE0	1	1.00
dismpishp	1	0.98
cccohE0_C	1	1.11
cccohE0_O	1	1.25
nccohE0	1	1.00
ncotherE0	1	1.00
FrInelLow_pi	1	1.03
FrInelHigh_pi	1	1.10
FrPiProd_pi	1	0.95
FrAbs_pi	1	0.98
FrCExLow_pi	1	1.06
FrCExHigh_pi	1	1.05

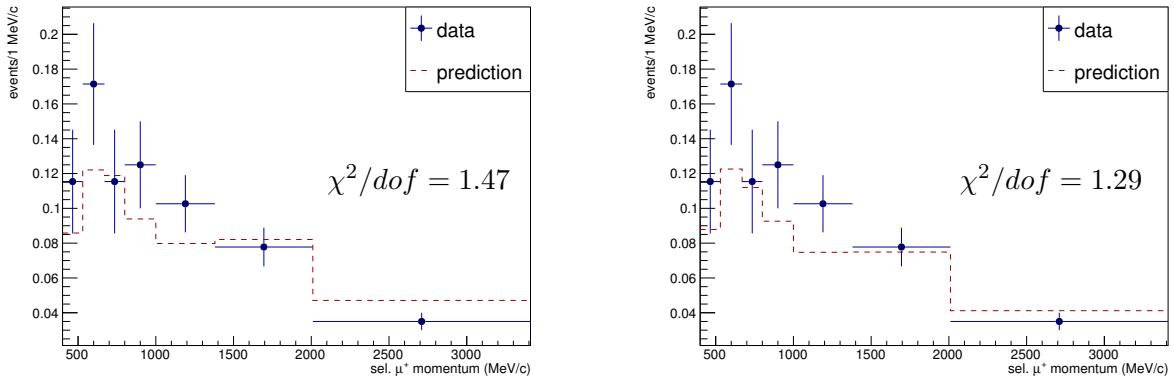

Figure 6.5: Water-in CC-1π selected muon reconstructed momentum in data compared to pre-fit MC prediction (left) and the post-fit MC prediction (right). The χ^2 calculated using all bins in the analysis (not just the integrated momentum bins displayed) is also given.

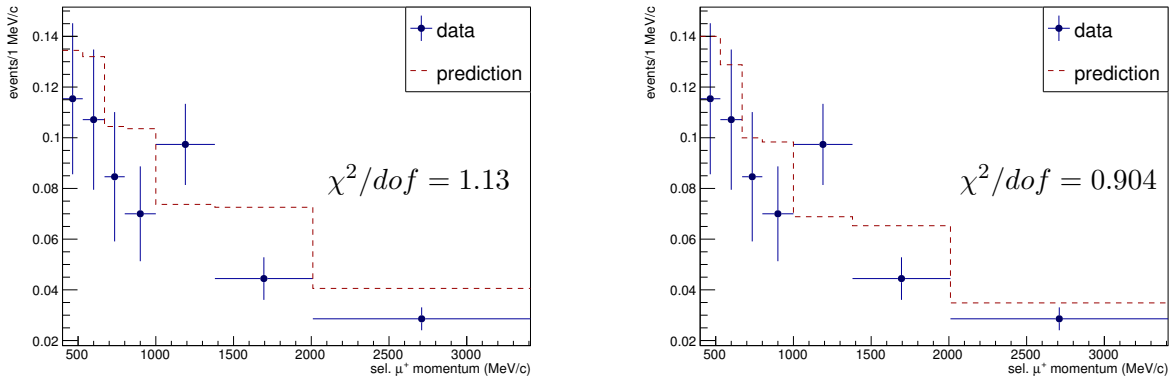

Figure 6.6: Water-out CC-1π selected muon reconstructed momentum in data compared to pre-fit MC prediction (left) and the post-fit MC prediction (right). The χ^2 calculated using all bins in the analysis (not just the integrated momentum bins displayed) is also given.

Chapter 7

RESULTS

Following the results from the initial unblinding presented in the previous section, the fully unblinded results in the signal region of the analysis will now be presented. First, the direct results from the fit in all parameters of the fit will be presented followed by the end result of the analysis: the unfolded CC-0π cross section on water.

7.1 Fit Results

Figure 7.1 gives the L-curve for the fits to real data. We see very similar results compared to the mock data studies presented before. A regularization strength of $p = 1$ still seems reasonable. For the remainder of this section, a regularized result will refer to those produced with the regularized fit with a strength of $p = 1$. Figure 7.2 gives the unfolded event rate in each analysis bin for both the regularized and unregularized cases.

Figures 7.3 and 7.4 give the post-fit values and uncertainties for every parameter included in the fit for the regularized case. Additionally figures 7.5 through 7.8 give an overlay of each fit parameter's post-fit value and uncertainty in both the regularized and unregularized fits.

Figures 7.9 and 7.10 give the fit output covariance matrices in both the unregularized and regularized fits.

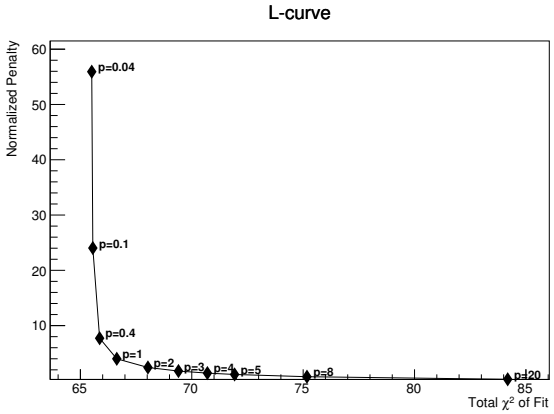

Figure 7.1: L-curve for the fits performed to the real data.

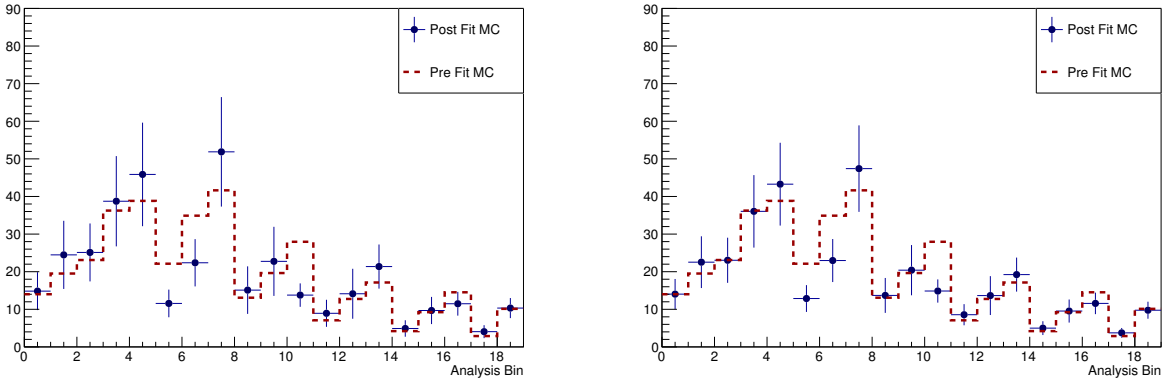

Figure 7.2: The unfolded event rate on water normalized by analysis bin width for the fits to real data in the unregularized fit (left) and regularized fit (right).

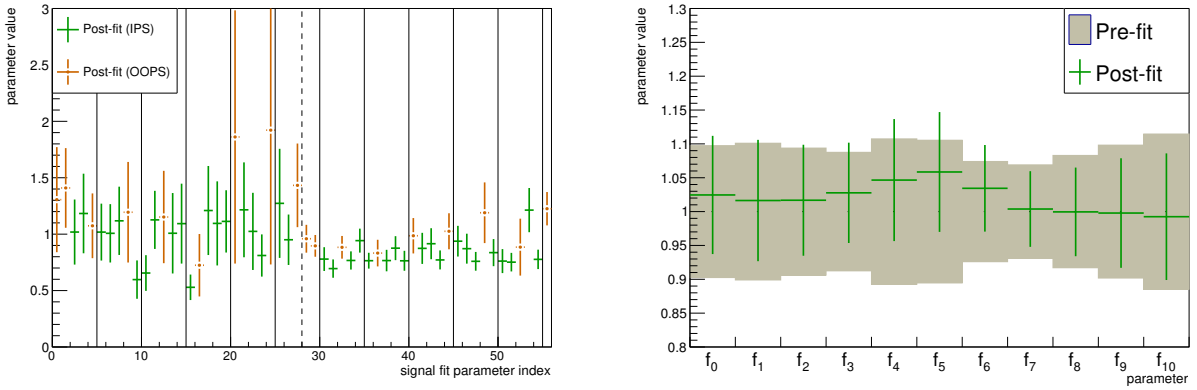

Figure 7.3: Signal c_i and d_i and flux fit parameters post-fit values and uncertainties in the regularized fits to real data.

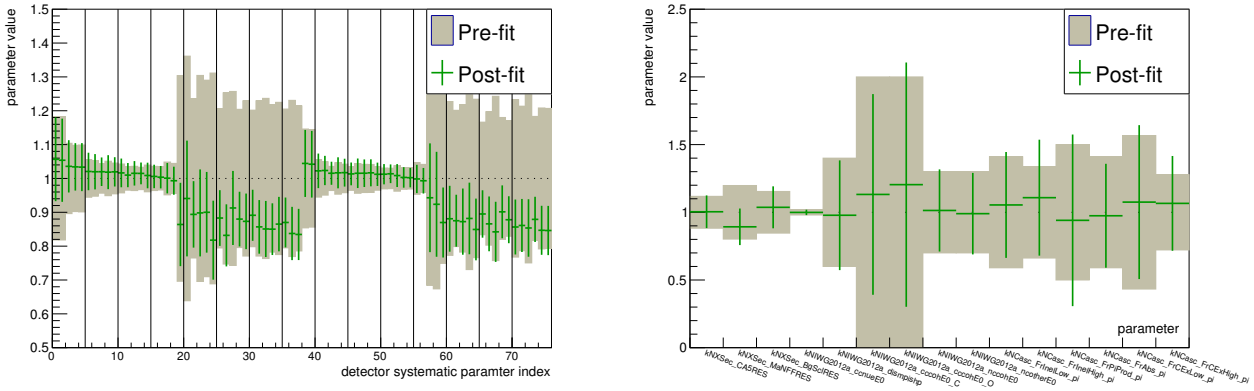

Figure 7.4: Detector systematic and background model fit parameters post-fit values and uncertainties in the regularized fits to real data.

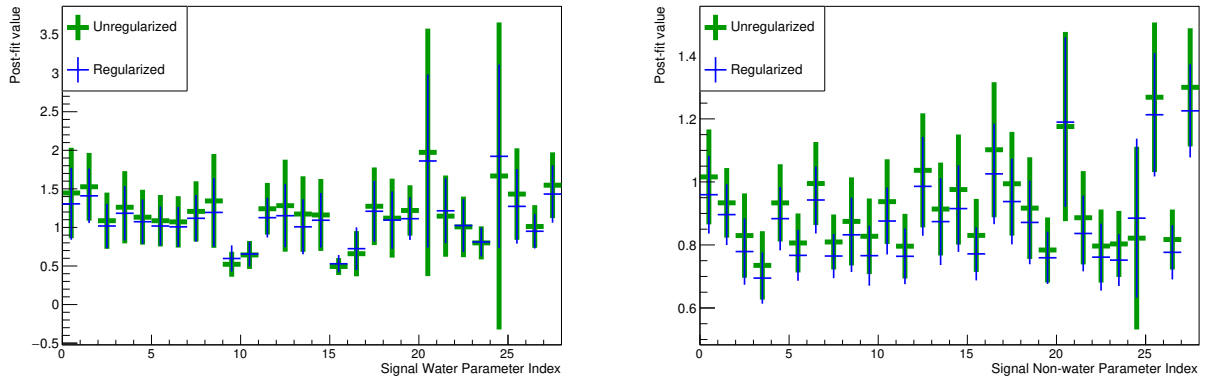

Figure 7.5: Signal parameters post-fit values and uncertainties overlaid for the regularized and un-regularized fits to real data.

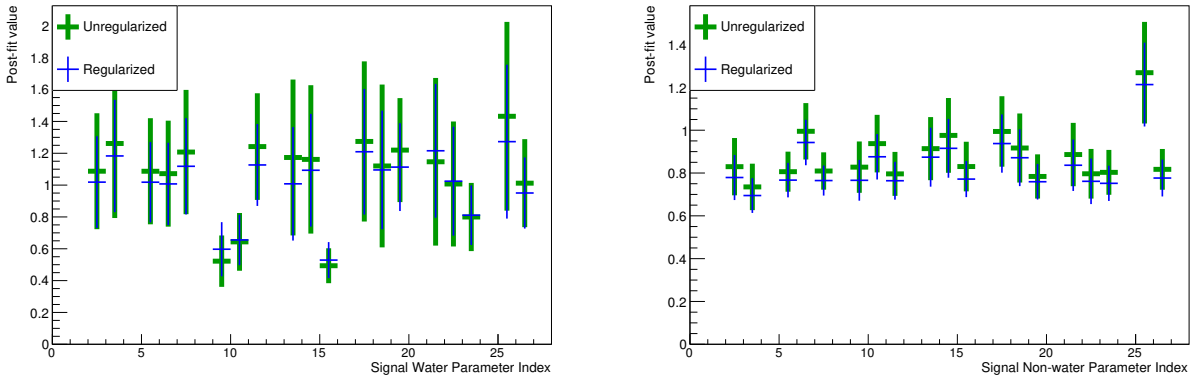

Figure 7.6: Signal in-phase-space parameters post-fit values and uncertainties overlaid for the regularized and un-regularized fits to real data.

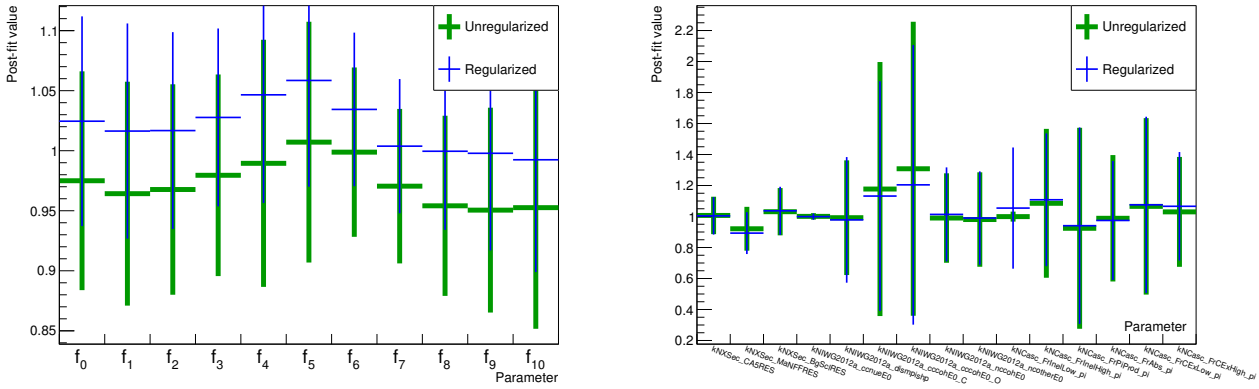

Figure 7.7: Flux and background model parameters post-fit values and uncertainties overlaid for the regularized and un-regularized fits to real data.

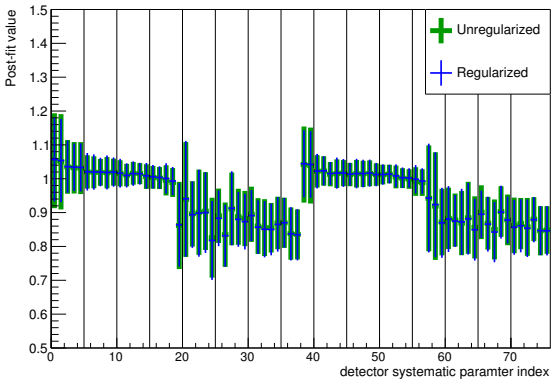

Figure 7.8: Detector systematic parameters post-fit values and uncertainties overlaid for the regularized and un-regularized fits to real data.

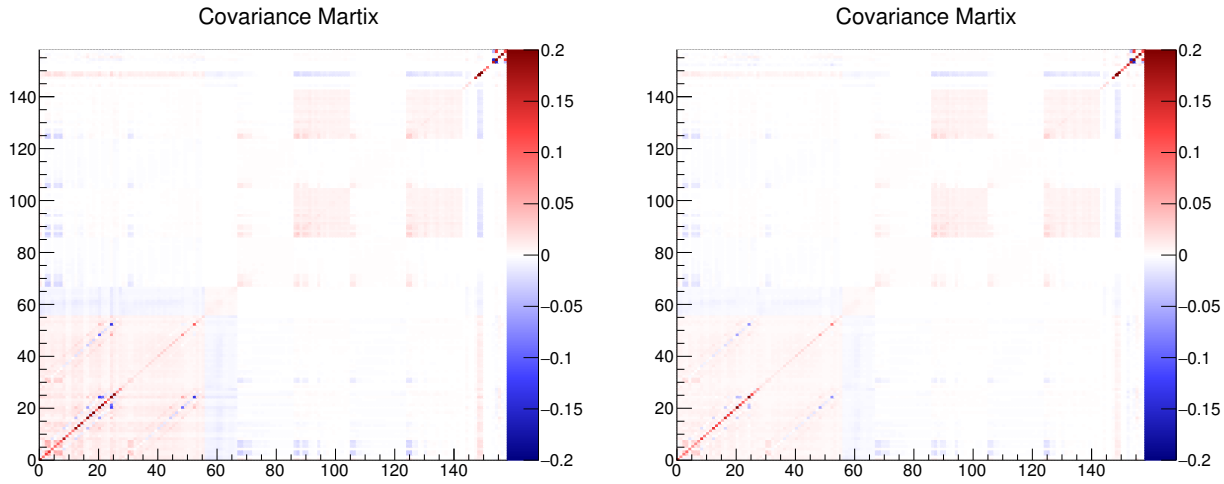

Figure 7.9: Full fit output covariance matrix for the unregularized (left) and regularized (right) fits to data. The indecies on both axes are those given in table 5.7.

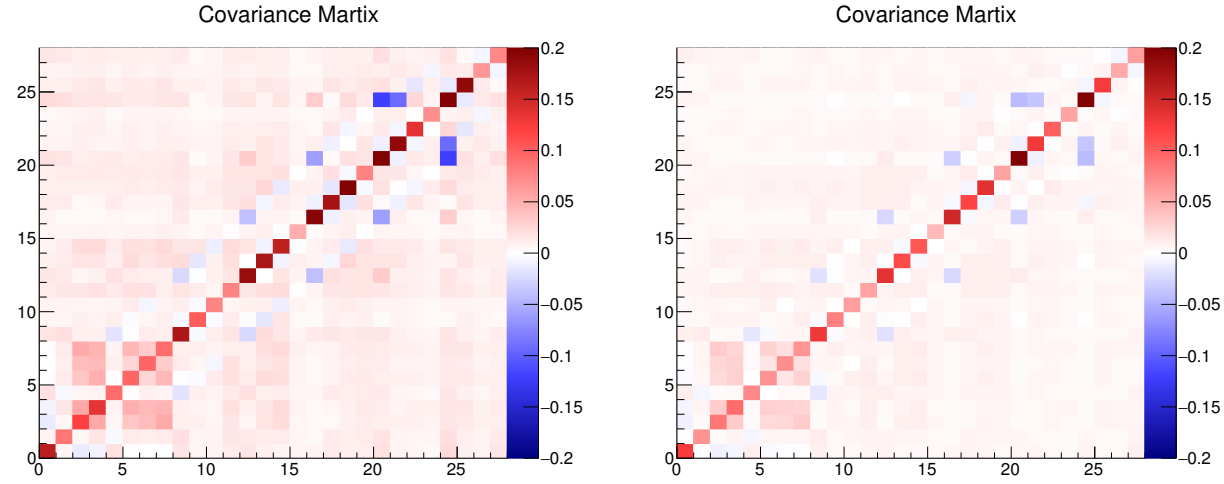

Figure 7.10: Covariance matrix for the 28 signal water fit parameters. Covariance matrix for the 28 signal water fit parameters in the unregularized (left) and regularized (right) fits to data.

7.2 Unfolded Cross Section

Following the fit results for the unfolded event rates presented in the previous section, the methods discussed in section 5.8 are used to produce the double differential cross section on water.

Figures 7.11 and 7.12 give the result in each analysis bin for the case with regularization in the fit, displayed by the selected μ^+ true momentum and $\cos\theta$. Integrating over the $\cos\theta$ bins in each momentum bin gives the single differential (by momentum) result in figure 7.13. The final covariance matrix for the double differential result is given in figure 7.14.

Figures 7.15 and 7.16 give the same results in the case with no regularization in the fit.

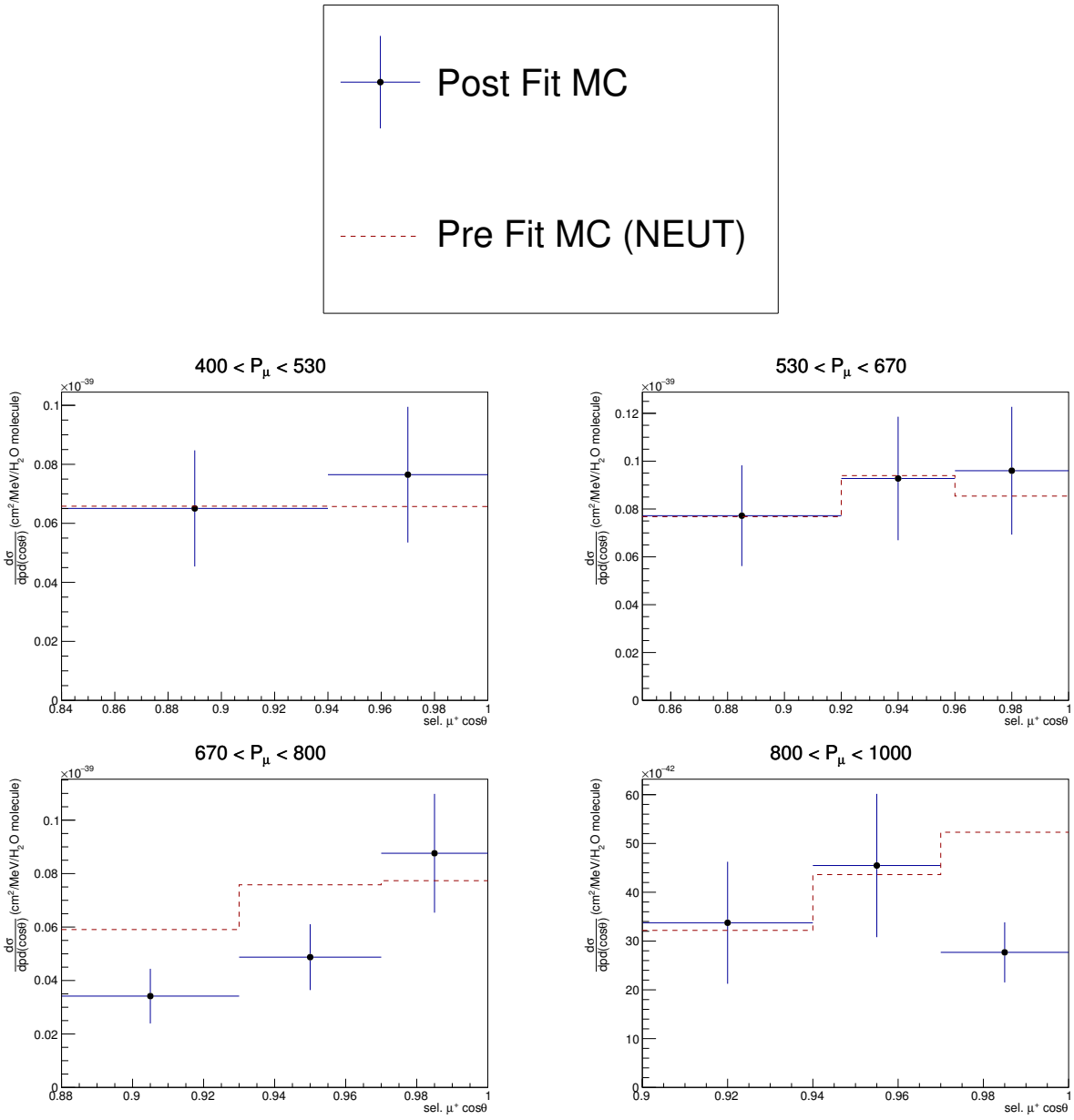

Figure 7.11: Double differential cross section in each of the 19 analysis bins. Overlaid are the result for the regularized case (Post Fit MC) and the NEUT prediction (Pre-fit MC). Error bars include all sources of uncertainty considered in the analysis.

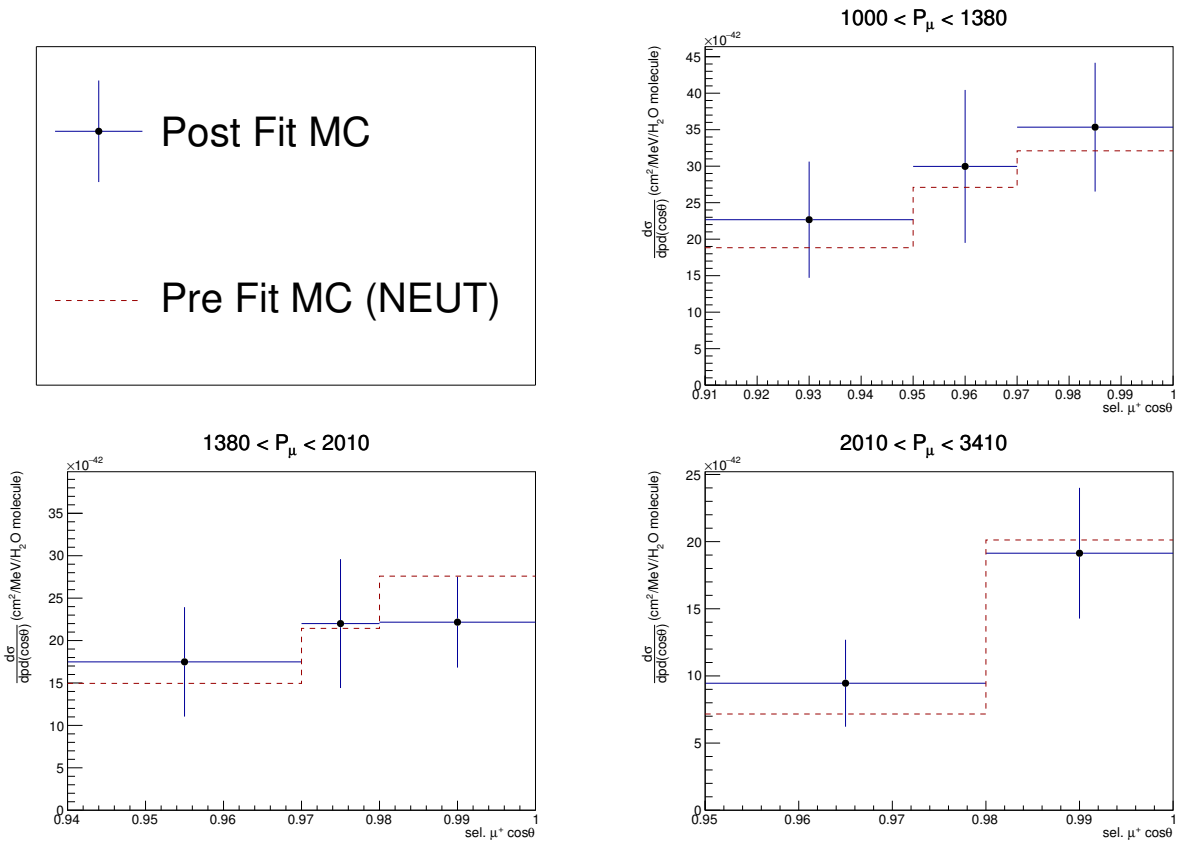

Figure 7.12: Double differential cross section in each of the 19 analysis bins. Overlaid are the result for the regularized case (Post Fit MC) and the NEUT prediction (Pre-fit MC). Error bars include all sources of uncertainty considered in the analysis.

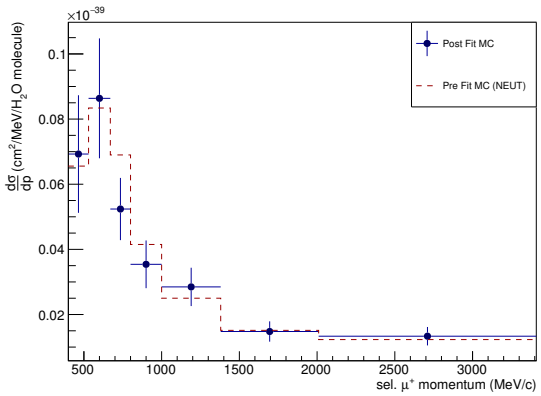

Figure 7.13: Single differential cross section in each of the 7 true momentum bins. Overlaid are the result for the regularized case (post-fit MC) and the NEUT prediction (pre-fit MC). Error bars include all sources of uncertainty considered in the analysis.

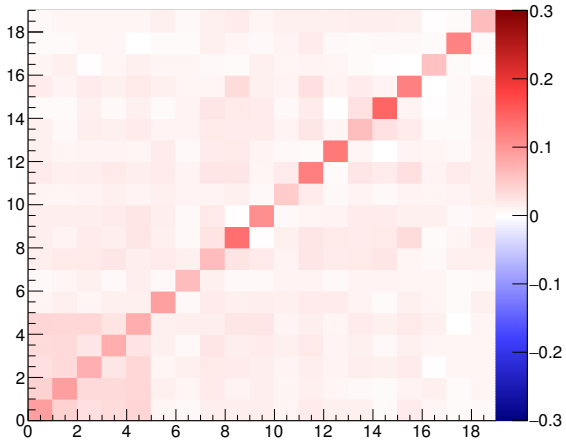

Figure 7.14: Covariance matrix for the regularized double differential result.

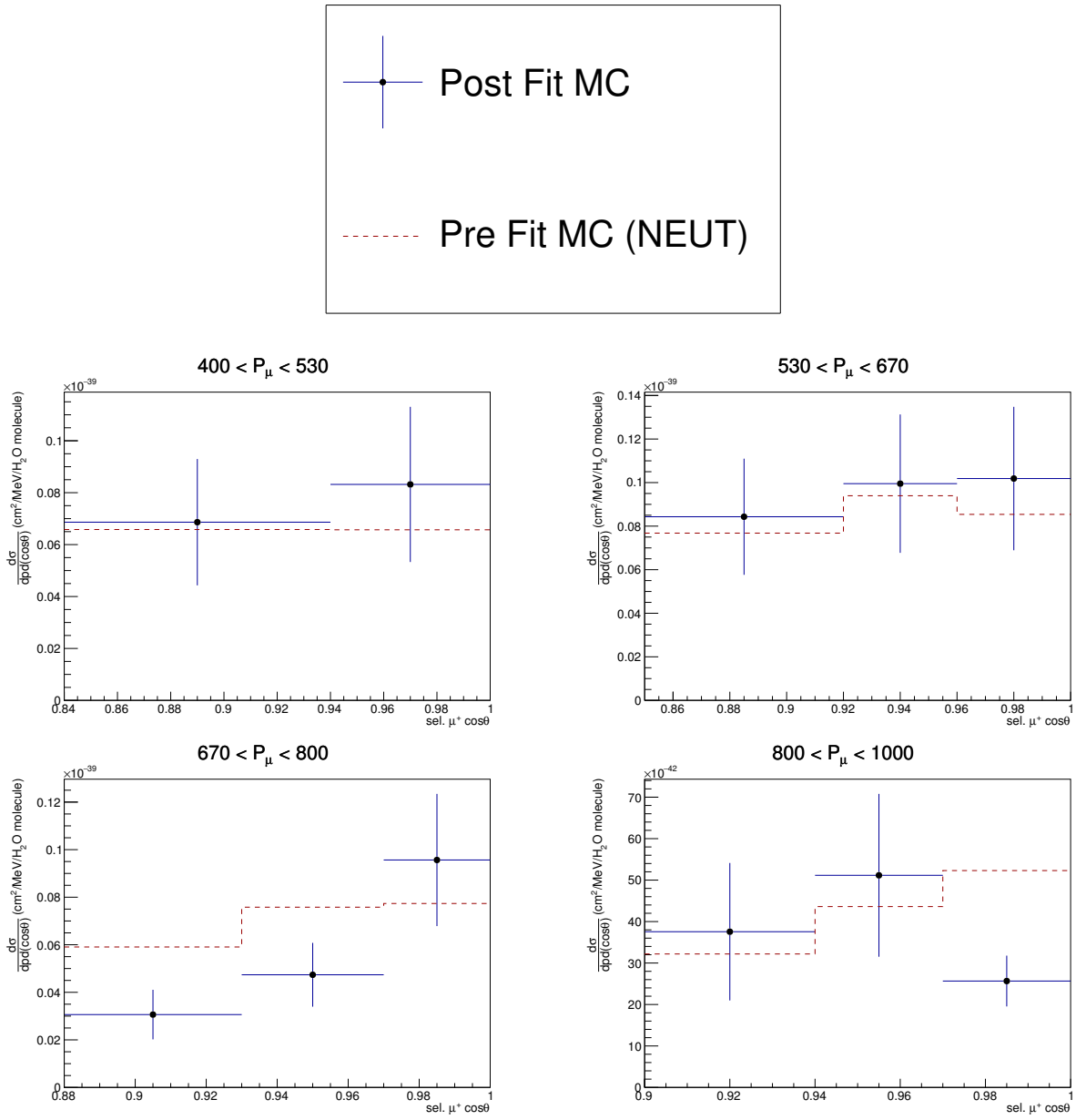

Figure 7.15: Double differential cross section in each of the 19 analysis bins. Overlaid are the result for the unregularized case (Post Fit MC) and the NEUT prediction (Pre-fit MC). Error bars include all sources of uncertainty considered in the analysis.

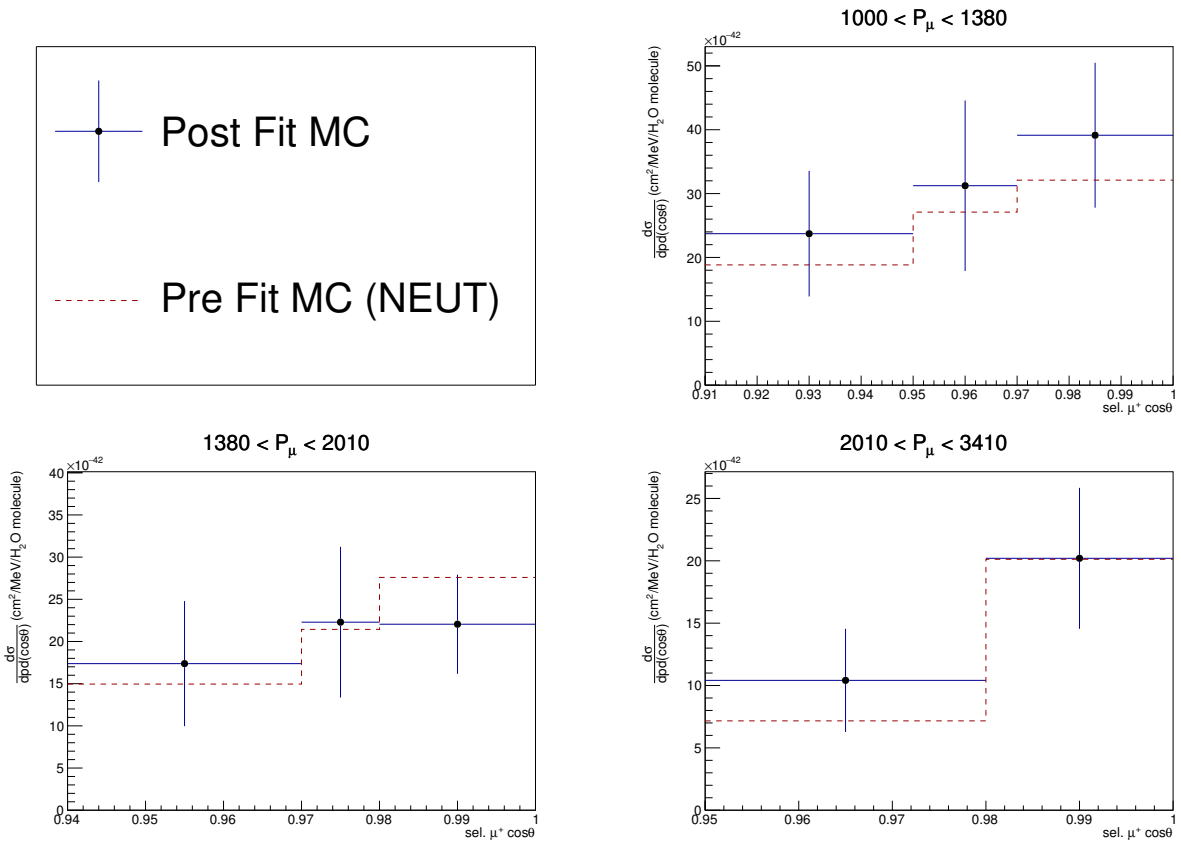

Figure 7.16: Double differential cross section in each of the 19 analysis bins. Overlaid are the result for the unregularized case (Post Fit MC) and the NEUT prediction (Pre-fit MC). Error bars include all sources of uncertainty considered in the analysis.

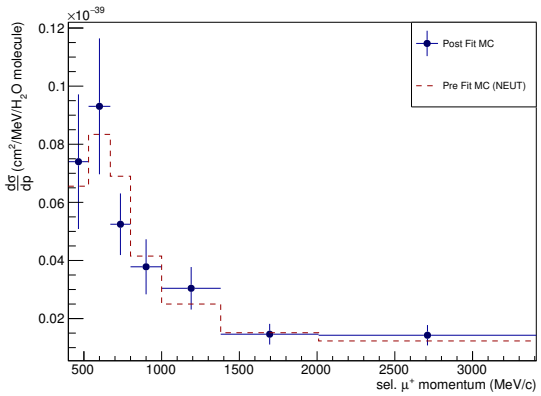

Figure 7.17: Single differential cross section in each of the 7 true momentum bins. Overlaid are the result for the unregularized case (Post Fit MC) and the NEUT prediction (Pre-fit MC). Error bars include all sources of uncertainty considered in the analysis.

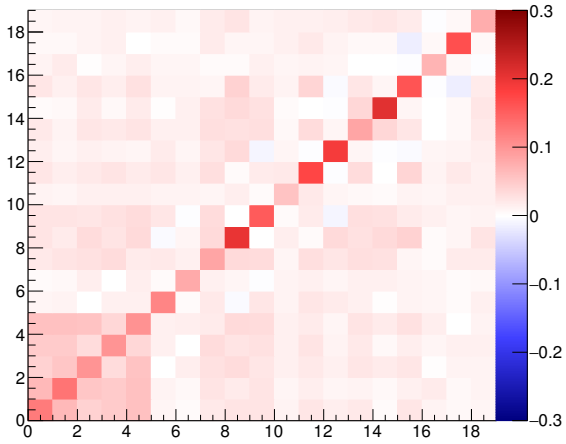

Figure 7.18: Covariance matrix for the unregularized double differential result.

7.3 GENIE Unfolding

As a test of potential bias introduced in the unfolding procedure by the particular interaction generator used in the input MC simulation, a brief study was performed where an MC generated with GENIE was used for parts of the analysis instead of NEUT. As a reminder, the MC simulation is used for the following from equation 3.6:

- Nominal selected event rate predictions for both signal and backgrounds: $N_i^{signal,bkgd}$
- Detector response: smearing matrix, S_{ij}
- Response functions for the background event rates: $w(a)$
- Detector systematic covariance matrix

In the performed study, the GENIE simulation was used only for the first two points above and the nominal NEUT simulation was used for everything else so that the choice of neutrino interaction generator's effect only on the unfolding (detector response) could hopefully be studied.

Using the described configuration, fits were ran with the real data. Figures 7.19 and 7.20 show the reconstructed phase space fit results for the sidebands. We see that while NEUT is still used for the model parameterization and response functions, there is still enough freedom for the fit to adequately predict the background component in the selections.

Figure 7.21 overlays the final differential cross section in each true kinematic bin with full uncertainty where NEUT was used for the efficiency correction in both cases. Also given is the residual formed in each true kinematic bin:

$$r = \frac{\mu_N - \mu_G}{\sigma_N}$$

where μ_N and μ_G are the central values in each bin from the final cross sections and σ_N is the NEUT uncertainty in each bin. Figures 7.22 through 7.24 give the post-fit values and uncertainties for each parameter in the fit overlaid for the NEUT and GENIE fits.

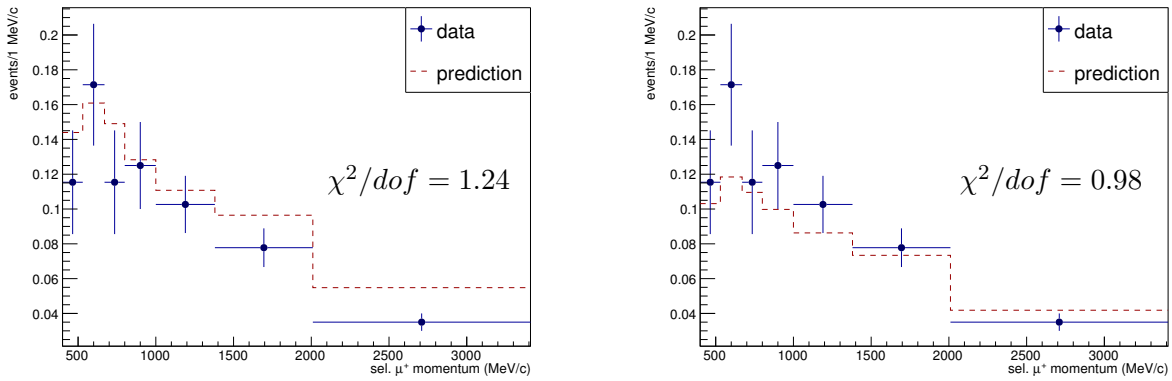

Figure 7.19: Water-in CC-1π selected muon reconstructed momentum in data compared to pre-fit MC prediction (left) and the post-fit MC prediction (right). The χ^2 calculated using all bins in the analysis (not just the integrated momentum bins displayed) is also given.

We see very good agreement ($\chi^2/dof \approx 0.3$) between to the two and conclude that the unfolding procedure is relatively unaffected by the choice of NEUT vs GENIE for the interaction generator.

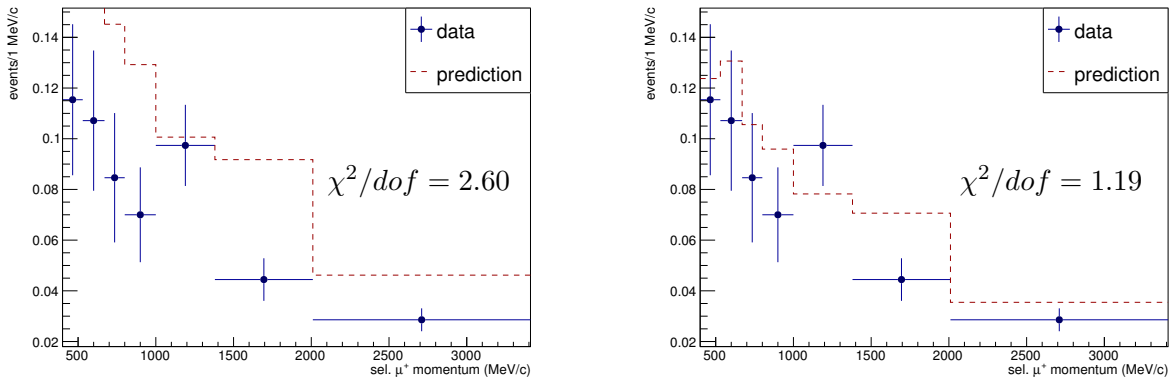

Figure 7.20: Water-out CC-1π selected muon reconstructed momentum in data compared to pre-fit MC prediction (left) and the post-fit MC prediction (right). The χ^2 calculated using all bins in the analysis (not just the integrated momentum bins displayed) is also given. The observed discrepancy in the pre-fit results is expected as GENIE and NEUT have significantly different predictions for CC pion production event rates.

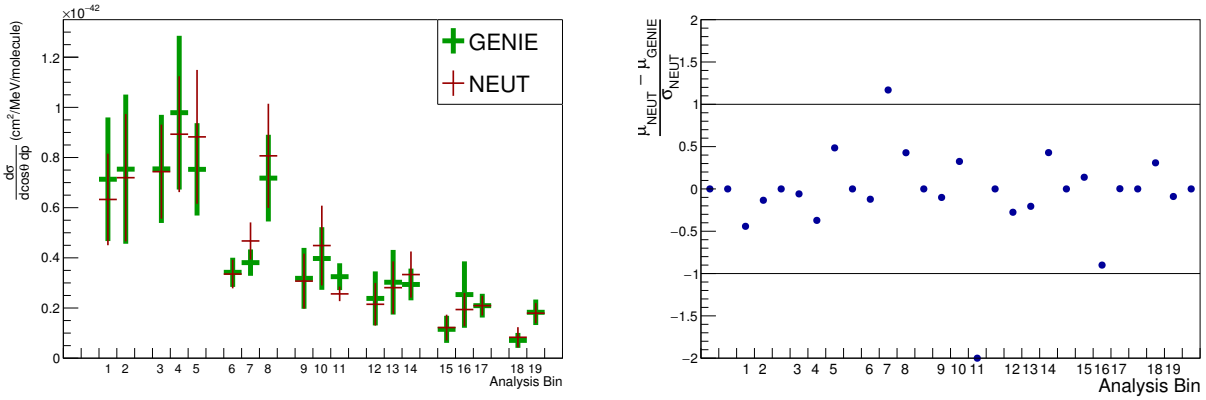

Figure 7.21: Overlay of the unfolded cross sections with NEUT and GENIE used for the detector response (left) and residual formed from the central values and NEUT case errors (right). The χ^2/dof between the NEUT and GENIE result is 0.29.

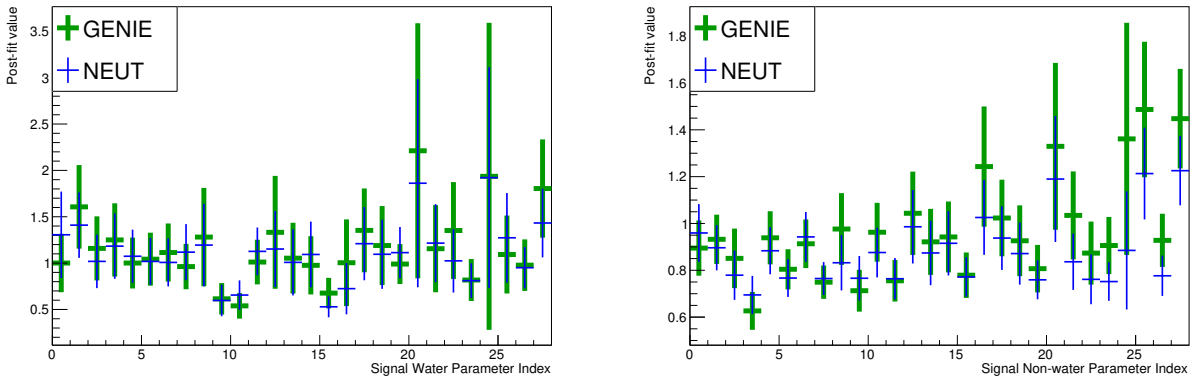

Figure 7.22: Overlay of the signal fit parameters for the NEUT-GENIE unfolding fits.

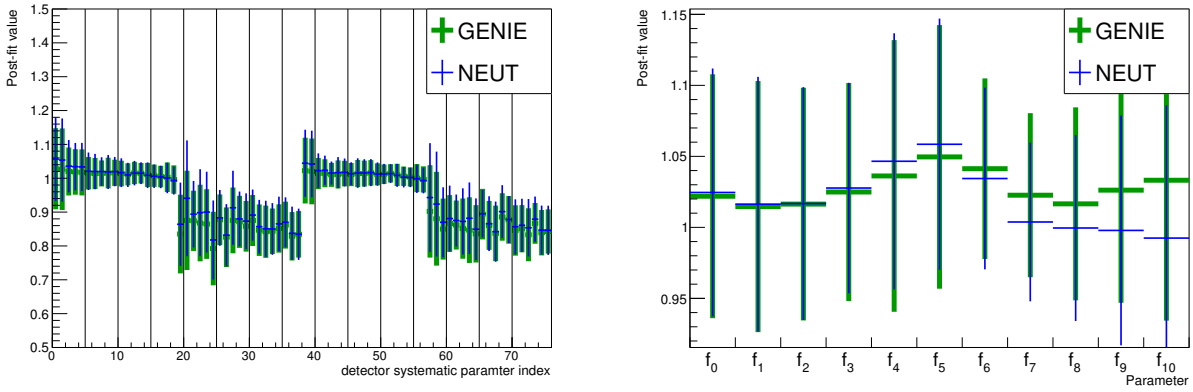

Figure 7.23: Overlay of the detector and flux systematic parameters for the NEUT-GENIE unfolding fits.

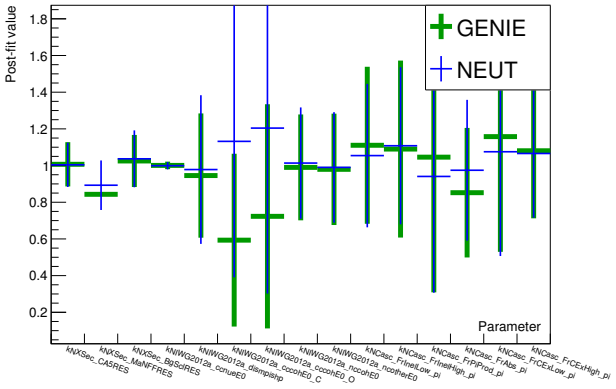

Figure 7.24: Overlay of the background model systematic parameters for the NEUT-GENIE unfolding fits.

7.4 Discussion

In summary, a forward folded likelihood fitting analysis was performed successfully for a interaction target isolated, double-differential cross section. Across many fake data tests, the analysis framework was shown to be sensitive to the CC-0π on water signal and unbiased towards the input simulation. A form of Tikhonov regularization was studied, but was seen to not be necessary in the fits to real data. This likely follows in part from the very good agreement observed between the MC simulation and real data set analyzed. The background model parameterization was seen to be sufficient for good post-fit agreement in the CC-1π sideband region. Using the GENIE neutrino interaction generator instead of NEUT for the nominal signal and background event rates and detector response matrix showed little to no effect on the unfolded data results. Although NEUT and GENIE have very similar models for the CC-0π signal, the background models are significantly different so that this test still demonstrates the model independent nature of the analysis framework.

The resulting CC-0π double differential cross section on water is a world first measurement of its kind that has the potential to help further the understanding of underlying neutrino cross section models both internally at T2K and for whole of the neutrino cross section community. The final results of the analysis are the cross sections in the case of no regularization in the fit. The regularization was seen to introduce a slight bias towards the input MC as expected while reducing the undesired oscillatory behavior that comes in unfolding problems. In the real data fits, the anti-correlations in the post-fit covariance matrix were much smaller than in the fake data fits where regularization was thought to be needed. Because of this, it was decided that it is safer to consider only the case with no regularization as the final result of the analysis.

Table 7.1 gives the cross section in each analysis bin and the definition of those bins with the corresponding covariance matrix given in 7.2 through 7.4.

Integrating over all analysis bins gives a single bin total cross section of:

$$\sigma = (7.844 \pm 1.316) \times 10^{-39} \frac{\text{cm}^2}{\text{water molecule}}$$

where the NEUT and GENIE prediction for the same total cross section are:

$$\sigma_{\text{NEUT}} = 7.526 \times 10^{-39} \frac{\text{cm}^2}{\text{water molecule}}, \quad \sigma_{\text{GENIE}} = 7.416 \times 10^{-39} \frac{\text{cm}^2}{\text{water molecule}}$$

As can be seen in the one bin numbers and the plots presented previously in this chapter, good agreement is seen between the measured cross section in data and the T2K NEUT prediction.

Table 7.1: Final central values for the measurement of the double differential CC-0π cross section on water.

Analysis Bin	Cross Section ($\times 10^{-41} \frac{\text{cm}^2(\text{MeV/c})^{-1}}{\text{water molecule}}$)	Bin Definition (p in MeV/c)
1	6.864	$400 < p \leq 530$ and $0.84 < \cos\theta \leq 0.94$
2	8.318	$400 < p \leq 530$ and $0.94 < \cos\theta \leq 1.0$
3	8.432	$530 < p \leq 670$ and $0.85 < \cos\theta \leq 0.92$
4	9.951	$530 < p \leq 670$ and $0.92 < \cos\theta \leq 0.96$
5	10.19	$530 < p \leq 670$ and $0.96 < \cos\theta \leq 1.0$
6	3.064	$670 < p \leq 800$ and $0.88 < \cos\theta \leq 0.93$
7	4.737	$670 < p \leq 800$ and $0.93 < \cos\theta \leq 0.97$
8	9.565	$670 < p \leq 800$ and $0.97 < \cos\theta \leq 1.0$
9	3.755	$800 < p \leq 1000$ and $0.90 < \cos\theta \leq 0.94$
10	5.116	$800 < p \leq 1000$ and $0.94 < \cos\theta \leq 0.97$
11	2.566	$800 < p \leq 1000$ and $0.97 < \cos\theta \leq 1.0$
12	2.372	$1000 < p \leq 1380$ and $0.91 < \cos\theta \leq 0.95$
13	3.123	$1000 < p \leq 1380$ and $0.95 < \cos\theta \leq 0.97$
14	3.914	$1000 < p \leq 1380$ and $0.97 < \cos\theta \leq 1.0$
15	1.737	$1380 < p \leq 2010$ and $0.92 < \cos\theta \leq 0.96$
16	2.229	$1380 < p \leq 2010$ and $0.96 < \cos\theta \leq 0.98$
17	2.205	$1380 < p \leq 2010$ and $0.98 < \cos\theta \leq 1.0$
18	1.041	$2010 < p \leq 3410$ and $0.95 < \cos\theta \leq 0.98$
19	2.020	$2010 < p \leq 3410$ and $0.98 < \cos\theta \leq 1.0$

Table 7.2: Final covariance matrix for the measurement of the double differential CC-0π cross section on water.

	1	2	3	4	5	6
1	0.1257	0.06581	0.04253	0.04882	0.05872	0.008221
2	0.06581	0.1327	0.05395	0.04999	0.05949	0.01282
3	0.04253	0.05395	0.1	0.03283	0.05548	0.0005719
4	0.04882	0.04999	0.03283	0.1019	0.03867	0.01454
5	0.05872	0.05949	0.05548	0.03867	0.1045	0.01307
6	0.008221	0.01282	0.0005719	0.01454	0.01307	0.1158
7	0.004641	0.007837	0.01666	-0.0004141	0.01725	0.00365
8	0.02032	0.02645	0.02734	0.03204	0.01833	0.02133
9	0.02614	0.01971	0.03275	0.02486	0.03525	-0.003957
10	0.02574	0.02585	0.02256	0.0281	0.03374	0.02443
11	0.01081	0.009326	0.01316	0.01408	0.01407	0.01274
12	0.02318	0.01683	0.02055	0.02674	0.01833	0.02455
13	0.01735	0.01032	0.01399	0.01262	0.01045	0.01896
14	0.0218	0.01225	0.0241	0.02065	0.02583	0.01369
15	0.004615	0.00615	0.01785	0.006306	0.01765	0.002001
16	0.02242	0.01524	0.0241	0.01695	0.02837	0.01288
17	0.01141	0.01787	0.001159	0.00953	0.01545	0.009802
18	0.00643	0.007511	0.0106	0.0131	0.0003522	0.005381
19	0.009497	0.01067	0.01206	0.01303	0.01145	0.01441

Table 7.3: Final covariance matrix for the measurement of the double differential CC-0π cross section on water.

	7	8	9	10	11	12
1	0.004641	0.02032	0.02614	0.02574	0.01081	0.02318
2	0.007837	0.02645	0.01971	0.02585	0.009326	0.01683
3	0.01666	0.02734	0.03275	0.02256	0.01316	0.02055
4	-0.0004141	0.03204	0.02486	0.0281	0.01408	0.02674
5	0.01725	0.01833	0.03525	0.03374	0.01407	0.01833
6	0.00365	0.02133	-0.003957	0.02443	0.01274	0.02455
7	0.08018	0.0143	0.008712	-0.002962	0.0113	0.01408
8	0.0143	0.08447	0.03536	0.0321	0.009341	0.0301
9	0.008712	0.03536	0.2013	-0.0005354	0.0153	0.004889
10	-0.002962	0.0321	-0.0005354	0.1561	0.003693	0.01937
11	0.0113	0.009341	0.0153	0.003693	0.05695	0.02071
12	0.01408	0.0301	0.004889	0.01937	0.02071	0.1764
13	0.008842	0.0234	0.03597	-0.008833	0.009631	-0.001615
14	0.01509	0.02999	0.0279	0.03001	0.00784	0.03266
15	0.01472	0.02909	0.03446	0.02811	0.003933	-0.001167
16	0.01091	0.01056	0.04295	0.01973	0.01215	0.03942
17	0.01022	0.005793	0.004333	0.01492	0.01029	0.01175
18	0.004524	0.01961	0.01037	0.01047	0.01361	0.02221
19	0.008063	0.01798	0.02606	0.01204	0.0145	0.01464

Table 7.4: Final covariance matrix for the measurement of the double differential CC-0π cross section on water.

	13	14	15	16	17	18	19
1	0.01735	0.0218	0.004615	0.02242	0.01141	0.00643	0.009497
2	0.01032	0.01225	0.00615	0.01524	0.01787	0.007511	0.01067
3	0.01399	0.0241	0.01785	0.0241	0.001159	0.0106	0.01206
4	0.01262	0.02065	0.006306	0.01695	0.00953	0.0131	0.01303
5	0.01045	0.02583	0.01765	0.02837	0.01545	0.0003522	0.01145
6	0.01896	0.01369	0.002001	0.01288	0.009802	0.005381	0.01441
7	0.008842	0.01509	0.01472	0.01091	0.01022	0.004524	0.008063
8	0.0234	0.02999	0.02909	0.01056	0.005793	0.01961	0.01798
9	0.03597	0.0279	0.03446	0.04295	0.004333	0.01037	0.02606
10	-0.008833	0.03001	0.02811	0.01973	0.01492	0.01047	0.01204
11	0.009631	0.00784	0.003933	0.01215	0.01029	0.01361	0.0145
12	-0.001615	0.03266	-0.001167	0.03942	0.01175	0.02221	0.01464
13	0.1916	0.009558	-0.00354	-0.00587	0.009351	0.01098	0.0169
14	0.009558	0.08407	0.0376	0.02314	1.103e-05	0.006583	0.02222
15	-0.00354	0.0376	0.2099	0.01001	0.0008091	0.006767	0.02294
16	-0.00587	0.02314	0.01001	0.1627	-0.003424	-0.01665	0.01811
17	0.009351	1.103e-05	0.0008091	-0.003424	0.07102	0.007426	-0.002788
18	0.01098	0.006583	0.006767	-0.01665	0.007426	0.1678	0.00655
19	0.0169	0.02222	0.02294	0.01811	-0.002788	0.00655	0.07824

Bibliography

[1] http://www.pbs.org/wgbh/nova/neutrino/danc-03.html.

[2] https://simple.wikipedia.org/wiki/standard_model.

[3] T. Campbell. *Massive Neutrinos and the See Saw Mechanism*. Master's thesis, Colorado State University, 2014.

[4] F. Halzen and A. D. Martin. *Quarks and Leptons: An Introductory Course in Modern Particle Phsysics*. Wiley, 1984.

[5] C. Giunti and K. C. Wook. *Fundamentals of Neutrino Physics and Astrophysics*. Oxford, 2007.

[6] http://www.hyper-k.org/en/neutrino.html.

[7] N. Abgrall et al. (NA61/SHINE Collaboration). *NA61/SHINE Facility at the CERN SPS: Beams and Detector System.* Journal of Instrumentation **9**. 2014.

[8] D. Drakoulakos et al. *FERMILAB-PROPOSAL-0938*, 2004.

[9] K.S. McFarland. Nuclear Physics B—Proceedings Supplements, 159 2006.

[10] P. Rubinov L. Bellantoni. *D0 note 4845*, 2005.

[11] K. Olchanski S. Ritt, P. Amaudruz. *MIDAS (Maximum Integration Data Acquisition System) http://midas.psi.ch* , 2001.

[12] N. Abgrall et al. *Time Projection Chambers for the T2K Near Detectors* Nuclear Instruments and Methods A, 2011.

[13] A. Ferrari et al. *SLAC-R–773*, 2005.

[14] R. Brun et al. *CERN Report No. DD-EE-84-1*, 1987.

[15] Y. Hayato. Nuclear Physics B - Proceedings Supplements **112**, 171, 2002.

[16] D. J. Gross and C. L. Smith. Nuclear physics b **14**, 337, 1969.

[17] E. J. Moniz et al. Phys. rev. lett. **26**, 445, 1971.

[18] C. Andreopoulos et al. *arXiv preprint 1510.05494*, 2015.

[19] A. Finch. *ND280 Software Workbook* .

[20] S. Agostinelli et al. Nuclear Instruments and Methods in Physics Research Section A: Accelerators, Spectrometers, Detectors and Associated Equipment **506**, 250, 2003.

[21] Daniel Ruterbories. *Measurement of the Total Flux Averaged Neutrino Induced Neutral Current Elastic Scattering Cross Section with the T2K Pi-Zero Detector*. PhD thesis, Colorado State University, 2014.

[22] https://en.wikipedia.org/wiki/hough_transform.

[23] https://en.wikipedia.org/wiki/kalman_filter.

[24] T. Yuan. *Measurement of the Muon-Neutrino Charged-Current Cross Section on Water with Zero Outgoing Pions*. PhD thesis, University of Colorado, 2016.

[25] A. Cervera. *The Highland2 Framework*.

[26] S. Baker and R. Cousins. Nucl. Instrum. Methods Phys. Res. **437**. 1984.

[27] http://lcgapp.cern.ch/project/cls/work-packages/mathlibs/minuit/index.html.

[28] K. Abe et al. (T2K Collaboration). *Measurement of Double-Differential Muon Neutrino Charged-Current Interactions on C8H8 without Pions in the Final State using the T2K Off-Axis Beam.* Physical Review D **93**, 112012, 2016.

[29] S. Dolan. *Probing Nuclear Effects in Neutrino-Nucleus Scattering at the T2K Off-Axis Near Detector Using Transverse Kinematic Imbalances*. PhD thesis, Oxford University, 2017.

[30] T2K. http://www.t2k.org/asg/xsec/meetings/2015/niwg-11092015/cccohwt.